Constraining the Parameters on the Late Time Redshift Evolution of the Stellar Mass - Halo Mass Relation

by

Jesse Benjamin Golden-Marx

A dissertation submitted in partial fulfillment
of the requirements for the degree of
Doctor of Philosophy
(Astronomy and Astrophysics)
in The University of Michigan
2019

Doctoral Committee:

Associate Professor Christopher J. Miller, Chair
Professor Eric Bell
Professor David Gerdes
Associate Professor Keren Sharon

Jesse Benjamin Golden-Marx

jessegm@umich.edu

ORCID iD: 0000-0002-6394-045X

For my family.

ACKNOWLEDGEMENTS

This dissertation represents the culmination of my time as a graduate student in the Astronomy Department at the University of Michigan. For the past four years I worked under the tutelage of Prof. Chris Miller. Four years ago, when I chose to switch advisors and projects, Chris took a chance on me when few other faculty members in the Michigan Astronomy Department were willing to do so. Chris's enthusiasm about and passion for understanding galaxy clusters was evident from my first meeting with him. Over the past four years, Chris has been especially supportive and helpful. Whether giving me feedback on my progress as a scientist, helping me better understand Bayesian statistics, or teaching me how to efficiently write papers, Chris has been a wonderful mentor. I have learned so much from working with Chris, and I am lucky to have had him as my advisor and mentor. I hope that throughout my career we will continue to collaborate, whether on large surveys or smaller projects.

I would also like to thank the remaining members of my dissertation committee–Prof. Keren Sharon, Prof. Eric Bell, and Prof. David Gerdes–for being a supportive and caring dissertation committee. I have appreciated getting to know each of you and discussing your thoughts on my research. Moreover, I would like to thank each of you for taking the time to read this dissertation, which is strengthened because of your comments.

Throughout my time at Michigan, I have gained many wonderful friends and colleagues who have helped to make astronomy more fun and exciting. I particularly am grateful to my fellow Michigan graduate students–Dan Gifford, Matt Miller, Jeb Bailey, Meghin Spencer, Hui Li, Juliette Becker, Ryan Farber, Adam Smercina, Gillen Brown, Juan Remolina, Tyler Gardner, Paco Holguin, Benjamin Setterholm, and Cam Pratt–as well as my friends and collaborators, Guillaume Mahler and Yuanyuan Zhang. I have had many stimulating discussions with each of you about different aspects of our own research, and many of you have helped me figure out different nuances of python coding. Additionally, we've had great fun outside of the office: participating in intramural sports, playing racquetball, going running, attending Michigan football games and Utah Jazz games, watching DC Comics movies, or just hanging out. All these experiences have shaped my time as a graduate student and made it particularly memorable.

Additionally, I would like to thank my family in Ann Arbor: my cousin Margaret Hannon, her husband Dave, and their two sons Henry and Max. Experiencing Ann Arbor with you all has been wonderful and has brought us all closer together. Thank you so much for your support and for sharing so many lunches, dinners, holidays, and celebrations with me. Also, a special thanks to Henry and Max; playing games and reading to you has always provided me with a stress relief during the times when I needed to relax. Because of all of you, Ann Arbor will always be a home away from home.

I would particularly like to thank my parents, Catherine Golden and Michael Marx, for their continued help, love, and support throughout my entire academic journey. Their experience as professors serves as an inspiration for me as I set forth on my own academic journey. I greatly appreciate that whenever I needed to talk to youwhether it was about frustrations with research, planning an upcoming trip, or just about things I've read in the newsyou are both always ready to talk, offer advice, and help guide me to do my very best. I wouldn't have gotten my Ph.D. without your love and support. Thank you so much for always believing in me and supporting me every step of the way.

Lastly, I want to thank my brother, collaborator, and best friend, Emmet Golden-Marx. Graduate school was our first experience living apart, and it has only brought us closer together. Over daily conversations and text messages about TV shows, comic books we've read, or research questions, you have always supported me, and I am forever grateful for our close bond. We've had so many fun memories over the past 6 years: Boston ComicCon, a Birthright trip to Israel, visits home to Saratoga Springs, and trying the many vegan restaurants in Ann Arbor and Boston; the list goes on and on. Thank you so much for always answering my questions and reading drafts of my papers. I look forward to collaborating with you and working together throughout our careers.

Since two chapters of this dissertation have been published, I would like to thank the anonymous referees for their helpful comments on Chapters III and IV. Additionally, some of the work presented in this dissertation is based upon work supported by the National Science Foundation under Grant No. 1311820. The Millennium Simulation databases used in this paper and the web application providing online access to them were constructed as part of the activities of the German Astrophysical Virtual Observatory (GAVO). Funding for SDSS-III has been provided by the Alfred P. Sloan Foundation, the Participating Institutions, the National Science Foundation, and the U.S. Department of Energy Office of Science. The SDSS-III web site is http://www.sdss3.org/. SDSS-III is managed by the Astrophysical Research Consortium for the Participating Institutions of the SDSS-III Collaboration, including the University of Arizona, the Brazilian Participation Group, Brookhaven National Laboratory, Carnegie Mellon University, University of Florida, the French Participation Group, the German Participation Group, Harvard University, the Instituto de Astrofisica de Canarias, the Michigan State/Notre Dame/JINA Participation Group, Johns Hopkins University, Lawrence Berkeley National Laboratory, Max Planck Institute for Astrophysics, Max Planck Institute for Extraterrestrial Physics, New Mex-

ico State University, New York University, Ohio State University, Pennsylvania State University, University of Portsmouth, Princeton University, the Spanish Participation Group, University of Tokyo, University of Utah, Vanderbilt University, University of Virginia, University of Washington, and Yale University.

TABLE OF CONTENTS

CHAPTER

LIST OF FIGURES

Figure

LIST OF TABLES

<u>**Table**</u>

ABSTRACT

We are currently in an era where our current observational capabilities have allowed for an unprecedented number of observations of galaxy clusters. These observations, along with state-of-the art cosmological simulations of galaxy clusters, can be used to constrain the connection between the central galaxy within a cluster and the cluster's dark matter halo. This physically motivated and statistical galaxy-halo connection greatly improves our understanding of how the growth and evolution of central galaxies is intertwined with that of the of underlying and unseen dark matter halos that these galaxies reside in. In this dissertation, I address the galaxy-halo connection via the stellar mass - halo mass (SMHM) relation. The major contributions of this dissertation are to incorporate physically motivated parameters related to the galaxy cluster's galactic population and environment that allow us to tighten the observational constraints on the SMHM as well as characterize how these parameters and the galaxies and clusters they describe evolve in the last 6 billion years.

The specific contributions of the work presented in this dissertation are as follows. In Chapter III, I identify a trend between the magnitude gap, the difference in brightness between the central galaxy and fourth brightest cluster member galaxy, and stellar mass; at fixed halo mass, stellar mass and magnitude gap are linearly correlated due to the central galaxy's hierarchical assembly. Using a hierarchical Bayesian Markov Chain Monte Carlo (MCMC) framework, introduced in Chapter III, which quantifies the parameters of the SMHM relation as well as the impact of incorporating the magnitude gap, I find that magnitude gap is indeed a latent third parameter in the

SMHM relation. Moreover, incorporating the magnitude gap significantly decreases the intrinsic scatter in the SMHM relation and explains the differences between previously published results. In Chapter IV, I extend the analysis of Chapter III to higher redshifts ($z < 0.3$) by revising the hierarchical Bayesian framework to account for redshift evolution. Using this approach, I, for the first time, identify statistically significant redshift evolution in the slope of the observed SMHM relation, which informs us about the late-time growth of the central galaxy. Additionally, I find that the slope of the SMHM relation depends on the aperture used to define the central galaxy's radial extent, which highlights that the outer regions of central galaxies are more strongly correlated with the host halo than the core. Lastly, in Chapter V, I extend our study of redshift evolution out to $z < 0.6$ using Dark Energy Survey data, which allows us to further constrain central galaxy growth and also characterize how the magnitude gap-stellar mass stratification evolves over the last 6 billion years.

CHAPTER I

Introduction

The work presented in this dissertation improves the constraints on the slope, β, and the intrinsic scatter in stellar mass at fixed halo mass, σ_{int}, associated with the galaxy cluster stellar mass - halo mass (SMHM) relationship using hierarchical Bayesian statistical methods and the incorporation of a novel, physically motivated, third parameter in the SMHM relation, the magnitude gap. Additionally, incorporating the magnitude gap as a latent parameter in the SMHM relation allows us to place the first strong observational constraints on the late-time evolution of the SMHM relation. Throughout this dissertation, I treat observations from multiple data sets in a homogeneous manner. Additionally, I have built a well-tested Bayesian MCMC infrastructure that measures the parameters associated with the SMHM relation and can detect any redshift evolution.

To contextualize the questions addressed in this dissertation and the significance of the results, it is important to understand the theoretical backbone this dissertation is built on, the galaxy-dark matter halo connection. Therefore, in this introduction, I explain the galaxy-dark matter halo connection, which links two of the primary components of galaxy clusters, and introduce how this correlation characterizes the formation and co-evolution of the brightest central galaxy (BCG) and the dark matter halo that the BCG forms, evolves, and resides within. Additionally, I explain the

SMHM relation with respect to the galaxy-dark matter halo connection, present the current status of the SMHM relation, explain how the SMHM relation is studied using observations, simulations, and empirical models, and introduce open areas of research that this dissertation addresses.

1.1 The Galaxy-Dark Matter Halo Connection

Galaxy clusters are the most massive gravitationally bound systems in the universe. These structures are characterized as having total (halo) masses greater than $10^{14} M_\odot$ and radial extents on the order of Mpcs. The three primary components that make up galaxy clusters are dark matter, contained within the underlying dark matter halo; the stellar mass, contained in galaxies, of which a significant fraction is found within the BCG (e.g., *Jones and Forman*, 1984; *Lin and Mohr*, 2004; *Aguerri et al.*, 2011; *Harrison et al.*, 2012); and hot X-ray gas. X-ray observations of galaxy clusters, suggest that the BCG is located near the X-ray center of the cluster, which serves as a proxy for the center of the dark matter halo's potential well (e.g., *Jones and Forman*, 1984; *Rhee and Latour*, 1991; *Lin and Mohr*, 2004; *Lauer et al.*, 2014). BCGs are dynamically massive (e.g., *Bernardi et al.*, 2007; *von der Linden et al.*, 2007; *Brough et al.*, 2011; *Proctor et al.*, 2011) and compared to similarly massive galaxies are observed to be radially extended (e.g., *Schneider et al.*, 1983; *Schombert*, 1986; *Zhang et al.*, 2018).

My dissertation focuses on the correlation between the cluster's dark matter halo and the BCG. Specifically, how the evolution and growth of the stellar mass of the BCG and host cluster are correlated and how this correlation evolves over time. As discussed in depth in Section 1.2, our modern understanding of galaxy formation posits that all galaxies form at the center of individual dark matter halos (e.g., *White and Rees*, 1978; *Kaiser*, 1984). Inside a cluster halo, these individual halos are referred to as subhalos. Thus, unlike other cluster members or satellite galaxies, the unique location of the BCG, near the center of the galaxy cluster's dark matter halo, lead astronomers to identify a correlation between the BCG's properties and those of the cluster's dark matter halo. This correlation is representative of the galaxy cluster portion of the galaxy-dark matter halo (galaxy-halo) connection, the physical and statistical link between multiple properties, obtained from observations and/or simulations, of the central galaxy and the host dark matter halo (*Wechsler and Tinker*, 2018).

One fundamental observation, which underscores the galaxy-halo connection, is that in both the local universe (e.g., *Norberg et al.*, 2002; *Zehavi et al.*, 2005, 2011) and at higher redshifts (e.g., *Coil et al.*, 2006; *Zheng et al.*, 2007; *Wake et al.*, 2011; *Leauthaud et al.*, 2012) more luminous central galaxies are found to have a higher clustering measurement, indicative of residing in a more massive dark matter halo. The relationship between the mass of the central galaxy and the mass of the cluster's dark matter halo is referred to as the stellar mass-halo mass (SMHM) relation, which is the primary focus of this dissertation. The SMHM relation is a central component of the galaxy-halo connection, which as discussed in *Wechsler and Tinker* (2018), can be used to infer cosmological parameters, probe the distribution of dark matter, and, as focused on in this dissertation, relate the formation and evolution of central galaxies to their host dark matter halos (e.g., *Tinker et al.*, 2017; *Gu et al.*, 2016). Although the galaxy-halo connection is a nouveau concept, the physical origins of why galaxies and their dark matter halos are intrinsically related is not. Rather, this connection stems from our current understanding of galaxy formation in a Λ Cold Dark Matter (ΛCDM) universe.

1.2 Structure Formation in the Λ CMD Universe

The cosmological principle assumes that the spatial distribution of matter in the universe is homogeneous and isotropic on all scales. However, if this were true on the smallest scales, structure would be unable to form because no region would preferentially gravitationally attract dark matter and baryons away from another region. Therefore, structure formation requires slight deviations from perfect uniformity. Here, I briefly summarize how dark matter halos and the galaxies inside these halos form as a result of these initial inhomogeneities, based on the model presented in *White and Rees* (1978).

1.2.1 Dark Matter Halo Formation

Our current understanding of dark matter halo formation is that the galaxy clusters observed today form as a result of the primordial density perturbations in the quantum field (e.g., *White and Rees*, 1978). Theoretically, these small perturbations rapidly grow over a short time as a result of cosmic inflation. The indirect observational support for inflation resulted from the Cosmic Background Explorer (COBE), a satellite that measured the cosmic microwave background (CMB) and found anisotropies in the CMB that match the theoretical predictions of cosmologically inflated Gaussian initial density perturbations (*Smoot et al.*, 1992).

These initial pertubations grow over time as a result of gravitational instabilities, which *Jeans* (1902) first proposed as a method of astronomical structure formation. Growth resulting from gravitational instability occurs when the gravitational force from over-dense regions attracts dark matter from under-dense regions, creating the initial dark matter halo structure. In contrast, under-dense regions have a weak gravitational force, which leads to the formation of sparsely populated voids. These initial overdensities grow linearly until $\frac{\delta\rho}{\rho} \sim 1$, when the overdensity collapses (*White and Rees*, 1978), where ρ is the mass density. Since these overdensities are composed of collisionless dark matter particles, no shock occurs when an overdensity collapses. Eventually these systems reach a quasi-equilibrium, forming a dark matter halo (*Gunn and Gott*, 1972).

1.2.2 Galaxy Formation

Unlike dark matter, baryonic matter is initially coupled to radiation (photons) and therefore unable to collapse immediately. Once baryons decouple and are no longer supported by photon pressure, they collapse gravitationally. Since dark matter halos have already formed, decoupled baryons are gravitational drawn to the dark matter halos. Thus, dark matter halos serve as the underlying structure within which galaxies form. However, unlike dark matter, baryons are collisional, and when they collapse into the dark matter halo, the collision shock heats and energizes the baryonic gas, which results in baryons having a greater velocity or temperature than the dark matter halo's escape velocity. Thus, before collapsing onto the dark matter halo, the baryons must radiatively cool to a temperature below the virial limit. Over time, the gas within a dark matter halo/proto-galaxy cools via processes such as bremsstrahlung, "breaking radiation", and H_2 formation, which radiate away energy, leaving the baryons with only angular momentum, creating a gaseous disk at the center of the dark matter halo's potential well. Once the gas collapses into a disk, clumps of gas collapse under their own local self-gravity, which is stronger than the gravity from the dark matter halo, and create the first stars within a proto-galaxy.

The previously described scenario is a "bottom-up" galaxy formation model (*Peebles*, 1965), where small structures form first. For galaxies, these are small individual galaxies/proto-galaxies, which are later followed by the formation of clusters of galaxies. As described in Section 1.3, both cluster dark matter halos and their BCGs form and grow hierarchically via merging with the surrounding smaller dark matter halos or the galaxies housed within them, respectively (*De Lucia and Blaizot*, 2007).

1.3 BCG and Halo Hierarchical Growth

1.3.1 Dark Matter Halo Growth

The initial dark matter halos were significantly smaller than the galaxy cluster dark matter halos observed today because like galaxies, in a ΛCDM universe, dark matter halos grow “bottom-up;” smaller halos merge together via hierarchical clustering (*White and Rees*, 1978) mostly at later times to create cluster sized halos (e.g., *De Lucia and Blaizot*, 2007). Galaxy cluster halos grow via mergers of the primary subhalo, which hosts the BCG, with smaller subhalos, which also host galaxies at their centers. Simulations suggest that dark matter halos do not merge automatically; instead, cluster sized halos tidally strip subhalos and then merge (e.g., *Ghigna et al.*, 2000; *De Lucia et al.*, 2004; *Gao et al.*, 2004; *Kravtsov et al.*, 2004). In simulations, the dark matter halo merger is complete once the subhalo dissolves (*De Lucia and Blaizot*, 2007).

Dark matter halo structure formation is best visualized using a halo merger tree, as shown in Figure 1.1, which originally appeared in *De Lucia and Blaizot* (2007). Figure 1.1 illustrates that individual subhalos within clusters grow as a result of mergers with smaller subhalos (in orange) forming a dominant BCG hosting subhalo (shown in green). The orange subhalos have yet to dissolve into the primary subhalo, which highlights that at redshift $z = 0.0$, the cluster dark matter halo still contains smaller subhalos. The triangles represent halos that haven't been accreted onto the cluster's dark matter halo and become subhalos. Based on Figure 1.1, it is necessary to clarify that, from the viewpoint of dark-matter only cosmological simulations, the dominant subhalo, which hosts the BCG, is not identical to the cluster-sized halo (which contains all green and orange subhalos). However, this dominant subhalo accounts for a significant majority of mass within the cluster-sized halo, and observationally, we are unable to distinguish between these two dark matter halos. Therefore, for the

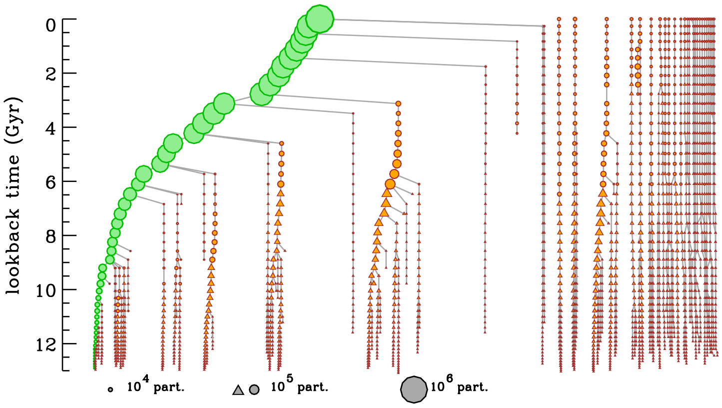

Figure 1.1: Dark Matter Halo Merger Tree. This figure, from *De Lucia and Blaizot* (2007), is the merger tree of a cluster-sized dark matter halo. The green circles represent the primary subhalo of the cluster halo, which hosts the BCG, while the orange circles represent smaller subhalos that have yet to merge with the primary subhalo, and the triangles represent subhalos which have not fallen into the cluster halo.

purpose of this dissertation, we treat the primary subhalo (hosting the BCG) and the cluster halo as the same.

1.3.2 BCG Stellar Mass Growth: The Two-Phase Formation Scenario

As noted in Section 1.2, a galaxy/proto-galaxy forms at the center of most dark matter halos (for halos massive enough to attract baryons and not have stellar feedback completely quench star formation and blow out or heat the remaining cold gas). Dark matter halos grow via mergers, which in turn lead to the hierarchical mergers of the BCG (*White and Rees*, 1978; *Peebles*, 1982; *Blumenthal et al.*, 1984; *White and Frenk*, 1991; *De Lucia and Blaizot*, 2007). Dark matter halo hierarchical growth is therefore the physical motivation for the link between the central galaxy and the cluster's dark matter halo. Although the merger growth is inter-connected, BCG mergers occur after dark matter halo mergers because the BCG's (and other galaxy's) central location allows these galaxies to be largely unimpacted by the tidal forces from the accreting dark matter halo until after the subhalo merges with the primary (BCG hosting) subhalo. After the halo dissolves, BCG mergers occur on a dynamical friction timescale (*De Lucia and Blaizot*, 2007). Dynamical friction is a process that removes energy from the forward motion of galaxies as they pass nearby to one another, transferring the energy to the random motion of their interior stars. This process thus slows down the galaxies and increases the internal energy of the galaxy, which results in the galaxy that is less bound, and thus more susceptible to tidal stripping. The timescale for dynamical friction is proportional to $1/(M_{satellite})$, such that mergers take longer for lower mass satellite galaxies. Therefore, it follows that any observed stellar mass growth in the BCG (from mergers) occurs well after the growth in the cluster's dark matter halo.

Although mergers are the dominant cause of BCG stellar mass growth (*De Lucia and Blaizot*, 2007; *Oser et al.*, 2010), BCG growth/evolution is more complex than just the hierarchical growth scenario described for dark matter halos (Section 1.3.1). BCGs can increase their total stellar mass via star formation (in-situ growth) as well as major and minor mergers (ex-situ growth). However, for BCGs, these processes occur at uniquely different times. Our current theoretical understanding for BCG formation is a two-phase formation scenario (*Oser et al.*, 2010), where BCGs form inside-out (*van Dokkum et al.*, 2010). At high redshifts, z>2, the BCG's dense core forms via in-situ star formation, after which, the outer envelope assembles via the accretion of satellite galaxies that also form at $z > 2$ (this accretion happens in a similar manner to what is described in Section 1.2.1). Thus, the two-phase formation scenario is characterized by the early assembly of stars within galaxies, and the late assembly of the final galaxies themselves (*De Lucia and Blaizot*, 2007; *Oser et al.*, 2010).

Currently, a sizeable amount of observational evidence supports the two-phase formation scenario. Perhaps the most significant evidence comes from *van Dokkum et al.* (2010), which measured the stellar mass growth of the core and outer envelope of massive galaxies over the redshift range $0 < z < 2$, as shown in Figure 1.2. Figure 1.2 highlights that the BCG's core is fully formed by a redshift of $z = 2.0$ and undergoes little stellar mass growth since, a trend that is also found observationally by *Tiret et al.* (2011). In contrast, all recent BCG stellar mass growth occurs in the outer envelope, which suggests that the majority of stellar mass growth (particularly during late-times) for massive galaxies results from minor mergers (*Tiret et al.*, 2011). Moreover, additional observations of the evolution of the luminosity function of red galaxies find that over the redshift range $0 < z < 1$, the majority of stellar mass growth is built up as a result of recent mergers, not in-situ star formation (e.g., *Brown et al.*, 2007; *Faber et al.*, 2007).

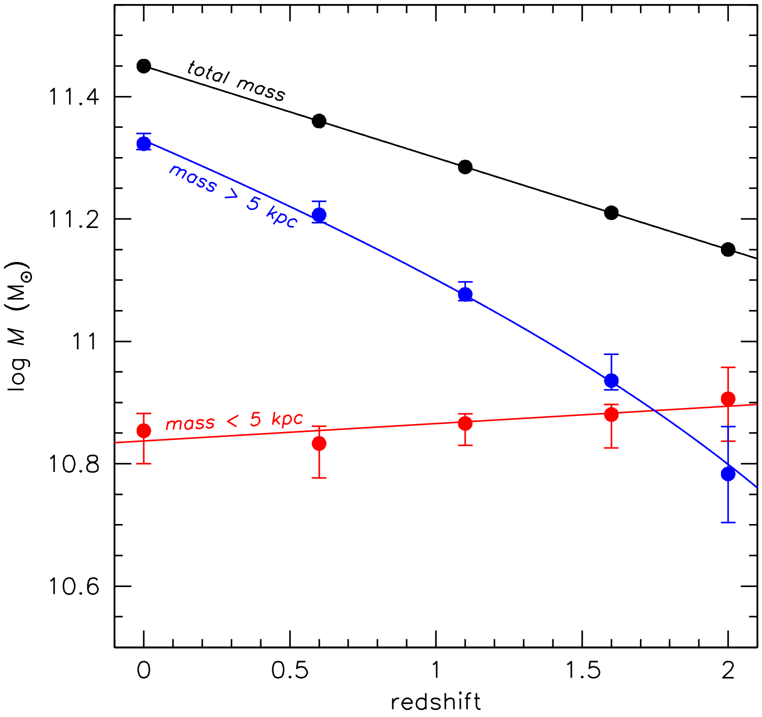

Figure 1.2: The Growth of the Inner and Outer Portions of BCGs. This figure, from *van Dokkum et al.* (2010), shows how the stellar mass contained within the core of the BCG (r < 5kpc) and outer region of the BCG (r > 5kpc) grow with redshift. The stellar mass contained within core stays relatively constant over time, while the stellar mass in the outer envelope increases by a factor of 4.

1.3.2.1 In-Situ Growth of BCGs

As suggested by *Oser et al.* (2010) and shown in Figure 1.2 from *van Dokkum et al.* (2010), in-situ star formation, which results from the efficient cooling and contraction of molecular gas clouds, dominates the stellar mass growth of BCGs over the redshift range $z > 2$, creating a dense central region (*Oser et al.*, 2010). This model of high redshift in-situ growth is in good agreement with the monolithic collapse model (e.g., *Eggen et al.*, 1962; *Partridge and Peebles*, 1967; *Larson*, 1969; *Searle et al.*, 1973; *Larson*, 1975), in which galaxies form as a result of the gravitational collapse of massive gas clouds, and the more recent "cool flow" model (*Kereš et al.*, 2005; *Dekel et al.*, 2009), where large amounts of gas in the intra-cluster medium cool via bremsstrahlung, to form a burst of stars.

One key aspect of the two-phase formation scenario is that stars form early. Using semi-analytic models, *De Lucia and Blaizot* (2007) suggest BCG in-situ growth occurs at remarkably uniform times, such that 50% (80%) of stars form by $z \approx 5$ ($z \approx 3$); similar results are also found observationally for giant red galaxies (*Nelan et al.*, 2005), a description which can be used to characterize BCGs. Thus, star formation dominates BCG stellar mass growth at early times. However, the dominance of in-situ star formation growth does not persist; *Oser et al.* (2010) find that for massive galaxies, the fraction of in-situ formed stars is $\approx$20%, making hierarchical merging far more significant to the overall stellar mass growth of BCGs.

On the surface, the two-phase formation scenario appears to suggest BCG star formation efficiency, or alternatively star formation quenching, depends on redshift, such that star formation efficiency is higher at high redshifts. However, empirical models of galaxy formation (*Behroozi et al.*, 2013b) suggest star formation efficiency only weakly depends on redshift and is instead more strongly dependent on halo mass, with a peak efficiency around $M_{halo} = 10^{12} M_{\odot}$, which is where two-thirds of all star formation occurs. In a hierachical universe, halo quenching still results in star formation occurring at high redshifts, where the halo mass is lower, in agreement with the observations supporting the two-phase formation scenario. Despite the results from *Behroozi et al.* (2013b), more recently, *Tinker* (2017) compare the results of galaxy formation models to observations, which suggest that galaxy quenching (i.e., the process where star formation shuts off when a threshold stellar mass is reached) is the only viable quenching mechanism. In the context of the two-phase BCG formation model, galaxy quenching is also plausible if star formation is quenched once the homogeneous (as discussed in the next paragraph) BCG core is formed (z>2).

One significant observational consequence of the two-phase formation scenario is that BCG cores are remarkably uniform, as shown in *Huang et al.* (2018), which compares the surface mass density of massive galaxies with different total stellar masses (stellar masses integrated out to radii greater than 100kpc) and finds that within 5kpc, the profiles are indistinguishable. This result agrees with results from *Lauer et al.* (2014) that find a small dispersion in BCG luminosity within 14.3kpc. This homogeneity is significant because early BCG photometry measured only the light contained within the central aperture (see Chapter II for a discussion of how BCG magnitudes should be measured and how they are done so in this dissertation). The homogeneity of the central region of the BCG further led BCGs to be suggested as cosmological "standard candle" candidates (*Sandage*, 1972a,b; *Gunn and Oke*, 1975). However, as shown in *van Dokkum et al.* (2010), these earlier measurements do not account for recent stellar mass growth, found in the outer envelope of the BCG, which when accounted for demonstrate that BCGs are not homogeneous (*Huang et al.*, 2018).

1.3.2.2 Ex-Situ Growth of BCGs

Following the formation of the BCG's dense core, the BCG's stellar mass grows as a result of hierarchical major and minor mergers, which result from the mergers of the underlying dark matter halos. This hierarchical growth accounts for the majority of BCG stellar mass growth (*De Lucia and Blaizot*, 2007; *Oser et al.*, 2010; *Tonini et al.*, 2012) and simulations (*Oser et al.*, 2010) suggest that the fraction of accreted mass increases with BCG stellar mass up to ≈ 80% for the most massive galaxies. Thus, ex-situ growth dominates BCG stellar mass growth. As further validation that hierarchical merging results in the BCGs observed today, semi-analytic models of BCG hierarchical growth reproduce the observed redshift evolution in BCG color (*Tonini et al.*, 2012).

Hierarchical merging also leads to a BCG's characteristically large radial extent. Simulations suggest that BCG radial extents increase with the fraction of ex-situ stars (*Oser et al.*, 2010) because these stars are accreted at radii greater than the effective radius of the BCG's core (*Naab et al.*, 2009). Thus, since a BCG's radial extent increases with the number of mergers and the BCG's central location within the cluster make BCGs more likely to have mergers than non-central galaxies (*Solanes et al.*, 2016), it follows that compared to similarly massive galaxies, BCGs are more radially extended (*Bernardi et al.*, 2007; *von der Linden et al.*, 2007; *Lauer et al.*, 2007). Therefore, hierarchical growth is responsible for increasing both the BCG's stellar mass and radial extent.

As noted in Section 1.2.2, hierarchical assembly is driven by the mergers of the underlying dark matter halos. Like for dark matter halos, BCG hierarchical growth can also be visualized using a merger tree, as shown in Figure 1.3, which originally appeared in *De Lucia and Blaizot* (2007). This merger tree illustrates that in the *De Lucia and Blaizot* (2007) semi-analytic model, BCGs grow "bottom up;" the smallest structures form first. Moreover, based on the B-V color of each galaxy, this model follows a two-phase formation scenario, since early on, galaxies transition from star forming (blue/green color) to being "red and dead." Figure 1.3 also highlights that BCG stellar masses grow predominately through mergers between the BCG and other

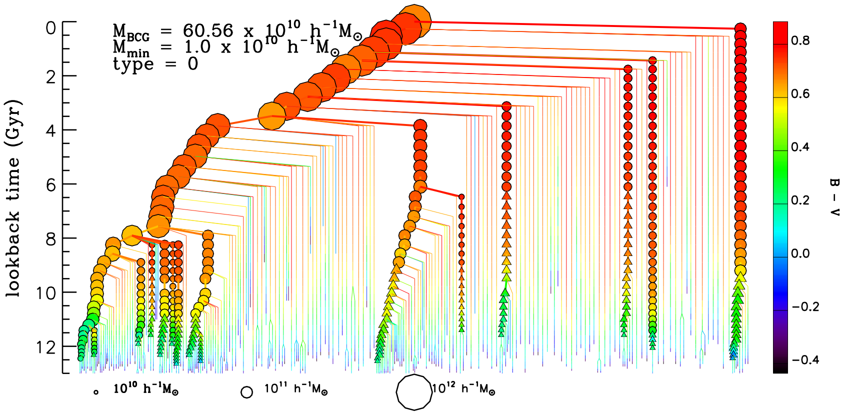

Figure 1.3: BCG Merger Tree. This figure, from *De Lucia and Blaizot* (2007), is a BCG merger tree. At each time step, all circles represent galaxies within the cluster. The circles on the left represent the progenitor of the BCG. Each circle is color coded based on the B-V color and the red color is indicative of a "red and dead" galaxy that is no longer actively forming stars. The minimum galaxy mass shown here is $M_* = 10^{10} M_\odot$. The triangles represent galaxies that have not been accreted onto the cluster.

similarly “red and dead” galaxies within their host cluster halo. Based on the final distribution of galaxies within the cluster shown in Figure 1.3, BCGs account for a significant fraction of the total stellar mass within the cluster, in agreement with observations (e.g., *Lin and Mohr*, 2004; *Harrison et al.*, 2012).

Although the two-phase formation scenario is a rather new concept, aspects of this formation model, such as major/minor mergers resulting in BCG formation have been long studied using simulations and observations. *Dubinski* (1998) used N-body simulations and found merging naturally led to the formation of a central galaxy with surface brightness and velocity dispersion profiles matching those of BCGs. Additionally, many observations suggest that the stellar mass of the BCG increases predominately as a result of dry mergers (e.g., *van Dokkum*, 2005; *Bell et al.*, 2006; *Khochfar and Silk*, 2006; *Naab et al.*, 2006; *van der Wel et al.*, 2009; *Nipoti et al.*, 2009, 2012), which occur when “red and dead” galaxies merge, resulting in little to no new star formation. These galaxies have no excess gas that can then be condensed to form stars as a result of the merger. Although not specified, dry mergers are also apparent in the merger tree shown in Figure 1.3.

While BCGs grow via mergers, not all are major mergers, where the ratio of the merging galaxies is greater than 1:3. As noted by *De Lucia and Blaizot* (2007) and shown in Figure 1.3, most accreted stellar mass comes from galaxies with $M_* \approx 10^{10} M_\odot$, much lower than than of the BCG ($M_* \approx 10^{11.5} M_\odot$). Moreover, *Moody et al.* (2014) and *Oser et al.* (2012) find that the mass ratio between the merging galaxy and the BCG decreases over time (as shown in Figure 1.3), such that late time growth is driven exclusively through minor mergers. In addition to major and minor mergers, other dynamical processes such as tidal stripping and galaxy harrassment also increase the stellar mass of the BCG, particularly in the outermost envelopes. Although these processes are responsible for BCG growth, not all accreted stars become part of the BCG. As discussed in depth in Section 2.4.1, a fraction of accreted stars are ejected from the BCG and become part of the intra-cluster light (ICL), the faint diffuse light that characteristically surrounds the BCG (see Figure 2.2). Therefore, the final mass of the BCG does not equal the sum of the mass from all progenitor galaxies unless the ICL is included.

1.3.2.3 Overall Growth of BCGs

While the two-phase formation scenario for BCGs is accepted, no strong consensus exists for the late time growth ($0.0 < z < 0.5$) of the BCG's stellar mass. In simulations and semi-analytic models, this growth is sizeable, with estimates that BCGs grow by a factor of 1.5-2 (*De Lucia and Blaizot*, 2007; *Guo et al.*, 2011; *Shankar et al.*, 2015). In contrast, many observations find little to no detectable growth over this same redshift range (*Lidman et al.*, 2012; *Lin et al.*, 2013; *Oliva-Altamirano et al.*, 2014; *Burke et al.*, 2015; *Inagaki et al.*, 2015; *Bellstedt et al.*, 2016; *Zhang et al.*, 2016; *Cooke et al.*, 2018). This lack of consistency between observations and simulations/semi-analytic models likely results from differing delineations between the ICL and BCG outer envelope as well as an incorrect modelling of how and when the ICL forms. For example, as noted by *Zhang et al.* (2016), the ICL is fully formed in the *Guo et al.* (2011) semi-analytic model of the MILLENNIUM simulation at $z = 1.0$; however, observations suggest that most growth in the ICL and outer BCG envelope occurs at late times (*van Dokkum et al.*, 2010; *Burke et al.*, 2015). As further evidence that ICL treatment may explain this discrepancy, the semi-analytic model from *Contini et al.* (2018), which grows the ICL via tidal stripping between the BCG and merging satellites find that by $z = 0.4$, BCG growth stagnates and the more recent growth occurs in the ICL, in agreement with observational results of BCG and ICL growth (*Burke et al.*, 2015).

1.3.3 Observational Consequences of Hierarchical Growth: The Magnitude Gap

As shown in Figure 1.3 and noted by *De Lucia and Blaizot* (2007), BCGs grow predominately by merging with smaller galaxies. If these mergers are efficient, *D'Onghia et al.* (2005), using N-body/hydrodynamical simulations, find that hierarchical merging naturally creates a large elliptical galaxy surrounded by fainter galaxies, similar to the end result of the merger tree shown in Figure 1.3. Therefore, it is unsurprising that accretion of intermediate and low mass galaxies results in the formation of a bright central galaxy, as well as in a dip in the cluster's luminosity function (*Zarattini et al.*, 2015; *Solanes et al.*, 2016). This luminosity dip can be more easily quantified observationally using the magnitude gap, the difference in brightness in the r-band between the BCG and 2nd (*Jones et al.*, 2003) or 4th (*Dariush et al.*, 2010) brightest cluster member within 0.5 R_{vir}. Much of the recent published works that study the magnitude gap focus on its use to define Fossil Group Galaxies, large, isolated, x-ray bright elliptical galaxies in group sized halos, which are characterized by large magnitude gaps (e.g., *Jones et al.*, 2003; *D'Onghia et al.*, 2005; *von Benda-Beckmann et al.*, 2008; *Dariush et al.*, 2010; *Harrison et al.*, 2012). However, for the context of the analysis presented in this dissertation, the magnitude gap is a tool to characterize BCG hierarchical growth. Thus, unlike with Fossil systems, we do not make arbitrary cutoffs in magnitude gap to define our clusters.

The magnitude gap has long been theorized to result from galaxy interactions (*Tremaine and Richstone*, 1977) and more recently from the merging of galaxies within clusters (e.g., *Ostriker et al.*, 2019). Hierarchical growth is responsible for the magnitude gap and it's subsequent growth because the BCG's central location with respect to the cluster's gravitational potential well, makes BCGs more likely to merge with fainter galaxies than the 2nd brightest galaxy. Therefore, BCGs grow at the expense of the second brightest galaxy (*Sandage and Hardy*, 1973; *Solanes* *et al.*, 2016). Given the nature of hierarchical growth, it is unsurprising that BCG stellar mass and magnitude increase with the number of mergers (*Hansen et al.*, 2009; *Solanes et al.*, 2016). Thus, since the magnitude of the 2nd or 4th brightest galaxy remains fixed (or decreases if either the 2nd or 4th brightest galaxy merges with the BCG) while the BCG grows, hierarchical growth of the BCG increases the magnitude gap (*Ostriker and Hausman*, 1977; *Solanes et al.*, 2016), yielding a linear correlation between BCG stellar mass and magnitude gap (*Harrison et al.*, 2012; *Golden-Marx and Miller*, 2018).

In a hierarchical growth scenario, BCGs that have the largest magnitude gaps have undergone the most mergers (*Solanes et al.*, 2016). If we assume the merger (dynamical friction) timescale is relatively constant (i.e., the merging galaxies have similar stellar masses), then at a fixed halo mass, BCGs that have undergone the most mergers should be the BCGs that form earliest. Since dark matter halo mergers cause BCG merger stellar mass growth (after some dynamical friction timescale), it follows that in this simplistic picture, the earliest assembling clusters have the most massive BCGs with the largest magnitude gaps. This idyllic picture is unfortunately just that, an idealized version of the truth. As noted in *Deason et al.* (2013) and *Kundert et al.* (2017), a fraction of clusters have magnitude gap values that are impacted by either recent mergers or by the infall of bright galaxies to within 0.5R_{vir}. These examples highlight that some scatter is expected in any correlation between the magnitude gap and formation redshift; however, this can be accounted for when BCGs and their magnitude gaps are treated in a purely statistical manner and not as individual systems.

The trend between stellar mass and formation redshift, the redshift when half of the final halo mass assembles, is shown in Figure 1.4, from *Matthee et al.* (2017). While *Matthee et al.* (2017) use the EAGLE hydrodynamic simulation, this correlation is also measured within the semi-analytic models of the MILLENNIUM simulation

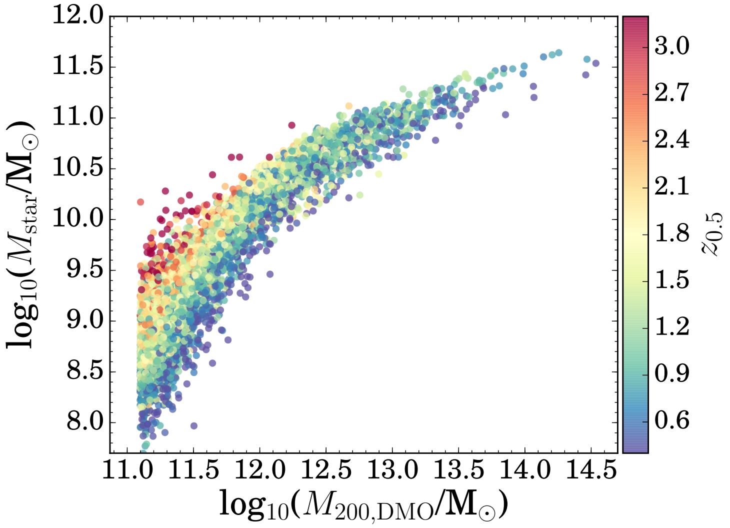

Figure 1.4: Stellar Mass - Halo Mass Relation and Formation Redshift. This figure, from *Matthee et al.* (2017), is the SMHM relation for the EAGLE hydrodynamic simulation color coded by the formation redshift of the halo. This figure highlights that, particularly at low halo masses, early forming clusters have higher BCG stellar mass.

(*Zehavi et al.*, 2018) and the Illustris hydrodynamic simulation (*Artale et al.*, 2018), so the stellar mass-formation redshift correlation is independent of the physical models used to build the EAGLE simulation. Figure 1.4 highlights, particularly at low halo masses, that at a fixed halo mass, the more massive BCGs form earlier. Unfortunately, this trend is not as evident for high halo masses ($M_{halo} > 10^{14} M_\odot$), the mass range analyzed in this dissertation, due to the small simulation box size, which results in a small number of clusters, as well as the larger scatter between formation redshift and stellar mass at higher halo mass (*Zehavi et al.*, 2018). However, the similarities between this trend and the trends shown in Chapters III, IV, and V between the stellar mass and the magnitude gap at fixed halo mass, support the idea that magnitude gap relates to the formation redshift in a hierarchical universe. *Zehavi et al.* (2018) also note that earlier forming halos house more massive central galaxies and have fewer satellite galaxies because an earlier formation time allows for more mergers within a cluster, which may lead to a larger magnitude gap (*D'Onghia et al.*, 2005; *von Benda-*

Beckmann et al., 2008; *Solanes et al.*, 2016). While these trends support a correlation between formation redshift and magnitude gap due to hierarchical growth, *Matthee et al.* (2017) propose that the trend between stellar mass and formation redshift may instead result from earlier forming halos having a higher concentration and forming more stars when feedback is less efficient.

The correlation between formation redshift and magnitude gap has been previously investigated in the context of fossil group galaxy formation. *D'Onghia et al.* (2005) and *von Benda-Beckmann et al.* (2008) used N-body simulations to study fossil group formation and found a weak linear trend between formation redshift and magnitude gap. However, the strength and statistical significance of this relationship is unquantified. Although this dissertation does not address the relationship between magnitude gap and formation redshift beyond hinting at its existence, this is a topic I plan to investigate over the next few years as a postdoc at Shanghai Jiao Tong University. As discussed in depth in Chapter VI, currently, I am planning to use use cosmological simulations, along with machine learning and Bayesian statistical techniques, to measure the strength and scatter of the magnitude gap formation redshift correlation. If a correlation exists, then the magnitude gap may serve as an observational proxy for formation redshift, a cluster property which while readily available in simulations, we are currently unable to measure, even via proxy.

1.4 Quantifying the Galaxy-Halo Connection: The Stellar Mass - Halo Mass Relation

Sections 1.2 and 1.3 describe how the galaxy-halo connection results from the hierarchical assembly of the cluster's dark matter halo, which in turn leads to the assembly of the BCG. Two different approaches are used to study and characterize the galaxy-halo connection: observations (e.g., *Lin and Mohr*, 2004; *Kravtsov et al.*, 2018; *Zhang et al.*, 2016; *Golden-Marx and Miller*, 2018, 2019), which do not rely on simulated data, and semi-analytic or empirical models, which rely on the abundance matching technique to obtain the dark matter halo masses (e.g., *Behroozi et al.*, 2010; *Moster et al.*, 2010; *Behroozi et al.*, 2013a; *Moster et al.*, 2013; *Reddick et al.*, 2013; *Tinker et al.*, 2017; *Behroozi et al.*, 2018; *Moster et al.*, 2018). The work presented in this dissertation does not use empirical models or abundance matching. However, these models and techniques are commonly used when parameterizing the galaxy-halo connection and SMHM relation, so here I briefly summarize the abundance matching ansatz.

A fundamental observation of the galaxy-halo connection is that more massive central galaxies live in more massive dark matter halos (e.g., *Norberg et al.*, 2002; *Zehavi et al.*, 2005; *Coil et al.*, 2006; *Zheng et al.*, 2007; *Wake et al.*, 2011; *Zehavi et al.*, 2011; *Leauthaud et al.*, 2012). The abundance matching ansatz is built on this concept and creates a one-to-one matching that links the most massive galaxies observed in a statistically complete sample, such as SDSS (*Behroozi et al.*, 2010; *Moster et al.*, 2010; *Behroozi et al.*, 2013a; *Moster et al.*, 2013), or a sample with a well understood completeness, to the most massive dark matter halos from a cosmological simulation. Specifically, semi-analytic models often use sub-halo abundance matching (SHAM), which take all subhalos from a dark matter only simulation and uses the subhalos to match to observed galaxies (e.g., *Kravtsov et al.*, 2004; *Tasitsiomi et al.*, 2004; *Vale and Ostriker*, 2004; *Reddick et al.*, 2013). Moreover, since observations suggest that a sizeable scatter between BCG stellar mass and dark matter halo mass exists, recent SHAM matching models (e.g., *Behroozi et al.*, 2010, 2013a; *Tinker et al.*, 2017) also incorporate scatter to better recreate realistic data.

From a purely observational standpoint, for the most massive clusters, where a plethora of observational techniques (discussed in Section 1.4.1) can be used to estimate halo mass, the galaxy-halo connection community's over-reliance on SHAM techniques can be viewed as problematic. As discussed in Chapter III, SHAM distinctly separates the observed BCG from the halo it resides in, which removes any link between inherent, currently unaccounted for latent parameters, such as the magnitude gap, that can be used to tighten the correlation between BCG stellar mass and halo mass (*Golden-Marx and Miller*, 2018). The absence of a correlation with secondary parameters may be somewhat accounted for using conditional abundance matching, a technique where following the standard SHAM approach, a secondary parameter, such as galaxy color, is then one-to-one matched to the stellar mass in narrow bins of halo mass (*Hearin and Watson*, 2013), resulting in a more realistic model of how galaxies populate dark matter halos. Despite this newer technique, it is my opinion that given the proliferation of observational data of clusters currently available (SDSS, DES, the Hyper Suprime Subaru Strategic Program, SPT) as well as upcoming data releases (DESI, LSST), purely observational data should be used whenever possible. However, I note, for low halo masses ($M_{halo} < 10^{13} M_{\odot}$), it is far more difficult to estimate halo masses, and abundance matching is a useful technique for this lower halo mass range.

1.4.1 The Stellar Mass - Halo Mass relation

The link between the stellar mass of the central galaxy and the halo mass of the dark matter halo, better known as the stellar mass-halo mass (SMHM) relation, is a primary aspect of the galaxy-halo connection, and has been measured extensively using observational data (e.g., *Lin and Mohr*, 2004; *Harrison et al.*, 2012; *Lin et al.*, 2013; *Zhang et al.*, 2016; *Lin et al.*, 2017; *Kravtsov et al.*, 2018; *Golden-Marx and Miller*, 2018, 2019), empirical models, (e.g., *Behroozi et al.*, 2010; *Moster et al.*, 2010; *Behroozi et al.*, 2013a; *Moster et al.*, 2013; *Tinker et al.*, 2017; *Behroozi et al.*, 2018; *Moster et al.*, 2018), and simulations (e.g., *Gu et al.*, 2016; *Matthee et al.*, 2017; *Pillepich et al.*, 2018). While this dissertation focuses on observationally measuring

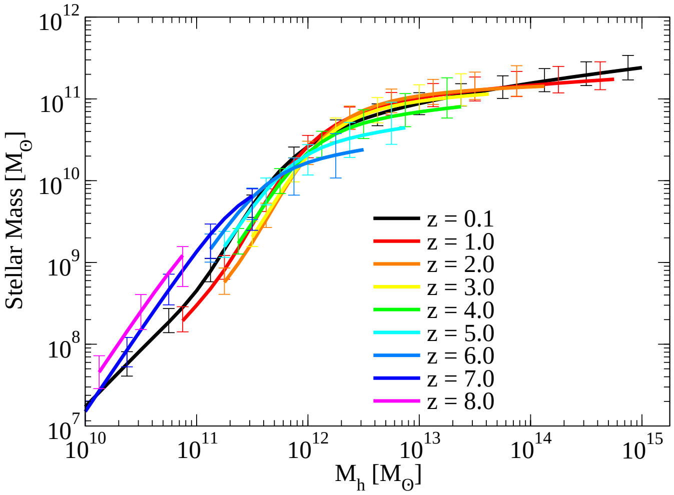

Figure 1.5: Stellar Mass - Halo Mass Relation Across all Halo Masses. This figure, from *Behroozi et al.* (2013a), is the SMHM relation determined using the SDSS luminosity function abundanced matched to halos masses from the Bolshoi dark matter only simulation. This figure illustrates how the SMHM relation evolves as both a function of halo mass and redshift.

the SMHM relation for galaxy clusters, it is important to understand that the SMHM relation extends to low mass halos, where halo mass is predominately estimated using SHAM.

The shape of the SMHM relationship is shown in Figure 1.5, from *Behroozi et al.* (2013a). This SMHM relation is constructed using the SDSS luminosity/stellar mass function abundance matched (with scatter) to halo masses from the Bolshoi dark matter only simulation. The SMHM relation's shape is fit by a double power law, of the general form:

$$\log_{10}(M_*) = Normalization + \beta_1(\log_{10}(M_{halo}/M_{halo_0})) + \beta_2(\log_{10}(M_{halo}/M_{halo_0}) \quad (1.1)$$

where β_1 and β_2 are the slopes of the high and low halo mass regime, respectively, and M_{halo_0} is the location of the pivot point. The pivot point, where star formation efficiency peaks (*Behroozi et al.*, 2013b) is measured at $M_{halo} \approx 10^{12} M_{\odot}$ and as shown in Figure 1.5 is independent of redshift (*Behroozi et al.*, 2013a). The slopes of the high and low halo mass SMHM relations differ because of the different feedback processes that quench star formation in each regime. At the low halo mass end, stellar feedback, predominately from supernovae, is the dominant process, while at the high mass end, supernovae feedback is not energetic enough to quench star formation; instead, AGN feedback, from supermassive black holes quenches star formation (e.g., *McNamara and Nulsen*, 2007; *Cattaneo et al.*, 2009; *Fabian*, 2012). Thus, star formation efficiency peaks at the pivot point because many galaxies of this size lack AGN while having potential wells large enough to render stellar feedback negligible. One additional feature introduced in Figure 1.5 is that there may be some modest evolution in the slope of the SMHM relation with redshift, which will be discussed in Section 1.4.4.

While the SMHM relation extends to low halo masses, purely observational studies focus on the cluster mass regime, which is fit by a single power law, as done in Chapters III, IV, and V. However, even for the cluster mass regime, stellar mass and halo mass are difficult to estimate (discussed in Sections 1.4.1.1 and 1.4.1.2) because neither is directly observable. Therefore, it is unsurprising that the earliest observational SMHM relations used proxies for these measurements. *Edge* (1991) found a linear correlation between the absolute magnitude used as a proxy for stellar mass, and the X-ray luminosity used a proxy for halo mass. Similarly, *Lin and Mohr* (2004) identify a similar scaling relation between the BCG luminosity used as a proxy for stellar mass, and the halo mass, estimated via a scaling relation between X-ray luminosity and halo mass. These initial results highlight that the linear trend between stellar and halo mass is not a property of SHAM and show that a sizeable scatter exists in stellar mass at fixed halo mass. Despite the difficulty in estimating stellar and halo masses, recent versions of the SMHM relation no longer use proxies for these measurements. Therefore, it is important to understand how these masses can be estimated and what systematic uncertainties are associated with these estimates.

1.4.1.1 Measuring Stellar Mass

Although the earliest versions of the SMHM relation used absolute magnitude or luminosity, more recent SMHM relations use estimates for the BCG's stellar mass, which may correlate better with halo mass than luminosity (*Tinker et al.*, 2017). Since a variety of versions of the SMHM relation are published, it is important to remind the reader that in this dissertation, the stellar mass in the SMHM relation is just the stellar mass contained within the BCG, not the sum of all stellar mass within the cluster.

Observational estimates of BCG stellar masses rely on accurate BCG photometry measured in multiple wavelength bands (at least two for color measurements). As discussed further in Chapter II, BCG magnitudes are difficult to determine observationally because of the inability to disentangle the BCG and ICL (as shown in Figure 2.1). Additionally, photometric issues relating to the background plague BCG magnitudes, as is the case for low-redshift SDSS photometry (e.g., *Bernardi et al.*, 2007; *von der Linden et al.*, 2007; *Kravtsov et al.*, 2018). Once BCG magnitudes are obtained and the associated uncertainty in their magnitudes is calibrated, BCG stellar mass can be estimated.

Stellar masses are generally estimated using spectral energy distribution (SED) fitting (*Shankar et al.*, 2014; *Zhang et al.*, 2016; *Tinker et al.*, 2017; *Golden-Marx and Miller*, 2019, e.g.,), done using programs such as EzGal (*Mancone and Gonzalez*, 2012). SED fitting relies on the photometric apparent magnitudes and their associated uncertainties, as well as the redshift of the cluster/BCG. To estimate stellar mass, a variety of SEDs are generated using multiple formation redshifts, metallicities, star formation histories, and normalization parameters for a fixed stellar population synthesis (sps) model (e.g., *Bruzual and Charlot*, 2003). For each BCG, the best fit SED is determined by minimizing the chi-squared statistic between the observed and modelled BCG magnitudes measured in the same wavelength bands. Using the best fit

SED, stellar mass is estimated assuming an initial mass function (IMF) (e.g., *Salpeter*, 1955; *Kron*, 1980; *Chabrier*, 2003). In *Golden-Marx and Miller* (2019) and Golden-Marx et al. (in prep.), this approach is used for the *Bruzual and Charlot* (2003) sps model and a *Salpeter* (1955) IMF, with a fixed metallicity, formation redshift, and star formation history to model a "red and dead" fiducial BCG. To determine BCG stellar masses, we marginalize over the normalization parameter. A second, similar approach, used in *Golden-Marx and Miller* (2018), is to use a color-dependent, stellar mass-to-light ratio, such as *Bell et al.* (2003), which uses galaxy evolution models and a fixed IMF (diet *Salpeter* (1955) for *Bell et al.* (2003)) to estimate stellar mass. For both approaches, the uncertainty associated with the BCG stellar mass estimate is determined by combining the uncertainty in the observed BCG color with the uncertainty associated with the SED fit, which results from the choice of sps model and other intrinsic uncertainties (*Tonini et al.*, 2012).

In the past few years, one primary and potentially sizeable discrepancy between published versions of the SMHM relation is believed to stem from inconsistencies in how BCG magnitudes are measured, which in turn leads to inconsistencies in stellar mass measurements. This problem is particularly relevant for low-redshift SDSS data. As discussed in depth in Chapter II, if the SDSS background is overestimated, this leads to an underestimation of the BCG's stellar mass (*Bernardi et al.*, 2007; *von der Linden et al.*, 2007).

1.4.1.2 Measuring Cluster Halo Mass

Like stellar mass, halo mass is also not directly observable. It is measured using dynamical approaches, such as the caustic technique (*Andreon and Hurn*, 2010; *Gifford et al.*, 2013; *Gifford and Miller*, 2013; *Andreon*, 2015; *Gifford et al.*, 2017), weak gravitational lensing (*Leauthaud et al.*, 2012), or through proxies, such as X-ray brightness (*Lin and Mohr*, 2004; *Harrison et al.*, 2012; *Kravtsov et al.*, 2018) or

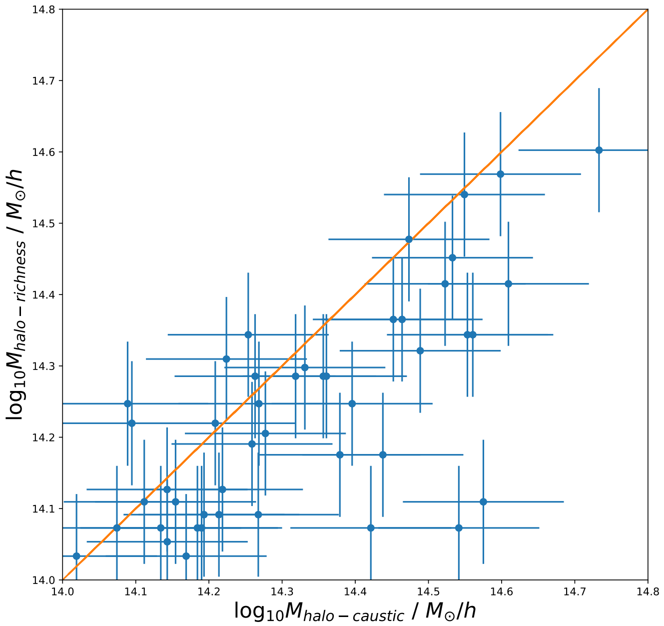

Figure 1.6: Mass - Richness and Caustic Halo Mass Comparison. This figure compares the caustic halo mass estimate and the mass-richness halo mass estimate for the SDSS-C4 (*Miller et al.*, 2005) cluster sample used in the analysis presented in *Golden-Marx and Miller* (2018) and *Golden-Marx and Miller* (2019). This figure highlights that these two halo mass estimates are within 1-1.5σ of one another.

the mass-richness relation (*Rykoff et al.*, 2012; *Rozo et al.*, 2015; *Simet et al.*, 2017; *McClintock et al.*, 2019). While these techniques and their associated uncertainties all differ, for clusters with halo masses measured using multiple techniques, the halo masses are measured consistently, as illustrated by Figure 1.6, which shows a comparison between the caustic halo mass estimates and the mass-richness relation halo masses for the C4 clusters (*Miller et al.*, 2005) used in *Golden-Marx and Miller* (2018) and *Golden-Marx and Miller* (2019). Figure 1.6 shows that these halo mass estimates are within 1-1.5σ of one another, with only a small offset and scatter. Similar evidence for this consistency is shown in *Andreon* (2015).

In this dissertation, I use the caustic technique (*Golden-Marx and Miller*, 2018) and the mass-richness relation (*Golden-Marx and Miller*, 2019) to estimate halo masses. Therefore, here I present a summary of these two techniques in Sections 1.4.1.3 and 1.4.1.4, respectively.

1.4.1.3 Caustic Halo Masses

The caustic technique dynamically measures the cluster's halo mass using the escape velocity profile of galaxies along the line of sight of the cluster to trace the cluster's gravitational potential. This technique has been used in a variety of works to infer halo mass (e.g., *Diaferio and Geller*, 1997; *Diaferio*, 1999; *Andreon and Hurn*, 2010; *Gifford et al.*, 2013; *Gifford and Miller*, 2013; *Gifford et al.*, 2017; *Golden-Marx and Miller*, 2018). The caustic technique relies on the principle that in a system where the cluster's dynamics are controlled by the halo's gravitational potential, there exists a radius-velocity phase space (left side of Figure 1.7) where the edge of the phase space is defined by Equation 1.2, where v_{esc} is the escape velocity and Φ is the cluster's gravitational potential (e.g., *Gifford et al.*, 2013).

$$v_{esc}^2(r) = -2\Phi(r) \tag{1.2}$$

While Equation 1.2 is simple, accurately measuring the gravitational potential and integrating it is difficult. Instead, we use a form introduced by *Diaferio and Geller* (1997), based on the partial mass differential equation $dm = 4\pi\rho(r)r^2dr$, which directly leads to estimating the caustic halo mass via Equations 1.3, 1.4, and 1.5,

$$GM(< R) = \int_0^R -2G\pi v_{esc}^2(r)\frac{\rho(r)r^2}{\Phi(r)}dr \tag{1.3}$$

where ρ is the density,

$$GM(< R) = \int_0^R \mathfrak{F}_\beta(r) < v_{los,esc}^2(r) > dr \tag{1.4}$$

$v_{los,esc}$ is the line-of-sight escape velocity, and $\mathfrak{F}_\beta(r)$ is a caustic calibration term, which is believed to be constant between radii of 1 - $3R_{200}$ (*Diaferio*, 1999), and is defined by Equation 1.5.

$$\mathfrak{F}_\beta(r) = -2G\pi \frac{\rho(r)r^2}{\Phi(r)} dr \tag{1.5}$$

Gifford et al. (2013) find $\mathfrak{F}_\beta(r) = 0.65$, which is used in *Golden-Marx and Miller* (2018).

Observationally, caustic masses are measured by identifying the radius velocity phase space of galaxies using spectroscopically measured line-of-sight peculiar velocities. As shown in Figure 1.7, in the radius-velocity phase space, the extrema values are used to identify the caustic. One observational difficulty with caustic halo mass is that unlike in simulations, where we have the 3D information, allowing for a very clean caustic edge, in observations, we use a single line-of-sight, which adds additional uncertainty to our velocity measurement as well as our caustic mass estimate. Thus, projection effects, which result in the inclusion of foreground interlopers in the caustic phase-space diagram, are responsible for much of the observed scatter in caustic mass estimates (*Gifford et al.*, 2013). The uncertainty associated with this mass estimate is reduced by using more galaxies to construct the caustic phase space; however, based on the work of *Gifford et al.* (2013), when caustic profiles are not stacked, this uncertainty plateaus at $\approx 30\%$ when more than 50 galaxies are used. The caustic uncertainty can be further reduced using only cluster members, identified via the red sequence, to construct the caustic or by stacking multiple caustic phase spaces (*Gifford et al.*, 2017).

While the caustic technique is particularly useful at low redshifts ($z < 0.1$) where

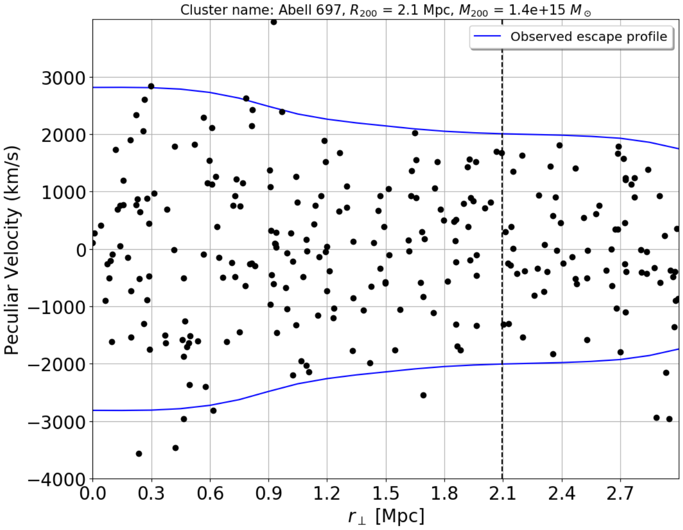

Figure 1.7: Galaxy Cluster Caustic Phase Space Diagram. This figure was provided by Vitali Halenka. It shows the peculiar velocities of cluster galaxies plotted against the distance from the cluster center. Additionally, the observed caustic profile is shown in blue.

good spectroscopic coverage exists for a large sample of clusters (from SDSS), currently this method cannot be used for statistically large samples of clusters at higher redshifts because we lack large high-redshift spectroscopic surveys. However, the impending influx of spectroscopic data from DESI and LSST should allow us to expand the use of the caustic technique to higher redshifts through stacked radius-velocity phase spaces. In doing so, we will determine whether the scatter associated with this measurement remains constant as a function of redshift (as discussed in Chapter VI).

1.4.1.4 Mass - Richness Relation

One of the earliest methods of observationally estimating cluster masses is the mass-richness relation (e.g., *Abell*, 1958), which relies on the observed linear relation between cluster richness and halo mass, as shown in Figure 1.8, which originally appeared in *Andreon and Hurn* (2010). Observationally, the mass-richness relation relies on estimating richness, a measure of the galactic content within a cluster. Addi-

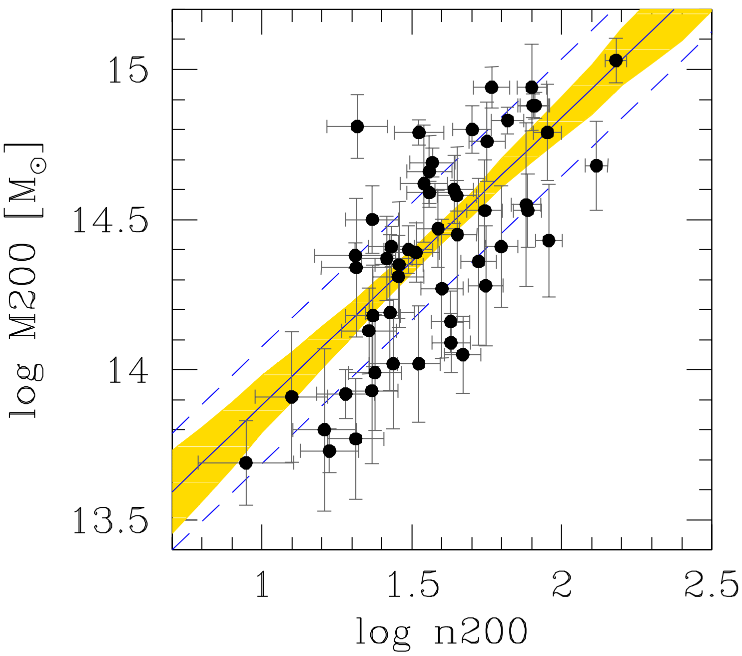

Figure 1.8: Mass - Richness Relation. This figure, from *Andreon and Hurn* (2010), shows the linear, mass-richness relation. This analysis used caustic halo masses. The solid line is the median mass-richness fit, the dashed lines show the intrinsic scatter, and the yellow region is the 1σ fit to the mass-richness relation.

tionally, unlike the caustic technique, the mass-richness relation relies on a correlation measured between a cluster's richness and a previously measured halo mass, done via weak gravitational lensing (*Rozo et al.*, 2009; *Simet et al.*, 2017; *McClintock et al.*, 2019), the caustic technique, as shown in Figure 1.8 from *Andreon and Hurn* (2010), and X-ray halo masses (*Rozo et al.*, 2009; *Rykoff et al.*, 2012).

Like for caustic measurements, richness based halo masses are highly susceptible to impure cluster samples. Since richness is a measure of the number of galaxies contained within a cylinder centered on the cluster (*Andreon and Hurn*, 2010), this can easily lead to the inclusion of foreground interloper galaxies (*Abell et al.*, 1989), which introduce scatter in the mass-richness relation. Like for the caustic technique, foreground contamination is reduced by identifying cluster members either spectroscopically or via the red sequence as done in redMaPPer (*Rykoff et al.*, 2014) and by applying a magnitude limit (*Abell et al.*, 1989). Additionally, because we measure the number of cluster members within a cylinder, the mass-richness relation is sensitive to the radius within which the richness is measured. Therefore, the accuracy of the mass-richness relation depends on both the accuracy of the calibration mass measurements as well as the richness measurement.

Despite these difficulties, the proliferation of photometric observations of galaxy clusters out to high redshifts over the past twenty years from SDSS and DES have made this observationally inexpensive method of estimating halo mass increasingly more common (*Andreon and Hurn*, 2010). Moreover, to its benefit, recent estimates have found that the intrinsic scatter associated with the mass-richness relation is quite low (*Andreon*, 2015; *Rozo et al.*, 2015; *Golden-Marx and Miller*, 2019), making it an ideal method to measure halo masses in large cluster catalogues across a wide range in redshift. However, as discussed in Chapter VI, it is unknown whether the scatter associated with mass at fixed richness remains constant over time.

1.4.2 Intrinsic Scatter in the SMHM relation

The SMHM relation is determined by measuring the linear correlation between the BCG stellar mass and cluster halo mass. However, this is not a perfect one-to-one relationship; some associated intrinsic scatter, σ_{int}, exists in stellar mass at fixed halo mass. This scatter is referred to as intrinsic because astronomers currently are unable to explain what causes the spread in stellar mass at fixed halo mass comes from [1]. Currently, σ_{int} is measured to be on the order of ≈ 0.15dex in observations (*Zu and Mandelbaum*, 2015; *Kravtsov et al.*, 2018; *Golden-Marx and Miller*, 2018, 2019), empirical models (*Reddick et al.*, 2013; *Tinker et al.*, 2017) and simulations (*Gu et al.*, 2016; *Pillepich et al.*, 2018). Moreover, simulations suggest that this small scatter results primarily from the BCG's hierarchical assembly (*Nipoti et al.*, 2009; *Gu et al.*, 2016; *Solanes et al.*, 2016).

Although σ_{int} is small, it has a large impact on the slope of the SMHM relation. As discussed in *Shankar et al.* (2014) and shown in Figure 1.9, from *Tinker* (2017), the slope of the SMHM relation is particularly sensitive to σ_{int}, such that overapproximating σ_{int} flattens the slope. Figure 1.9 highlights the importance of understanding the measured value of σ_{int} and its impact in characterizing the SMHM relation. However, it is not easy to accurately measure because, as done in *Tinker* (2017), the intrinsic scatter is difficult to deconvolve from the estimate of the total uncertainty on the stellar mass. These parameters are related such that: $\sigma^2_{M_*,tot} = \sigma^2_{int} + \sigma^2_{M_*,meas}$. Therefore, to place strong constraints on σ_{int}, we need strong priors on the measurement uncertainty of the stellar mass (*Wechsler and Tinker*, 2018).

---

[1] σ_{int} is not the same as the intrinsic scatter in halo mass at fixed stellar mass (*Wechsler and Tinker*, 2018)

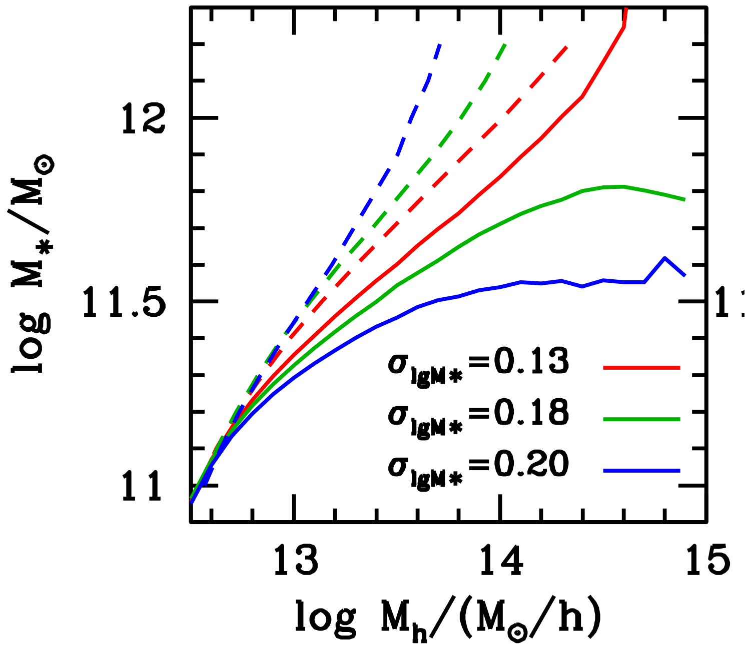

Figure 1.9: Relationship Between the Slope of the SMHM Relation and the Intrinsic Scatter. This figure, from *Tinker* (2017), highlights that the measured slope of the SMHM relation depends on σ_{int}. If σ_{int} is overapproximated, then the slope is flattened, and if σ_{int} is underapproximated, the slope is steepened.

1.4.3 Bayesian vs. Frequentist Approach to studying the SMHM Relation

To quantify the SMHM relation astronomers rely on statistical techniques. There are two primary statistical approaches: frequentist statistics and Bayesian statistics. For a frequentist approach, the probability is associated with with the frequency of an event/detection. Moreover, the model is treated as fixed and the data as random. In contrast, for a Bayesian approach, the probability is a statement of the knowledge about a parameter used to describe an event/detection. In this approach, the probability is associated with the measurement parameters and not the observational data. These definitions highlight that these two approaches are at odds with one another based on how they view observational data (*VanderPlas*, 2014). In a Bayesian approach the data is viewed as the observed truth, while in a frequentist approach the data is viewed as one random draw with an associated mean and variance. Additionally, Bayesian statistics allows for the incorporation of priors, which impose limitations on the measured parameters based on what we already know about the model. Therefore, for conclusions drawn from the observed data about the model, the Bayesian approach is the correct statistical approach (*VanderPlas*, 2014).

As discussed throughout this chapter, the goal of the galaxy-halo connection and the SMHM relation is to describe the correlation between properties of the central galaxy and properties of the host dark matter halo. These goals are associated with creating a model that best describes our observations. Given that the Bayesian approach allows for astronomers to determine the probability and uncertainty associated with each parameter for a given model, it is unsurprising that the majority of statistical works that study the galaxy-halo connection rely on Bayesian statistics. Moreover, since the goal of this dissertation is not to constrain the data (whether from the SDSS-C4, SDSS-redMaPPer, or DES-redMaPPer sample), but to determine whether we can model the SMHM relation with a third parameter (the magnitude gap), I naturally use Bayesian statistics. Additionally, I note that the resultant model from a Bayesian approach can be used to generate data in cosmological simulations, which rely on such models to relate the central galaxy and halo characteristics. Given the direct alignment of the Bayesian principles with the goals of this dissertation, Bayesian statistical techniques allow me to best address the goals set forth.

1.4.4 Current Status of the SMHM relation

The SMHM relation has been investigated in recent years using observations (e.g., *Oliva-Altamirano et al.*, 2014; *Gozaliasl et al.*, 2016; *Zhang et al.*, 2016; *Lin et al.*, 2017; *Kravtsov et al.*, 2018; *Golden-Marx and Miller*, 2018, 2019), simulations (e.g., *Gu et al.*, 2016; *Pillepich et al.*, 2018), and empirical models (e.g., *Tinker et al.*, 2017; *Behroozi et al.*, 2018; *Moster et al.*, 2018). As a result of these varied approaches, a general consensus exists about the nature of the SMHM relation. Here, I briefly review the current consensus or lack thereof on the values of the scatter, amplitude, and slope of the SMHM relation.

The best agreed upon measurement associated with the SMHM relation is that $\sigma_{int} \approx 0.15$dex (e.g., *Gu et al.*, 2016; *Tinker et al.*, 2017; *Zu and Mandelbaum*, 2015; *Kravtsov et al.*, 2018; *Pillepich et al.*, 2018; *Golden-Marx and Miller*, 2018). Although a consensus exists, astronomers are still actively investigating whether all of σ_{int} is truly intrinsic as well as how this scatter evolves with halo mass. Recent observational (e.g., *Zu and Mandelbaum*, 2015), semi-analytic (e.g., *Somerville et al.*, 2012; *Henriques et al.*, 2015), empirical (e.g., *He et al.*, 2013; *Behroozi et al.*, 2018) and computational studies (e.g., *Gu et al.*, 2016; *Matthee et al.*, 2017; *Pillepich et al.*, 2018) have measured how σ_{int} changes with halo mass and find that σ_{int} may decrease slightly with increasing halo mass. However, this change may actually just result from the transition of in-situ to ex-situ dominated stellar mass growth, and not halo mass alone (*Gu et al.*, 2016). Recent works have also examined whether including additional third parameters in the SMHM relation reduces σ_{int}. *Zentner et al.* (2014) and *Matthee et al.* (2017) found that a fraction of σ_{int} results from differences in the cluster's formation redshift, which suggests that some difference in BCG stellar masses is related to halo assembly, as suggested in Section 1.3.3 and Chapter VI. Thus, σ_{int} may be further reduced, which would allow us to more tightly estimate the halo mass of a cluster given the BCG stellar mass and posterior distributions of the associated parameters. The reduction of σ_{int} is a primary focus of this dissertation, particularly Chapter III.

While a consensus value for the scatter exists, there is less agreement for the slope and amplitude of the SMHM relation. *Shankar et al.* (2014) note most observational SMHM relations lie above the *Moster et al.* (2013) empirical SMHM relation and Figure 1.10 highlights such amplitude differences for five previously published SMHM relations from *Behroozi et al.* (2013a), *Moster et al.* (2013), *Lin and Mohr* (2004), *Tinker et al.* (2017), and *Kravtsov et al.* (2018), all scaled to the same IMF. Of note, the *Behroozi et al.* (2013a), *Moster et al.* (2013), and *Tinker et al.* (2017) relations are for empirical models, while the *Lin and Mohr* (2004) and *Kravtsov et al.* (2018) relations are measured using observational data. It has been suggested that the majority of the amplitude difference, particularly between the *Behroozi et al.* (2013a) and *Kravtsov et al.* (2018) SMHM relations, result from how BCG magnitudes are estimated (*Wechsler and Tinker*, 2018). The *Behroozi et al.* (2013a) result uses SDSS Petrosian magnitudes and the *Kravtsov et al.* (2018) result integrates the BCG light profiles out to infinity to measure BCG magnitudes. While the differences in magnitude measurements are indeed important, the work presented in this dissertation illustrates that at least ≈ 0.5 dex of amplitude difference remains unaccounted for by BCG magnitude measurements.

Like the amplitude, the slope of the SMHM relation also lacks an agreed upon value at low redshifts. Of importance, this dissertation does not claim to definitively

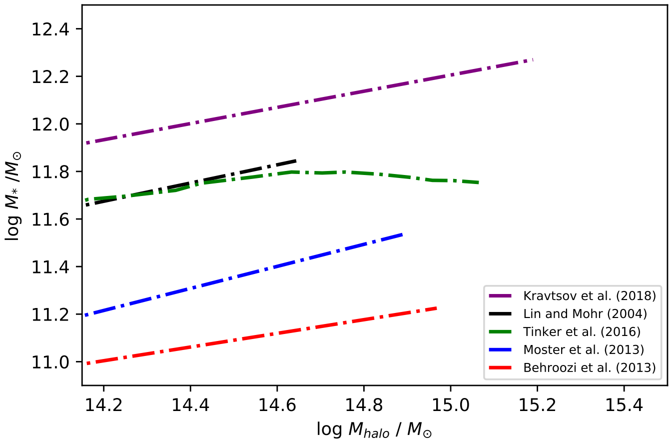

Figure 1.10: Published SMHM Relations with Differing Amplitudes. This figure shows the SMHM relations from *Behroozi et al.* (2013a), *Moster et al.* (2013), *Lin and Mohr* (2004), *Tinker et al.* (2017), and *Kravtsov et al.* (2018), all scaled to the same IMF, which highlights the discrepancy between the amplitudes of published SMHM relations.

determine the correct SMHM relation slope, instead it focuses on characterizing the slope's evolution. However, for the purpose of comparing the results presented here to those from prior works, it is necessary to note prior estimates for the slope's value. Recent observational results, such as *Zhang et al.* (2016) and *Lin et al.* (2017) suggest that the slope of the SMHM relation is low (< 0.35). However, results from simulations *De Lucia and Blaizot* (2007) and *Pillepich et al.* (2018) suggest that the slope is much steeper, 0.45-0.60. As hinted at in *Zhang et al.* (2016), the Illustris TNG 300 simulation (*Pillepich et al.*, 2018), and the EMERGE semi-analytic model (*Moster et al.*, 2018), this discrepancy may result from the choice of radius within which the BCG's stellar mass is measured, a topic which is investigated in depth in Chapter IV of this dissertation.

Another aspect of the SMHM relation this dissertation focuses on is the redshift evolution of the slope and σ_{int} (see Chapter IV and Chapter V). Since both BCGs and their dark matter halos grow hierarchically, the SMHM relation is expected to have some evolution over the last 6 billion years. While this has been investigated observationally (e.g., *Oliva-Altamirano et al.*, 2014; *Gozaliasl et al.*, 2016), using empirical models (e.g., *Behroozi et al.*, 2013a; *Moster et al.*, 2013), and in simulations (e.g., *Gu et al.*, 2016; *Pillepich et al.*, 2018), the results of each approach do not agree. Observations are unable to constrain the redshift evolution of the SMHM relation's slope because the slope's uncertainty is large (> 0.2) (*Oliva-Altamirano et al.*, 2014; *Gozaliasl et al.*, 2016). Empirical models (*Behroozi et al.*, 2013a; *Moster et al.*, 2013) suggest that between $z = 0.0$ and $z = 1.0$, the slope decreases by $\approx 50\%$. In contrast to emipirical models, results from Illustris TNG300 (*Pillepich et al.*, 2018) suggest little redshift evolution out to $z = 1.0$. Similarly, the redshift evolution of σ_{int} (*Gu et al.*, 2016; *Matthee et al.*, 2017; *Behroozi et al.*, 2018; *Moster et al.*, 2018; *Pillepich et al.*, 2018) is inconsistent and may depend on the initial conditions of the simulations and empirical models. It is important to note that the lack of consistency between observations, empirical models, and simulations, may result from differences in how stellar masses and halo masses are measured. Thus, from both an observational and empirical viewpoint, prior to the work presented in this dissertation, the late-time redshift evolution of both parameters remains unclear.

Although the expected late time redshift evolution is unclear, using N-body simulations, *Gu et al.* (2016) study the hierarchical growth of BCGs with respect to the long term evolution of the SMHM relation. Figure 1.11, which originally appeared in *Gu et al.* (2016), shows that over a significant amount of cosmic time, the slope of the SMHM relation slightly steepens and σ_{int} increases. Moreover, *Gu et al.* (2016) claim that both σ_{int} and the SMHM relation's slope increase as a result of hierarchical merging, which in turn increases the diversity of the BCG's progenitor history. Therefore, any detected evolution in the slope of the SMHM relation may result from recent hierarchical growth. Additionally, an increase in slope over time suggests that merger growth is more efficient in more massive halos.

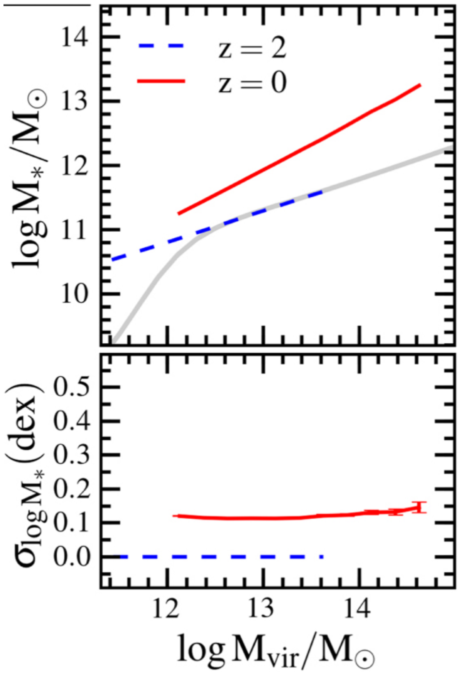

Figure 1.11: Redshift Evolution of the Slope and Intrinsic Scatter in the SMHM Relation. This figure originally from *Gu et al.* (2016), shows how the slope and σ_{int} evolve between z=2 (in blue) and z=0 (in red). Over this time, σ_{int} increases, resulting in a slightly steeper slope.

1.4.5 What can we learn from the SMHM relation

One of the primary uses of the SMHM relation is to characterize how galaxies populate dark matter halos. However, the SMHM relation can also be used to constrain semi-analytic and empirical models of galaxy formation and evolution (*Shankar et al.*, 2014; *Wechsler and Tinker*, 2018) as well as to constrain cosmological parameters. Here, I summarize a variety of results that highlight uses of the SMHM relation and associated scatter.

Characterizing AGN feedback is a vital process for understanding the star formation history of massive galaxies. For clusters, the amplitude of the SMHM relation can be used to constrain the amount of AGN feedback (*Kravtsov et al.*, 2018). If this feedback is modeled to be more significant than in the real universe, the amplitude of the SMHM relation would be lower in semi-analytic models and simulations than in observations because BCGs would have lower stellar masses. From the standpoint of

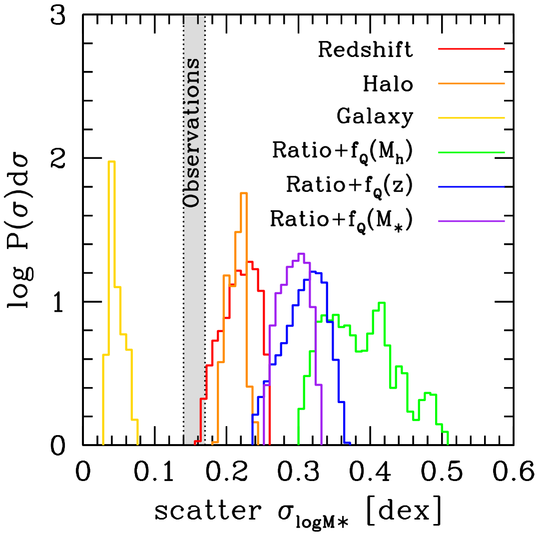

Figure 1.12: Posterior Distibution of Instrinsic Scatter for Different Galaxy Quenching Models. This figure, from *Tinker* (2017), shows how the posterior distribution for σ_{int} changes for different types of quenching models. Based on the comparisons to the observed σ_{int}, it is clear that only galaxy quenching is viable.

a two-phase formation scenario, this would likely mean that AGN feedback quenched the formation of the BCG's core (the region actively grown via star formation) at a higher redshift. Additionally, this would decrease the stellar mass of the merging galaxies, which may also host AGN, so it would also decrease the amount of mass gained via ex-situ mergers. However, it is important to note, that when comparing results from observations and semi-analytic/empirical models, attention must be paid to measure the stellar mass in both models and observations consistently.

While the amplitude informs us about AGN feedback, the scatter of the SMHM relation informs us about the processes that quench star formation in massive galaxies, as shown in Figure 1.12, from *Tinker* (2017). Figure 1.12 compares the posterior distributions for σ_{int} that result from different quenching models, including galaxy quenching, halo quenching, and redshift quenching (for each of these star formation is shut off when the central galaxy/cluster reaches a threshold stellar mass, halo mass, or redshift). Based purely on the observed σ_{int}, *Tinker* (2017) claim that only galaxy quenching yields a low enough σ_{int} to agree with observational measurements.

Additionally, as shown in *Gu et al.* (2016), σ_{int} also constrains models of halo assembly due to smooth accretion. In simulations, smooth accretion occurs when the total halo mass is the sum of all subhalos as well as any free dark matter particles within the cluster's radial extent. If smooth accretion does not occur, the total halo mass is the sum of the subhalos, and σ_{int} is lower. Based on the observed σ_{int}, halo assembly models grow via smooth accretion (*Gu et al.*, 2016). Additionally, *Gu et al.* (2016) also use σ_{int} to characterize BCG formation and find that at the high mass end, hierarchical growth is responsible for all of the observed scatter, while at the lower halo mass end, the scatter results from in-situ star formation.

As noted in Section 1.4.1, neither stellar mass or halo mass are directly observable. However, because stellar mass estimates can come directly from photometry, they are generally easier to observationally estimate. Therefore, once accounting for the posterior distributions associated with well-constrained SMHM relation parameters, the SMHM relation can be used to determine the halo mass distribution for a sample of clusters. By comparing the inferred halo mass distribution to halo mass distributions from cosmological dark matter only simulations the estimates obtained via the SMHM relation can be used to infer and place constraints on cosmological parameters. Of note, since the halo mass function evolves with redshift, it is important to either use a homogeneous sample of clusters centered on a single redshift or use a SMHM relation that accounts for the redshift evolution of the measured parameters.

1.5 Questions Addressed in this Dissertation

In the previous sections, I introduced the galaxy-halo connection and described how this connection results from the hierarchical assembly of dark matter halos, which in turn are responsible for BCG hierarchical growth. Moreover, I have explained how the galaxy-halo connection naturally leads to the SMHM relation, how this relation is measured, and how this relation can be used to constrain models of galaxy and halo formation and evolution. Although this is well studied in observations, simulations, and empirical models, there is still much for us to learn, particularly on the observational end, where we are just beginning to probe higher redshifts and construct statistically significant samples of higher redshift clusters using surveys and instruments such as DES and the South Pole Telescope.

As noted in the recent galaxy-halo connection review paper (*Wechsler and Tinker*, 2018), placing tighter constraints on the parameters associated with the galaxy-halo connection over a range in halo mass, redshift, and environment will greatly improve our understanding of this connection as well as our ability to improve our simulations and empirical models of galaxy/halo formation. In Chapters III, IV, and V of this dissertation, I focus on the latter two characteristics. First as shown in *Golden-Marx and Miller* (2018), I account for environment, by introducing the magnitude gap, which characterizes the cluster's galactic population, as a third latent parameter within the SMHM relation. In doing so, I significantly tighten the constraints on both the slope and σ_{int}. This result illustrates that a large portion of σ_{int} results from comparing clusters hosting BCGs in different stages of their hierarchical growth. Second, in *Golden-Marx and Miller* (2019), I study the late-time evolution of the SMHM relation. Incorporating the magnitude gap allows us to place tighter constraints on the SMHM relation's slope, which allows us to, for the first time, observationally detect statistically significant late-time evolution in the slope of the SMHM relation. Additionally, in Golden-Marx et al. (in prep.), I confirm the results of *Golden-Marx and Miller* (2019) using higher redshift data and confirm that the parameter associated with the magnitude gap also evolves. Throughout this dissertation, particularly in Chapters IV and V, I highlight how we create a homogeneous sample of galaxy clusters across multiple observational surveys (DES and SDSS) which use multiple cluster finding algorithms (C4 (*Miller et al.*, 2005) and redMaPPer *Rykoff et al.* (2014)) to observationally characterize how the SMHM relation and thus the underlying relationship between BCG formation and halo assembly evolve. Therefore, here, in this dissertation, using Bayesian statistical methods, we observationally address the impact of both environment and redshift on the galaxy-halo connection via the SMHM relation, and not only detect, but place statistically significant constraints on how the observed SMHM relation for a sample of clusters with homogenous measurements evolves over the redshift range $0.03 < z < 0.60$.

CHAPTER II

How to measure a BCG's magnitude

2.1 Abstract

BCGs are radially extended compared to similarly massive non-central galaxies, and are often surrounded by halos of diffuse intra-cluster light (ICL; *Zwicky*, 1951). These characteristics make BCG photometry quite complex. Therefore, it is vital to understand how different BCG magnitude measurements are obtained and the fraction of the BCG's light contained within each measurement. Moreover, as outlined in this chapter, specific procedures should be taken to accurately measure low-redshift BCG magnitudes (e.g., *Bernardi et al.*, 2007; *von der Linden et al.*, 2007). In this section, we describe different computational and modelling techniques SDSS and DES use to estimate BCG magnitudes and how we measure BCG magnitudes using SDSS radial light profiles (*Golden-Marx and Miller*, 2018, 2019) and DES photometry (Golden-Marx et al. in prep.). This chapter serves to expand upon the discussion presented in Section 3.3, Section 4.4, and Section 5.4.

2.2 How is a Galaxy's Magnitude Measured

Photometry, the measure of an astronomical object's light or flux, is a fundamental part of astronomy. The apparent magnitude, given by Equation 2.1, quantifies the

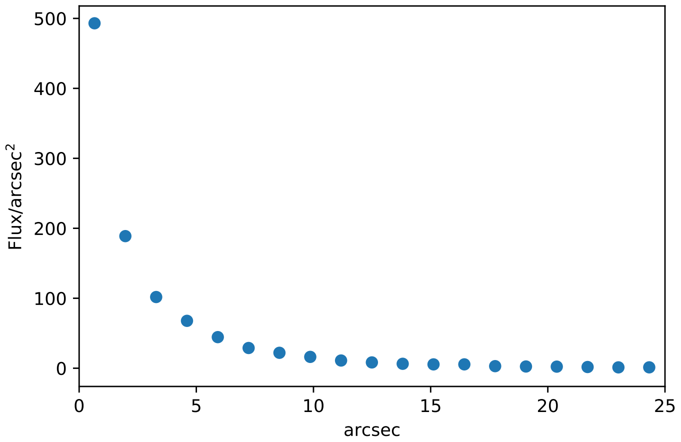

Figure 2.1: DES BCG Radial Flux Profile. The radial flux profile of a Dark Energy Survey BCG, plotted in Flux/arcsec^2 vs arcseconds.

amount of flux observed in a fixed waveband measured on earth (via CCDs on modern telescopes).

$$m = normalization - 2.5 \times \log_{10}(Flux) \tag{2.1}$$

Today, astronomers accurately measure the brightness of most astronomical objects. However, for BCGs, the focus of this dissertation, accurate photometric measurements remain surprisingly difficult.

Unlike similarly massive galaxies, BCGs are radially extended and surrounded by halos of faint, diffuse ICL, which make it difficult to accurately distinguish the BCG from the background light. Moreover, BCG light profiles highlight that while BCGs have bright central cores the outer envelopes gradually decrease in brightness until the galaxy's light and background are indistinguishable, as shown in Figure 2.1. Therefore, the inability to clearly separate the BCG from the ICL and background make it critical to understand BCG photometry and how different magnitude measurements truncate BCG light profiles, which impact the BCG's magnitude and in turn the stellar mass estimate. BCG magnitudes are a fundamental measurement used throughout this dissertation because accurate photometry is required to measure both the BCG's stellar masses as well as the magnitude gap of the cluster.

The outline for the remainder of this chapter is as follows. In Section 2.3, I describe different approaches used to measure galactic magnitudes. In Section 2.4, I discuss the difficulties that exist when measuring BCG photometry. In Section 2.5, I discuss how SDSS magnitudes are measured in *Golden-Marx and Miller* (2018) and *Golden-Marx and Miller* (2019). In Section 2.6, I discuss how our BCG magnitudes are measured for our DES data (Golden-Marx et al. in prep.).

2.3 Magnitude Types

The two primary types of galactic magnitudes are aperture and model magnitudes. Aperture magnitudes measure the total flux within a fixed radial region on the sky, generally measured in arcseconds(") or pixels, but which, if the galaxy's redshift is known, can be converted to physical units, such as kpc. Model magnitudes fit a galaxy's radial light profile to either an exponential or power law function, which is used to estimate a galaxy's total magnitude. For both methods, magnitudes are calculated independently for each wavelength band. Therefore, for both approaches, the measurement accuracy associated the magnitude depends on the photometric depth as well as the fraction of the galaxy's light contained within the selected radial aperture or the accuracy of the fitting function compared to the observed light profile.

Since my work in *Golden-Marx and Miller* (2018) and *Golden-Marx and Miller* (2019) uses SDSS photometry, and my work in Golden-Marx et al. (in prep.) uses DES photometry, I briefly summarize the available magnitudes provided by SDSS and DES. Both SDSS and DES provide model magnitudes fit to either a *de Vaucouleurs* (1948) profile, where n=4, (Equation 2.2)

$$I(r) = I_0 e^{-7.67[r/r_e]^{1/n}} \tag{2.2}$$

or to an exponential *Sérsic* (1963) profile, where n=1, (Equation 2.3).

$$I(r) = I_0 e^{-1.68[r/r_e]^{1/n}} \tag{2.3}$$

For both models, r_e is the scale radius, I(r) is the surface brightness profile, and I_0 is the intensity at $r = 0$. Model magnitudes are calculated for each SDSS ugriz band and DES griz band. Additionally, SDSS provides cmodel magnitudes, a linear combination of the *de Vaucouleurs* (1948) and *Sérsic* (1963) profiles.

SDSS also provides *Petrosian* (1976) magnitudes, used in *Golden-Marx and Miller* (2018). In Section 2.5, I describe how we measure Petrosian magnitudes. Since each galaxy has a unique radial surface brightness profile, aperture magnitudes do not consistently account for the same fraction of light from a galaxy. The Petrosian magnitude accounts for this discrepancy by measuring a constant fraction of a galaxy's total flux. The Petrosian magnitude is measured at the Petrosian radius (r_p), which is calculated using the Petrosian ratio, given by Equation 2.4, where I(r') is the azimuthally averaged radial surface brightness profile.

$$R_p(r) = \frac{\frac{\int_{0.8r}^{1.25r} dr' 2\pi r' I(r')}{\pi(1.25^2 - 0.8^2)r^2}}{\frac{\int_0^r dr' 2\pi r' I(r')}{\pi r^2}} \tag{2.4}$$

For SDSS, r_p is the radius, where $R_p(r_p) = 0.2$, and Petrosian magnitudes are calculated within $2.0r_p$. Since Petrosian magnitudes have a designated radial end point, they do not contain a galaxy's entire light profile; instead they represent $\approx 90\%$ of a galaxy's light, which encloses a similar fraction of light to a *de Vaucouleurs* (1948) profile with n=4 and a *Sérsic* (1963) profile of n=1 (*Blanton et al.*, 2001). Although SDSS provides Petrosian radii and magnitudes, they can also be calculated using the azimuthally averaged radial flux profiles provided by SDSS for each wavelength band, similar to Figure 2.1, as done in *Golden-Marx and Miller* (2018). As discussed in Section 2.5, this information can also be used to measure fixed physical aperture magnitudes by converting pixels to arcseconds to distance (if a redshift is known).

For the DES data, we also use the *Kron* (1980) magnitudes, see Section 2.6. Similar to Petrosian magnitudes, Kron magnitudes rely on the Kron ratio, given by Equation 2.5, to determine the radius containing a fixed amount of flux.

$$R_1(r) = \frac{\int_0^r dr' 2\pi r'^2 I(r')}{\int_0^R dr' 2\pi r' I(r')} \tag{2.5}$$

The Kron radius, r_k, is where the Kron ratio is equal to 0.1 times the sky flux and the Kron magnitude is measured at $\approx 2.0 r_k$. The Kron magnitude is a luminosity weighted magnitude estimated to account for $\approx 90\%$ of the light within a galaxy, like the Petrosian magnitude.

2.4 Difficulties for BCGs

As introduced in section 2.2, BCG photometry is difficult to measure accurately. One primary reason is that BCGs are often located in crowded environments, surrounded by satellite galaxies, as a result of the BCG's unique location near the center of the dark matter halo's gravitational potential well, as shown in Figure 2.3. BCG photometry is further complicated because BCGs are also often surrounded by halos of diffuse ICL (*Zwicky*, 1951; *Welch and Sastry*, 1971; *Oemler*, 1976; *Lin and Mohr*, 2004), see Figure 2.2. Therefore, it is difficult to consistently disentangle a BCG's light profile from the background and ICL. While a simplistic solution, suggested by *Kravtsov et al.* (2018), is to measure BCG magnitudes by integrating their light profile to infinity, the dense environment and inability to distinguish the BCG's outer envelope from the ICL and then the background (*Kravtsov et al.*, 2018; *Zhang et al.*, 2018), make this approach problematic because it will likely result in including light that is part of the cluster, but not associated with the BCG, in the BCG magnitude and stellar mass estimate. Since BCG photometry is not straightforward, in

Figure 2.2: SDSS BCG with ICL. An SDSS-C4 galaxy cluster featuring a BCG surrounded by a large diffuse ICL halo.

Sections 2.4.1 and 2.4.2, I introduce the ICL, explain ICL formation, the impact the ICL has on BCG magnitude measurements, and explain the difficulties in accurately measuring BCG light profiles, particularly for SDSS photometry.

2.4.1 ICL

BCGs are surrounded by ICL, which can extend as far out as 1Mpc (*Zhang et al.*, 2018) from the BCG's core, and enclose light from multiple bright galaxies (e.g., *Lauer et al.*, 2014), as shown in Figure 2.2. Despite the fact that new observations have greatly improved our understanding of the ICL (*Zibetti et al.*, 2005; *Zhang et al.*, 2018), ICL is not a new concept; it was first theorized by *Zwicky* (1937) and first observed in the Coma cluster (*Zwicky*, 1951, 1952). Moreover, BCG extended envelopes have long been thought to be associated with the ICL (*Uson et al.*, 1991). Despite being well studied, a consensus definition of the ICL does not exist. Currently, in both observations and simulations, astronomers are unable to disentangle the BCG's light profile from the ICL, making it impossible to determine where these regimes overlap (*Lin and Mohr*, 2004; *Kravtsov et al.*, 2018; *Zhang et al.*, 2018). Due to this difficulty, for the analysis in this dissertation, I follow from the ICL definition introduced in *Pillepich et al.* (2018), where a fixed radius is used to separate the BCG and ICL such that the diffuse light outside the fixed radius (in our case 100kpc (*Golden-Marx and Miller*, 2019)) centered on the BCG is defined as the ICL and all of the light located within that same radius is treated as the BCG.

As noted in Section 1.3.2, the ICL's formation results from BCG hierarchical growth (*Murante et al.*, 2007). As previously noted, BCGs follow a two-phase (*Oser et al.*, 2010) formation scenario, where the central region of the BCG forms via in-situ star formation at $z > 2$ and remains unchanged (*van Dokkum et al.*, 2010), while the outer region of the BCG ($r > 5kpc$) grows hierarchically (*De Lucia and Blaizot*, 2007) by accreting satellite galaxies. During hierarchical growth, a fraction, suggested to be greater than or equal to 50% (*Lidman et al.*, 2012; *Groenewald et al.*, 2017; *Burke et al.*, 2015), of ex-situ stars are ejected from the BCG/merging galaxy and form the ICL. Therefore, as the BCG hierarchically assembles, the ICL simultaneously grows as well.

Recent simulations suggest that the ICL forms from stars dispersed from their host galaxies via processes including tidal stripping and galaxy-galaxy mergers (*Murante et al.*, 2007; *Contini et al.*, 2014). *Contini et al.* (2014) suggest that the majority of the ICL is built up via tidal stripping of massive satellite galaxies, which can occur when satellites fall to the inner region of a cluster, allowing tidal forces to strip stars from the satellite galaxy's outer regions, while a small fraction of the ICL results from galaxy-galaxy mergers. In contrast, *Murante et al.* (2007) find that for high mass galaxies, the majority of ICL results from galaxy-galaxy mergers, while tidal stripping dominates for low mass galaxies. Despite this inconsistency, both *Murante et al.* (2007) and *Contini et al.* (2014) find that the ICL assembles relatively recently

($z < 1.0$), compared to the core of the BCG, which assembles at $z > 2$ (*Oser et al.*, 2010; *van Dokkum et al.*, 2010). These results agree with observations from *Burke et al.* (2015), which use Cluster Lensing and Supernova survey with *Hubble*survey, covering the redshift range $0.18 < z < 0.90$, and find that the stellar mass of the ICL increases by a factor of 4-5 due to minor mergers, while the stellar mass within the BCG remains fixed.

Since the ICL and BCG are inherently related, it is important to understand how the ICL impacts BCG photometry and stellar mass estimates. For example, light outside 20kpc accounts for a significant fraction of a BCG's total light (*Gonzalez et al.*, 2005). Moreover, measuring the BCG's outer envelope and ICL allow us to constrain BCG growth (*Conroy et al.*, 2007; *van Dokkum et al.*, 2010; *Burke et al.*, 2015; *Huang et al.*, 2018). Thus, incorporating ICL and the region surrounding the BCG's core, is crucial to accurately measuring the BCG's total mass as well as the parameters of the SMHM relation (*Moster et al.*, 2018). The ICL is also an important component of galaxy clusters. For example, the stellar mass budget of the ICL increases with halo mass (*Lin and Mohr*, 2004), such that 10-50% of the cluster's total light is found within the ICL (*Zibetti et al.*, 2005; *Gonzalez et al.*, 2007; *Burke et al.*, 2015; *Zhang et al.*, 2018). Additionally, the ICL luminosity may even trace the underlying parent dark matter halo mass distribution (*Zhang et al.*, 2018).

2.4.2 BCG light profile difficulties

In addition to BCGs being surrounded by diffuse ICL they are also often located within dense galactic regions near the core of the galaxy cluster. When galactic magnitudes are measured, they include all flux within a radial region, including scattered light from diffuse objects that make up the background. To account for this light, the background flux should be measured by masking galaxies and using the flux from areas of the sky unoccupied by neighboring galaxies. Therefore, accurately measuring

BCG magnitudes requires correctly measuring the background and not incorporating regions dominated by neighboring galaxies or ICL. If the background flux is overestimated, the galaxy's flux, and stellar mass will be underestimated.

For extended galaxies in crowded regions, common characteristics of BCGs, the SDSS photometric pipeline overestimates the background (*Bernardi et al.*, 2007; *Lauer et al.*, 2007; *von der Linden et al.*, 2007), resulting in photometry that may be underestimated by as much as 1.0-1.5 magnitudes (*Bernardi et al.*, 2007; *Lauer et al.*, 2007; *Golden-Marx and Miller*, 2018). An example of an SDSS BCG in a crowded field is shown in Figure 2.3. The SDSS background subtraction problem is well documented, (*Bernardi et al.*, 2007; *Lauer et al.*, 2007; *von der Linden et al.*, 2007; *Kravtsov et al.*, 2018) and corrections, as discussed in Section 2.5, exist (e.g., *von der Linden et al.*, 2007); however, to date, this problem has not been fully resolved and still exists for new SDSS photometry.

The SDSS background subtraction problem results from how the SDSS photometric pipeline measures the background flux. SDSS provides two background measurements, a local and a global sky background. The global sky background is measured within a box of 2048 x 1498 pixels (13.5 x 9.8 $arcmin^2$). In contrast, the local sky background, which is used in the SDSS photometric reduction pipeline, is measured at every location within a box of 256 x 256 pixels (1.7 x 1.7 $arcmin^2$). Since the local sky background is small ($\approx 2\%$ of the global sky background in area) local sky backgrounds are inherently susceptible to being biased to higher values by diffuse light from neighboring galaxies or the ICL. To account for the incorrect background measurement, the global sky background can be used for more accurate photometry, as described in depth in Section 2.5 and in *von der Linden et al.* (2007).

Figure 2.3: SDSS BCG in a Crowded Environment. An example of an SDSS BCG that is found in a crowded region.

2.5 Measuring BCG Magnitudes for SDSS

2.5.1 Golden-Marx & Miller 2019 Magnitudes

For our stellar mass and magnitude gap measurements in *Golden-Marx and Miller* (2018), we apply the *von der Linden et al.* (2007) correction to the SDSS photometry to measure BCG magnitudes. Here, we summarize how we measure Petrosian magnitudes using the SDSS azimuthally averaged radial profiles and how we apply the *von der Linden et al.* (2007) correction.

2.5.1.1 Measuring the Petrosian Magnitude

As noted in Section 2.4.2, SDSS magnitudes overapproximate the background, leading to an underapproximation of the BCG magnitude and stellar mass. However, the *von der Linden et al.* (2007) correction is designed to be applied to a radial light profile measured at the Petrosian radius. Therefore, to use this approach, we first must accurately reproduce SDSS Petrosian magnitudes using the azimuthally averaged radial flux profiles, similar to Figure 2.1. For the analysis in *Golden-Marx and Miller* (2018), we used the SDSS g-, r-, and i-band fluxes.

SDSS provides radially binned flux per arcsec^2 measurements for radial bins measured out to the local sky background level. This flux/arcsec^2 measurement can be converted to a flux by multiplying the value measured at each radius by the area of each annulus in arcsec^2. The total flux as a function of radius is then calculated by coadding the flux in each annulus. This flux is then converted from nanomaggies to magnitudes using Equation 2.6,

$$m = \frac{-2.5}{\ln(10)}[\frac{\text{asinh}(\frac{f}{f_0})}{2b} + \ln(b)] \tag{2.6}$$

where b is a waveband dependent softening parameter, which represents the 1σ noise of the sky in a PSF aperture in a 1" seeing and f_0 is the zero point of the magnitude scale. To convert the sky aperture (in radians) to a physical aperture (in kpc), which is needed to compare Petrosian radii measurements, I use the cluster redshift, estimated either via the C4 (*Miller et al.*, 2005) or redMaPPer (*Rykoff et al.*, 2014) cluster finder algorithms, to determine the luminosity distance assuming a ΛCDM cosmology, and simple trigonometry. For each wavelength band I then fit a univariate spline function, a one dimensional smoothing fit, which uses piece-wise polynomials to linearly interpolate between the measured data, to the light profile to measure the magnitude at all radii between the measured values. For this fitting, I set the degree of smoothing for the spline to 3 and the smoothing factor to 0.0000000001. An example fit is shown for the i-band magnitude measurement of an SDSS-C4 BCG in Figure 2.4. To determine how well my interpolated light profiles match the SDSS profiles, I compared my measurement of the Petrosian magnitude taken at the SDSS Petrosian radius, to the SDSS value. Figure 2.5 highlights the absolute magnitude

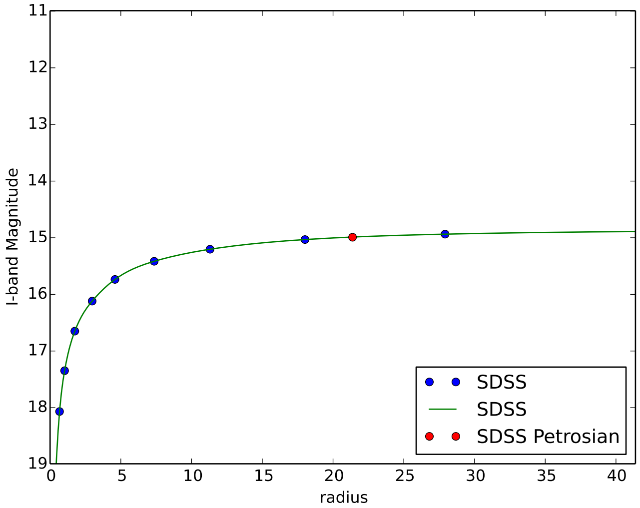

Figure 2.4: SDSS Light Profile. This is an SDSS-C4 BCG light profile for the i-band. The light profile shows how the univariate spline interpolation function works.

difference between my measurement of the Petrosian magnitude (taken at the SDSS Petrosian Radii) and the SDSS value. Since the majority of data have an absolute difference on the order of $< 10^{-2}$ magnitudes, Figure 2.5 highlights that my light profiles are far more accurate than the associated measurement uncertainty of SDSS (≈ 0.02 (*Lauer et al.*, 2007)).

To calculate Petrosian magnitudes, I calculate r_p, using Equation 2.4, which requires the flux measured as a function of radius. For this flux measurement, I fit a second univariate spline function (with the same parameters) to interpolate the flux as a function of radius. I then evaluate Equation 2.4 at each point along my linear interpolation and identify r_p where $R_p(r_p) = 0.225$. This value is slightly larger than the SDSS value, 0.2, which may be due to small differences between my algorithm and the SDSS algorithm, such as a different spline fitting. 0.225 was selected because it minimized the uncertainty between my r_p, and thus my Petrosian magnitudes, and the SDSS values. The results of this choice are shown in Figure 2.6, which compares my r_p for the g- and r-bands to those measured by the SDSS photometric pipeline.

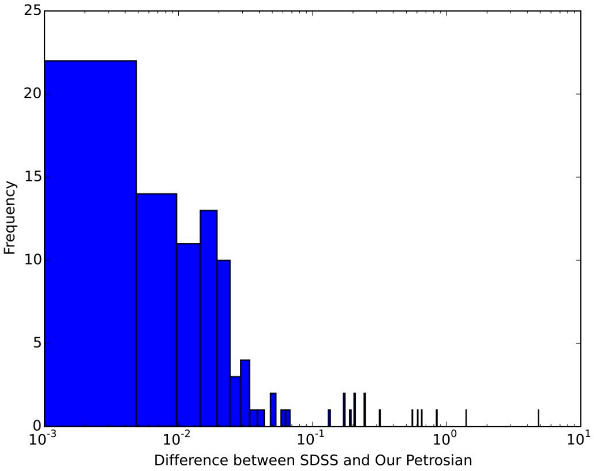

Figure 2.5: SDSS Petrosian Magnitudes vs. My Petrosian Magnitudes. This is a distribution comparing the absolute value of the difference between the SDSS Petrosian magnitude and my measurement of the magnitude, measured at $2.0r_p$, where r_p is given by SDSS.

The one-to-one nature of Figure 2.6 highlights that following this approach, I accurately remeasure r_p and thus, when combined with the results of Figures 2.4 and 2.5 am able to remeasure the Petrosian magnitudes with high precision as well.

2.5.1.2 Measuring Background Corrected Petrosian Magnitudes

Since low-redshift SDSS photometry suffers from a background subtraction error, I apply the correction described in *von der Linden et al.* (2007). For this analysis, I rely upon Equations 2.7, 2.8, and 2.9, from *von der Linden et al.* (2007),

$$LR_i = -2.5\log(L_i/L_{nb}) \tag{2.7}$$

where LR_i is the luminosity ratio between the ith galaxy and its neighbor (nb). L_{nb}, the luminosity of the neighbor, is defined by Equation 2.8,

$$L_{nb} = \frac{\sum_{j\in galaxies} L_j w_j}{\sum_{j\in galaxies} w_j} + 10(\frac{\sum_{j\in stars} L_j w_j}{\sum_{j\in stars} w_j}) \tag{2.8}$$

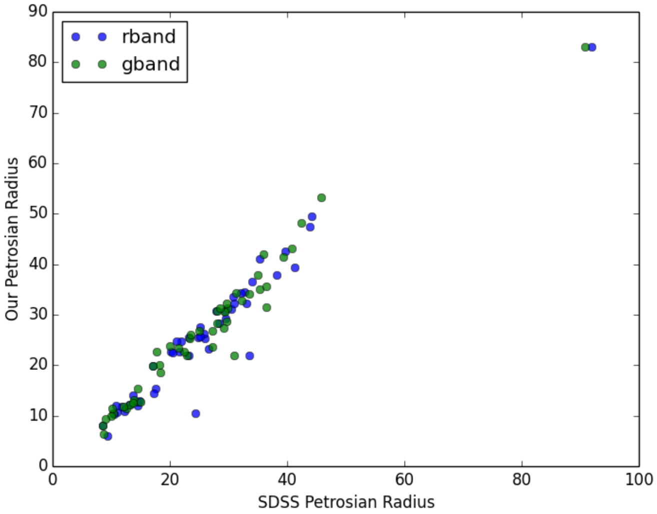

Figure 2.6: SDSS Petrosian Radius vs. My Petrosian Radii. This scatter plot compares the SDSS Petrosian radii measured in the g- and r-bands to my measurement of the Petrosian radii for those same bands. The one-to-one nature of this figure highlights that I am able to accurately remeasure r_p.

where L_j is the luminosity of the jth star or galaxy and w_j is the weighting factor associated with that star or galaxy, given by Equation 2.9,

$$w_j = e^{-(\frac{d_{i,j}^2}{2(2r_{p,i})})^2} \tag{2.9}$$

where, $d_{i,j}$ is the distance between the galaxy and its neighbor, and $r_{p,i}$ is the SDSS Petrosian radius of the galaxy.

Using Equations 2.7, 2.8, and 2.9, I calculate the luminosity ratio for each galaxy, which, along with a comparison between the local and global sky backgrounds determines the fraction of the background difference added to the SDSS flux profiles. To determine the fraction of the background difference added to the light profile, I follow guidelines from *von der Linden et al.* (2007):

1). If δ_{sky} = sky$_{local}$ - sky$_{global}$ < 0.0, no correction is applied; the backgrounds are equivalent.

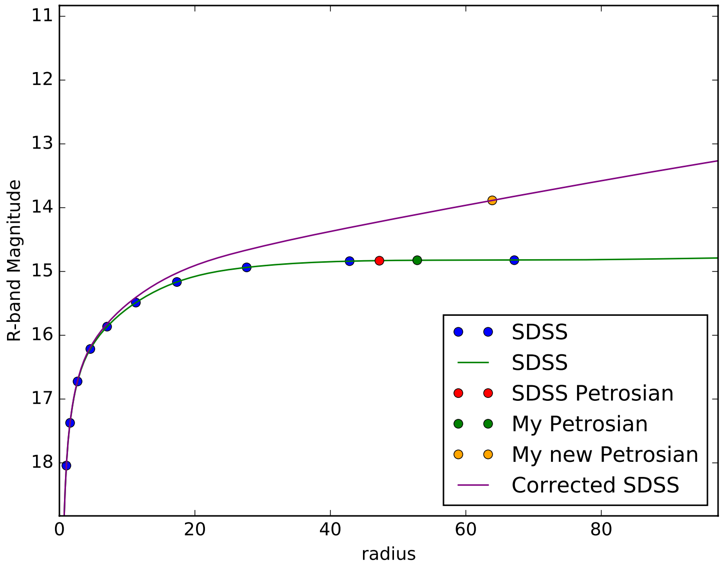

Figure 2.7: Corrected SDSS Light Profile. This is a corrected light profile for an SDSS-C4 BCG plotted as a funtion of radius in kpc. The light profile illustrates the impact of incorporating the *von der Linden et al.* (2007) background correction to the SDSS light profile. Additionally, comparing the red and yellow points illustrates how the background correction changes r_p as well as the Petrosian magnitude.

2). If $\mathrm{LR}_i \leq$ -2.5, then a sky fraction (f_{sky}) of 0.7 is applied.

3). If $\mathrm{LR}_i \geq$ -1.0, then $\mathrm{f}_{sky} = 0.5$. This is a different value of f_{sky} than used in *von der Linden et al.* (2007). We chose 0.5 for the lower limit based on a comparison to the photometry from *Postman and Lauer* (1995). The difference between our approach and that described in *von der Linden et al.* (2007) likely exists because *von der Linden et al.* (2007) used SDSS data release 4 (*Adelman-McCarthy et al.*, 2006), while we use data release 12 (*Aihara et al.*, 2011).

4). If -2.5 $< \mathrm{LR}_i <$ -1, f_{sky} is a continuous linear function of LR_i with minimum and maximum values of 0.5 and 0.7, respectively.

Using these guidelines, I determined the amount of flux required to correct the SDSS background. $\mathrm{f}_{sky} \times \delta_{sky}$ is then added to each radial flux measurement, after which r_p and the Petrosian magnitudes are recalculated using the new flux profiles. An example of a corrected light profile is shown in Figure 2.7, which highlights that the *von der Linden et al.* (2007) correction can change both the Petrosian magnitude by up to ≈1.0 magnitudes as well as r_p.

To calibrate the maximum and minimum f_{sky} value used in this analysis, we use the 40 BCGs found in both the SDSS-C4 (*Miller et al.*, 2005) and the *Postman and Lauer* (1995) samples. The *Postman and Lauer* (1995) data has excellent photometry and does not utilize the SDSS pipeline. Figure 2.8 illustrates that the accuracy of our magnitudes compared to the *Postman and Lauer* (1995) magnitudes (in red) is ≈0.1 magnitudes, far less than the average *von der Linden et al.* (2007) correction, which is ≈ 0.5 magnitudes. The small dispersion between our corrected SDSS magnitudes and the *Postman and Lauer* (1995) magnitudes highlights that using the *von der Linden et al.* (2007) correction accurately accounts for the SDSS background subtraction error. Based on the comparison to the *Postman and Lauer* (1995) sample, for *Golden-Marx and Miller* (2018) we use 0.1 magnitudes as our photometric accuracy for our stellar mass and magnitude gap measurements. Additionally, we only apply the *von der Linden et al.* (2007) correction if it is greater than 0.1 magnitudes in each of three bands used in the analysis.

2.5.1.3 Measuring Magnitudes in Golden-Marx & Miller 2019

In *Golden-Marx and Miller* (2019), we chose to no longer use the Petrosian magnitudes. Instead, we use aperture magnitudes for our stellar mass estimates and model magnitudes for our magnitude gaps. We no longer use Petrosian magnitudes because we wanted to remove bias in our measurement of the SMHM relation, particularly the slope, associated with the magnitude measurements made using r_p, which differs greatly across the SDSS-C4 clusters; the average value of $2.0r_p$ is $56.2^{+33.9}_{-19.5}$ kpc. Thus, while the Petrosian ratio measures where 90% of a galaxy's flux is, it leads to a comparison of different regions of each BCG, such that we compare the inner region of one BCG to the outer envelope of another, which in the context of the two-phase

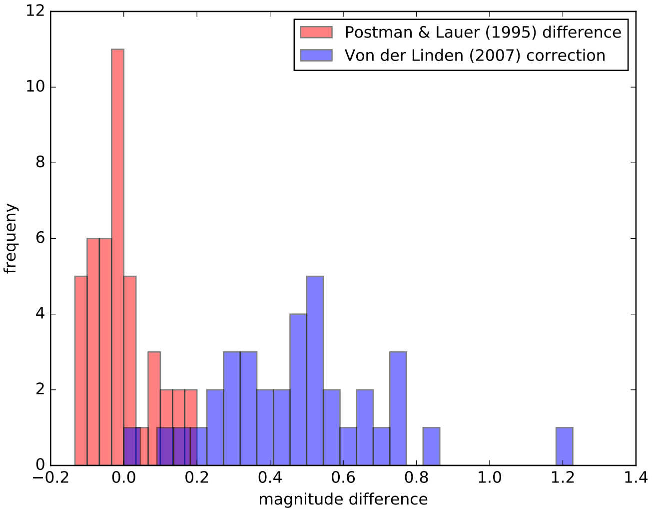

Figure 2.8: Photometric Accuracy vs. *von der Linden et al.* (2007) Correction. We compare our background corrected Petrosian BCG magnitudes to the magnitudes in *Postman and Lauer* (1995), based on deeper imaging. The red distribution shows the difference between our BCG Petrosian magnitudes and the *Postman and Lauer* (1995) magnitudes after this correction is made. Our algorithm recovers the *Postman and Lauer* (1995) magnitudes to within ±0.1 magnitudes, which we define as the statistical uncertainty of our BCG magnitudes. The blue distribution shows the *von der Linden et al.* (2007) correction applied to our SDSS Petrosian magnitudes in the r-band, which is much greater than the uncertainty in our magnitude measurement.

formation scenario (*Oser et al.*, 2010), leads to a comparison of two very different BCGs. Additionally, as shown in *Golden-Marx and Miller* (2019), the slope of the SMHM relation increases with radial aperture, so using the Petrosian magnitudes may bias our slope measurement and detection of late time evolution in the SMHM relation.

As explained in depth in Chapter IV, we use fixed 100kpc aperture magnitudes because the the slope of the SMHM relation becomes consistent, no longer increasing, at this radius. 100kpc represents a radial extent within which the vast majority of the stellar mass is contained (*Huang et al.*, 2018) and a possible transition regime between the BCG and ICL (*Zhang et al.*, 2018). To measure BCG magnitudes and stellar masses at 100kpc, we followed the same process described in Section 2.5.1.1 except that instead of measuring the magnitude at $2.0r_p$, we truncate these magnitude measurements at 100kpc.

Additionally, unlike in *Golden-Marx and Miller* (2018), we no longer use the *von der Linden et al.* (2007) correction in *Golden-Marx and Miller* (2019). Given that much emphasis was placed on the necessity of this correction in *Golden-Marx and Miller* (2018) and in Section 2.5.1, this choice was not made lightly. One primary reason we no longer used the *von der Linden et al.* (2007) correction was that the data from SDSS-redMaPPer (*Rykoff et al.*, 2014), covers the total redshift range $0.03 < z < 0.30$, which includes redshifts where the SDSS background correction is no longer problematic. The SDSS-redMaPPer sample covers a much higher range in redshift than *Golden-Marx and Miller* (2018), where $z_{med} = 0.086$. Additionally, the *von der Linden et al.* (2007) correction only applies to $\approx 30\%$ of our BCGs and the distribution of BCGs with a correction is uniform across the range in redshift space, halo mass, stellar mass, and magnitude gap covered by the SDSS-C4 sample. Therefore, since the impact of this correction was uniform across the SDSS-C4 data, we chose to no longer apply this correction, such that all of our data was treated in a homogeneous manner.

By no longer using the *von der Linden et al.* (2007) corrected Petrosian magnitudes, we greatly reduce the statistical uncertainty associated with the magnitude measurements and thus our stellar mass measurements as well. Although the *von der Linden et al.* (2007) corrected magnitudes correct the background, their use also introduces additional statistical uncertainty to our stellar mass measurement because of both the uncertainty associated with the *von der Linden et al.* (2007) correction as well as the difficulty in accurately measuring r_p.

Since applying the *von der Linden et al.* (2007) correction is an important part of this dissertation, espescially Chapter III, I measured how incorporating the *von der Linden et al.* (2007) correction to the 100kpc magnitudes would impact the results of *Golden-Marx and Miller* (2019). Incorporating the *von der Linden et al.* (2007) correction increases the stellar mass and magnitude gap of a sizeable fraction of our BCGs. However, the primary results based on the posterior distribution for the redshift evolution model presented in *Golden-Marx and Miller* (2019) do not change. The posterior values measured when the *von der Linden et al.* (2007) correction is applied at 100kpc and when it is not are within 1σ of one another as shown in Chapter IV. Moreover, we find that the strength of the redshift evolution of the slope is now a $> 4\sigma$ detection. Additionally, we note that the offset, α, is slightly lower because the average stellar mass of our sample has increased and that γ is slightly higher because of the increase in stellar mass (or BCG magnitude), which leads to a larger magnitude gap measurement. Based on this analysis, we find that the strength of the redshift evolution parameter associated with the slope is unimpacted by our choice to not use the *von der Linden et al.* (2007) correction. Therefore, our results do not suggest that the evolution we observe results from not incorporating the *von der Linden et al.* (2007) correction.

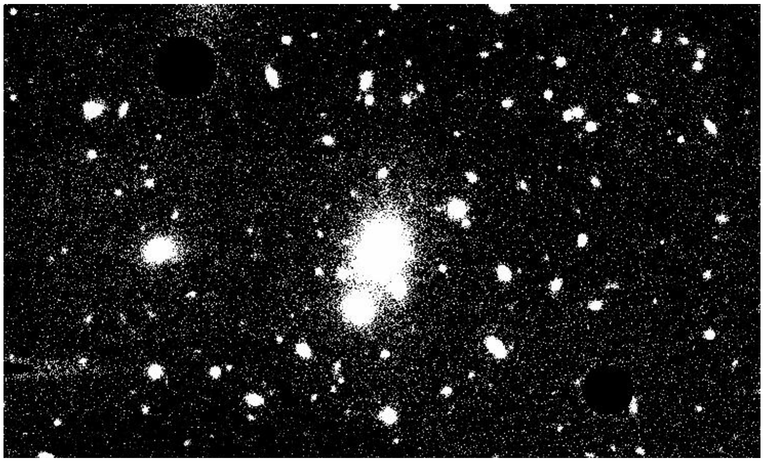

Figure 2.9: Coadded DES BCG Photometry. This is a coadded image centered on a DES-redMaPPer BCG.

2.6 Measuring BCG magnitudes for DES

In Golden-Marx et al. (in prep.), we extend our analysis to higher redshifts ($0.2 < z < 0.6$) using DES photometry. Unlike SDSS, DES does not provide radial light profiles for its BCGs; instead, only model magnitudes are provided. Since the measurements presented in *Golden-Marx and Miller* (2019) result from our use of fixed physical aperture magnitudes, we cannot use model magnitudes to measure stellar mass. Therefore, to measure the magnitude within 100kpc, we must measure the photometry directly from the fits images, following the procedure described in *Zhang et al.* (2018), which was designed to study the ICL of DES clusters over the redshift range $0.2 < z < 0.3$. Here, I summarize the relevant portions of the methodology from *Zhang et al.* (2018), expanding on what is described in Section 5.4.

To measure the DES light profiles, we use the RA, Dec, and redshift measurements of each BCG, identified using the DES redMaPPer catalog for the DES Year 3 data. First I coadd and stack all DES photometric images within 0.15° from the BCG, as shown in Figure 2.9. The coadding process masks previously detected objects in DES, as shown in the upper left and lower right corners of Figure 2.9. Using these coadded images, along with lists of all objects in the DES coadd catalog, which

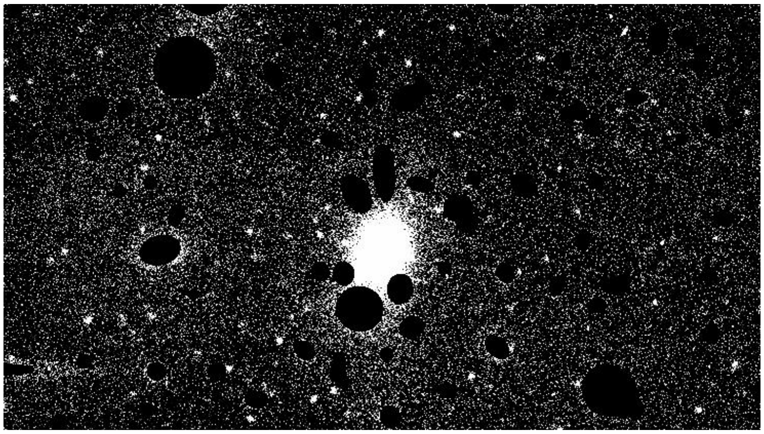

Figure 2.10: Masked DES BCG Photometry. This is a coadded image centered on a DES-redMaPPer BCG that masks the remaining bright galaxies.

reaches a 10σ completeness limit at 22.5 in the i-band (*Zhang et al.*, 2018), we mask all objects brighter than 30.0 magnitudes in the i-band, excluding the BCG, as shown in Figure 2.10. As described in Section 5.4.2, the masking limit was selected to minimize the difference between DES and SDSS photometry using BCGs in both samples. The masking radius used for this analysis is 2.5 r_k, which represents where $\approx$ 90% of the luminosity is contained. As shown in Figure 2.10, masking removes the majority of excess light associated with the neighboring galaxies, which allows for a cleaner measurement of the BCG and ICL radial light profile. Of note, the flux measurement is the average pixel value excluding the masked region since in some cases, neighboring galaxies are closer to the BCG than shown in Figure 2.10, and the edges of the BCG can be masked. Using these measurements, as was the case for the SDSS photometry, we assume spherical symmetry in the BCG light profiles when we integrate over circular radial apertures. An example of an i-band light profiles for one of our DES BCGs is shown in Figure 2.11. These light profiles include a background subtraction, where the background is determined by taking the median value of the radial regions beyond 500kpc from the BCG. Using the light profile, I follow the same procedure described in Section 2.5.1.3, where I integrate the light profile out to 100kpc. This process is repeated for each of the DES griz-band magnitudes; however,

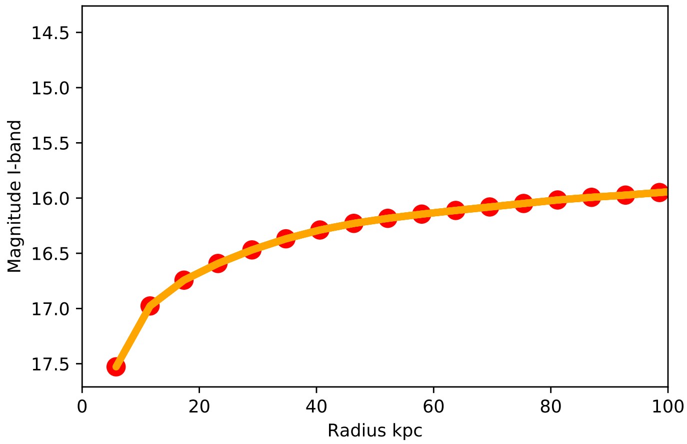

Figure 2.11: DES Reduced Light Profile. This is a reduced light profile integrated out to 100 kpc for a DES-redMaPPer BCG. The red dots are the radial magnitude measurements and the orange line is the linear interpolation fitting.

to maintain homongeneity with the SDSS data, we calibrate the uncertainty in the magnitudes and measure the stellar masses using g-, r-, and i-band photometry. Of note, due to the correlation between SED colors and redshift, we use r-, i- , and z-band photometry for clusters at $z > 0.40$ to measure the stellar masses.

Additionally, we note that the SDSS griz and DES griz wave bands are not the same. To determine if differences in SDSS and DES photometry exist, we use a sample of 61 BCGs in both DES and SDSS-redMaPPer to compare the estimates for the stellar mass and BCG magnitude. We find that when the SDSS griz magnitudes are converted to DES griz magnitudes, the colors and magnitudes are within 1σ of one another, yielding stellar masses which are also in 1σ agreement with those of SDSS, such that any offset is within the uncertainty. This agreement highlights that using the procedures outlined here we have a homogeneous set of stellar mass measurements over the redshift range $0.03 < z < 0.60$. We note that despite the homogeneity of our measurements, the SDSS and DES stellar masses and magnitude gaps do have differing uncertainties.

2.7 Conclusion

Photometry is a fundamental part of astronomy. For large photometric surveys such as SDSS and DES it is vital to understand the different photometric measurements as well as their systematic uncertainties. Despite the prevalence of photometric data, measuring BCG magnitudes remains problematic because unlike other galaxies, BCGs are located in crowded environments and surrounded by ICL. Therefore, it is important, particularly at low redshifts, as done in *Golden-Marx and Miller* (2018), to accurately account for these features in background measurements to ensure that the BCG magnitudes are uninfluenced by neighboring galaxies and ICL. Additionally, as evidenced in *Golden-Marx and Miller* (2019) it is also important to measure light from the outer regions of BCGs (out to 100kpc) because this is the region where information about a BCG's recent merger history is found (e.g. *Oser et al.*, 2010; *van Dokkum et al.*, 2010; *Huang et al.*, 2018). Therefore, only after this careful approach can BCG magnitudes with estimated magnitude uncertainties be trusted and used to measure the stellar mass of BCGs and the magnitude gaps, two of the three fundamental measurements central to this dissertation.

CHAPTER III

The Impact of Environment on the Stellar Mass-Halo Mass Relation

Results in this chapter were published in: ***Golden-Marx, Jesse B.***, *& Miller, Christopher J. 2018. The Impact of Environment on the Stellar Mass-Halo Mass Relation. The Astrophysical Journal, 860, 2*

3.1 Abstract

A large variance exists in the amplitude of the Stellar Mass – Halo Mass (SMHM) relation for group and cluster-size halos. Using a sample of 254 clusters, we show that the magnitude gap between the brightest central galaxy (BCG) and its second or fourth brightest neighbor accounts for a significant portion of this variance. We find that at fixed halo mass, galaxy clusters with a higher magnitude gap have a higher BCG stellar mass. This relationship is also observed in semi-analytic representations of low-redshift galaxy clusters in simulations. This SMHM-magnitude gap stratification likely results from BCG growth via hierarchical mergers and may link assembly of the halo with the growth of the BCG. Using a Bayesian model, we quantify the importance of the magnitude gap in the SMHM relation using a multiplicative stretch factor, which we find to be significantly non-zero. The inclusion of the magnitude gap in the SMHM relation results in a large reduction in the inferred intrinsic scatter in the BCG stellar mass at fixed halo mass. We discuss the ramifications of this result in the context of galaxy formation models of centrals in group

and cluster-sized halos.

3.2 Introduction

At the heart of galaxy clusters lie brightest central galaxies, or BCGs. These galaxies are bright, often $10L_\star$, where $L_\star$ is the characteristic luminosity of the galaxy luminosity function (e.g., *Schombert*, 1986), and extremely massive as shown by dynamical mass estimates (e.g., *Bernardi et al.*, 2007; *von der Linden et al.*, 2007; *Brough et al.*, 2011; *Proctor et al.*, 2011). Studies have also shown that BCGs can account for a substantial fraction of the total light emitted from a galaxy cluster (e.g., *Jones et al.*, 2000; *Lin and Mohr*, 2004; *Aguerri et al.*, 2011; *Harrison et al.*, 2012). Additionally, BCGs are often found near the X-ray centers of galaxy clusters (e.g., *Jones and Forman*, 1984; *Rhee and Latour*, 1991; *Lin and Mohr*, 2004; *Lauer et al.*, 2014). These massive central galaxies can also be more spatially extended than similarly massive elliptical galaxies (*Bernardi et al.*, 2007; *Lauer et al.*, 2007) and are often surrounded by halos of diffuse intracluster light (e.g., *Zwicky*, 1951; *Welch and Sastry*, 1971; *Oemler*, 1976; *Lin and Mohr*, 2004).

We note that not all central galaxies match the standard definition of a BCG. *Skibba et al.* (2011) and *Lange et al.* (2018) suggest that as many as 40% of massive, low redshift clusters have the equivalent of a satellite galaxy as their central. In contrast, *Lauer et al.* (2014) find that only 15% of all BCGs in their low redshift sample have a separation between the X-ray center and BCG greater than 100 kpc. While these results differ, it is likely that some fraction of BCGs are not always located at the cluster center-of-mass.

Researchers have been studying BCGs to understand their growth history for over forty years (e.g., *Ostriker and Tremaine*, 1975; *Ostriker and Hausman*, 1977; *Hausman and Ostriker*, 1978; *Malumuth and Richstone*, 1984; *Merritt*, 1985; *Fabian*, 1994; *Aragon-Salamanca et al.*, 1998; *Dubinski*, 1998; *De Lucia and Blaizot*, 2007; *Ruszkowski and Springel*, 2009; *Lidman et al.*, 2012; *Laporte et al.*, 2013; *Lin et al.*, 2013; *Lauer et al.*, 2014; *Nipoti*, 2017). Under the hierarchical structure formation paradigm, we might naturally expect some trends in the observable properties of BCGs to be caused by growth mechanisms that are not characteristic of the wider galaxy population. For instance, *Lauer et al.* (2014) conclude that the extended envelopes present in many BCGs are formed by processes within the cluster core region. They also suggest that especially bright BCG luminosities stem from accretion into more massive clusters.

In practice, a property used to differentiate BCGs from non-BCGs is the "magnitude gap," a measure of the difference in brightness between the BCG and some lesser galaxy within the cluster. Early on, it was suggested that BCGs and their magnitude gaps evolve through a process that differs from normal galaxies (e.g., *Tremaine and Richstone*, 1977; *Schneider et al.*, 1983; *Bhavsar and Barrow*, 1985; *Postman and Lauer*, 1995; *Bernstein and Bhavsar*, 2001; *Vale and Ostriker*, 2008). However, some recent studies, which use large cluster samples, argue that BCGs are simply statistical draws from the extreme bright end of the galaxy luminosity function (e.g., *Lin et al.*, 2010; *Paranjape and Sheth*, 2012). While this debate is not entirely settled, there exists a growing consensus that at least some component of the BCG population is distinct from the nominal distribution of elliptical galaxies (e.g., *Loh and Strauss*, 2006; *Vale and Ostriker*, 2008; *Collins et al.*, 2009; *Lin et al.*, 2010; *Lauer et al.*, 2014; *Shen et al.*, 2014; *Zhang et al.*, 2016).

From a theoretical perspective, *Milosavljević et al.* (2006) showed that excursion-set merger probabilities and the standard theory of dynamical segregation can explain the distribution of BCG magnitude gaps in low redshift clusters. At the same time, state-of-the-art cosmological simulations with semi-analytic and semi-empirical prescriptions for the growth of the stellar properties of galaxies also support the observational consensus of standard hierarchical mechanisms as the dominant influence on the growth of BCGs (e.g., *Croton et al.*, 2006; *De Lucia and Blaizot*, 2007; *Tonini et al.*, 2012; *Shankar et al.*, 2015). In other words, both the theory and data are converging onto a scenario that links the growth of BCGs to the earliest formation environments of their host halos.

Recently, *Solanes et al.* (2016) used dissipationless simulations of young and pre-virialized groups to show that the magnitude gap between the BCG and second brightest cluster galaxy correlates with the initial stellar mass fraction of the parent cluster halo. This correlation suggests that the observed magnitude gap can inform us about the underlying normal mass (both stellar and baryonic) of a cluster. For example, by identifying clusters with large magnitude gaps, we may simultaneously be identifying clusters with high stellar mass fractions during the epoch of BCG formation. Additionally, *Solanes et al.* (2016) found that the magnitude gap contains information about the BCG's merger history. In agreement with hierarchical growth, they found that a BCG's stellar mass increases with the number of progenitor galaxies (i.e., the number of mergers). Moreover, *Solanes et al.* (2016) found that BCGs grow at the expense of the second brightest galaxy in the cluster. Thus, as the BCG brightens, the cluster member identified as the 2nd brightest galaxy becomes fainter, relative to the BCG, leading to an increase in the magnitude gap. Combining these results implies that the magnitude gap not only correlates with the stellar mass of the BCG, but also provides information about the BCG's merger history.

One way to extend our understanding of how BCG properties relate to the host halo is to utilize the observed stellar mass – halo mass (SMHM) relation for clusters, which directly compares the amount of stellar mass within the central galaxy of the halo (i.e., the BCG) to the overall halo mass, including the baryonic and dark matter within the cluster. One of the earlier cluster-scale SMHM relations, presented in Figure 3 of *Lin and Mohr* (2004), illustrates that the BCG luminosity, which relates to the BCG stellar mass, linearly correlates with the halo mass. Since the work of *Lin and Mohr* (2004), there have been many characterizations of the SMHM relation (e.g., *Yang et al.*, 2009; *Moster et al.*, 2010; *Behroozi et al.*, 2010, 2013a; *Moster et al.*, 2013; *Tinker et al.*, 2017; *Kravtsov et al.*, 2018) across a much larger range in halo mass.

When one compares the high-mass end of the SMHM relation from *Lin and Mohr* (2004), *Hansen et al.* (2009), *Behroozi et al.* (2010), *Moster et al.* (2010), *Behroozi et al.* (2013a) *Bernardi et al.* (2013), *Moster et al.* (2013), *Tinker et al.* (2017), and *Kravtsov et al.* (2018) there are differences in the inferred amplitude as large as an order of magnitude in stellar mass at fixed halo mass (see Figure 3.17). One challenge when comparing published cluster-scale SMHM relations is that they use different cluster/BCG samples with different selection criteria. Additionally, there are differences in how BCG stellar masses are inferred (i.e., different initial mass functions (IMFs), stellar population synthesis (SPS) models, and star formation histories), and how cluster (halo) masses are measured. There can even be differences in how the BCG magnitudes are measured (e.g., *Kravtsov et al.*, 2018). A fair comparison between the previously published cluster-scale SMHM relations has yet to be reported.

Harrison et al. (2012) presented a cluster-scale SMHM relation and compared a sample of high magnitude gap X-ray clusters, fossil galaxies, to a normal-magnitude gap cluster population. In both cases, clusters were X-ray selected to minimize selection variations, and the BCG stellar masses were inferred using the same model. Instead of halo masses, cluster X-ray temperature was used as a halo mass proxy. In other words, *Harrison et al.* (2012) compared the SMHM relation for two cluster samples whose only difference was the magnitude gap. They found that for a given halo mass, galaxy clusters with larger magnitude gaps have BCGs with higher stellar masses than clusters with smaller magnitude gaps. This bifurcation between large-gap and small-gap clusters has also been previously observed for both cluster and group size halos in both simulations (*Díaz-Giménez et al.*, 2008; *Kundert et al.*, 2017) and in other observed samples (*Zarattini et al.*, 2014; *Trevisan et al.*, 2017). In addition, the *Harrison et al.* (2012) results suggest that perhaps as much as half of the scatter in BCG stellar mass at fixed halo mass may be accounted for by the magnitude gap. These previous results and studies lead us to explore the possibility that the SMHM relation contains the magnitude gap as a latent variable which, if properly accounted for, could reduce the intrinsic scatter in the stellar mass at fixed halo mass and simultaneously inform us about the formation history of both the BCG and the parent halo.

The outline for the remainder of the paper is as follows. In Sections 3.3 and 3.4 we describe the observational and simulated data used to determine the stellar masses, halo masses, and magnitude gaps that are used in our analysis of the SMHM relation. In Section 3.5 we describe the Bayesian MCMC model used to evaluate the SMHM relation. In Section 3.6 we present the results of our analysis for both the observations and simulations, which includes a quantitative measure on the impact of incorporating the magnitude gap. Lastly, we discuss our results in the context of galaxy formation scenarios in Section 3.7.

Except for the case of the simulated data, in which the cosmological parameters are previously defined (*Springel et al.*, 2005), for our analysis, we assume a flat ΛCDM universe, with Ω_M=0.30, Ω_Λ=0.70, H=100 h km/s/Mpc with h=0.7.

3.3 The Data

We use data from the Sloan Digital Sky Survey data release 12 (SDSS DR12; *Alam et al.*, 2015) to identify the clusters, measure the cluster masses, identify the BCGs, characterize their magnitude gaps, and estimate their stellar masses. We discuss each of these in the following subsections.

3.3.1 The SDSS-C4 Clusters and Dynamical Masses

We use galaxy clusters identified using the C4 algorithm (*Miller et al.*, 2005) on the SDSS DR12 data (*Alam et al.*, 2015). The algorithm identifies 970 clusters between $0.03 \leq z \leq 0.18$. As described in detail in *Miller et al.* (2005), the C4 algorithm uses the four colors from the SDSS galaxy main sample and applies a non-parametric algorithm to identify statistical over-densities in color and position space. As stated in *Miller et al.* (2005), only galaxies with spectra are used to identify candidate clusters, the larger SDSS photometric sample is then used to quantify the BCG magnitudes and the magnitude gap.

We then use the spectroscopically confirmed clusters to create radius/velocity phase-spaces of the galaxies projected along the line-of-sight to the clusters and relative to the mean velocity of the cluster members. We calculate "caustic" masses according to the algorithm defined in *Gifford et al.* (2013) for each cluster. Specifically, we identify the phase-space edge as a proxy for the projected escape velocity profile of each cluster individually. To infer masses from the projected escape velocity, the "caustic" technique requires a calibration term based on the unknown velocity anisotropy β. This term is typically referred to as $\mathcal{F}_\beta$ and we choose a value that calibrates "caustic" masses in N-body simulations, $\mathcal{F}_\beta$ = 0.65 (*Gifford et al.*, 2013). The uncertainty on $\mathcal{F}_\beta$ results from the projection of the three-dimensional velocities along the line-of-sight and is the dominant component of the error on the caustic cluster masses. *Gifford et al.* (2013) used simulations to also calculate the scatter in the true mass versus the "caustic" mass as a function of the number of galaxies used to construct the phase-spaces. This scatter, caused by the line-of-sight projection is the dominant component of the error in the caustic masses (*Gifford and Miller*, 2013; *Gifford et al.*, 2017). The mass error can be large for poorly sampled phase-spaces (e.g., 0.9 dex when N_{gal}=10) and has a floor of about 0.3 dex for well-sampled phase-spaces ($N_{gal} >$ 150). Therefore, we use heteroskedastic cluster mass errors based on Table 1 of *Gifford et al.* (2013).

3.3.2 Candidate Cluster Sample

To construct the cleanest SMHM relation for our C4 clusters, we applied additional cuts to the cluster sample. These cuts are summarized in Table 3.1. We require $\log_{10}(M_{caustic}$ $/(M_{\odot}/h)) \geq 14.0$ to ensure higher completeness of our sample. This cut reduces the total number of clusters from 970 to 420. We then further reduced our sample by analyzing the caustic phase space, velocity histogram, and red sequence within R_{vir} from the cluster center for each cluster. We removed 32 clusters which had either a broad and unpeaked velocity histogram, indistinguishable red sequence within R_{vir}, or poorly defined caustic phase space, leaving us with a sample of 388 clusters. The number of galaxies used to construct the cluster phase-spaces ranged from 31 to 1074 with a median of 122 for the remaining clusters. Additionally, 6 more clusters were removed due to photometric issues in the SDSS pipeline, leaving us with 382 clusters.

For the purpose of measuring the magnitude gap between the BCG and 2nd or 4th brightest galaxies, we also require that each cluster contain 4 members identified using the red sequence within 0.5 R_{vir}.[1] Our process of identifying cluster members will be described in further depth in Section 3.3.4. This cut reduced our final sample by 12 clusters, leaving us with an initial sample of 370 clusters. Additional cuts were made based solely on BCG photometry, which we describe below.

---

[1] We use 0.5 R_{vir} to determine these magnitude gaps because it is the standard radius used in the definitions of fossil galaxies presented in *Jones et al.* (2003) and *Dariush et al.* (2010).

3.3.3 BCG Identification and Characterization

For the majority of clusters the BCG is clearly the brightest galaxy and can be easily identified algorithmically using the red-sequence; however, not all clusters have a clear and distinctive BCG (*von der Linden et al.*, 2007; *Lauer et al.*, 2014). Therefore, we visually inspect images of each cluster in regions out to 0.5 R_{vir} radial. For approximately 70% of our galaxy clusters, the visual checks confirm the BCGs through a simple selection algorithm (e.g., *von der Linden et al.* (2007)). In the other cases, the BCGs are identified after allowing for positional offsets from the originally defined cluster centers (still within 0.5 Mpch^{-1}), or by allowing for BCG colors that are bluer than the red sequence (by up to 0.2 magnitudes in $g - r$ color). In these cases, we selected elliptical BCGs that had positions, redshifts, and colors which matched the cluster and red sequence. In a few (<2.5%) cases, it was not clear which of the two brightest galaxies was the BCG, so we chose at random. Since the brightness and color of these galaxies are similar, this choice will make no discernible difference in the measurements of either the stellar mass, magnitude gap, or cluster (halo) mass.

3.3.3.1 BCG Stellar Mass Measurements

To estimate BCG stellar masses, we require accurate extinction corrected BCG apparent magnitudes. The SDSS DR12 photometric pipeline overestimates the light contribution from the local background for large, extended objects, and crowded fields. Therefore, BCGs are likely to be affected by this background overestimation, which would lead to an under-approximation of the stellar mass (e.g., *Bernardi et al.*, 2007; *von der Linden et al.*, 2007; *Harrison et al.*, 2012; *Bernardi et al.*, 2013).

We correct the BCG Petrosian magnitudes using the prescription outlined in the appendix of *von der Linden et al.* (2007) applied to the SDSS DR12 apparent g-, r-, and i-band magnitudes of our BCGs. The *von der Linden et al.* (2007) correction works by adding a fraction of the difference between the SDSS local and global sky backgrounds to each individual galaxy's light profile. Since the original *von der Linden et al.* (2007) correction was calibrated using SDSS DR4 data, we re-calibrate the algorithm to correct SDSS DR12 data.

Postman and Lauer (1995) utilize deep imaging to create precise light-profiles to measure BCG total magnitudes for a small subset of our cluster sample. In Figure 3.1, we compare the results of our corrected BCG magnitudes against the *Postman and Lauer* (1995) BCG magnitudes. We find that our background corrected magnitudes recover the more carefully measured *Postman and Lauer* (1995) BCG magnitudes to within 0.1 magnitudes, which we define as the statistical floor for all of our BCG magnitudes. Note that we only apply the re-calibrated *von der Linden et al.* (2007) correction to our galaxies when the difference between the local sky background and the global sky background is positive and when the correction itself is greater than our baseline precision (0.1 mags) in each of the bands used in our final analysis (r and i).

Of our 370 BCGs, we find that 28% require a *von der Linden et al.* (2007) correction greater than our photometric accuracy, 0.1 magnitudes in both the r- and i-bands. Additionally, the median r-band *von der Linden et al.* (2007) correction is 0.51 magnitudes as shown in Figure 3.2, which underscores the importance of correcting the SDSS photometric measurements prior to estimating stellar masses. Also, we find that the BCG magnitude corrections are uncorrelated with their magnitude gaps.

After applying the *von der Linden et al.* (2007) correction to our SDSS light profiles, we used the cluster redshifts and apply a k-correction for the r- and i-band magnitudes using the kcorrect (v 4.1.4) code (*Blanton and Roweis*, 2007) to obtain our final BCG apparent magnitudes.

To estimate stellar masses, we used the color-dependent M/L ratio from *Bell et al.* (2003) using the r-i color.[2] Our choice of a color-dependent M/L ratio (*Bell et al.*, 2003) makes the stellar mass and associated error measurement used in our model, described in Section 3.5, dependent on the identification of "red and dead" elliptical galaxies. To verify that this description matches our selected BCGs, we compare the color of each individual BCG to the color of a fiducial BCG, which we model using the EzGal SED modeling software (*Mancone*

---

[2] We only use the r-i color to estimate stellar mass, so the requirement that the *von der Linden et al.* (2007) corrections be ≥ 0.1 magnitudes is only applied to the r- and i-bands. The g-band was not used in our final stellar mass estimates.

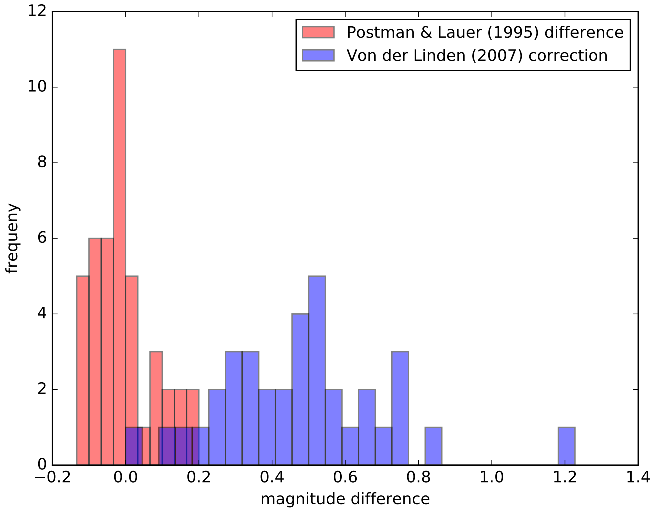

Figure 3.1: Photometric Accuracy vs. *von der Linden et al.* (2007) Correction. We compare our background corrected Petrosian BCG magnitudes to the total magnitudes in the *Postman and Lauer* (1995) sample, which is based on deeper imaging and has a more accurate background. The red distribution shows the difference between our BCG Petrosian magnitudes and the *Postman and Lauer* (1995) magnitudes (within the Petrosian radius) after this correction is made. We find that our algorithm can recover the *Postman and Lauer* (1995) magnitudes to within ±0.1 mags, which we define as the statistical floor of our BCG magnitudes. The blue distribution shows the level of the correction to the SDSS Petrosian magnitude r-band that we apply based on our algorithm. Of note, 81% of the matches to the *Postman and Lauer* (1995) sample required a correction.

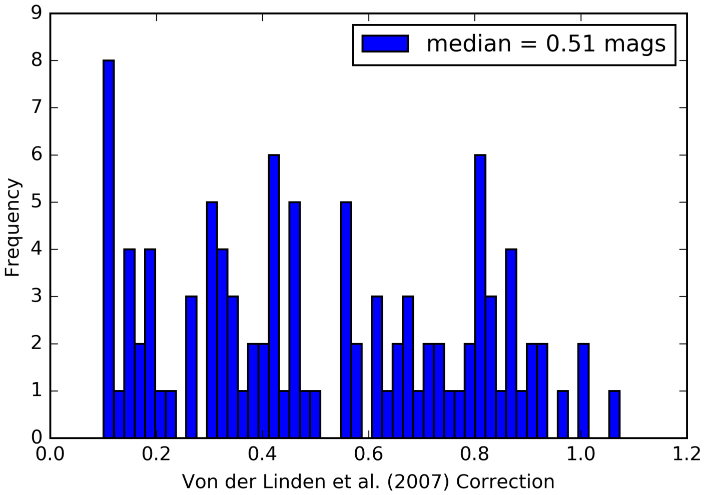

Figure 3.2: Average *von der Linden et al.* (2007) Correction. The distribution of the *von der Linden et al.* (2007) r-band corrections ≥ 0.10 magnitudes for our SDSS-C4 BCGs. The majority of corrections are large, which highlights the importance of background corrections prior to estimating stellar masses.

and Gonzalez, 2012), assuming a *Bruzual and Charlot* (2003) SPS model, a *Chabrier* (2003) IMF, a formation redshift of 4.9, and a redshift matching the individual BCG's. However, neither the choice of IMF or z_{form} strongly impacts the modeled color. We confirm that our selected BCGs are "red and dead" if their measured color is within 0.1 magnitudes of the color of our fiducial BCG at the same redshift.

We apply this criteria based on our fiducial BCG because the *Bell et al.* (2003) M/L ratio we use to estimate the stellar mass is color dependent. Therefore, we remove BCGs whose colors do not match the fiducial BCG model colors because such colors resulted in non-physical stellar mass determinations based on our nominal SED analysis. If we naively incorporate this data, we see strong deviations from Gaussianity, in that 30 of the BCGs that don't match the fiducial model are outliers in the SMHM versus M14 relation. Instead of selectively removing just the outliers, we chose to exclude all BCGs that do not match our fiducial model from the analysis, even though the majority fit the relation. Another approach would be to fit an additional outlier component in our model and an even better solution would be to conduct a detailed SED modeling analysis of all of the

BCGs, investigating which dust models and star formation histories best fit the colors. Both of these approaches are beyond the scope of this effort. Our sample is large enough to be selective against the quality of the SED model fits. We note that removing a random selection of 25% of the BCGs of our final sample does not change our results. Applying this color restriction removed 90 clusters, reducing our total sample to 280 clusters. Therefore, roughly three-quarters of the BCGs can be characterized as agreeing with our fiducial "red and dead" model; of the BCGs that were removed, 44% are > 0.1 magnitudes bluer and 56% are > 0.1 magnitudes redder than that of our fiducial BCG model.

3.3.4 Quantifying the Magnitude Gap

For our analysis, we chose to measure the magnitude gap between the BCG and fourth brightest cluster member (M14) and the BCG and second brightest cluster member (M12). To do this, after identifying the BCG in each cluster, we identify red sequence galaxies within 0.5 R_{vir} to determine the cluster membership and magnitude gap. We used M14 and M12 as well as the 0.5 R_{vir} for our membership and magnitude gap measurements because these were the magnitude gaps and radial extent used in the standard definitions of fossil group galaxies from *Jones et al.* (2003) and *Dariush et al.* (2010). We fit the individual cluster red sequences in six distinct SDSS colors (u-g , g-r, g-i, i-r, i-z, and r-z) for all galaxies with an r-band magnitude brighter than m_r=19 within the 0.5 R_{vir} region.

We then characterize the magnitude gap using galaxies within 3σ of the fit to the red sequence for the u-g, g-r, and g-i colors and 2σ for the i-r, i-z, r-z colors. We note that we do not require galaxy spectroscopy for cluster membership; however, whenever possible, we do utilize available SDSS spectroscopic redshifts and remove any potential cluster member with $|z_{gal} - z_{clus}| > 3\sigma/c$. In Figure 3.3, we present an example color magnitude diagram for one of our clusters to highlight the impact of incorporating the available spectroscopic redshifts to further remove remaining foreground contaminants (the point with an x through it in Figure 3.3). Doing so leads to a fainter 4th brightest galaxy and an increase in the magnitude gap. We note that spectroscopic information is not available for all red sequence candidates and that the incorporation of available spectroscopic redshifts only

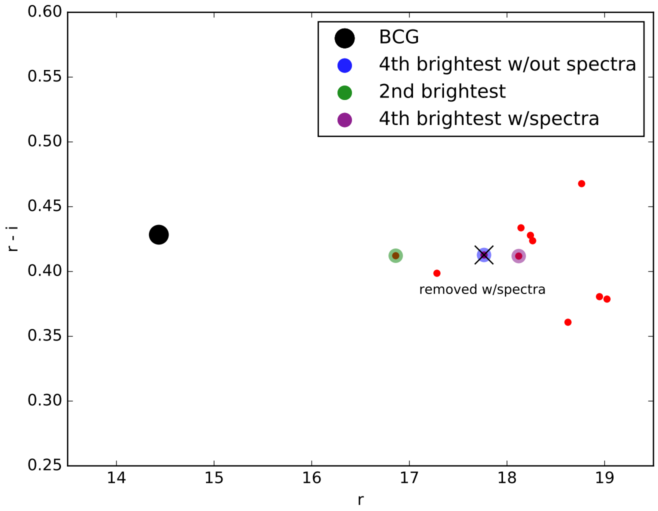

Figure 3.3: Example SDSS-C4 Color Magnitude Diagram. A sample color-magnitude diagram from one of our SDSS-C4 clusters. This figure illustrates the impact of incorporating the spectroscopic redshift information. The black point is the BCG, the green point is the 2nd brightest galaxy, the blue point is the 4th brightest galaxy when not using available spectroscopic information, and the purple point is the 4th brightest galaxy when using spectroscopic information. This color magnitude diagram highlights that using the limited spectroscopic information further removes foreground contaminants, leading to a better identification of the 4th brightest galaxy in the cluster.

changes the 4th brightest galaxy for 5% of our clusters. We further address the use of galaxy redshifts and red-sequence membership in Section 3.4, where we use a simulated sky survey to constrain systematic uncertainties due to projection effects in the magnitude gaps. Additionally, we do not require the BCG to have a spectrum to place it within the spectroscopically confirmed cluster. Since the measurement of the magnitude gap is dependent upon fitting a red sequence, as previously noted, we remove the 12 clusters from our sample which either had fewer than 4 members or for which we are unable to fit a red sequence for the cluster members within 0.5 R_{vir}.

After identifying the second and fourth brightest cluster members, we apply k-corrections using the cluster redshifts and kcorrect (v 4.1.4) code (*Blanton and Roweis*, 2007) to obtain our final fourth and second brightest member apparent magnitudes. We then measure the two unique magnitude gaps, M14 and M12, in the r-band. Unlike the BCGs the majority of second and fourth brightest galaxies are neither extended nor located in dense regions; therefore, we do not apply a *von der Linden et al.* (2007) correction.

Using the final sample of 280 clusters, we ran a completeness analysis following a similar approach to what is described in *Colless* (1989), *Garilli et al.* (1999), *La Barbera et al.* (2010), and *Trevisan et al.* (2017). To determine the completeness, we first convert the apparent magnitudes for our BCGs and 4th (2nd) brightest members to R-band absolute magnitudes, then bin the absolute magnitudes by apparent magnitude, and calculate the 95% limit in each bin. Using this upper limit, we fit a linear relation between the upper limit and apparent magnitude of each bin and determine the absolute magnitude that corresponds to an apparent magnitude of $m_r = 19$, the upper limit we applied to our SDSS galaxy catalogs. We chose this rather bright upper limit to minimize additional photometric measurement uncertainties in our analysis. We note that the absolute magnitude limit for the 2nd brightest galaxies is dimmer than the limit for the 4th brightest because we require at least 4 members in the red-sequence.

Next, we follow the same procedure, but instead bin the absolute magnitude as a function of magnitude gap and determine the 95% limit in each bin, which leads to an upper limit on the M14 (M12) magnitude gap of 3.58 (3.035). After applying these cuts, we remove 44 (26)

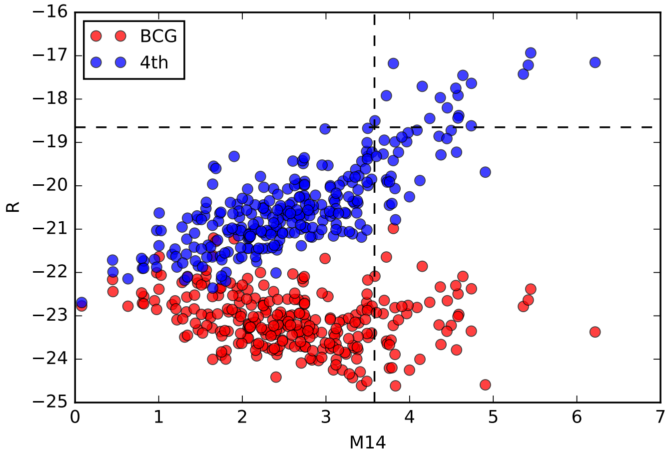

Figure 3.4: M14 Completeness Analysis. R-band absolute magnitude versus M14. This is used to determine the completeness of our SDSS-C4 sample. The vertical and horizontal lines represent the limits in M14 and absolute magnitude, respectively. The BCGs are shown in red and the 4th brightest cluster members are shown in blue.

additional clusters, as shown in Figures 3.4 and 3.5, leaving us with a total sample of 236 (254) "red and dead" elliptical BCGs with magnitude gap measurements. If we apply more stringent cutoffs for both the magnitude gap and absolute magnitude, we find no significant difference in the posterior distributions.

3.3.5 Final Sample Summary

After applying the different criteria, summarized in Table 3.1 we are left with our final sample which contains either 236 or 254 clusters, depending on the magnitude gap used. Our sample can be characterized as having $\log_{10}(M_{halo}/(M_{\odot}/h)) \geq 14.0$, which are measured using the caustic technique on well sampled radius-velocity phase spaces. The halo mass uncertainties of the clusters in our final sample range from 0.31 - 0.46 dex with a median of 0.32 dex. For each cluster the BCG is a "red and dead" elliptical galaxy with a color that is within 0.1 magnitudes of the color of our fiducial BCG. Moreover, each cluster has a clearly defined red sequences with greater than four members, including 2nd or 4th brightest galaxies whose absolute magnitudes and associated magnitude gaps fall within our completeness criteria.

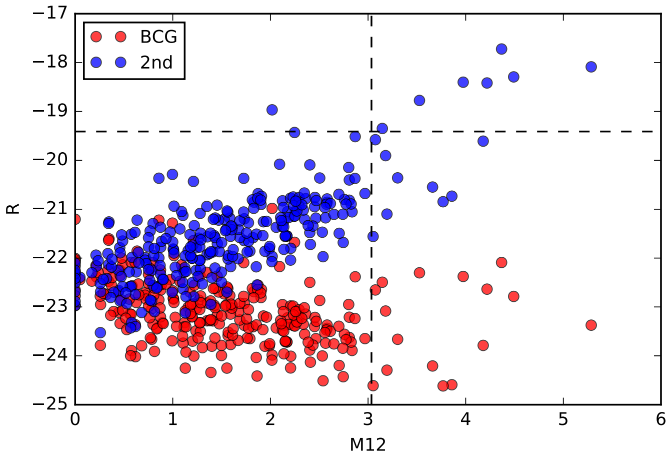

Figure 3.5: M12 Completeness Analysis R-band absolute magnitude plotted against M12. This is used to determine the completeness of our SDSS-C4 sample. The vertical and horizontal lines represent the upper limits in M12 and absolute magnitude, respectively. The BCGs are shown in red and the 2nd brightest cluster members are shown in blue.

SDSS-C4 Final Sample: Summary of removed clusters

Section Critera	Number Removed	Number Remaining
C4 clusters		970
$\log_{10}(M_{caustic}/(M_{\odot}/h)) \geq 14.0$	450	420
Broad unpeaked velocity histogram, unidentifiable red sequence, poorly defined caustic	32	388
Photometric errors	6	382
No red sequence within $0.5R_{vir}$	12	370
BCG color does not match “red and dead” fiducial BCG	90	280
Completeness analysis	44 (26)	236 (254)
Final sample		236 (254)

Table 3.1: SDSS-C4 Final Sample: Summary of Removed Clusters. This represents the results of the completeness analysis for the sample done using the M14 (M12) magnitude gaps.

3.4 Simulated Data

In addition to studying the impact of the magnitude gap on the SMHM relation in the SDSS-C4 cluster sample, we also analyzed this trend in simulations using the *Guo et al.* (2011) and *Henriques et al.* (2012) prescriptions of the semi-analytic representations of low-redshift galaxy clusters in the MILLENNIUM simulation. We chose these semi-analytic models because the galaxies grow hierarchically, which as *Solanes et al.* (2016) suggest, may relate to the magnitude gap. We note that the *Henriques et al.* (2012) prescription is constructed by taking the semi-analytic redshift snapshots from *Guo et al.* (2011) and stitching them together to create a mock light-cone (*Henriques et al.*, 2012). We use both the 3D information from this light-cone as well as the full projected data in our analyses that follow.

In our analysis of the simulations, we aim to treat the simulated data in a similar manner to the SDSS-C4 observational measurements of stellar mass, halo mass, and magnitude gap. In doing so we generate two catalogs; a sample that uses all of the 3D information provided for the cluster (i.e., halo masses measured within $r_{200}\times$ ρ_{crit}, galaxy positions in x, y, z, and semi-analytic stellar masses, and magnitudes) and a projected sample, which instead uses only 2D information (i.e., caustic-inferred cluster masses, RA, Dec, redshift, apparent magnitudes, and inferred stellar masses).

When using the 3D data, we use the stellar masses for each central halo's galaxy directly from *Henriques et al.* (2012). For both the 3D and 2D data, we identify the BCG as the brightest red-sequence galaxy within $0.5R_{vir}$. We then use the red-sequence to define the magnitude gaps. We estimate the BCG stellar masses for the 2D sample using the same *Bell et al.* (2003) M/L ratio conversion based on the r-i color. Finally, the projected cluster masses were determined using the caustic technique (2D) (*Gifford et al.*, 2013). In other words, the 2D projected data are treated almost identically to the real SDSS data, except for visual classification and identification of the BCG.

Determining cluster membership and the magnitude gap was done slightly differently for our simulations because we have different available information. For the 3D sample, we use the positional information (x, y, z) to determine if a galaxy is within 0.5 $R_{sim,vir}$. For the galaxies within this sphere, we use the red sequence to determine cluster membership. For the 2D projected sample, we followed the same steps outlined for our own observations. We use RA and Dec, to determine if a galaxy is within a circle of 0.5 R_{vir} centered on the BCG. Next we check to see if $|z_{gal} - z_{clus}| < 3\sigma/c$, where σ is the measured velocity dispersion. For those remaining cluster members, we use the red sequence to determine membership. We note that the measurements in our 2D projected catalog introduce error in the halo mass, from the caustic measurements, stellar mass, and magnitude gap. Understanding how to incorporate these additional errors was crucial in creating our Bayesian MCMC model for the SMHM relation, as described in Section 3.5.

Of note, unlike with our observations, the simulated BCGs are treated as being "red and dead". Furthermore, because we have access to the complete 3D simulation box, we do not perform a completeness test to remove some of the clusters with either extremely large magnitude gaps or fainter second and fourth brightest galaxies. Additionally, we apply the same mass thresholds on both the 2D and 3D simulations and the SDSS-C4 data such that the observed mass is $\log_{10}(M_{caustic}/(M_{\odot}/h)) \geq 14.0$ and the underlying halo mass distribution for the simulated data is an approximation of the *Henriques et al.* (2012) mass function truncated at $\log_{10}(M_{halo}/(M_{\odot}/h)) \geq 14.0$. We note that if we adjust this halo mass thresholds by 0.1 dex in either direction the results of the posterior distributions are within one sigma of those presented in Figures 3.6 and 3.7.

3.5 The Hierarchical Bayesian Model

Unlike other quantitative analyses of the SMHM relation (e.g., *Yang et al.*, 2009; *Moster et al.*, 2010, 2013), we do not use a two component power law to describe our SMHM relation. Instead, we use a single component power law, because we are only concerned with the high mass portion, $\log_{10}(M_{halo}/(M_{\odot}/h)) \geq 14.0$, of the SMHM relation. Additionally, we do not allow for redshift evolution in this low-redshift dataset ($z \leq 0.18$, $z_{median} = 0.086$) unlike other published SMHM relations (e.g., *Behroozi et al.*, 2013a; *Moster et al.*, 2013) because the results of these prior studies suggest the change of the slope of the SMHM relation over this redshift range is smaller than the precision of the posteriors for the slope of our Bayesian MCMC analysis.

We assume a linear model for our data, given by Equation 3.1,

$$\log_{10}(M_*) = \alpha + \beta(\log_{10}(M_{halo})) + \gamma(M14) \tag{3.1}$$

which is parameterized by a slope, β, y-intercept, α, and the "stretch" parameter related to the magnitude gap, γ. For the remainder of the analysis, we refer to the log (base 10) BCG stellar masses as y, the log (base 10) cluster (or halo) masses as x, and magnitude gaps as z.

To determine the appropriate values for α, β, and γ, as well as the intrinsic scatter, σ_{int}, in our relation, we use a Bayesian MCMC analysis to maximize the sum of the log-likelihoods for each cluster. The Bayesian approach can briefly be described as convolving the prior information for a given model with the likelihood of the observations given the model, which yields the posterior distribution, or the probability of observing the data given the model. We use a Bayesian analysis because it allows us to easily account for all prior information. It is hierachical in the sense that we model both the errors on our parameters, as well as the uncertainty on those errors.

Throughout our Bayesian likelihood analysis, the MCMC model generates values for stellar mass, halo mass, and magnitude gap, which are directly compared to the respective observed measurements given the errors in the data. The comparison between the model generated data and our observations allows us to construct posterior distributions for all of our free parameters, from which we can determine the most likely values for α, β, γ, and σ_{int} as shown in the triangle plots presented in Sections 3.6.1.2 and 3.6.2.2. In the following subsections and Table 3.2, we provide all of the details regarding our model.

3.5.1 The Observed Quantities

We use the observed BCG magnitudes and colors to create a stellar mass, y_{0i}, which we treat as an observable. There is also an error on the observed stellar masses, which we treat as Gaussian, so the observed stellar mass is:

$$y_{0i} \sim \mathcal{N}(y_i,\, \sigma^2_{y_i}). \tag{3.2}$$

where y_i is the underlying (and unknown) true stellar mass and σ_{y_i} is the modeled uncertainty on the measurement. We model the observed uncertainty on the stellar mass as a beta distribution centered on a measured value, $\sigma_{y_{0i}}$. This value can vary depending on whether we are analyzing the real or the simulated data (more details below). The use of the beta distribution allows for stochasticity and additional uncertainty (e.g., systematic bias) in our observed stellar mass errors.

$$\sigma_{y_i} = \sigma_{y_{0i}} \pm \mathcal{B}(a, b) \tag{3.3}$$

where $a = 0.5$ and $b = 100$ are the shape parameters of the beta distribution. These shape parameters add up to ±0.06 dex to our BCG stellar mass error estimates.

For the observed cluster masses, we use the observed radius-velocity phase-spaces to produce observed caustic masses. We apply a lower mass threshold of $1 \times 10^{14}\mathrm{M}_{\odot}/h$ and thus use a truncated normal defining the cluster caustic masses:

$$x_{0i} \sim \mathrm{T}\mathcal{N}(x_i,\, \sigma^2_{x_i}, x_{0min}, x_{0max}). \tag{3.4}$$

where x_i is the underlying (and unknown) true halo mass, σ_{x_i} is the modeled uncertainty on the mass measurement and x_{0min} and x_{0max} specify the lower and upper limits on the observed caustic masses in the sample. We note that for the simulations, we apply the same observational halo mass limit. In practice, for the SDSS-C4 data, we use the "observed" uncertainty, $\sigma_{x_{0i}}$, on each cluster mass, which is based on the mapping between the number of galaxies in the phase-space to the caustic mass uncertainty as quantified in simulations

(*Gifford et al.*, 2013). Because there is some uncertainty due to the use of simulations, we add an additional stochastic component drawn from the beta probability distribution:

$$\sigma_{x_i} = \sigma_{x_{0i}}(N_{phase_i}) \pm \mathcal{B}(a, b) \tag{3.5}$$

where $a = 0.5$ and $b = 100$ are the shape parameters of the beta distribution. As before, this additional uncertainty ranges up to ± 0.06 dex.

We treat the observed magnitude gap similarly to the halo masses. The observed gap is drawn from a truncated Normal distribution:

$$z_{0i} \sim T\mathcal{N}(z_i, \sigma_{z_i}^2, z_{0min}, z_{0max}). \tag{3.6}$$

where z_i is the underlying (and unknown) true magnitude gap, σ_z is the modeled uncertainty on the magnitude gap, and z_{0min} and z_{0max} represent the lower and upper limits on the magnitude gap, set by the completeness analysis. We note that for the simulated data, we do not use a truncated Gaussian because we do not apply the completeness limits, as described in Section 3.4. For the uncertainties on the magnitude gap, we compared the distribution of our "observed" gaps to the distribution of true 3D gaps using the simulations. Additionally, for our SDSS-C4 clusters, we add an uncertainty, $\sigma_{z_{0i}}$, of 0.1 magnitudes to account for the photometric measurement uncertainty of our BCG magnitudes. Since this is also calibrated using simulations, we include an additional stochastic component using the beta probability distribution.

$$\sigma_{z_i} = \sigma_{z_0 i} \pm \mathcal{B}(a, b) \tag{3.7}$$

where $a = 0.5$ and $b = 100$ are the shape parameters of the beta distribution. Like before, this addition ranges up to ± 0.06 to the error in magnitude gap.

Given the above likelihoods for an observed BCG (x_{0i}, y_{0i}, and z_{0i}), we sum the log of the likelihoods defined by the χ^2 distribution since all of our probability distributions are Gaussian. We will map the posterior using an MCMC approach. However, we still need to define the unobserved parameters and their prior probability distributions.

3.5.2 The Unobserved Quantities

For each cluster i, our model returns a true log stellar mass (y_i) given the true magnitude gap (z_i), the true log halo mass (x_i), and the parameters that relate them (α, β, γ). We also allow for intrinsic scatter, σ_{int}, in our relationship. Thus, we model y_i as:

$$y_i = \mathcal{N}(\alpha + \beta x_i + \gamma z_i, \sigma_{int}^2). \tag{3.8}$$

We note in Equation 3.8 that the halo masses, the magnitude gaps, and the parameters α, β, and γ which together yield a BCG stellar mass are the true values. The Bayesian model regresses against the observed stellar masses, cluster masses, and magnitude gaps self-consistently. We define the relationship as being *causal* and relating the true underlying BCG stellar mass to the halo mass and the magnitude gap. The parameters that we are interested in are the intercept, slope, stretch, and intrinsic scatter. All other parameters are treated as nuisance parameters and are marginalized over when we present the posterior probability distributions.

We do not use uniform priors on the halo masses or the magnitude gaps because there is no reason to expect it in the real universe. The prior on halo masses x_i, is the mass function of the halos given from the 3D *Henriques et al.* (2012) data, modeled as a truncated Gaussian with a mean and width, which are treated as free parameters that are given by a fit to this mass function. For this analysis, we truncate the halo mass function at $x_i = 14.0$. We find no significant difference in our posteriors if we lower this threshold to $x_i = 13.8$. In other words, our results are not sensitive to the exact truncation limit we use on the underlying mass function. The prior on the magnitude gaps is defined by the observed magnitude gap distribution modeled as a Gaussian where the mean and width are free parameters given by this magnitude gap distribution. For the means and widths of both the magnitude gap and halo mass, the free parameters are modeled as Normal distributions. [3]

---

[3] For simplicity, in Table 3.2 the value for the mean and width of x_i and z_i are our initial values for these modeled parameters. The values given by the Normal distributions at each step, which can differ from the initial values, are used in our Bayesian MCMC analysis. We note that our results are not sensitive to details of the initial values for either the halo masses or magnitude gaps.

In terms of the measurement uncertainties, our priors change depending on whether we are analyzing the simulations (3D or 2D) or the real data. For the 3D simulations, we assume there is zero uncertainty in the stellar masses, the halo masses, and the magnitude gaps. For the 2D simulated data, we use $\sigma_y = 0.03$, which we determine by measuring the scatter in the difference between true stellar masses and the inferred stellar masses from the *Bell et al.* (2003) relation. The 2D phase-spaces are better sampled than the observed data, and so we use a uniform value close to the lower limit (0.35 dex) of the scatter in the caustic mass from *Gifford et al.* (2013). The error in the magnitude gap for the simulated data is again negligible, since the dominant component (the photometric error) is not present.

We use uninformative uniform priors on the intrinsic scatter, σ_{int}, and on the intercept, α. For the slope, β, and the stretch factor, γ, we use a linear regression prior of the form $-1.5 \times \log(1 + \text{value}^2)$.

In Table 3.2, we summarize all of our likelihood forms and priors not previously described in Section 3.5.1.

We can express the entire posterior probability then as:

$$p(\alpha, \beta, \gamma, \sigma_{int}, x_i, z_i, \sigma_{y_i}, \sigma_{x_i}, \sigma_{z_i} | y_{0i}, x_{0i}, z_{0i}, \sigma_{y_{0i}}, \sigma_{x_{0i}}, \sigma_{z_{0i}}) \propto \underbrace{P(y_{0i}|\alpha, \beta, \gamma, \sigma_{y_i}, \sigma_{int}, x_i, z_i)\ P(x_{0i}|x_i, \sigma_{x_i})\ P(z_{0i}|z_i, \sigma_{z_i})}_{\text{likelihood}} \times \underbrace{p(x_i)\ p(z_i)\ p(\sigma_{x_i})\ p(\sigma_{y_i})\ p(\sigma_{z_i})\ p(\alpha)\ p(\beta)\ p(\gamma)\ p(\sigma_{int})}_{\text{priors}} \tag{3.9}$$

We note that this is actually a *hierarchical Bayes model*, since the priors on true halo masses and true magnitude gaps (x_i and z_i) depend on models themselves (e.g., the underlying halo mass function or a distribution of the magnitude gap data). We do not include those terms in equation 3.9 or in Table 3.2 for compactness, but they are described in the above text. Additionally, since we allow for errors in all of our observables, this is an extension of what was originally shown for a simpler Bayesian line-fitting analysis in *Gull* (1989).

Bayesian Analysis Parameters for the SDSS-C4 Nominal Sample using M14

Symbol	Description	Prior
α	The offset of the SMHM relation	$\mathcal{U}$(-100,100)
β	The high-mass power law slope	Linear Regression Prior
γ	The stretch factor, which relates to M14	Linear Regression Prior
σ_{int}	The uncertainty given by the width of the intrinsic stellar mass distribution	$\mathcal{U}(0.0, 0.5)$
y_i	The underlying distribution in stellar mass given by Equation 3.8	$\mathcal{N}(\alpha + \beta x_i + \gamma z_i, \sigma^2_{int})$
x_i	The underlying halo mass function from *Henriques et al.* (2012), approximated as a truncated Normal	T$\mathcal{N}$(14.0,0.35^2,14.0,15.1)
z_i	The underlying magnitude gap distribution	$\mathcal{N}$(2.4,0.71^2)
$\sigma_{y_{0i}}$	The uncertainty between the observed stellar mass and intrinsic stellar mass distribution	0.19
$\sigma_{x_{0i}}$	The uncertainty between the caustic halo mass and underlying distribution given by *Gifford et al.* (2013)	$\sigma_{x_{0i}}(N_{phase_i})$
$\sigma_{z_{0i}}$	The uncertainty between the underlying and observed magnitude gap distribution	0.10

Table 3.2: Bayesian Analysis Parameters for the SDSS-C4 Nominal Sample using M14. $\mathcal{U}(a, b)$ refers to a uniform distribution where a and b are the upper and lower limits. The linear regression prior is of the form $-1.5 \times log(1 + value^2)$. $\mathcal{N}(a, b)$ refers to a Normal distribution with mean and precision of a and b. T$\mathcal{N}(a, b, c, d)$ is a truncated Normal distribution with mean, a, precision, b, lower limit, c, and upper limit, d. For σ_{x_i}, the value is dependent on the number of galaxies used in the caustic phase space and is obtained from *Gifford et al.* (2013). Additionally, we note that for x_i and z_i, the means and widths given in this table are the initial values. The mean and widths are modeled as normal distributions whose values are used at each step in the Bayesian MCMC analysis. The results are not sensitive to those initial values.

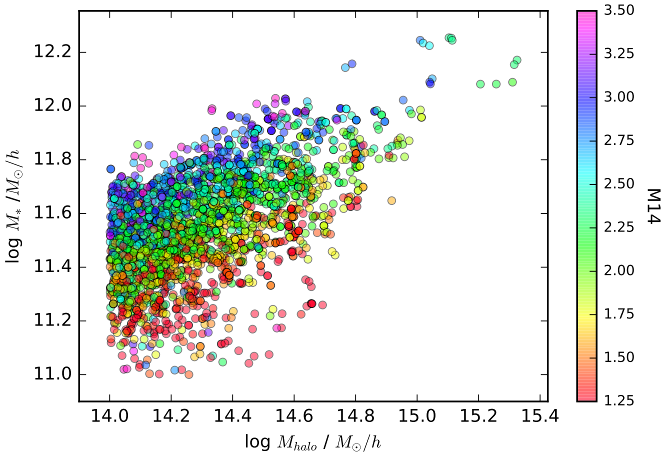

Figure 3.6: *Henriques et al.* (2012) 3D SMHM Relation Accounting for the Magnitude Gap. The SMHM relation for the 3D sample of the *Henriques et al.* (2012) prescription of the MILLENNIUM simulation. In the simulated universe we see a smooth magnitude gap – stellar mass stratification.

3.6 Results

In this section, we present the SMHM relation incorporating either M14 or M12 and the results of our Bayesian MCMC model for both the simulated and the SDSS-C4 observed data.

3.6.1 MILLENNIUM Simulation

3.6.1.1 SMHM Relation

Here we present the qualitative results of our analysis of the SMHM relation for high mass clusters found in the 3D and 2D (projected) versions of the *Henriques et al.* (2012) prescription of the MILLENNIUM simulation.

Figure 3.6 shows the stellar masses plotted against the halo masses, which both come directly from the simulation, for the 3D cluster sample. The BCGs are color-coded, where red represents small magnitude gap BCGs and purple high-gap BCGs (for M14). Figure 3.7 presents the SMHM relation for the 2D projected sample, where the stellar masses are estimated using the *Bell et al.* (2003) M/L ratio relation, and

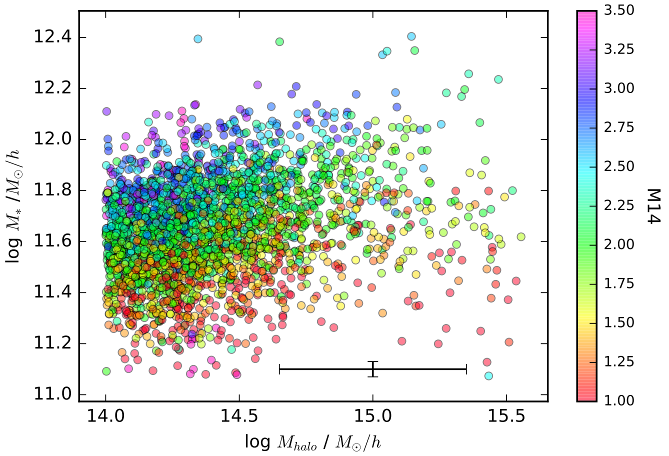

Figure 3.7: *Henriques et al.* (2012) 2D SMHM Relation Accounting for the Magnitude Gap. The SMHM relation for the 2D projected sample of the *Henriques et al.* (2012) prescription of the MILLENNIUM simulation. The black bar shows the average error in halo mass, 0.35 dex, and stellar mass, 0.03 dex. Even when using data with measurement errors in stellar mass, halo mass, and magnitude gap, a similarly smooth magnitude gap – stellar mass stratification exists in the simulated data, like in Figure 3.6.

the halo masses are determined using the caustic technique on the projected phase-spaces. Again, the BCGs are color-coded according to their magnitude gap (M14), which is determined using the projected data.

For Figures 3.6 and 3.7, the magnitude gap color bar does not span the entire range of observed M14 values (0-4.3). Instead, since the M14 distribution can be approximated as a Gaussian centered at an M14 value of ∼2.1, we selected a range which eliminates the Gaussian wings to better highlight the difference in stellar mass at fixed halo mass for clusters with differing magnitude gaps.

Figures 3.6 and 3.7 show that a relationship clearly exists between the magnitude gap and stellar mass at a fixed halo mass in the semi-analytic prescription of the MILLENNIUM simulation. Recall that *Harrison et al.* (2012) identified a bifurcation between clusters with high magnitude gaps and low magnitude gaps; high gap clusters have a larger stellar mass at fixed halo mass than low gap clusters. Our analysis illustrates that in the MILLENNIUM simulation, there is a continuous stratification in the BCG stellar masses at fixed halo mass due to the magnitude gap. These qualitative results are unchanged when using M12 (not shown) instead of M14.

3.6.1.2 Quantitative Impact

To quantitatively evaluate if the magnitude gap can be treated as a latent parameter in the SMHM relation, we use our MCMC model, Bayesian formalism, and linear SMHM relation (Equation 3.8) described in Section 3.5. To convey these results, we present triangle plots that show the posterior distributions of α, β, γ, and σ_{int} plotted against one another for both the 3D and 2D *Henriques et al.* (2012) samples. Each of these plots is generated after 10 million steps (including an approximate 2 million step burn in). We marginalize over all other nuisance parameters from Equation 3.9. We present the results from the *Henriques et al.* (2012) simulations using M14 for the magnitude gap. All of the results from the posterior distributions are presented in Table 3.3.

For our 2D Bayesian analysis, we use strong priors on the error distributions, stellar masses, and magnitude gaps, because (a) we can measure the uncertainties and (b) there are no observational uncertainties. In the 3D analysis, we also use strong priors on the halo masses, since we do not use the inferred caustic masses.

Figures 3.8 and 3.9 show convergence for each of the four variables. In these same figures, we see that α and β are covariant, which follows since they represent the intercept and slope, respectively. Of greater importance, neither remaining variable pair is covariant, which emphasizes that neither γ or σ_{int} are inherently tied to our measurement of the slope.

When we look beyond the distributions and at the values of the posterior distributions shown in Figures 3.8 and 3.9, we see that the best fit estimates for α, β, γ, and σ_{int} are within 1 or 2σ of one another. In other words, for these parameters, the model which includes uncertainty can correctly recover the 3D truth, where there is

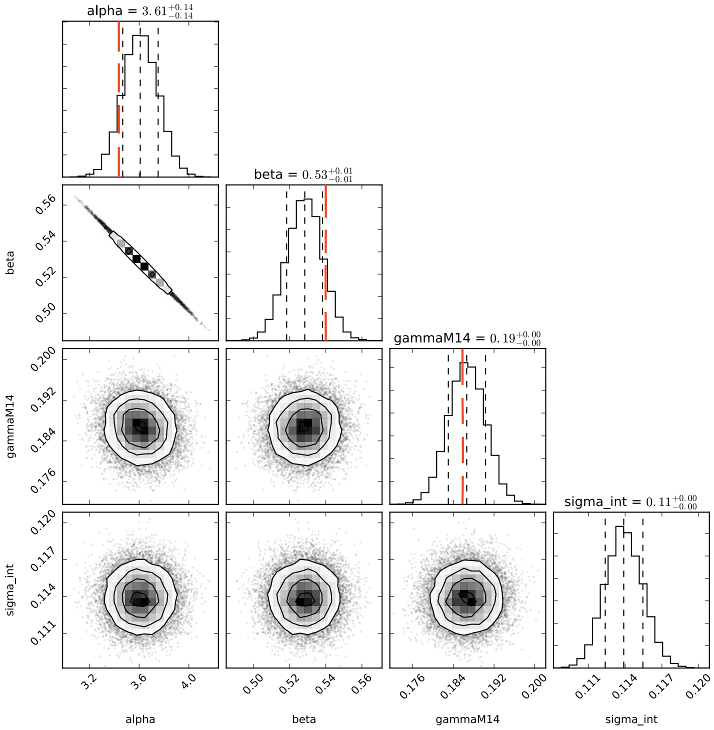

Figure 3.8: Bayesian MCMC Posterior Distribution for the *Henriques et al.* (2012) 3D Sample. The posterior distribution functions for α, β, γ, and σ_{int} for the *Henriques et al.* (2012) 3D sample. The red lines represent estimates for α, β, and γ done by binning the stellar mass, halo mass, and magnitude gap and applying a linear fit. This figure was constructed using M14. In our analysis of the *Henriques et al.* (2012) sample, γ is significantly non-zero. Additionally, our Bayesian analysis results agree with the simple linear binned estimates for each parameter.

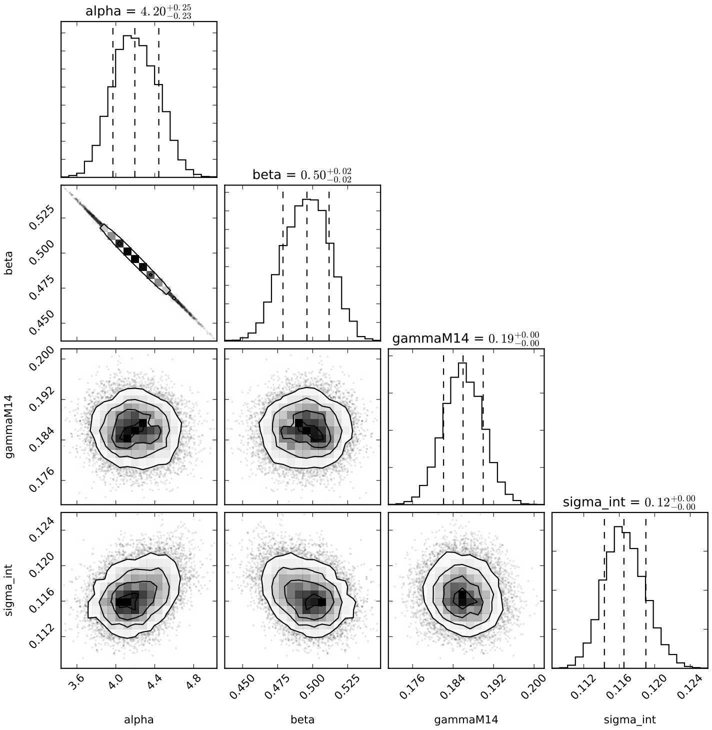

Figure 3.9: Bayesian MCMC Posterior Distribution for the *Henriques et al.* (2012) 2D Sample. The posterior distribution functions for α, β, γ, and σ_{int} for the *Henriques et al.* (2012) 2D projected sample. This figure was constructed using M14. The posteriors agree with our results for the 3D sample shown in Figure 3.8. Again, we find that γ is definitively non-zero.

no uncertainty. The ability to reproduce the results of the 3D model using the 2D projected sample is key because these samples represent the same underlying distribution, but with different uncertainties in each measurement. Since the posteriors of α, β, γ, and σ_{int} in the 2D projected sample (Figure 3.9) agree with those from the 3D sample (Figure 3.8), we conclude that if we can accurately account for the uncertainty in stellar mass, halo mass, and magnitude gap, then we can measure the underlying posterior distributions of α, β, γ, and σ_{int} for the SDSS-C4 sample even though we have no 3D dataset.

We also looked at varying the scatter on the magnitude gap by adding a small uncertainty, 0.05, to the magnitude gaps to account for the fact that a fraction of our 2D light-cone "observed" gaps do not exactly agree with the true magnitude gaps. However, this made no difference to the posterior distribution shown in Figure 3.9.

The most significant result shown in Figures 3.8 and 3.9 is that γ is significantly non-zero. To highlight this further, we bin the 3D simulated data according to magnitude gap and halo mass and measure the binned stellar mass directly. From this we can directly (albeit crudely) estimate α, β, and γ, using linear fits. The results are shown as the red vertical dashed bars in Figure 3.8. This measurement highlights that for the *Henriques et al.* (2012) prescription of the MILLENNIUM simulation, the magnitude gap is indeed a latent parameter found in the SMHM relation and should be incorporated into other SMHM relations.

Additionally, we note that the quantitative results for the analysis done using M12, shown in Table 3.3, and M14 are well within 2σ of one another for both α, β and σ_{int}. However, we find that γ is slightly smaller when M12 is used than when M14 is used in our analysis. We posit that this difference results from the different magnitude gap distributions associated with each respective sample.

3.6.1.3 Model without Magnitude Gap

To determine the impact of the magnitude gap on σ_{int}, we ran our Bayesian MCMC model using a linear relation, similar to the formalism used for the high halo mass portion of *Yang et al.* (2009) and *Moster et al.* (2010, 2013). To do this, we replace Equation 3.8 with:

$$y_i = \mathcal{N}(\alpha + \beta x_i, \sigma_{int}^2). \tag{3.10}$$

where α and β are the intercept and slope and σ_{int} is the intrinsic scatter. For these models, we measured the posterior distributions for α, β, and σ_{int}.

Using the same Bayesian formalism and MCMC model described in Section 3.5, but instead using Equation 3.10, we find that $\sigma_{int} = 0.159 \pm 0.002$ and $\sigma_{int} = 0.160 \pm 0.003$ for the 3D and 2D catalogs, respectively. Therefore, comparing this posterior to those obtained when incorporating the magnitude gap, $\sigma_{int} = 0.114 \pm 0.002$ and 0.117 ± 0.002 (3D and 2D), we find that the intrinsic scatter significantly decreases due to the inclusion of the magnitude gap as a third parameter because the two values differ by greater than 3σ. Additionally, incorporating the magnitude gap reduces σ_{int} by by 28.3% in the 3D sample and 26.9% in the 2D projected sample. We also observe that the inclusion of the magnitude gap does not impact the measurement of the slope, β, because the posterior values determined when accounting for the magnitude gap and when not agree.

3.6.2 SDSS-C4 Sample

3.6.2.1 SMHM Relation

In this section, we present the qualitative results from our analysis of the SDSS-C4 samples using both M14 and M12. The SMHM relations shown in Figures 3.10 and 3.11 plot the stellar masses estimated using the *Bell et al.* (2003) M/L ratio relation against our caustic halo masses and utilize three non-uniform magnitude gap bins to

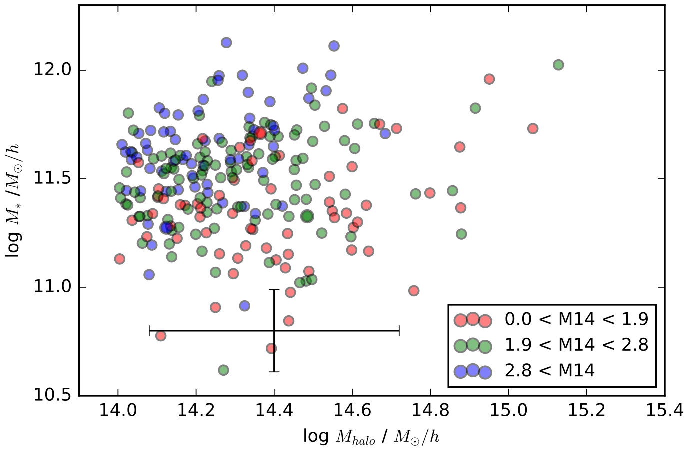

Figure 3.10: The SDSS-C4 SMHM Relation Accounting for M14. The SMHM relation for the SDSS-C4 sample of clusters binned via M14 measurements. The black bars represent the median error bars in caustic halo mass, 0.32 dex, and the error in stellar mass, 0.19 dex. Similar to the results of the *Henriques et al.* (2012) 2D projected data, shown in Figure 3.7, a magnitude gap – stellar mass stratification exists in the real universe, where measurement errors are found on all three parameters shown.

represent the clusters with high (blue), intermediate (green), and low (red) magnitude gaps.

We use three color bins, unlike in Figures 3.6 and 3.7, because a noisier color gradient exists in our SDSS-C4 observations. This additional noise is primarily caused by the photometric measurement error associated with the corrected BCG magnitudes for our SDSS-C4 observations. Additionally, the relative lack of redshift information, compared to the *Henriques et al.* (2012) data, results in our observed M14 and M12 values being more sensitive to our red sequence fit. The lack of clusters, 2700 in the simulations and 236 (M14) or 254 (M12) in the SDSS-C4 sample, also makes the gradient more difficult to clearly observe. Thus, binning the data by magnitude gap allows us to more easily convey the impact of incorporating the magnitude gap and the observed stratification. We chose non-uniform bin widths to emphasize the similarity between the M14 and M12 samples. Furthermore, a comparison between Figures 3.10 and 3.11 suggests that this stratification may be independent of the

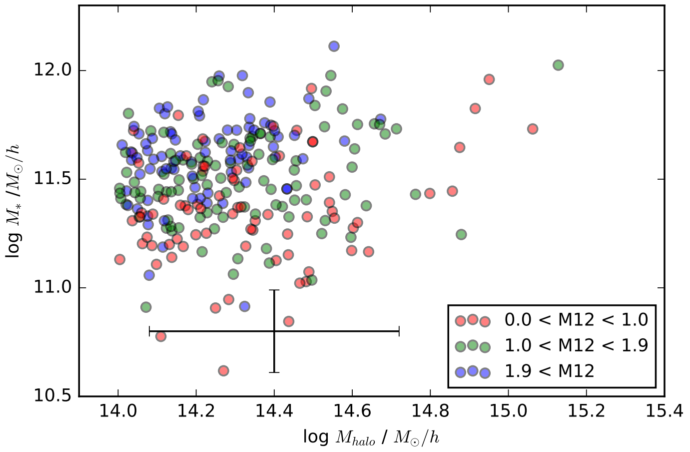

Figure 3.11: The SDSS-C4 SMHM Relation Accounting for M12. The SMHM relation for the SDSS-C4 sample of clusters binned using the M12 measurements. The black bars represent the median error bars in halo mass, 0.32 dex, and stellar mass, 0.19 dex. When compared to Figure 3.10, this figure highlights that a similar magnitude gap – stellar mass stratification is observed regardless of the choice of nth brightest cluster member.

choice of nth brightest cluster member used to measure the magnitude gap.

By binning our data, Figures 3.10 and 3.11 illustrate that a magnitude gap stratification with some scatter exists in the real universe. For a fixed halo mass, as the stellar mass increases, the color of the points transitions from red to green to blue, with some additional scatter, which represents that stellar mass and magnitude gap are positively correlated.

Just as for our analysis of the *Henriques et al.* (2012) prescription of the MILLENNIUM simulation, we clearly observe a trend relating magnitude gap and stellar mass at fixed halo mass. Furthermore, Figures 3.10 and 3.11 show that, like in the simulations, a bifurcation between high and low magnitude gap clusters (fossils and non-fossils) is an oversimplification. Instead, we treat this relationship as a stratification, which is independent of the optical and X-ray definitions of fossil galaxies, and instead extends to all clusters because at fixed halo mass, as the magnitude gap between the BCG and any selected nth brightest member increases, on average, the

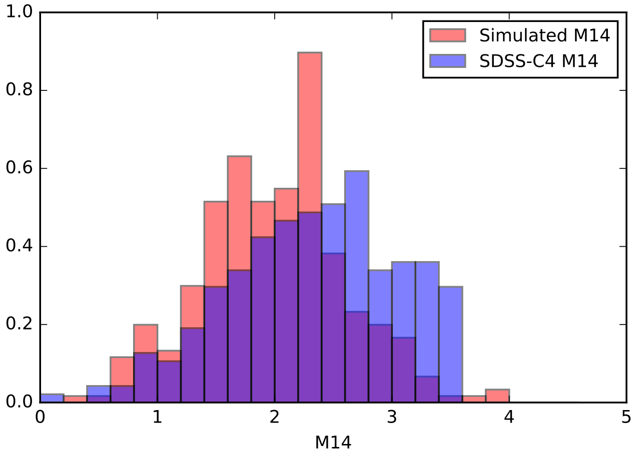

Figure 3.12: SDSS-C4 M14 and *Henriques et al.* (2012) M14 Distributions. The distribution for the SDSS-C4 M14 values and the distribution for the 2D projected *Henriques et al.* (2012) M14 values. The similarity highlights that our 4th brightest SDSS-C4 cluster members are accurately identified using the red sequence and available redshift information.

stellar mass of the BCG similarly increases. Thus, allowing the magnitude gap to be treated as a relative proxy for the stellar mass of a BCG.

Additionally, we highlight the accuracy of our magnitude gap measurements by looking at how the distributions of the magnitude gap measured in our SDSS-C4 data compare to those measured in our 2D *Henriques et al.* (2012) projected data. In Figures 3.12 and 3.13, we have normalized the distributions for comparison, which results in a y-axis that represents a relative number. We find that the overall shape of the distributions for the SDSS-C4 data (in blue) and the *Henriques et al.* (2012) data (in red) are quite similar. The primary difference is that the SDSS-C4 magnitude gap values are slightly larger, which may result from projection effects, due to the lack of available redshift information or our red sequence fitting.

3.6.2.2 Quantitative Impact

As done in Section 3.6.1.2, we evaluate the impact of incorporating the magnitude gap into our SMHM relation using the previously described (Section 3.5) MCMC

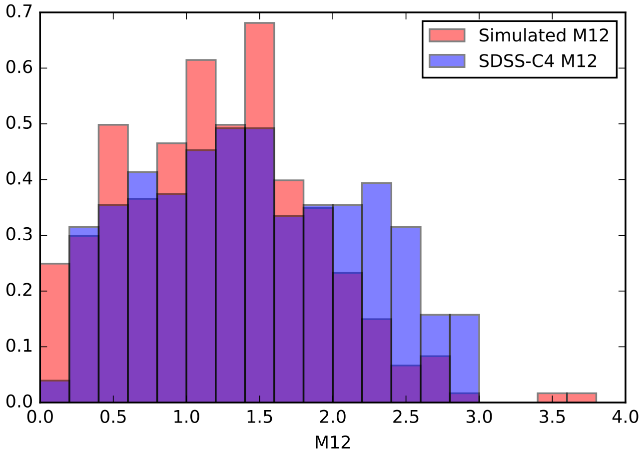

Figure 3.13: SDSS-C4 M12 and *Henriques et al.* (2012) Distributions. The distribution for the SDSS-C4 M12 values and the distribution for the 2D projected *Henriques et al.* (2012) M12 values. A comparison illustrates that our 2nd brightest SDSS-C4 cluster members are accurately identified using available redshift information and red sequence fitting.

model, Bayesian formalism, and linear SMHM relation (Equation 3.8). The model used for our SDSS-C4 sample differs slightly from that used for the simulated data because of minor differences related to our estimation of the uncertainties in the measurements of stellar mass, halo mass, and magnitude gap. For halo mass, we used the relation between the number of galaxies used to construct the caustic phase space and the measurement uncertainty presented in *Gifford et al.* (2013), while for the 2D simulated light-cone data, we used a fixed error of 0.35 dex, since it has a deep magnitude limit. For the stellar mass, we increased the measurement uncertainty from 0.03 dex (sims) to 0.19 dex. We reached 0.19 dex by assuming a 0.1 dex error in the M/L ratio (*Bell et al.*, 2003) and combining it with the 0.1 magnitude precision in both the BCG's r- and i-band magnitudes used to determine the color used in the *Bell et al.* (2003) relation. For the magnitude gap, due to the BCG photometry, we also assumed an uncertainty of 0.1 magnitudes, in contrast to 0.0 magnitudes used in the simulations. Since we use the SDSS Petrosian magnitudes for our 4th and 2nd brightest galaxies, we assume that the measurement uncertainties associated with

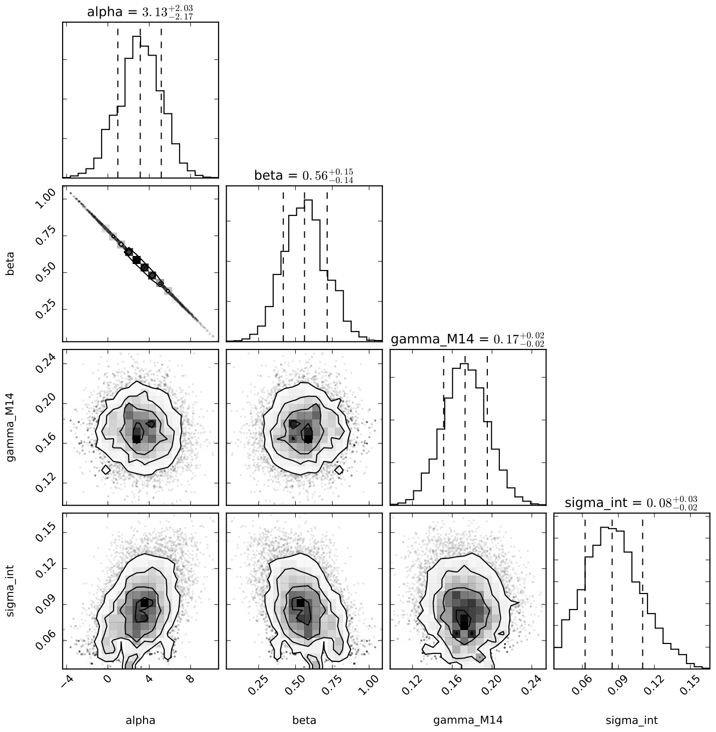

Figure 3.14: The Bayesian MCMC Posterior Distributions for the SDSS-C4 Sample with M14. The posterior distributions for α, β, γ, and σ_{int} for the SDSS-C4 sample measured using M14. Like in the *Henriques et al.* (2012) 2D projected sample, shown in Figure 3.9, we see that γ is definitely non-zero in the real universe. Additionally, we find that σ_{int} is below 0.1 dex.

those magnitudes are negligible. Additionally, for each uncertainty, we add a random β distribution term to our error estimates to encapsulate the uncertainty associated with each one of our error estimates, given by Equations 3.3, 3.5, and 3.7.

Using this approach, we present triangle plots, shown in Figures 3.14 and 3.15, which show the distributions of α, β, γ, and σ_{int} for both the SDSS-C4 M14 and M12 samples. Each plot was generated after 10 million steps including an approximate 2 million step burn in.

Figures 3.14 and 3.15 show the marginalized 1D or 2D posteriors after convergence. We see that only α and β are covariant, as was the case for our simulations and is expected in a linear regression. Additionally, the values based on the posteriors for α,

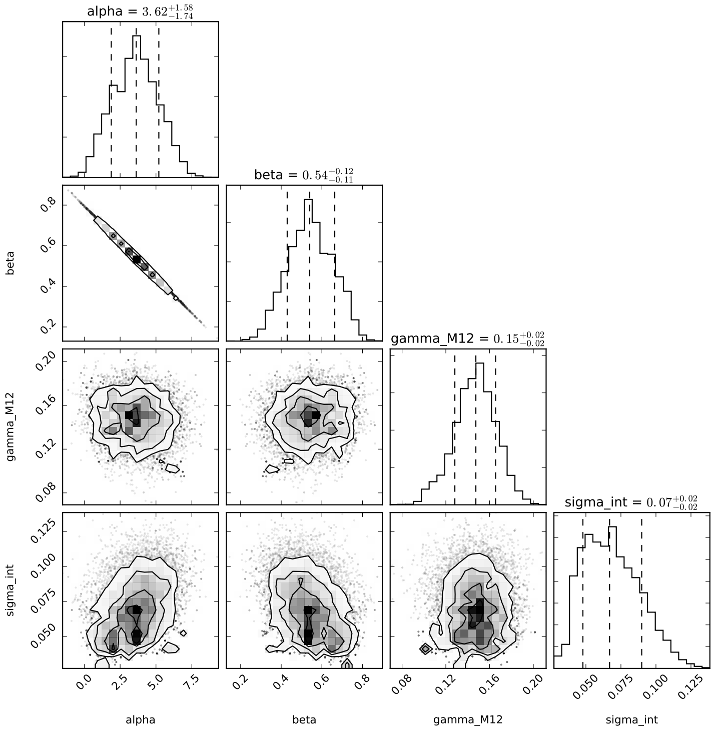

Figure 3.15: The Bayesian MCMC Posterior Distributions for the SDSS-C4 Sample with M12. The posterior distributions for α, β, γ, and σ_{int} for the SDSS-C4 sample measured using M12. The posteriors agree with the results shown in Figure 3.14. Similarly, γ is significantly non-zero, and σ_{int} is well below 0.1 dex.

β, γ, and σ_{int} when determined using M14 are within 1σ of their counterparts done using M12 (see Table 3.3). Thus, the choice of nth brightest galaxy used to measure the magnitude gap appears to have little impact on the measured parameters, which strengthens our argument that the magnitude gap-stellar mass stratification is not dependent on our choice of nth brightest cluster member, based on Figures 3.10 and 3.11. We note that the posterior constructed using M12 leads to a slightly lower value of γ as observed in the *Henriques et al.* (2012) simulated data; however, since the error bars are larger on the posteriors of our SDSS-C4 data than on the posteriors of the *Henriques et al.* (2012) data, these γ posteriors are in agreement.

The primary result from Figures 3.14 and 3.15 is that γ is definitively non-zero in our SDSS-C4 sample, as we observed in the *Henriques et al.* (2012) simulation. This observation highlights that we must treat the magnitude gap as a latent third parameter in the SMHM relation. Additionally, we note that for the first time, the observational estimate for the intrinsic scatter has moved below a precision of 0.1 dex. We discuss the implications of these results further in Section 3.7.

Recall that for the 2D simulated data, we varied the scatter of the magnitude gap but found no difference in the results. We investigate this again in the SDSS-C4 data. In the nominal analysis, we assume that the magnitude gaps have a measurement error of 0.1 magnitudes. As described earlier, we include an additional stochastic uncertainty on this error using a beta distribution, which adds as much as ± 0.06 magnitudes to the gap error. As we push this up to larger magnitude gap errors we begin to see the stretch factor γ changing its median in the posterior at $\sigma_{z_i}(M14) = 0.4$. However, given that we have used all available spectroscopic information for our clusters, have well-determined red-sequence membership, and that we have re-created the gap measurement distribution in a realistic mock sky, we are confident that our gap measurements are as accurate as we describe (0.1 magnitudes). Additionally, we also examine the sensitivity of our results on our measurement uncertainties for stellar mass and halo mass. We find that if we vary the uncertainty in halo mass by 25% the results of our posterior are all in agreement with our results presented in Table 3.3. When we vary the uncertainty in stellar mass by 25%, we see the same trend between slope and error measurement presented in Figure 10 of *Tinker et al.* (2017). Additionally, all of the parameters, except σ_{int} are in agreement with their values in Table 3.3. The discrepancy for σ_{int} is expected due to the relationship between error in stellar mass and intrinsic scatter. We further justify our choice of 0.19 dex for the measurement error in stellar mass in Sections 3.6.2.3 and 3.7.2.

3.6.2.3 Model without incorporating the Magnitude Gap

To determine the impact of incorporating the magnitude gap on σ_{int} for the observed SMHM relation, we again use the MCMC model and Bayesian formalism, but instead use the linear relation, Equation 3.10, presented in Section 3.6.1.3, which does not incorporate the magnitude gap. The results of this analysis are shown via a triangle plot in Figure 3.16, which compares the posterior distributions of α, β, and σ_{int}. As with our previous MCMC runs, we see a convergence and find that only α and β are covariant, while σ_{int} does not depend on either parameter. When comparing the results of this analysis to Figures 3.14 and 3.15 we find that the values of the slope, β, are in agreement with one another.

The primary reason we ran an analysis using the model without the stretch parameter (Equation 3.10) was to determine the impact of the magnitude gap on σ_{int}. Of note, the σ_{int} we measure using our two component linear model, 0.159 ± 0.021, is in excellent agreement with the best prior estimates of the intrinsic scatter from both observations and simulations for the high mass portion of the SMHM relation, 0.15 dex (*Pillepich et al.*, 2018), 0.16 dex (*Tinker et al.*, 2017), and 0.17 dex (*Kravtsov et al.*, 2018), which highlights the consistency of our measurements with other studies. When we compare the results of our model without the magnitude gap to those pre-

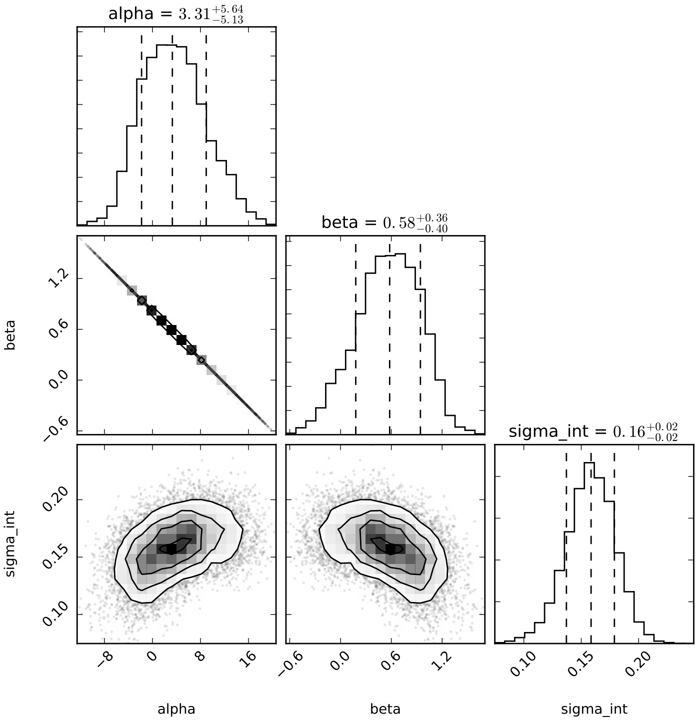

Figure 3.16: The Bayesian MCMC Posterior Distribution for the SDSS-C4 Data without M14. Distribution The posterior distributions for α, β, and σ_{int} for the SDSS-C4 sample measured without incorporating the magnitude gap. A comparison to Figures 3.14 and 3.15 highlights that β is unchanged when incorporating the magnitude gap; however σ_{int} is significantly higher when the magnitude gap is unaccounted for.

sented in Section 3.6.2.2 which incorporate it, we find that including the magnitude gap significantly reduces the median value of σ_{int} by either 0.074 or 0.092 dex. Thus, incorporating the magnitude gap leads to either a 45% or 58% decrease in the intrinsic scatter. Additionally, we note that the values of the intrinsic scatter obtained when incorporating the magnitude gap are not within one sigma of the estimate obtained when not incorporating it. Thus, the magnitude gap is a latent parameter in the SMHM relation that significantly reduces the intrinsic scatter in this relation and allows us to enter the realm of sub 0.1 dex precision.

For comparison, we find that the reduction of σ_{int} is far greater for the SDSS-C4 data than what we find in the *Henriques et al.* (2012) prescription of the MILLENNIUM simulation. This may result from the error bars for our posterior distributions being larger for our SDSS-C4 observations than for the simulations. Alternatively, unlike in our SDSS-C4 observations, where we assumed that the uncertainty in the stellar mass is 0.19 dex, for the 3D *Henriques et al.* (2012) prescription of the MILLENNIUM simulation, we assumed that the stellar mass had no measurement uncertainty associated with it. However, this is likely an underapproximation, because there is likely some additional uncertainty associated with those stellar mass estimates.

In addition to the reduction in the inferred intrinsic scatter, we find that the size of the error bars on the posterior distribution of the slope, β, significantly decreases when the magnitude gap is incorporated. As shown in Figures 3.14 and 3.15, β has error bars of approximately 0.15 and 0.11 dex respectively. In contrast, when we don't incorporate the magnitude gap, the error bars on β increase to between 0.36 and 0.40 dex, as shown in Figure 3.16. Thus, the uncertainty associated with our slope decreases by between 0.21 to 0.29 dex, when we include the magnitude gap in our analysis. This decrease likely occurs because for a fixed magnitude gap we use fewer points spread over a smaller range in stellar mass to fit the slope, making it more tightly constrained. Therefore, incorporating the magnitude gap not only allows us to significantly reduce the intrinsic scatter in the stellar mass at fixed halo mass, it also allows us to reduce the uncertainty on our measurement of the slope.

To verify that the three parameter model (given by Equation 3.8) does indeed reproduce the data better than the two parameter model (given by Equation 3.10), we use the posterior predictive distribution to compare the values of the stellar mass and magnitude gap given by each of the models. For comparison, we measure the R coefficient to be R=0.428 for our observed SDSS-C4 data. When averaged over the MCMC trace in our Bayesian model, we find that the two parameter model yields an $\langle R \rangle = 0.169$, while the three parameter model yields $\langle R \rangle = 0.410$, which allows us to conclude that the 2 parameter model does not reproduce the observed correlation between stellar mass and magnitude gap that is observed in our data.

Additionally, to further verify that the reduction of σ_{int} results from incorporating the magnitude gap, and not just the inclusion of a randomly selected third parameter, we reran our Bayesian analysis using randomized values of M14 in Equation 3.8. Doing so removes the correlation between M14 and stellar mass, and results in a posterior distribution with a γ that is equal to 0.0 ± 0.02. Furthermore, the other parameters contained in this posterior, including the measurement of σ_{int}, agree with the values presented in Figure 3.16, which further highlights that the reduction in σ_{int} and measurement of non-zero γ result because stellar mass and M14 are correlated due to the hierarchical growth of the BCG. Therefore, it is the incorporation of this specific third parameter, the magnitude gap, and not any random third parameter, that leads to the significant reduction in σ_{int}.

Posterior Distribution Results

Data	Magnitude Gap	α	β	γ	σ_{int}
Henriques et al. (2012)-3D	Not Incorporated	4.31 ± 0.20	0.51 ± 0.01		0.159 ± 0.002
Henriques et al. (2012)-2D	Not Incorporated	4.04 ± 0.27	0.53 ± 0.02		0.160 ± 0.003
Henriques et al. (2012)-3D	M14	3.61 ± 0.14	0.53 ± 0.01	0.187 ± 0.004	0.114 ± 0.002
Henriques et al. (2012)-2D	M14	4.19 ± 0.23	0.50 ± 0.02	0.186 ± 0.004	0.117 ± 0.002
SDSS-C4	M14	3.13 ± 2.09	0.56 ± 0.15	0.173 ± 0.022	0.085 ± 0.024
SDSS-C4	Not Incorporated	$3.31^{+5.64}_{-5.13}$	$0.58^{+0.36}_{-0.40}$		0.159 ± 0.021
Henriques et al. (2012)-3D	M12	4.07 ± 0.15	0.51 ± 0.01	0.147 ± 0.004	0.124 ± 0.002
Henriques et al. (2012)-2D	M12	3.66 ± 0.24	0.55 ± 0.02	0.158 ± 0.004	0.123 ± 0.003
SDSS-C4	M12	$3.62^{+1.58}_{-1.74}$	$0.54^{+0.12}_{-0.11}$	0.147 ± 0.019	0.067 ± 0.020
SDSS-C4, Abundance Matching	Not Incorporated	-0.33 ± 0.15	0.84 ± 0.01		

Table 3.3: SDSS-C4 Posterior Distribution Results

3.7 Discussion

3.7.1 Comparisons to the Literature

We have presented results that show that in both a simulated semi-analytic model of a low-redshift universe and in the observed universe, there is a stratification in stellar mass with the magnitude gap at fixed halo mass for cluster-sized halos. This result is found at high confidence, such that the measured stretch factor γ is many standard deviations away from zero. The inclusion of the magnitude gap as a latent parameter in the cluster-scale SMHM relation reduces the scatter $\Delta(\log \mathrm{M}_* | \log \mathrm{M}_{\mathrm{halo}})$ by a significant amount. At the same time, it also reduces the error bar on the inferred slope, β.

The physical importance of the detection of the magnitude gap as a latent variable (albeit an observational one) directly relates to the BCG growth history. This history is built into the *Henriques et al.* (2012) and *Guo et al.* (2011) prescriptions of the MILLENNIUM simulation, in which BCGs grow hierarchically via major and minor mergers (*De Lucia and Blaizot*, 2007). The more massive BCGs are those that have undergone more mergers, and in agreement with *Solanes et al.* (2016), have the largest magnitude gaps. Therefore, the observation of a magnitude gap stratification in the SDSS-C4 data acts as observational evidence that in the real universe, BCGs predominantly grow hierarchically. Additionally, we posit that the magnitude gap may be able to trace the assembly history of both the BCG and the cluster.

As we have shown, in agreement with *Solanes et al.* (2016), that clusters with the largest magnitude gaps and stellar masses have likely undergone more mergers than small gap, low stellar mass clusters. If a similar dynamical timescale for the mergers that occur in each cluster exists, then the clusters with the largest stellar mass and magnitude gaps would likely be the clusters that formed first. This hypothesis is supported by Figure 7 of *Matthee et al.* (2017). Using the hydronamical EAGLE simulation, *Matthee et al.* (2017) construct a stellar mass halo mass relation over the halo mass range of $11.0 < \log_{10}(M_{200,DMO}/M_{\odot}) < 14.5$, in which individual clusters are color coded by the redshift when half of the halo mass was assembled. This SMHM relation agrees with our previously stated assumption, and shows that a stratification between the stellar mass and formation time exists in the EAGLE simulation; at a fixed halo mass, the most massive galaxies are found in the halos that form at the earliest redshift (*Matthee et al.*, 2017). This stratification appears to exist, but is difficult to analyze at halo masses close to our range of interest because the EAGLE simulation does not contain enough high halo mass clusters. Thus, a direct comparison between our studies would be difficult at this time because we cannot yet determine how and if the magnitude gap stratification relates to the formation redshift stratification and if the magnitude gap accurately scales with the formation redshift to trace the assembly of the cluster.

Although it remains uncertain whether the magnitude gap traces the assembly history of the halo, the discovery of the stellar mass - magnitude gap stratification does solve a pragmatic issue that has existed for the observed cluster-scale SMHM relation. As discussed in Section 3.2, a large discrepancy exists between published SMHM relations in the high mass regime, highlighted by Figure 10 in *Tinker et al.* (2017). This discrepancy includes both purely observational studies (like ours and *Kravtsov et al.* (2018)), and those that require a strong theoretical prior from the use of abundance matching models (e.g., *Behroozi et al.*, 2010; *Moster et al.*, 2010; *Behroozi et al.*, 2013a; *Moster et al.*, 2013; *Tinker et al.*, 2017). For a fixed halo mass, the estimates for the stellar mass differ by as much as $0.5 - 1.0$ dex. In Figure 3.17, we show numerous SMHM relations from the literature after normalizing to a Salpeter IMF. On this figure we also highlight our model SMHM relations (plural), in gray, given a specific magnitude gap, where the light gray band defines the 1σ error bar from the posterior. By varying the average magnitude gap (M14) for a sample from 0.0 to 4.0 (the range covered in Figure 3.4), the stellar masses can vary by as as much as 0.7 dex at fixed halo mass. Thus the gap as a latent variable can explain the majority of the offsets in the published SMHM relations, assuming those published results used samples with different average magnitude gaps.

Based on our model, across the top of our SMHM relation are the largest gap systems, i.e., those classified as fossil galaxies (*Harrison et al.*, 2012). The *Kravtsov et al.* (2018) sample is small and only a half dozen clusters overlap with our data where we can verify the magnitude gap (using identical data and techniques) to be $\langle M14 \rangle \sim 2.5$, which would classify the sample as representative of fossils. *Kravtsov et al.* (2018) also used "total" magnitudes as opposed to our Petrosian magnitudes, thus further increasing the magnitude gap (*Graham et al.*, 2005). Moving down in stellar mass in Figure 3.17, consider the cluster sample used in *Lin and Mohr* (2004), which like the *Kravtsov et al.* (2018) sample, is based on X-ray selection. In this case, 14 clusters overlap with our sample and we measure $\langle M14 \rangle \sim 2$, which is indeed lower than the *Kravtsov et al.* (2018) average. Across the bottom end of the relation are the systems with small values of magnitude gaps. The lower two literature relations in Figure 3.17 are not based on cluster identifications at all, but simply use galaxy samples. These samples are sorted according to inferred stellar mass and matched to a simulation. In other words, all intrinsically bright galaxies are included in the cluster-scale *Behroozi et al.* (2013a) and *Moster et al.* (2013) analyses, including those which

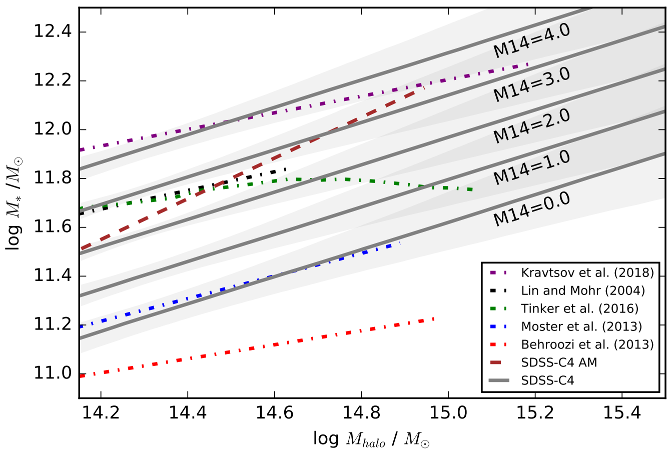

Figure 3.17: Comparison of the SMHM-M14 Relation to Previously Published SMHM Relations. The dot-dashed lines are 5 different previously published SMHM relations, from *Behroozi et al.* (2013a), *Moster et al.* (2013), *Tinker et al.* (2017), *Lin and Mohr* (2004), and *Kravtsov et al.* (2018). The dashed brown line represents our SDSS-C4 relation in which halo masses were estimated via abundance matching. The solid gray lines represent the best fit for our SMHM relation done using M14 for five different values of M14. The shaded region represents the 1σ region surrounding each of the 5 magnitude gap fits. Each of the stellar masses for this figure is scaled to a Salpeter IMF. The gray lines highlight that incorporating the magnitude gap can account for as much as 0.7 dex in stellar mass and may account for the majority of offsets between previously reported SMHM relations.

do not reside in cluster-scale environments. Because of the lack of the use of confirmed clusters in their samples, it would not be surprising that the average magnitude gaps of the centrals in halos $\geq 10^{14} M_{\odot}$ are small. Our relation does not intersect with the results from *Behroozi et al.* (2013a) because *Behroozi et al.* (2013a) use SDSS Petrosian magnitudes which have not been corrected for the systematic background subtraction errors.

It is difficult to make a fair comparison of the literature SMHM relations for numerous reasons noted earlier. However, in the context of our model, the above exercise provides a reasonable explanation for the large amplitude variations in the SMHM seen in the literature. Such a variation would be expected if the mean magnitude gap of the observed samples is not held fixed.

Many other works (e.g., *Behroozi et al.*, 2010; *Moster et al.*, 2010; *Behroozi et al.*, 2013a; *Moster et al.*, 2013; *Tinker et al.*, 2017) rely upon abundance matching to measure the SMHM relation. The one-to-one matching of the BCGs with the largest stellar mass to the largest values of cluster masses from simulations pays no regard to the magnitude gap and results in the loss of information about the BCG's growth history. At the same time, we show that ignoring the magnitude gap results in a large increase in the inferred intrinsic scatter (see Section 3.6.2.3). In Figure 3.17, we plot our SMHM relation for the SDSS-C4 BCGs based on abundance matching to the *Henriques et al.* (2012) light-cone halo catalog. The fit lies within our expectations for the full model, but with a steeper slope.

3.7.2 Impact on Galaxy Formation Models

At lower halo masses we expect in-situ star formation, the accretion of gas, as well as stellar and/or AGN feedback to play some role in the growth of stellar mass over time since $z \sim 2$. While at the highest halo masses, we expect all of these processes to have finished by $z = 2$, leaving only hierarchical growth as the dominant mechanism to increase a galaxy's stellar mass since $z \sim 2$. However, the reported observed intrinsic scatter is nearly constant with halo mass at around $\sigma(M_*) < 0.2$ dex (*Gu et al.*, 2016).

Gu et al. (2016) used abundance matching and investigated the origin of scatter at fixed halo mass by following the hierarchical buildup of both dark and stellar mass in simulations. *Gu et al.* (2016) concluded from their model and simulations that there should be a strong mass-dependent scatter in the SMHM relation. Similarly, this conclusion was also reached using the hydrodynamical EAGLE simulation, where *Matthee et al.* (2017) estimate the intrinsic scatter in stellar mass at fixed halo mass using different parametric fits of the true and predicted stellar masses to the halo mass and find that the intrinsic scatter decreases, by approximately 0.1 dex, as the halo increases over the range of $11.0 < log10(M_h/M_\odot) < 13.0$. Assuming that the intrinsic scatter measurements reported in previous SMHM relations are dominated by lower mass halos ($log10(M_h/M_\odot) < 14.0$), our work provides the first observational evidence that the scatter in stellar mass decreases significantly for centrals within group and cluster sized halos, to levels as small as 0.067 dex at fixed halo mass and at fixed magnitude gap.

One obvious question is whether the measurement errors on our stellar masses are over-estimated. Recall that our stellar masses stem from the *Bell et al.* (2003) relation, which has a 0.1 dex uncertainty at z=0. Our BCG magnitudes also have a measurement error, which we estimate from the one-to-one comparison to the *Postman and Lauer* (1995) sample. These both are reasonable choices and incorporate our entire stellar mass error budget. Just as important, our inferred intrinsic scatter when we exclude the magnitude gap in our model is ~ 0.16 dex, nearly identical to *Tinker et al.* (2017) and *Kravtsov et al.* (2018). In other words, our choice of measurement error on our stellar masses allows for a consistent comparison with those works. When we use those same measurement errors and include the magnitude gap in our model, our intrinsic scatter drops to as low as 0.067 dex.

One challenge this presents to models like the one presented in *Gu et al.* (2016) is that our observed intrinsic scatter is less than half of the minimum scatter allowed in their model (0.16 dex) solely from hierarchical growth. One way to reach a smaller amount of scatter is to have a shallower SMHM relation at $z = 2$. Another option is that smooth accretion is actually not in play for BCGs (see Figures 4 and 5 in *Gu et al.* (2016)).

In this work, we have focused on the $z \sim 0$ universe. It is likely that the stretch factor evolves through time. This is something that can be tested in simulations using current semi-analytic models which follow the growth history of the BCG (e.g., *Guo et al.*, 2011). The observational challenge of an evolutionary analysis of the magnitude gap as a latent variable is to acquire good spectroscopic coverage per cluster or to understand any additional systematics which would increase the error in the magnitude gap measurement using photometric data.

CHAPTER IV

The Impact of Environment on Late Time Evolution of the Stellar Mass - Halo Mass Relation

Results in this chapter were published in: ***Golden-Marx, Jesse B.***, *& Miller, Christopher J. 2019. The Impact of Environment on the Late Time Evolution of Stellar Mass-Halo Mass Relation. Accepted for publication in ApJ.*

4.1 Abstract

At a fixed halo mass, galaxy clusters with larger differences in brightness between the brightest central galaxy (BCG) and fourth brightest cluster member ($\mathrm{m_{gap}}$), have larger BCG stellar masses. Recent studies have shown that by including $\mathrm{m_{gap}}$ as a latent parameter in the cluster stellar mass - halo mass (SMHM) relation, one can make more precise measurements of the SMHM relation's amplitude, slope, and intrinsic scatter. We use galaxy clusters from the Sloan Digital Sky Survey to measure the SMHM-$\mathrm{m_{gap}}$ relation and its evolution out to $z = 0.3$. Using a fixed comoving aperture of 100kpc to define the central galaxy's stellar mass, we report statistically significant negative evolution in the slope of the SMHM relation to $z = 0.3$ ($> 3.5\sigma$). The steepening of the slope over the last 3.5 Gyrs can be explained by late-time merger activity at the cores of galaxy clusters. We also find that the inferred slope depends on the aperture used to define the radial extent of the central galaxy. At small radii (20kpc), the slope of the SMHM relation is shallow, indicating that the core of the central galaxy is less related to the growth of the underlying host halo. By

including all of the central galaxy's light within 100 kpc, the slope reaches an asymptote value.

4.2 Introduction

The stellar mass - halo mass (SMHM) relation is one of the primary mechanisms used to quantify the galaxy-dark matter halo connection. For clusters ($\log_{10}(M_{halo}/(M_\odot/h)) \geq 14.0$), this linear relation relates the stellar mass of the brightest central galaxy (BCG) to the total cluster halo mass, including the dark matter. The inferred intrinsic scatter (σ_{int}) associated with this relation can be used to constrain the processes that quench star formation within galaxies (*Tinker*, 2017) as well as characterize the growth of their massive, underlying, dark matter halos (*Gu et al.*, 2016).

BCGs, the stellar mass portion of the cluster-scale SMHM relation, are massive, extended, luminous elliptical galaxies that account for a significant fraction of light emitted from their host cluster halos (e.g., *Schombert*, 1986; *Jones et al.*, 2000; *Lin and Mohr*, 2004; *Bernardi et al.*, 2007; *Lauer et al.*, 2007; *von der Linden et al.*, 2007; *Aguerri et al.*, 2011; *Brough et al.*, 2011; *Proctor et al.*, 2011; *Harrison et al.*, 2012). Unlike other cluster members, their location near the X-ray center of the cluster leads to their properties correlating with that of their host cluster halo (*Jones and Forman*, 1984; *Rhee and Latour*, 1991; *Lin and Mohr*, 2004; *Lauer et al.*, 2014). The current theory of BCG formation is the two-phase formation scenario, where a dense core forms at high redshifts via in-situ star formation and the outer portions of the BCG grow due to the hierarchical merging of satellite galaxies (*Oser et al.*, 2010). This theory is well supported by observations (*van Dokkum et al.*, 2010; *Huang et al.*, 2018) and dark matter only cosmological simulations which use semi-empirical or semi-analytic prescriptions for the stellar mass growth of central galaxies (e.g., *Croton et al.*, 2006; *De Lucia and Blaizot*, 2007; *Guo et al.*, 2011; *Tonini et al.*, 2012; *Shankar et al.*, 2015).

One observational measurement intrinsically tied to the stellar mass growth of the BCG is the magnitude gap ($\mathrm{m_{gap}}$), the difference in the r-band magnitude between the BCG and either the 2nd (M12) or 4th (M14) brightest cluster member within half of the radius that encloses 200× the critical density of the universe (R_{200}) (*Jones et al.*, 2003; *Dariush et al.*, 2010). For the purpose of this paper, we use the 4th brightest member, since it best identifies early forming clusters (*Dariush et al.*, 2010). Based on dissipationless simulations of young and pre-virialized groups, *Solanes et al.* (2016) find that the stellar mass of the central galaxy linearly increases with the number of progenitor galaxies, in agreement with hierarchical growth. Furthermore, BCGs grow at the expense of the 2nd brightest galaxy. Thus, as the BCG merges with the surrounding fainter galaxies, the stellar mass and magnitude of the BCG increase, relative to the 2nd or 4th brightest galaxy, increasing $\mathrm{m_{gap}}$. Therefore, $\mathrm{m_{gap}}$ is a latent third parameter in the cluster SMHM relation as shown in *Golden-Marx and Miller* (2018), which for the remainder of the paper will be referred to as GM&M18.

GM&M18 incorporate $\mathrm{m_{gap}}$ and alter the cluster-scale SMHM relation from

$$\log_{10}(M_*) = \alpha + \beta \log_{10}(M_{halo}), \tag{4.1}$$

to

$$\log_{10}(M_*) = \alpha + \beta \log_{10}(M_{halo}) + \gamma M14, \tag{4.2}$$

where α is the offset, β is the slope, γ is the $\mathrm{m_{gap}}$ stretch parameter, and M14 is the selected $\mathrm{m_{gap}}$. These parameters are measured for the SDSS-C4 cluster sample ($\log_{10}(M_{halo} / (M_\odot/h)) \geq 14.0$) (*Miller et al.*, 2005) with caustic halo masses (*Gifford et al.*, 2013) using a hierarchical Bayesian MCMC analysis. Incorporating γ into the SMHM relation reduces the inferred intrinsic scatter and uncertainties on the amplitude and slope of the SMHM relation (GM&M18).

BCGs grow hierarchically; therefore, the slope of the SMHM relation may change over time because at higher redshifts fewer mergers will have occurred and the stellar mass of the BCG will be lower (*Solanes et al.*, 2016). Moreover, dark matter halos are thought to grow hierarchically, as smaller subhalos merge with the cluster halo over time, so the average halo mass should also decrease (*White and Rees*, 1978; *Springel et al.*, 2005; *De Lucia and Blaizot*, 2007).

The redshift evolution of the SMHM relation has been investigated using observations, empirical models, and simulations. Observationally, *Oliva-Altamirano et al.* (2014) use BCGs and Brightest Group Galaxies from the Galaxy and Mass Assembly survey and find no evolution in the SMHM relation's slope over the redshift range $0.1 < z < 0.3$ while *Gozaliasl et al.* (2016) use a sample of X-ray selected galaxy groups and find that the SMHM relation's slope does not evolve over the redshift range $0.1 < z < 1.3$. Using empirical models and abundance matching techniques to infer halo masses, *Behroozi et al.* (2013a) and *Moster et al.* (2013) find that the slope evolves by 40-50% from z=0.0 to z=1.0. *Moster et al.* (2013) also find moderate evolution out to just z=0.5. In contrast, *Pillepich et al.* (2018) use the Illustris TNG300 cosmological hydrodynamical simulation and report little change in the slope between z=0.0 and z=1.0. In addition to the redshift evolution in the slope of the SMHM relation, the evolution of the intrinsic scatter has also been investigated using hydrodynamical simulations (*Matthee et al.*, 2017; *Pillepich et al.*, 2018), N-body simulations (*Gu et al.*, 2016), and empirical models (*Behroozi et al.*, 2018; *Moster et al.*, 2018). However, the results from these different approaches are inconsistent with one another, and may depend on the initial conditions of the simulations. The most likely reason no consensus exists for the redshift evolution of the intrinsic scatter and SMHM relation slope is due to differences in how the stellar and halo masses as well as the associated uncertainties are estimated in simulations, empirical models, and observations.

As previously noted, including $\mathrm{m_{gap}}$ as a latent parameter in the SMHM relation allows other parameters, such as the slope, to be measured with higher precision. Thus, Equation 4.2 plays a critical role in detecting redshift evolution of the SMHM relation. One can also allow the stretch parameter to evolve, which may provide information about the BCG merger history and the fraction of stellar matter from major and minor mergers that ends up as part of the intra-cluster light (ICL) that surrounds the BCG.

The outline for the remainder of this paper is as follows. In Section 4.3, we summarize the goals, methods, and results of GM&M18. In Section 4.4, we discuss the observations and simulated data used to measure stellar masses, halo masses, and $\mathrm{m_{gap}}$ values for our SMHM relation. In Section 4.5, we describe the hierarchical Bayesian MCMC model used to evaluate the redshift evolution of the SMHM relation. In Section 4.6, we describe how we use the low-redshift data to calibrate the higher redshift clusters and their observational errors. In Section 4.7, we present our results. In Section 4.8 we discuss our findings and conclude.

Except for the case of simulated data, in which the cosmological parameters are previously defined (*Springel et al.*, 2005), for our analysis, we assume a flat ΛCDM universe, with Ω_M=0.30, Ω_Λ=0.70, H=100 h km/s/Mpc with h=0.7.

4.3 Summary of Golden-Marx & Miller 2018

Much of the analyses in this paper build on GM&M18, so we briefly summary those results. GM&M18 set out to explain the discrepancy between amplitudes of previously published SMHM relations using the low redshift SDSS-C4 (*Miller et al.*, 2005) sample of clusters (z_{med} = 0.086). BCG Petrosian magnitudes were properly corrected for known SDSS background subtraction issues and stellar masses were determined using the *Bell et al.* (2003) M/L ratio conversion. Halo masses were measured individually for each cluster using the caustic technique (e.g. *Gifford et al.*, 2013). $\mathrm{m_{gap}}$ was measured using red sequence cluster members within $0.5\mathrm{R}_{vir}$ and introduced as a third parameterized variable into the linear SMHM relation. GM&M18 termed this third parameter the "stretch" parameter (γ) and found it to be non-zero with high statistical significance. GM&M18 also showed that $\mathrm{m_{gap}}$ plays an equally important role in the SMHM relation from semi-analytic galaxy catalogs, suggesting that it stems naturally from hierarchical growth (*Guo et al.*, 2011; *Henriques et al.*, 2012).

To achieve their results, GM&M18 developed a hierarchical Bayesian model which accounts for errors on all observables, including the intrinsic uncertainty in stellar mass at fixed halo mass (σ_{int}). The model also incorporates a level of uncertainty on the estimated errors. GM&M18 used simulated lightcone data based on the MILLENNIUM simulation (*Henriques et al.*, 2012) to test the model and its ability to accurately recover the true underlying SMHM-$\mathrm{m_{gap}}$ parameters using only projected measurements (e.g., projected dynamical cluster masses, projected $\mathrm{m_{gap}}$ values, and stellar masses inferred from galaxy magnitudes). In this new work, we use the same model, except that we add parameters to allow for redshift evolution in the amplitude, slope, stretch, and intrinsic scatter.

GM&M18 showed that the majority of the discrepancies in the reported amplitude of the cluster-scale SMHM can be explained by simply accounting for $\mathrm{m_{gap}}$ in the cluster sample selection. GM&M18 also noted that the inferred errors on the parameters in the SMHM relation as well as σ_{int} are significantly reduced (by as much as a factor of 2) after incorporating $\mathrm{m_{gap}}$ into the SMHM model.

4.4 Data

The observational data used for this analysis comes from the Sloan Digital Sky Surveys (SDSS) DR8 (*Aihara et al.*, 2011) and DR12 (*Alam et al.*, 2015). For the full cluster sample, we combine the SDSS-C4 (*Miller et al.*, 2005) sample used in GM&M18 with v6.3 of the SDSS-redMaPPer catalog (*Rykoff et al.*, 2014). The SDSS-C4 cluster sample used in GM&M18 is highly complete from $0.03 \leq z \leq 0.1$, while redMaPPer has high completeness over the range $0.10 \leq z \leq 0.35$ (*Groenewald et al.*, 2017). Since we are studying redshift evolution, we want our final sample of clusters to cover the widest possible redshift range. Therefore, we need to make measurements of halo masses, $\mathrm{m_{gap}}$ values, and BCG stellar masses for SDSS-C4 and redMaPPer clusters in a homogeneous fashion.

4.4.1 redMaPPer m_{gap}

The redMaPPer algorithm is a red-sequence-based photometric cluster finding algorithm. The redMaPPer red sequence model was constructed using a sample of spectroscopically confirmed clusters. Using this calibrated model, clusters are identified using luminosity and radial filters. redMaPPer also assigns a membership probability for cluster member galaxies, P_{mem}, which depends on the richness, cluster density profile, and background density. According to *Rykoff et al.* (2014), if $P_{mem} > 0.70$ a galaxy should be considered a member. These high-probability members are then used to estimate photometric redshifts which we use in our Bayesian MCMC analysis (Section 4.5.2). redMaPPer provides a probability for being the central galaxy for the five most likely candidate centrals and we identify the BCG as the most likely candidate.

Galaxy membership in the SDSS-C4 sample (GM&M18) differs from the redMaPPer sample due to color selection and sky apertures. SDSS-C4 cluster members are identified using individual cluster red sequences in six distinct SDSS colors (u-g, g-r, g-i, r-i, i-z, and r-z), which are fit using all potential cluster member galaxies with an r-band magnitude brighter than m_r=19 within 0.5 R_{vir} of the BCG, where R_{vir} is estimated using the caustic halo mass. We note that this includes two additional colors compared to the SDSS-C4 cluster-finding algorithm (*Miller et al.*, 2005). Cluster members are those galaxies simultaneously within 3σ of the red sequence for the u-g, g-r, and g-i colors and 2σ for the r-i, i-z, and r-z colors (GM&M18). The SDSS-C4 BCGs are visually confirmed and are identified as being the brightest in the red-sequence.

We calibrate the redMaPPer $\mathrm{m_{gap}}$ values to the SDSS-C4 $\mathrm{m_{gap}}$ measurements, where for both samples the 4th brightest is chosen from within the red-sequence. To calibrate these samples, we need to homogenize the membership of the clusters in color-magnitude space. As noted earlier, redMaPPer membership depends on a specified P_{mem} threshold. We determine this threshold using 112 clusters found in both catalogs. For these clusters, we match the density of galaxies within color-magnitude space between SDSS-C4 and redMaPPer by adjusting the latter's P_{mem} threshold. As we adjust P_{mem} and the sky aperture size, we can raise or lower the number of galaxies in the color-magnitude diagrams of the redMaPPer clusters.

We use only galaxies within an estimate of $0.5 \times R_{virial} \sim 0.5 \times R_{200}$. Although redMaPPer does not provide R_{200}, we can approximate R_{200} using Equation 4.3 from *Rykoff et al.* (2014),

$$R_{200} \approx 1.5 R_c(\lambda) \tag{4.3}$$

where λ is the redMaPPer cluster richness, and R_c is the redMaPPer cutoff radius, given

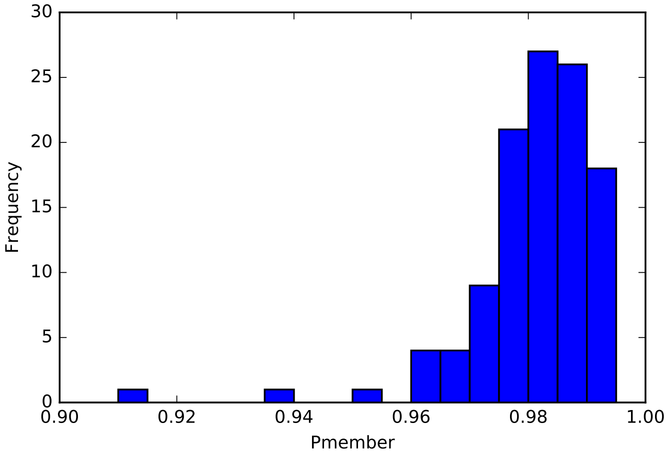

Figure 4.1: redMaPPer Membership Probability Compared to SDSS-C4 Red Sequence Membership. The distribution of the P_{mem} values required to match the number of cluster members brighter than r=18.0 in the SDSS-C4 and redMaPPer baseline sample. The median value is $P_{mem} = 0.984$.

by

$$R_c(\lambda) = 1.0h^{-1}Mpc(\lambda/100)^{0.2}. \tag{4.4}$$

Figure 4.1 shows that a median value of $P_{mem} = 0.984$ matches the two membership definitions with good precision. Therefore, we apply this P_{mem} threshold when identifying cluster members used to determine $\mathrm{m_{gap}}$ for the redMaPPer sample. We note that when we examine how the number of members changes as a function of P_{mem}, we observe little change in the range $0.7 < P_{mem} < 0.9$, but large decreases in membership at $P_{mem} > 0.9$.

Unlike in GM&M18, we no longer use Petrosian magnitudes. Instead, we measure $\mathrm{m_{gap}}$ as the difference between the k-corrected r-band model magnitudes of the BCG and 4th brightest cluster member. Applying our restrictive cluster member criterion and using the model magnitudes we find good agreement in the distribution of $\mathrm{m_{gap}}$ values for the overlapping redMaPPer and SDSS-C4 clusters. We discuss the errors on the $\mathrm{m_{gap}}$ measurements in Section 4.6.

4.4.2 redMaPPer Halo Mass

To determine halo masses for the redMaPPer sample, we use the mass-richness relation from *Simet et al.* (2017), given by Equation 4.5:

$$M_{halo}/(h^{-1}M_\odot) = 10^{14.344}(\lambda/40)^{1.33} \tag{4.5}$$

Here, λ is the standard redMaPPer richness, or galaxy count as given in *Rykoff et al.* (2014). The minimum redMaPPer richness we use is > 22, depending on the minimum mass threshold applied.

In GM&M18, we used individual dynamically inferred cluster masses from the caustic technique (*Gifford et al.*, 2013). However, to homogenize the analysis between the low-z SDSS-C4 and redMaPPer clusters, we require a mass-richness relation for the SDSS-C4 sample. For both samples, we need an estimate of the intrinsic scatter in mass at a fixed richness, which is discussed in Section 4.6.

4.4.3 Final redMaPPer Sample

We analyze the redshift evolution of the SMHM relation in two ways. First, we bin our data by redshift and determine the posteriors from our Bayesian MCMC model for each bin with the redshift evolution parameters set to 0.0. Second, we incorporate redshift evolution using four additional parameters in Equation 4.2 and fit against all of the redMaPPer clusters. For this analysis, we look at the redshift range $0.08 \leq z \leq 0.30$, where redMaPPer is suggested to be most complete (*Groenewald et al.*, 2017) and we have enough clusters for a statistically significant sample.

The total sample of 1005 redMaPPer clusters with stellar masses measured out to 100kpc, with greater than 4 members with $P_{mem} \geq 0.984$ within $0.5R_{200}$, and within $0.08 \leq z \leq 0.3$ has no mass limit applied. However, we do not expect the redMaPPer sample to have the same lower mass-limit throughout this redshift range and we must also check for $\mathrm{m_{gap}}$ incompleteness since SDSS is a flux-limited survey.

Therefore, the redMaPPer sample was divided into 4 redshift bins, each initially with

$\sim$ 251 clusters. For each bin, as done in GM&M18, we use a m_{gap} completeness analysis where we bin the absolute magnitude of the BCG and 4th brightest member against both the BCG's apparent magnitude and $\mathrm{m_{gap}}$ to determine the apparent magnitude limit of the sample (a redshift dependent limit) (*Colless*, 1989; *Garilli et al.*, 1999; *La Barbera et al.*, 2010; *Trevisan et al.*, 2017; *Golden-Marx and Miller*, 2018).

To account for halo mass incompleteness, for each redshift bin, the halo mass distribution can be approximated as a Gaussian, where the peak indicates the mass at which the sample starts to become incomplete. Instead of applying a model-dependent correction to the analysis, we apply a lower halo mass cut where the amplitude of the binned halo mass distribution decreases to 70% of the peak value to ensure high completeness as a function of redshift. This is a conservative choice which results in a redMaPPer richness threshold of $\sim$ 22, well above the detection limit for the redMaPPer algorithm. However, when combined with the m_{gap} completeness analysis, these cuts shrink our available sample down to 843 clusters, a reduction of $\sim$16%. A slightly more restrictive (higher) halo mass lower limit has no effect on our final results.

Since we study clusters out to $z = 0.3$ where the SDSS-redMaPPer sample is volume-limited, we do not apply any corrections for volume effects from Malmquist bias.

4.4.4 SDSS-C4 Sample and Richness-based Halo Masses

The SDSS-C4 clusters are nearly identical to those used in GM&M18. The samples differ because the stellar masses are estimated, as described in Section 4.4.5, within 100kpc, instead of within the Petrosian radius. Additionally, we use a mass-richness relation to infer the redMaPPer halo masses. Therefore instead of the individual dynamical cluster masses, we also use a mass-richness relation for the SDSS-C4 sample. For this analysis, we use only clusters with clean phase-spaces to ensure our richness measurement is meaningful and unimpacted by foreground and background contamination. Given these individual masses and the observed galaxy and background counts, we make a preliminary constraint on the SDSS-C4 mass-richness relation using techniques similar to *Andreon and Hurn* (2010). We find:

$$M_{halo}/(h^{-1}M_{\odot}) = 10^{14.195}(\lambda^{C4}/33.1)^{1.134}. \quad (4.6)$$

We note that the richnesses (λ^{C4}) for the SDSS-C4 sample are not calculated in the manner as in the redMaPPer richnesses. However, using the sample of clusters found in both the SDSS-C4 and in SDSS-redMaPPer, we find that the offset between the redMaPPer and C4 mass estimates is 0.1 dex, with a standard devation of 0.15 dex. As shown in Table 4.7.1, when this offset is removed, the results of our analysis do not change. A more detailed analysis of the SDSS-C4 mass-richness relation will be presented elsewhere (Miller et al. in preparation). Using this mass-richness relation, we apply the mass limits of $14.0 \leq \log_{10}(\mathrm{M_{halo}}/(\mathrm{M_{\odot}}/\mathrm{h})) \leq 14.7$. The upper limit was selected to eliminate Malmquist bias in the low redshift (and small volume) sample. Overall, these changes result in a sample of 142 clusters with clean richnesses used in this analysis.

4.4.5 BCG Stellar Masses

In GM&M18, we emphasized the importance of correcting the BCG magnitudes because of the SDSS background subtraction error (*Bernardi et al.*, 2007; *von der Linden et al.*, 2007; *Harrison et al.*, 2012; *Bernardi et al.*, 2013). This correction is a strong function of the apparent size of the galaxies and is especially problematic at low redshifts. The BCGs in redMaPPer are smaller in their apparent sizes and suffer much less from the known issues of the background light subtraction compared to the SDSS-C4 sample (*Bernardi et al.*, 2007; *von der Linden et al.*, 2007; *Harrison et al.*, 2012; *Golden-Marx and Miller*, 2018), so we do not need to re-measure the BCG light profiles to correct for missed light within selected radii of the BCGs and include additional uncertainties on the BCG stellar mass estimates. Instead, we use the stellar mass measured within a fixed and precise 100kpc radial extent, a choice which is justified in Section 4.6.1, which results in a much smaller uncertainty on the stellar masses. To measure the 100kpc magnitudes, we queried the SDSS DR12 (*Alam et al.*, 2015) database to obtain the SDSS azimuthally averaged radial light profile for each BCG and then integrated these profiles to 100kpc.

To calculate BCG stellar masses, unlike in GM&M18, we do not use the *Bell et al.* (2003) M/L ratio to estimate stellar mass because this relation is calibrated for z=0.0. Instead we use the EzGal SED modeling software (*Mancone and Gonzalez*, 2012) to estimate stellar mass. We note that GM&M18 found no differences in their fits to the SMHM relation when using the EzGal-based stellar masses versus the *Bell et al.* (2003)-based stellar masses.

When estimating stellar masses using EzGal, we use a *Bruzual and Charlot* (2003) stellar population synthesis model, a *Salpeter* (1955) IMF, a formation redshift of $z = 4.9$, and a constant metallicity of 0.4 $z_{\odot}$. We apply a Bayesian MCMC approach, done in emcee (*Foreman-Mackey et al.*, 2013). We treat the absolute magnitude (the normalization parameter selected for EzGal) as a free parameter, with a uniform prior, to determine the absolute magnitude that minimizes the chi-squared between the EzGal modelled g-, r-, and i-band magnitudes measured at the observed redshift and the SDSS g-, r-, and i-band magnitudes measured at 100 kpc. We note that initially, metallicity was treated as a free parameter. However, ≈ 99% had a minimum chi squared when the metallicity of 0.4 $z_{\odot}$ was chosen, so we removed this free parameter. Using this approach, we estimate the stellar mass uncertainty to be 0.08 dex, consistent with the suggestion from *Bell et al.* (2003). This is about half the uncertainty used in GM&M18, where the precision in determining the Petrosian radius and the induced error from the background correction dominate the error budget.

4.4.6 Simulated Data

In addition to studying the evolution of the SMHM - $\mathrm{m_{gap}}$ relation in the SDSS-C4 and redMaPPer data, we also analyze the same trend using the *Guo et al.* (2011) prescription of the semi-analytic representations of low-redshift clusters in the MILLENNIUM simulation. Unlike in GM&M18, we do not use the *Henriques et al.* (2012) prescription because it is magnitude limited to $K_s \approx 21.8$, which at z=0.3, corresponds to $r \approx 18$, far fainter than that of our observed sample. Also, the periodic replications within *Henriques et al.* (2012) may introduce additional, unaccounted for, noise in our MCMC model. For this analysis, we use the *Guo et al.* (2011) simulation boxes analyzed at redshifts of 0.089, 0.116, 0.144, 0.174, and 0.242, the redshifts which best match our binned sample and correspond to snapshot numbers 59, 58, 57, 56, and 54.

For the simulated data analysis we use the 3D information provided directly from the *Guo et al.* (2011) prescription of the MILLENNIUM simulation for each cluster, which includes halo masses, measured within $R_{200} \times \rho_{crit}$; the galaxy positions, x, y, z; R_{200}; the semi-analytic stellar masses; and the magnitudes. To determine cluster membership we use the positional information (x, y, z) to determine if potential cluster members are within 0.5 R_{200}. For those galaxies within this sphere, we identify galaxies within 2 standard deviations from the red sequence as cluster members. M14 is then measured as the difference between the 4th brightest member and BCG in the r-band. Since the BCG stellar masses are provided by the *Guo et al.* (2011) prescription of the MILLENNIUM simulation and we have access to the entire simulation box, we do not apply a completeness criteria to our simulated sample for each redshift bin. However, to make our samples comparable, we apply the halo mass distribution function of the binned SDSS-redMaPPer data to the simulation snapshot at the corresponding redshift.

4.5 The Hierarchical Bayesian Model

We use a hierarchical Bayesian MCMC analysis to determine the values of α, β, γ, σ_{int}, and the redshift evolution parameters given in Equation 4.7. The Bayesian approach can be described as convolving prior information for a given model with the likelihood of the observations given the model to yield the probability of observing the data given the model, or the posterior distribution up to a normalization constant called the Bayesian evidence.

To generate the posterior distributions for each of the parameters, our MCMC model generates values for the observed stellar masses, halo masses, and $\mathrm{m_{gap}}$ values at each step in our likelihood analysis, which are then directly compared to the observed measurements. As described in Section 4.3, we modified our previous MCMC model (GM&M18) to improve the speed of convergence. Our new model is summarized below.

4.5.1 Bayesian Model incorporating Redshift evolution

4.5.1.1 The Observed Quantities

For our redshift evolution model, we use similar equations and relations to quantify the observed or measured values for the halo mass and $\mathrm{m_{gap}}$ and the same relation for stellar mass as described in GM&M18. The $\log_{10}$ BCG stellar masses (y), $\log_{10}$ halo masses (x), and M14 values (z) are modeled as being drawn from Gaussian distributions with mean values (locations) taken from the observed data. The standard deviations are the errors on each measurement and include an estimate of the observational uncertainty (σ_{x_0}, σ_{y_0}, σ_{z_0}) and an additional stochastic component from a beta function $\beta(0.5, 100)$ (GM&M18), which allows for realistic uncertainty on the observational errors. These are treated statistically in the Bayesian model as free nuisance parameters σ_x, σ_y, and σ_z.

One modification we made to the likelihood and prior from GM&M18 is that we no longer model the underlying halo mass and $\mathrm{m_{gap}}$ distributions as truncated Normal distributions; instead, we use a Gaussian distribution and allow the halo mass values for any step of the trace to be below our lower limit. However, the median halo mass of each cluster generated in the MCMC chains reflects the halo mass lower limit listed in Table 4.3.

4.5.2 The Unobserved Quantities

The new version of this model incorporates redshift evolution through parameters on α, β, γ, and σ_{int}. As in GM&M18, we are only concerned with the cluster portion of the SMHM relation, which is modeled linearly. As such, Equation 4.2 becomes:

$$y_i = \alpha(1+\mathrm{z_{red}})^{\mathrm{n_1}} + (\beta(1+\mathrm{z_{red}})^{\mathrm{n_2}})\mathrm{x_i} + (\gamma(1+\mathrm{z_{red}})^{\mathrm{n_3}})\mathrm{z_i} \tag{4.7}$$

In Equation 4.7, $\mathrm{z_{red}}$ is the photometric redshift determined via red sequence fitting from redMaPPer (*Rykoff et al.*, 2014) or the spectroscopic redshift for the SDSS-C4 clusters, not to be confused with z, the short-hand for the $\mathrm{m_{gap}}$, M14. We assume a Gaussian likelihood form, with an intrinsic scatter that can also evolve with redshift: $\sigma_{int}(1+\mathrm{z_{red}})^{\mathrm{n_4}}$. The four parameters, n_1, n_2, n_3, and n_4, measure the redshift evolution of α, β, γ, and

σ_{int} respectively. When we use this model for the redshift binned sample described in Section 4.4.3, these parameters are set to 0.0, which reduces Equation 4.7 to Equation 4.2. This means that the zero redshift model used in GM&M18 is nested within our new model. By using nested models, we can interpret how much better a given model is (e.g., with redshift evolution vs. without) using only the posterior distribution.

Our Bayesian model regresses against the observed stellar mass, halo mass, and $\mathrm{m_{gap}}$ values simultaneously and self-consistently. We treat parameters that model the underlying distributions and their uncertanties as nuisance parameters and we marginalize over them when we present the posterior distributions in Section 4.7.1. All parameters in the Bayesian analysis are presented in Table 4.1 along with their priors. We discuss the strong priors on the observed uncertainties in Section 4.6.

We can express the entire posterior as:

$$\begin{aligned} p(\alpha, \beta, \gamma, \sigma_{int}, n_1, n_2, n_3, n_4, x_i, z_i, \sigma_{y_i}, \sigma_{x_i}, \sigma_{z_i}) \propto \\ \underbrace{P(y_{0i}|\alpha, \beta, \gamma, \sigma_{y_i}, n_1, n_2, n_3, n_4, \sigma_{int}, x_i, z_i)\ P(x_{0i}|x_i, \sigma_{x_i})\ P(z_{0i}|z_i, \sigma_{z_i})}_{\text{likelihood}} \\ \underbrace{p(x_i)\ p(z_i)\ p(\sigma_{x_i})\ p(\sigma_{y_i})\ p(\sigma_{z_i})\ p(\alpha)\ p(\beta)\ p(\gamma)\ p(\sigma_{int})\ p(n_1, n_2, n_3, n_4)}_{\text{priors}} \end{aligned} \tag{4.8}$$

where each i^{th} cluster is a component in the summed log likelihood.

Like the model presented in GM&M18, we use a *hierarchical Bayes model* because the priors on the true halo masses (x_i) and M14 values (z_i) depend on models themselves (the observed halo mass and M14 distributions).

4.6 Calibration

For this paper, we study a larger sample out to a higher redshift ($z \leq 0.3$) than in the SDSS-C4 sample ($z_{med} = 0.086$). The larger sample allows us to reduce the statistical noise in the data while the higher redshift allows us to search for late-time evolution in the SMHM relation (i.e., in the last ~ 3.5 billion years). Two important trade-offs when using the bigger and deeper redMaPPer data combined with the lower redshift SDSS-C4 data is that we need to calibrate the observables (see Section 4.4)

Bayesian Analysis Parameters for the
Combined SDSS-C4 and SDSS-redMaPPer Sample

Symbol	Description	Prior
α	The offset of the SMHM relation	$\mathcal{U}(-20,20)$
β	The high-mass power law slope	Linear Regression Prior
γ	The stretch parameter, which describes the stellar mass - M14 stratification	Linear Regression Prior
σ_{int}	The uncertainty in the intrinsic stellar mass at fixed halo mass	$\mathcal{U}(0.0, 0.5)$
y_i	The underlying distribution in stellar mass	Equation 4.7
x_i	The underlying halo mass distribution	$\mathcal{N}(14.28, 0.22^2)$
z_i	The underlying $\mathrm{m_{gap}}$ distribution	$\mathcal{N}(2.13, 0.57^2)$
n_1	The power law associated with the redshift evolution of α	$\mathcal{U}(-10.0, 10.0)$
n_2	The power law associated with the redshift evolution of β	$\mathcal{U}(-10.0, 10.0)$
n_3	The power law associated with the redshift evolution of γ	$\mathcal{U}(-10.0, 10.0)$
n_4	The power law associated with the redshift evolution of σ_{int}	$\mathcal{U}(-20.0, 20.0)$
$\sigma_{y_{0i}}$	The uncertainty between the observed stellar mass and intrinsic stellar mass distribution	0.08 dex
$\sigma_{x_{0i}}$	The uncertainty associated with the mass-richness relation	0.087 dex
$\sigma_{z_{0i}}$	The uncertainty between the underlying and observed $\mathrm{m_{gap}}$ distribution	0.15

Table 4.1: Bayesian Analysis Prameters for the SDSS-redMaPPer Nominal Sample using M14 and Incorporating Redshift Evolution. $\mathcal{U}(a, b)$ refers to a uniform distribution where a and b are the upper and lower limits. The linear regression prior is of the form $-1.5 \times \log(1 + value^2)$. $\mathcal{N}(a, b)$ refers to a Normal distribution with mean and variance of a and b. Additionally, we note that for x_i and z_i, the means and widths given in this table are example values belonging to the lowest SDSS-redMaPPer redshift bin.

and that we have less secure mean values of the observational uncertainties, such as the $\mathrm{m_{gap}}$ values and the halo masses.

4.6.1 Aperture Radius and the Slope of the SMHM relation

Because we are studying redshift evolution, we need to use a BCG aperture for the stellar masses that is unbiased due to the decrease in apparent size and signal-to-noise of the galaxies out to $z = 0.3$. Since we expect little physical growth in BCGs over this redshift range, we choose a fixed kiloparsec (kpc) aperture.

Zhang et al. (2016), using DES science verification data, measure the slope of the SMHM relation using photometry measured within four radial extents ranging from 15 to 60kpc and stellar masses estimated using EzGal (*Mancone and Gonzalez*, 2012) SED fitting. *Zhang et al.* (2016) detect a weak correlation (although their measurements are all within 1σ), such that stellar mass and halo mass are more strongly correlated at larger aperture radii, in agreement with observations of inside-out galaxy growth (e.g., *van Dokkum et al.*, 2010). We investigate this trend by re-integrating the SDSS light profiles at fixed physical radii of 10, 20, 30, 40, 50, 60, 70, 80, 90, and 100kpc for the 189 SDSS-C4 clusters with radial extents greater than 100kpc from GM&M18 and measure the SMHM-$\mathrm{m_{gap}}$ relation at each radial extent. For each Bayesian MCMC analysis, we use the same $\mathrm{m_{gap}}$, from the Petrosian magnitudes and the caustic halo masses with reduced uncertainty. This analysis was performed using the Bayesian formalism described in Section 4.5, with the redshift parameters set to 0.0. Additionally, we do a second analysis where we set γ to 0.0. The results are shown in Figure 4.2 for both analyses. Figure 4.2 also shows the slope measured by *Pillepich et al.* (2018) for the Illustris TNG300 simulation, where stellar masses are determined using the SUBFIND algorithm to identify and sum the stellar particles bound to a galaxy within a fixed 3D physical radii.

The primary takeaway from Figure 4.2 is that the choice of radial extent within which the BCG's stellar mass is measured significantly impacts the SMHM relation's slope. This result confirms the idea presented by *Zhang et al.* (2016) and suggests that the outer halo of the BCG is indeed tied to the underlying parent (cluster) halo. Moreover, our result observationally confirms a trend suggested by the EMERGE empirical model (*Moster et al.*, 2018). *Moster et al.* (2018) find that to match observational baryon conversion efficiencies at low redshifts, empirical models must incorporate a fraction of the ICL, since the baryon conversion efficiency of central galaxies (a proxy for stellar mass) in clusters, at fixed halo mass is underapproximated by empirical models when compared to observational results which generally measure BCG stellar masses within larger radii than those used in empirical models. Thus, similar to our results, *Moster et al.* (2018) find that the conversion efficiency, at fixed halo mass, which is similar to the slope of the SMHM relation, increases when parts of what have been previously classified as ICL are included in the stellar mass estimate of the BCG.

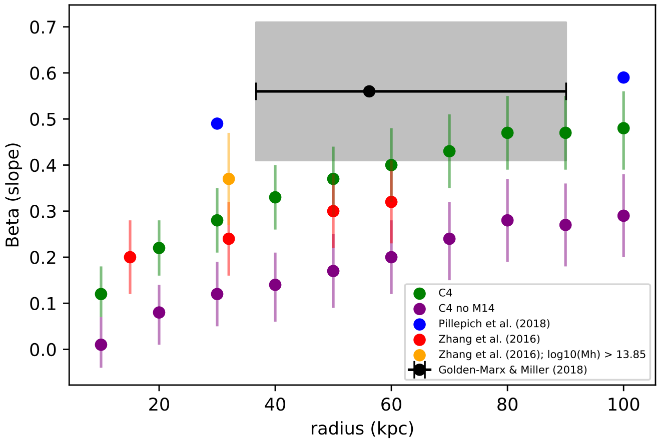

Figure 4.2: SMHM Relation Slope as a Function of Radius within which the BCG Stellar Mass is Measured. The slope of the SMHM relation as a function of the BCG's radial extent, where m_{gap} is incorporated (green) and when it is not (purple). The results of *Zhang et al.* (2016) are shown in red and yellow. The results from *Pillepich et al.* (2018) using ILLUSTRIS TNG300 are shown in blue. For comparison, the slope measurement from GM&M18 is shown in black with the gray bar. The radial range represents the median and standard deviations of the Petrosian radii for the SDSS-C4 sample. Measuring the stellar mass within a larger radial extent steepens the slope of the SMHM relation because the outer regions of BCGs are tied to the parent clusters. Additionally, incorporating M14 also steepens the slope, which is expected if M14 is related to BCG growth.

This trend between slope and radial extent is important because previously published SMHM relations often use model magnitudes or state that their stellar masses are estimated within Kron or Petrosian radii, which, unless the specific radial extents are provided, can lead to a biased comparison between published results, and an improper comparison between BCGs in large samples where those radii greatly differ. Additionally, the slope of the SMHM relation levels off around 80-100kpc, which shows that beyond this radial extent, we gain no additional information. This result agrees with the analysis of *Huang et al.* (2018), who use Hyper Suprime Cam Subaru Strategic Program (HSC SSP) observations of massive galaxies over the redshift range $0.3 < z < 0.5$ and find that the difference between the stellar mass within 100 kpc and the total stellar mass is on average $\sim$0.02 dex. Moreover, *Zhang et al.* (2018), who use DES Year 1 observations, study the ICL surrounding BCGs in the redshift range $0.2 < z < 0.3$, suggest that 100kpc marks the transition region between the ICL and BCG. Therefore, our choice of a 100kpc aperture for our BCG magnitudes accounts for the majority of the stellar mass in the BCG.

The second significant result we find is that the slope is statistically different depending on whether we use the latent m_{gap} and its stretch parameter in the SMHM relation. We found no significant difference in GM&M18 and attribute this to the use of the Petrosian magnitudes to estimate stellar masses. The Petrosian radius is a measured quantity which causes a blending of the underlying physical apertures depending on the BCG redshift. Therefore, not only does using a small aperture lead to a shallower slope, the absence of accounting for the BCG's assembly history, via $\mathrm{m}_{\mathrm{gap}}$, does as well.

At the largest radii, we find excellent agreement with the results from the ILLUSTRIS TNG300 simulation *Pillepich et al.* (2018). Unlike the *Guo et al.* (2011) semi-analytic galaxy treatment, ILLUSTRIS TNG is a full hydrodynamic N-body simulation that contains the following astrophysical properties: gas cooling and photoionization, star formation within an interstellar medium, stellar evolution and feedback, and black holes with feedback.

4.6.2 Error Calibration

The deeper redMaPPer sample lacks good spectroscopic coverage, so we expect some issues with projection when measuring $\mathrm{m_{gap}}$. In GM&M18, we used $\sigma_{z_0} = 0.1$ dex as our uncertainty in $\mathrm{m_{gap}}$, which is consistent with the 3D simulations for the spectroscopically complete low redshift SDSS-C4 sample and the precision of our Petrosian magnitudes. We expect a slightly larger σ_{z_0} for the redMaPPer sample because the reduction of the photometric error in the BCG magnitudes is offset by issues such as projection effects and the P_{mem} criterion when determining $\mathrm{m_{gap}}$. However, we need to determine a reasonable value to use for σ_{z_0} for the redMaPPer sample in our Bayesian analysis.

In addition to the above issue, by employing a mass-richness relation, the Bayesian analysis requires the scatter in mass at fixed richness $\sigma(M|\lambda)$. To date, this quantity is not well constrained. *Andreon* (2015) report this scatter to be as low as $\sigma(lnM_{200}|\lambda) < 0.05$ at 90% confidence. In contrast, *Rozo et al.* (2015) find a larger scatter of $0.17 - 0.21$, depending on what they assume for the intrinsic scatter in cluster SZ-based masses and its co-variance with the observed richness.

We begin the error calibration of the SDSS-C4 mass-richness scatter by conducting a simultaneous analysis of the SDSS-C4 SMHM relation using both the individual cluster caustic masses as well as the masses determined from the SDSS-C4 mass-richness relation. Regardless of the cluster mass used, we require the resultant parameters of the SMHM to agree within 1σ. In this analysis, we allow caustic mass errors $\sigma(M)_{data}$ to be a free parameter. The intrinsic scatter, $\sigma(M|\lambda)$ is then constrained by the observed scatter in the mass-richness relation: $\sigma(M|\lambda)^2_{obs} = \sigma(M)^2_{data} + \sigma(M|\lambda)^2_{intrinsic}$. Without the additional constraint from the

SMHM relation, our inferred $\sigma(M|\lambda)$ would be fully degenerate with the unknown true errors on the observational measurements.

To ensure the completeness of the sample, we use only the 128 clusters with $\log_{10}(M_{halo}/(M_{\odot}/h)) > 14.0$, regardless of whether it is the dynamically-inferred caustic mass or the richness-inferred mass. We find that $\sigma(\mathrm{lnM}_{200}|\lambda^{\mathrm{C4}}) = 0.20^{+0.03}_{-0.04}$ (where $\log_{10}$ and ln refer to the log base 10 and natural log, respectively). At the same time, we find that the simulation calibrated caustic errors provided in *Gifford et al.* (2013) are over-estimated by $\sigma(\mathrm{lnM}_{200}) = 0.19$, on average. We note that we could have just chosen $\sigma(\mathrm{lnM}_{200}|\lambda) = 0.20$ (*Rozo et al.*, 2015). However, the joint mass-richness and SMHM relation analysis suggests that $\sigma(\mathrm{lnM}_{200}|\lambda) \simeq 0.20$ is well motivated observationally. The full details of this analysis are beyond the scope of this work and can be found in C. J. Miller et al. (2019 - in preparation). However, this analysis gives us a purely data-inferred constraint on the appropriate intrinsic mass-richness scatter to use for the SDSS-C4 sample.

We still need to estimate the intrinsic scatter in the redMaPPer mass-richness relation, as well as uncertainties in $\mathrm{m_{gap}}$ values and the stellar masses for the redMaPPer sample. We choose to calibrate the redMaPPer observational uncertainties, $\sigma_{x_0}, \sigma_{y_0}$, and σ_{z_0} by defining a redMaPPer sub-sample which matches the SDSS-C4 redshift distribution function (down to $z = 0.081$) and apply the richness based mass limit $\log_{10}(M_{halo}/(M_{\odot}/h)) \geq 14.0$. With this new redMaPPer calibration sample, we treat $\sigma_{x_0}, \sigma_{y_0}$ and σ_{z_0} as nuisance parameters on a coarse grid in the Bayesian analysis and solve for their mean best values by requiring that the inferred slope, amplitude, stretch parameter, and intrinsic scatter of the redMaPPer calibration sample are within 1σ of the values found for the SDSS-C4 sample.

The posterior distributions for the calibration samples are given in lines 2 and 3 of Table 4.3. We find good agreement between the SDSS-C4 richness sample and the redMaPPer calibration sample for α, β, and γ, and σ_{int} when the stellar mass uncertainties are $\sigma_{y_0} \simeq 0.08$ dex, the magnitude-gap uncertainties are $\sigma_{z_0} \simeq 0.15$ and the inferred intrinsic scatter in the mass-richness relation is $\sigma(lnM_{200}|\lambda) = 0.20$, which corresponds to $\sigma_{x_0} = 0.087$ dex. The slope (β) and intrinsic scatter σ_{int} for the redMaPPer and SDSS-C4 low-redshift calibration samples are within 1σ of each other. The inferred stretch parameter γ and offset α differ between SDSS-C4 and redMaPPer by 1.5σ and the redMaPPer value for γ is closer to the result presented for the caustic-based SDSS-C4 sample in GM&M18.

To match the results of the SDSS-C4 richness sample, we adjust some measurement uncertainties from the values used in GM&M18 for the SDSS-C4 sample. σ_{y_0} is the same for the SDSS-C4 and SDSS-redMaPPer samples since have stellar masses estimated via EzGal (*Mancone and Gonzalez*, 2012) using the SDSS 100kpc BCG magnitudes. However, as previously discussed, this is a reduction from what was used in GM&M18, which is due to the *von der Linden et al.* (2007) corrected Petrosian magnitudes, which add uncertainty due to the background correction and measurement of Petrosian radii. σ_{z_0} is slightly larger, at 0.15 for the redMaPPer data due to our concerns about projection effects and our high P_{mem} criterion. Most importantly, σ_{x_0} is the same for the SDSS-C4 richness sample and the redMaPPer calibration sample, which highlights that despite using different mass-richness relations, the uncertainty associated with this mass estimate is relatively constant.

The above error calibration provides us with estimates of the uncertainties on the observables. The values we obtain are reasonable and in agreement with expectations. We do not have good estimates on the errors on these uncertainties in the observables. However, it is important to recall that Equation 4.8 does allow for uncertainty in the observed errors. So while we set an initial mean value using the techniques described in this subsection (i.e., σ_{x_0}, σ_{y_0}, σ_{z_0}), the observational errors applied in the Bayesian analysis are actually free (nuisance) parameters.

We make a final note that the subset used to calibrate the observable errors in the redshift overlap range between the SDSS-C4 and redMaPPer samples is different from the matched SDSS-C4/redMaPPer sample used to calibrate the redMaPPer membership probability threshold. These redMaPPer sub-samples each serve their own purposes and differ to maximize the amount of usable data. However, once the errors are calibrated between SDSS-C4 and redMaPPer, we can use all available redMaPPer and C4 data in the final analysis over the redshift range $0.03 \leq z \leq 0.3$. Without this calibration, there could be underlying and unaccounted systematic uncertainties between the two baseline samples which would cloud the statistical inference.

4.7 Results

4.7.1 Combined redMaPPer and SDSS-C4 Results

In this section, we present the qualitative and quantitative results from our analysis of the C4 and redMaPPer data. We highlight the qualitative results of this study in Figure 4.3, which compares the stellar masses estimated using EzGal (*Mancone and Gonzalez*, 2012) to the halo masses, estimated using the *Simet et al.* (2017) mass-richness relation. In addition, we include the 142 richness selected SDSS-C4 clusters, bringing our total sample to 985 clusters. The colorbar is based on the M14 values for each cluster. The data shown in Figure 4.3 encompasses the redshift range $0.03 \leq z \leq 0.30$. Therefore, the stratification observed in our low-redshift SDSS-C4 sample (at fixed halo mass, as stellar mass increases, so does M14) exists at higher redshifts than observed in GM&M18. Furthermore, although not shown, when the sample is binned by redshift, the stellar mass - M14 stratification also exists. Additionally, this stratification is present in the *Guo et al.* (2011) prescription of the MILLENNIUM simulation at each of the discrete redshift snapshots discussed in Section 4.4.6.

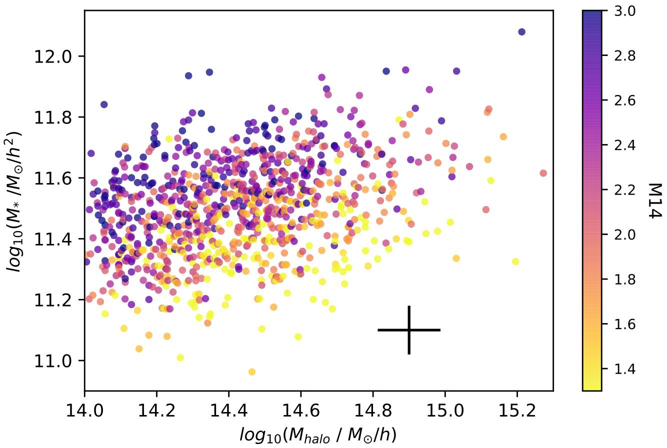

Figure 4.3: SHMH-M14 Relation for SDSS-C4 and SDSS-redMaPPer Samples. The SMHM relation for the combined redMaPPer and SDSS-C4 clusters colored via M14. As in GM&M18, we see that a stellar mass - m_{gap} stratification exists at higher redshifts. The black cross represents the error in halo mass, 0.087 dex, and stellar mass, 0.08 dex.

We evaluate the impact of incorporating m_{gap} and redshift into the SMHM relation using our previously described MCMC model (Section 4.5), Bayesian formalism, and linear SMHM relation (Equation 4.7). In Figure 4.4, we present a triangle plot which shows the 1D and 2D posterior distributions for each of the eight parameters, α, β, γ, n_1, n_2, n_3, n_4, and σ_{int}. For this analysis, as well as the initial calibration analysis, we shifted the x and y axis to eliminate the covariance between α and β. To do this, we subtracted the median values of the halo mass and stellar mass of the combined SDSS-C4 richness and SDSS-redMaPPer samples: (x_{med} = 14.41 and y_{med} = 11.50). The posterior results, as well as the posterior results when m_{gap} is not included, are presented in Table 4.7.1. The difference between these results is discussed in Section 4.8.

In Figure 4.4, excluding the original parameters and their associated redshift evolution parameters, only a few pairs of parameters are strongly covariant: α, and γ, α and n_3, γ and n_1, and n_1 and n_3. α and γ are covariant because of the shifted axis, which results in the location of α corresponding to where M14=0.0. Figure 4.4 illus-

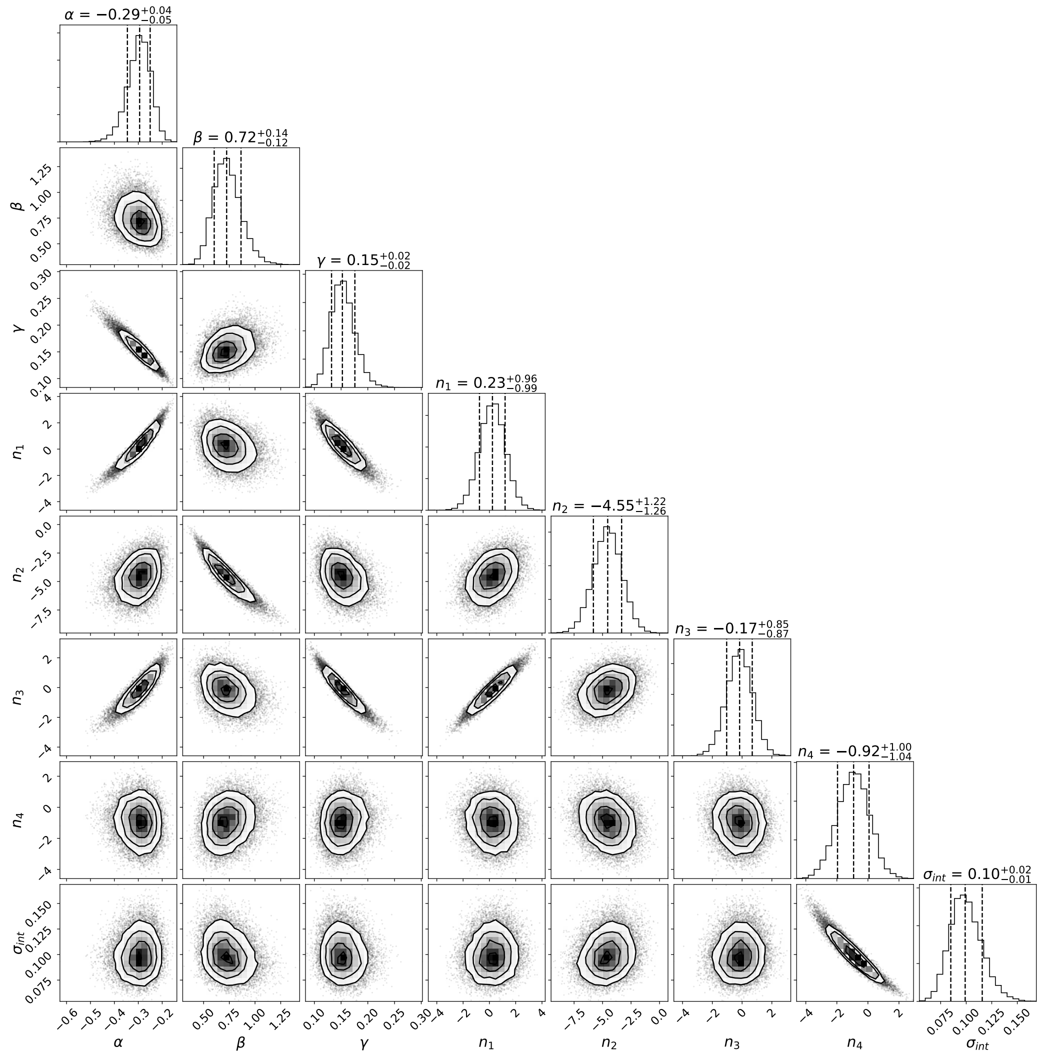

Figure 4.4: SMHM-M14 with Redshift Evolution Posterior Distributions. The posterior distribution for α, β, γ, n_1, n_2, n_3, n_4, and σ_{int}. As in GM&M18, we see that γ is significantly non-zero and σ_{int} is approximately 0.1 dex. We note that the posteriors measured here are extrapolations out to redshift=0.0. To see the values at the redshifts measured in our study, see Figures 4.5, 4.6, 4.7, and 4.8. The redshift parameter n_2 is the only parameter that is significantly non-zero. Therefore, some, albeit weak, redshift evolution in the slope of the SMHM relation can be detected over $0.03 \leq z \leq 0.3$.

Posterior Distribution Results with Redshift Evolution

Data	α(z=0)	β(z=0)	γ(z=0)	σ_{int}(z=0)	n_1	n_2	n_3	n_4
with M14	-0.34 ± 0.05	$0.72\ ^{+0.14}_{-0.12}$	0.16 ± 0.02	$0.107\ ^{+0.015}_{-0.013}$	$-0.39\ ^{+0.91}_{-0.88}$	-4.75 ± 1.29	$-0.59\ ^{+0.86}_{-0.88}$	$-1.26\ ^{+0.86}_{-0.88}$
without M14	$0.14\ ^{+0.03}_{-0.02}$	$0.37\ ^{+0.13}_{-0.10}$		$0.142\ ^{+0.016}_{-0.014}$	$-2.03\ ^{+1.27}_{-1.22}$	$-2.25\ ^{+1.86}_{-1.96}$		$-0.68\ ^{+0.67}_{-0.68}$
with M_{halo} C4 shifted	$-0.31\ ^{+0.05}_{-0.06}$	$0.72\ ^{+0.15}_{-0.14}$	0.14 ± 0.02	$0.109\ ^{+0.017}_{-0.015}$	$0.03\ ^{+1.08}_{-1.09}$	$-4.98\ ^{+1.41}_{-1.39}$	$0.41\ ^{+0.90}_{-0.94}$	$-1.49\ ^{+1.00}_{-0.96}$
without C4	$-0.44\ ^{+0.07}_{-0.09}$	$0.60\ ^{+0.13}_{-0.11}$	0.23 ± 0.04	$0.100\ ^{+0.021}_{-0.017}$	$-1.67\ ^{+1.12}_{-1.16}$	$-2.95\ ^{+1.26}_{-1.35}$	$-2.53\ ^{+1.01}_{-1.07}$	$-1.07\ ^{+1.13}_{-1.15}$
without M14 and C4	$0.18\ ^{+0.06}_{-0.04}$	$0.25\ ^{+0.08}_{-0.06}$		$0.149\ ^{+0.019}_{-0.017}$	$-4.92\ ^{+1.90}_{-1.99}$	$0.84\ ^{+1.61}_{-1.66}$		$-1.09\ ^{+0.77}_{-0.74}$
without z > 0.25	-0.34 ± 0.06	$0.75\ ^{+0.16}_{-0.13}$	$0.17^{+0.03}_{-0.02}$	$0.108\ ^{+0.018}_{-0.016}$	$-0.55\ ^{+1.17}_{-1.16}$	$-5.09\ ^{+1.43}_{-1.42}$	$-0.81\ ^{+1.02}_{-1.00}$	$-1.44\ ^{+1.10}_{-1.13}$
with *von der Linden et al.* (2007) correction	-0.28 ± 0.05	$0.85\ ^{+0.17}_{-0.15}$	0.20 ± 0.02	$0.102\ ^{+0.025}_{-0.022}$	$0.97\ ^{+1.00}_{-1.12}$	$-5.59\ ^{+1.39}_{-1.45}$	$-0.20\ ^{+0.67}_{-0.74}$	$-2.08\ ^{+1.66}_{-1.72}$

Table 4.2: Redshfit Evolution Bayesian MCMC Posterior Distributions

trates that the primary results presented in GM&M18 still hold true; γ is definitively non-zero, σ_{int} is ∼0.1 dex, and incorporating $\mathrm{m_{gap}}$ decreases σ_{int} by ~ 0.04 dex, or $\approx 30\%$. We note that the error bars on the redMaPPer values are similar to those presented in GM&M18 because of the addition of the redshift evolution parameters.

The most important takeaway from Figure 4.4 is the significance of the redshift evolution parameter, n_2, which is definitively non-zero. n_1 and n_3 are within 1σ of 0.0, while n_4 is slightly greater than 1σ from 0.0. n_2 is also the most interesting parameter because no covariance exists between n_2 and any parameter other than β, which signifies that for the first time, we detect statistically significant ($> 3.5\sigma$) redshift evolution in the slope of the SMHM relation. To improve our understanding of our measurements of the redshift evolution of α and γ, we need to eliminate the covariance between these parameters, without re-introducing covariance with β.

To reach these results, we have developed and implemented a detailed and careful analysis to ensure that the lower redshift SDSS-C4 data and the higher redshift SDSS-redMaPPer data are homogeneous. Specifically, we ensured that both datasets utilize the same underlying instrumentation (SDSS), the same underlying photometric detrending pipeline (SDSS), the same underlying spectroscopic pipeline (SDSS), the same physical fixed-aperture photometry for all BCGs, the same cluster galaxy membership to define the magnitude gap (as discussed in Section 4.4.1), the same algorithm and parameters to determine the stellar masses, the same mass-richness technique to infer cluster masses, the same cluster masses in the overlap sample (to within errors), and the same algorithm to measure completeness criteria defining the underlying cluster samples in both $\mathrm{m_{gap}}$ and cluster mass. However, it is possible that there is still some systematic error that we have missed in the SDSS-C4 sample that is dominating the evolution in the slope. The best we can do is remove this dataset from our Bayesian analysis, even though it is the only available data set complete below $z < 0.10$, thus limiting our ability to track late time evolution in the SMHM relation. We list the inferred parameters without the SDSS-C4 data in Table 4.7.1. The parameters are within 1σ for α, β, σ_{int}, n_1, n_2, and n_4, while γ and n_3 are within 1.5σ. After dropping the SDSS-C4 data, we still find evolution in the slope, albeit at a slightly lower (as expected) statistical significance (99% versus 99.9% when including SDSS-C4.) Therefore, we conclude that while including the C4 data strengthens our detection, it is not responsible for it. We conduct a similar analysis by dropping the highest redshift cluster data (Line 5 of Table 4.7.1). We find the evolution at a slightly higher significance (99.98%). Thus, we argue that the significance of the detection in the evolution of the slope is fairly robust to the upper and lower ends of the redshift distribution of our data.

Additionally, as shown in the last column of Table 4.7.1, we also determine how are results are impacted by our choice to no longer apply the *von der Linden et al.* (2007) correction to our BCG magnitudes used to estimate stellar masses. To do this, we applied this correction to all data that fit the criteria described in *von der Linden et al.* (2007) and GM&M18 and corrected both the BCG stellar mass and magnitude for those clusters impacted. We find that the inclusion of the *von der Linden et al.* (2007) correction to the BCG magnitudes has a minimal impact on the parameters of the SMHM relation. The posterior distributions for each parameter are within 1σ for the data with and without the *von der Linden et al.* (2007) correction. A direct comparison is shown in Section 4.7.4.

Posterior Distribution Results

Data	z_{min}	z_{max}	z_{med}	$log_{10}(M_{halo}/(M_{\odot}/h))_{min}$	$n_{clusters}$	$\alpha(z{=}z_{med})$	$\beta(z{=}z_{med})$	$\gamma(z{=}z_{med})$	$\sigma_{int}(z{=}z_{med})$
GM&M18	0.030	0.151	0.086	14.0	236	3.13 ± 2.09	0.56 ± 0.15	0.173 ± 0.022	0.085 ± 0.024
SDSS-C4 Richness	0.030	0.146	0.081	14.0	142	-0.23 ± 0.05	0.52 ± 0.08	0.122 ± 0.019	0.098 ± 0.012
redMaPPer calibration	0.081	0.146	0.098	14.0	70	-0.40 ± 0.06	0.48 ± 0.13	0.190 ± 0.024	0.087 ± 0.017
redMaPPer	0.081	0.135	0.113	14.00	222	-0.38 ± 0.04	0.42 ± 0.05	0.182 ± 0.016	0.092 ± 0.009
redMaPPer	0.135	0.169	0.153	14.06	208	-0.34 ± 0.03	0.44 ± 0.05	0.168 ± 0.014	0.068 ± 0.009
redMaPPer	0.169	0.208	0.184	14.17	203	-0.29 ± 0.03	0.30 ± 0.06	0.131 ± 0.015	0.087 ± 0.008
redMaPPer	0.208	0.300	0.247	14.39	210	-0.34 ± 0.03	0.32 ± 0.06	0.150 ± 0.013	0.082 ± 0.009
Guo et al. (2011)	0.089	0.089	0.089	14.00	815	-0.34 ± 0.01	0.44 ± 0.02	0.226 ± 0.006	0.093 ± 0.002
Guo et al. (2011)	0.116	0.116	0.116	14.00	458	-0.37 ± 0.02	0.45 ± 0.02	0.230 ± 0.008	0.093 ± 0.003
Guo et al. (2011)	0.144	0.144	0.144	14.06	212	-0.36 ± 0.03	0.45 ± 0.03	0.229 ± 0.014	0.105 ± 0.005
Guo et al. (2011)	0.175	0.175	0.175	14.17	199	-0.32 ± 0.02	0.41 ± 0.04	0.207 ± 0.011	0.089 ± 0.005
Guo et al. (2011)	0.242	0.242	0.242	14.39	42	-0.33 ± 0.06	0.33 ± 0.08	0.224 ± 0.025	0.089 ± 0.011

Table 4.3: Binned SMHM Relation Posterior Results. The *Guo et al.* (2011) data has the same z_{min} and z_{max} because these are data analyzed at individual snapshots, not data from a lightcone.

4.7.2 Comparison to Simulations and Binned Results

Here, we compare the trends shown for the binned SDSS-redMaPPer clusters to those measured in the *Guo et al.* (2011) prescription of the MILLENNIUM simulation. The results for each of the measured parameters, α, β, γ, and σ_{int} are presented in Table 4.3. For a more accurate comparison, the *Guo et al.* (2011) measurements are taken on data samples described in Section 4.4.6. Due to the limits of the *Guo et al.* (2011) prescription, using the halo mass distribution functions from the SDSS-redMaPPer data significantly decreases the number of clusters, particularly in the higher redshift simulation boxes, resulting in larger posterior uncertainties. To illustrate the trends we observe in Tables 4.7.1 and 4.3, in Figures 4.5, 4.6, 4.7, and 4.8, we present the redshift evolution of the offset (α), slope (β), stretch factor (γ), and intrinsic scatter (σ_{int}) respectively given by the posterior distributions shown in Figure 4.4.

Figure 4.6 illustrates that our redshift dependent Bayesian MCMC model finds that the slope of the SMHM relation decreases with increasing redshift for the combined SDSS-C4 and SDSS-redMaPPer clusters. In contrast, Figures 4.5, 4.7, and 4.8 illustrate that using our Bayesian MCMC model, we observe either no or weak redshift evolution in the amplitude, in agreement with the results from *Zhang et al.* (2016),

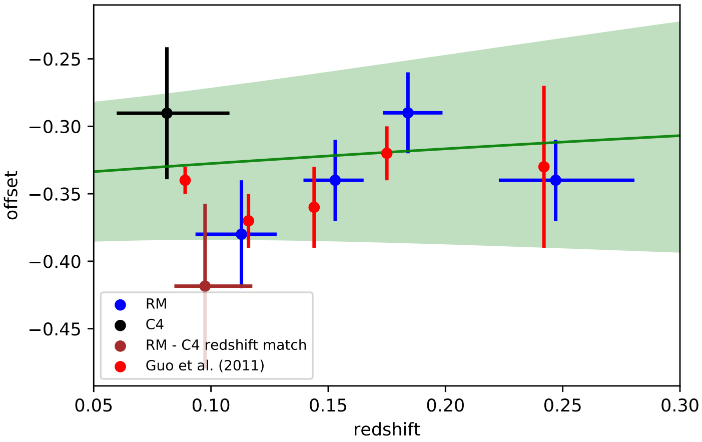

Figure 4.5: Redshift Evolution of α. The binned offsets and respective error bars are plotted as a function of redshift for the SDSS-redMaPPer binned and calibration samples, SDSS-C4 richness sample, and the *Guo et al.* (2011) prescription of the MILLENNIUM simulation. The green line represents the redshift evolution suggested from the posterior results presented in Figure 4.4. The green shaded region represents the combined total error from uncertainty on n_1 and α. This comparison highlights that the offset of the SMHM relation does not evolve over the redshift range $0.03 \leq z_{red} \leq 0.3$.

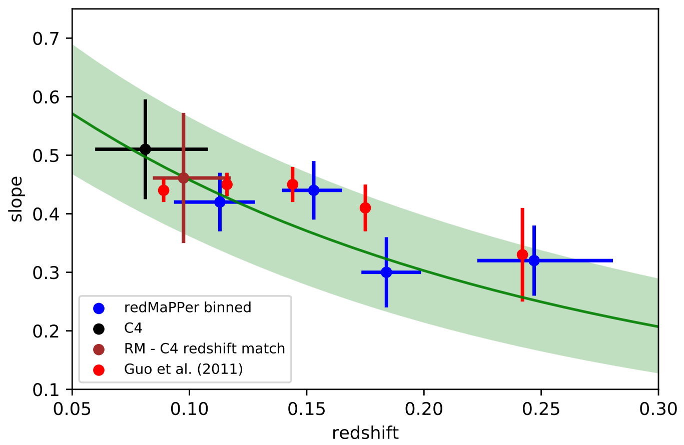

Figure 4.6: Redshift Evolution of β. The binned slopes and respective error bars are plotted as a function of redshift for SDSS-redMaPPer binned and calibration samples and the *Guo et al.* (2011) prescription of the MILLENNIUM simulation. The green line represents the redshift evolution suggested from the posterior results presented in Figure 4.4. The green shaded region represents the combined total error from uncertainty on n_2 and β. This comparison highlights that the slope of the SMHM relation evolves over the redshift range $0.03 \leq z_{red} \leq 0.3$.

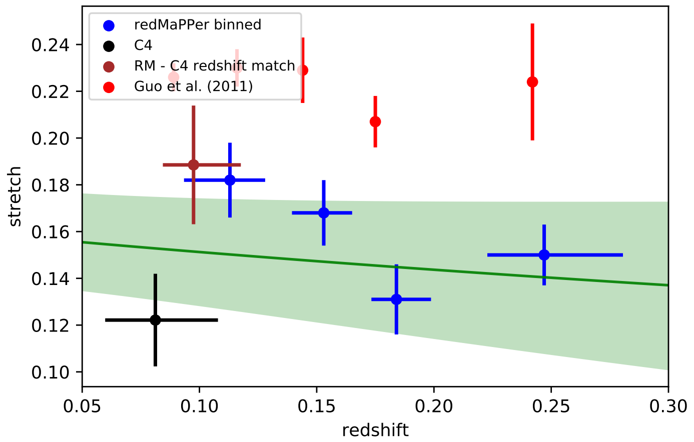

Figure 4.7: Redshift Evolution of γ. The binned stretch factors and respective error bars are plotted as a function of redshift for the SDSS-redMaPPer binned and calibration samples, SDSS-C4 richness sample, and *Guo et al.* (2011) prescription of the MILLENNIUM simulation. The green line represents the redshift evolution suggested from the posterior results presented in Figure 4.4. The green shaded region represents the total error incorporating both the uncertainty on n_3 and γ. This trend highlights that there is no redshift evolution in γ in this redshift range.

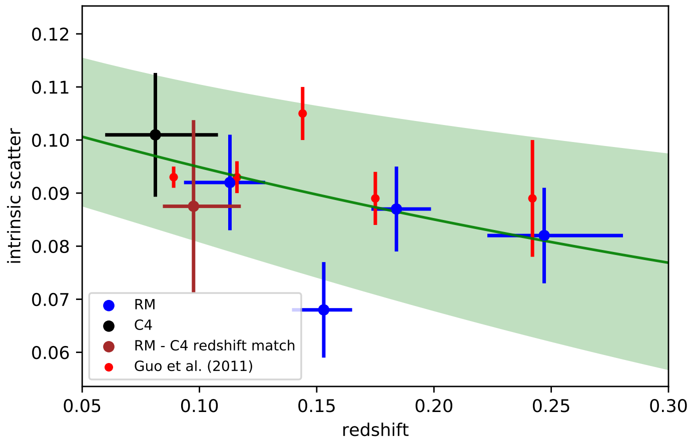

Figure 4.8: Redshift Evolution of σ_{int}. The binned intrinsic scatter and respective error bars are plotted as a function of redshift for the SDSS-redMaPPer binned and calibration samples and *Guo et al.* (2011) prescription of the MILLENNIUM simulation. The green line represents the redshift evolution suggested from the posterior results presented in Figure 4.4. The green shaded region represents the total error incorporating both the uncertainty on n_4 and σ_{int}. This trend highlights that there is weak redshift evolution in σ_{int}.

m_{gap} stretch parameter, and intrinsic scatter. Interestingly, the SDSS-redMaPPer data (blue points) for each of the four measured parameters and the *Guo et al.* (2011) MILLENNIUM simulation measurements show similar trends in how each parameter varies with redshift. Since the *Guo et al.* (2011) prescription of the MILLENNIUM simulation is modeled to look like the SDSS observational data, this is likely an artifact of the semi-analytic modeling. We discuss the meaning of these redshift evolution parameters in the context of hierarchical growth in Section 4.8.

4.7.3 Comparison to Golden-Marx & Miller 2018 results

The use of the richness-based masses compared to caustic-based masses reduces the uncertainties on the SMHM parameters, even for the smaller sample size. The offset α is different from the value presented in GM&M18 because we use a different method to estimate stellar mass, as discussed earlier, and have offset the axes by subtracting the median values of the stellar mass and halo mass. The slope (β) and the intrinsic scatter (σ_{int}) are statistically the same (within 1σ). The inferred stretch parameter γ is smaller (by $\sim 1.5\sigma$) in the richness-based SDSS-C4 SMHM relation, but still significantly non-zero. Therefore, the conclusions from GM&M18 hold when we switch to using richness-based masses for the SDSS-C4 sample. The measured posteriors for the entire SDSS-C4 richness sample (containing 142 clusters) can be found in Table 4.3 and agree with the posteriors for the calibration sample containing 128 clusters.

4.7.4 Impact of the *von der Linden et al.* (2007) Correction

Here we compare the impact of incorporating the *von der Linden et al.* (2007) correction on the BCG magnitudes or stellar masses to the results without such a correction. As such, Figures 4.9, 4.10, 4.11, and 4.12 compare the posterior distributions using the data without the *von der Linden et al.* (2007) correction (in green), which are the same as the results presented in Section 4.7.2, to the posterior distributions determined using the *von der Linden et al.* (2007) correction (shown in black). For α, β, and γ, as shown in Figures 4.9, 4.10, and 4.12, the posterior distributions are in excellent agreement with one another. For γ, we see that the median value is slightly larger when the *von der Linden et al.* (2007) correction is applied, which follows since we are increase the stellar mass and magnitude gap for a subset of the data; however, these posteriors are still within 1σ (see Figure 4.11. Additionally, we note that the lower-redshift offset for the two posterior distributions for α likely result because the median stellar mass is higher when we apply the *von der Linden et al.* (2007) correction.

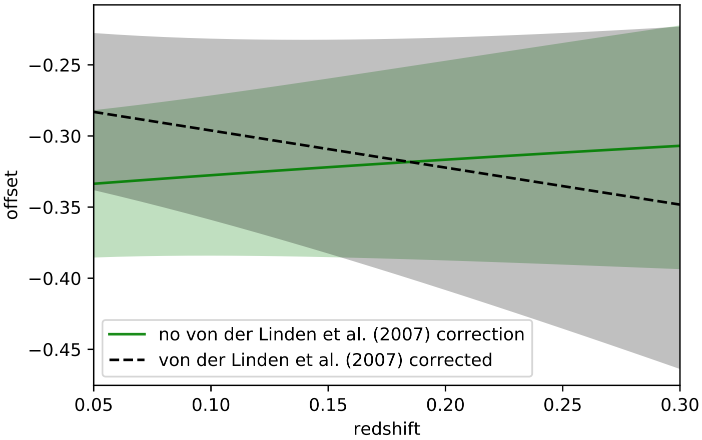

Figure 4.9: Impact of the *von der Linden et al.* (2007) Correction on the Redshift Evolution of α. The green line represents the redshift evolution suggested from the posterior results presented in Figure 4.4. The green shaded region represents the combined total error from uncertainty on n_1 and α. The black line represents the redshift evolution suggested by the posterior when the *von der Linden et al.* (2007) correction is applied and the black shaded region represents the combined total error. This comparison highlights that at there is no change in the offset as a result of the *von der Linden et al.* (2007) correction over this redshift range.

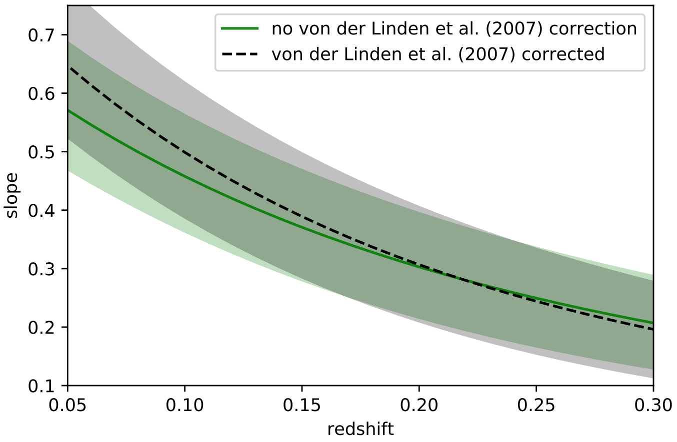

Figure 4.10: Impact of the *von der Linden et al.* (2007) Correction on the Redshift Evolution of β. The green line represents the redshift evolution suggested from the posterior results presented in Figure 4.4. The green shaded region represents the combined total error from uncertainty on n_2 and β. The black line represents the redshift evolution suggested by the posterior measured when the *von der Linden et al.* (2007) correction is applied and the black shaded region represents the total combined uncertainty for this data. This comparison highlights that the *von der Linden et al.* (2007) correction has no impact on the measured slope over this redshift range.

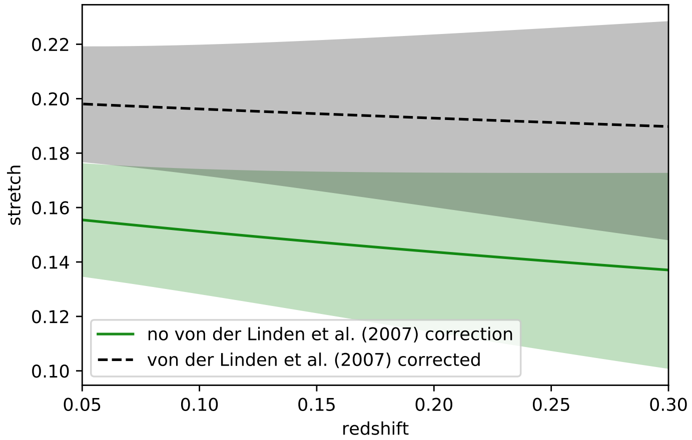

Figure 4.11: The Impact of the *von der Linden et al.* (2007) Correction on the Redshift Evolution of γ. The green line represents the redshift evolution suggested from the posterior results presented in Figure 4.4. The green shaded region represents the total error incorporating both the uncertainty on n_3 and γ. The black line represents the redshift evolution suggested from the posterior results measured when the *von der Linden et al.* (2007) correction is used and the black shaded region represents the combined uncertainty. This figure highlights that using the *von der Linden et al.* (2007) correction slightly increases γ, which follows since stellar mass and $\mathrm{m_{gap}}$ increase for a subset of the sample. However, despite this increases, the values are still within 1σ.

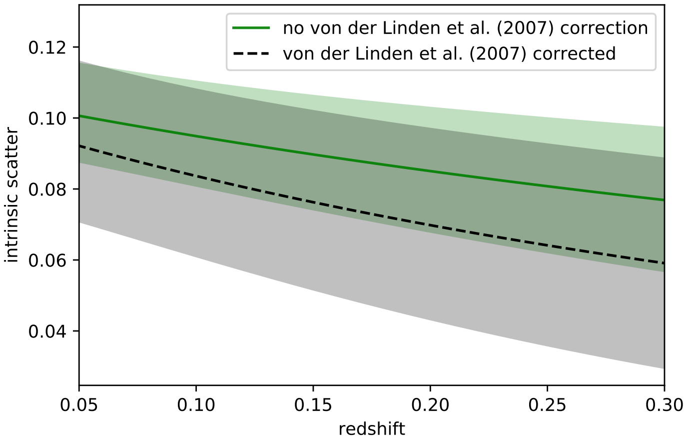

Figure 4.12: The Impact of the *von der Linden et al.* (2007) Correction on the Redshift Evolution of σ_{int}. The green line represents the redshift evolution suggested from the posterior results presented in Figure 4.4. The green shaded region represents the total error incorporating both the uncertainty on n_4 and σ_{int}. The black line reprsents the redshift evolution suggested by the posterior distribution which accounts for the *von der Linden et al.* (2007) correction and the black shaded region represents the 1σ uncertainty. This figure highlights that the *von der Linden et al.* (2007) correction has no impact on σ_{int}.

4.8 Discussion

The change of the SMHM relation's slope and σ_{int} can tell us about central galaxy hierarchical growth. In semi-analytic models, some researchers find stellar mass growth in BCGs at late times. Between the redshift range $z = 0.5$ and $z = 0.0$, *De Lucia and Blaizot* (2007) find that BCG stellar mass increases by a factor of 2, *Shankar et al.* (2015) find a growth factor of 1.5, and *Guo et al.* (2011) measure an increase in stellar mass by a factor of 1.9. The effect of BCG growth in *Guo et al.* (2011) can be seen on the slope of the SMHM in Figure 4.6, which decreases by $\sim$ 30% out to $z = 0.3$.

In this work, we extended our study of the cluster-scale SMHM relation to $z_{red} = 0.3$. By incorporating the stretch parameter and $\mathrm{m_{gap}}$ we reduce σ_{int} and the uncertainty on the slope in the SMHM relation allowing us to observe redshift evolution. As shown in Table 4.7.1, when $\mathrm{m_{gap}}$ information is not incorporated, we measure a much weaker redshift evolution parameter, n_2, for the slope. Instead of a $> 3.5\sigma$ detection, we measure a $< 1.5\sigma$ detection for n_2 if the C4 data is included and no detection when it is not. Therefore, it is only when incorporating $\mathrm{m_{gap}}$, that we see that the slope of the SMHM relation evolves over the redshift range $0.03 \leq z \leq 0.3$. Thus, environment strongly impacts the SMHM relation.

One can interpret the observed redshift evolution in the SMHM relation's slope in the context of results from *Gu et al.* (2016). When BCG's grow hierarchically, their stellar mass increases due to major and minor mergers. *Gu et al.* (2016) suggest that the steepening of the slope is related to σ_{int}, such that an increase in the σ_{int} corresponds to an increase in the slope and that the slope and σ_{int} are tied to the progenitor history of the BCG such that a wider range of progenitor galaxies yield a steeper slope and a larger σ_{int}. Additionally, a steeper SMHM relation results from a growth history where minor mergers dominate over major mergers. Moreover, the late time evolution in the slope we observe suggests that the BCGs residing in more massive halos undergo a greater growth over this period of time than those in less massive halos, which may result from differences in the galactic populations of high and low mass cluster halos.

In Figure 4.6, the *Guo et al.* (2011) SAMs show a similar decrease in the slope over the redshift range $0.03 \leq z \leq 0.3$. The similarity in this trend between the observations and simulations is interesting because other observational studies do not find a similar result (*Oliva-Altamirano et al.*, 2014; *Gozaliasl et al.*, 2016). This discrepancy was previously justified because the continued growth in simulations is in the stellar mass of BCG cores and not in the outer portion of BCG envelopes, the ICL (*Zhang et al.*, 2016), as is observed (*van Dokkum et al.*, 2010; *Burke et al.*, 2015). However, by comparing the stellar masses measured within a radial extent of 100kpc, we are not analyzing just the inner profile of the BCG, which is relatively constant over this redshift range (*van Dokkum et al.*, 2010), instead we are incorporating much of the radial regimes which have been previously treated as ICL. Therefore, the novelty of our detected evolution over the redshift range $0.03 < z < 0.30$ likely results from our choice to measure the BCG stellar mass within a large radial extent, which incorporates the radial regions where BCGs actively grow, and the incorporation of $\mathrm{m_{gap}}$, as previously discussed.

Our results also allow us to comment on the absence of a trend in the evolution of the $\mathrm{m_{gap}}$ stretch parameter over this redshift range, as shown in Figure 4.7. This can be interpreted as meaning that with respect to stellar mass, $\mathrm{m_{gap}}$ is constant. The lack of redshift evolution of γ in our data is expected because even though $\mathrm{m_{gap}}$ and stellar mass growth are correlated, since our stellar mass measurement accounts for the outer portion of the BCG, it likely accounts for any recent merger material which may change either $\mathrm{m_{gap}}$ or the stellar mass. If γ were to decrease with redshift, it means that as we move forward in time, $\mathrm{m_{gap}}$ increases with respect to the stellar mass. This would occur if the BCGs were to have mergers with brighter galaxies in the given redshift range and the resulting additional mass were to go predominately to stellar mass located in the outer envelope of these BCGs (in our case at radii greater than 100kpc). However, while stellar material from a merger is ejected into the ICL, major mergers involving the brightest galaxies are not common for BCGs in this redshift range (*Burke et al.*, 2015).

Since the growth in $\mathrm{m_{gap}}$ depends on BCG growth (*Solanes et al.*, 2016), our results suggest that $\mathrm{m_{gap}}$ values for BCGs at $z \approx 1$ would be much lower (although γ may not change). Furthermore, if in fact both stellar mass and $\mathrm{m_{gap}}$ continue to decrease at these higher redshifts, in agreement with hierarchical growth, then we may be able to enhance this analysis and better constrain the redshift evolution of the parameters of our SMHM relation if we extend our analysis out to redshifts of $z \geq 0.5$. This can be tested in simulations using current SAMs which follow the growth history of the BCG (e.g., *Guo et al.*, 2011), where SAMs have better agreement with observations (e.g., *Lidman et al.*, 2012; *Lin et al.*, 2013).

The observational challenge of extending our analysis of the SMHM-$\mathrm{m_{gap}}$ relation out to higher redshifts is to acquire good spectroscopic coverage for each cluster, again understand the additional systematic errors which increase the error associated with the photometric data used in each of the observed measurements in our SMHM relation, as well as to have deep enough photometry to measure the BCG light profiles out to large radial extents.

CHAPTER V

The Impact of Environment on Late Time Evolution of the Stellar Mass - Halo Mass Relation in the Dark Energy Survey

The results presented in this chapter are currently in prepartion for: ***Golden-Marx, Jesse B.****, Miller, Christopher J., & Zhang, Yuanyuan 2019. The Impact of Environment on the Late Time Evolution of the Stellar Mass-Halo Mass Relation in the Dark Energy Survey. However, I note that this paper is still very much a work in progress and the discussion and conclusions are currently in preliminary stages.*

5.1 Abstract

At fixed halo mass, galaxy clusters hosting galactic populations characterized by larger differences between the brightest central galaxy (BCG) and fourth brightest cluster member ($\mathrm{m_{gap}}$), have higher BCG stellar masses. Recent studies show $\mathrm{m_{gap}}$ is a latent parameter in the cluster stellar mass - halo mass (SMHM) relation, and incorporating this parameter yields more precise measurements of amplitude, slope, and intrinsic scatter of the SMHM relation, and also allows for detection of late time redshift evolution of the SMHM relation's slope. We use galaxy clusters from the Sloan Digital Sky Survey along with those observed as part of the Dark Energy Survey Year 3 to measure how the SMHM-$\mathrm{m_{gap}}$ relation evolves out to $z = 0.6$. By defining a central galaxy's stellar mass using a fixed comoving aperture of 100kpc, we report statistically significant negative evolution in the slope of the SMHM

relation to $z = 0.6$ ($> 3.0\sigma$) along with weaker evolution in the other parameters of the SMHM relation. The steepening of the slope, as well as the increase in both the magnitude gap stretch parameter, γ, and intrinsic scatter over the last 6 Gyrs likely result from late-time merger activity at the centers of galaxy clusters.

5.2 Introduction

The stellar mass - halo mass (SMHM) relation is one of the primary mechanisms that quantifies the galaxy-dark matter halo connection. For galaxy clusters ($log_{10}(M_{halo} /(M_{\odot}/h)) \geq 14.0$), this linear correlation compares the stellar mass of the brightest central galaxy (BCG) to the total halo cluster mass, which includes the dark matter. The parameters measured as part of the SMHM relation are often used to constrain galaxy formation models; the amplitude, α, constrains AGN feedback in central galaxies (*Kravtsov et al.*, 2018) and the intrinsic scatter in stellar mass at fixed halo mass (σ_{int}) constrains processes responsible for quenching star formation in BCGs (*Tinker*, 2017) and characterizing dark matter halo assembly (*Gu et al.*, 2016). Additionally, the redshift evolution of the slope, β, and σ_{int} provide insight into how BCGs grow/evolve over cosmic time (*Gu et al.*, 2016; *Golden-Marx and Miller*, 2019).

BCGs, the stellar mass portion of the cluster-scale SMHM relation, are massive, radially extended, elliptical galaxies, that emit a significant fraction of the total light within their host cluster (*Schombert*, 1986; *Jones et al.*, 2000; *Lin and Mohr*, 2004; *Bernardi et al.*, 2007; *Lauer et al.*, 2007; *von der Linden et al.*, 2007; *Aguerri et al.*, 2011; *Brough et al.*, 2011; *Proctor et al.*, 2011; *Harrison et al.*, 2012). BCG's are located near the cluster's X-ray center, which along with their hierarchical formation lead to correlations between BCG properties and those of the host cluster (*Jones and Forman*, 1984; *Rhee and Latour*, 1991; *Lin and Mohr*, 2004; *Lauer et al.*, 2014). BCG's are also surrounded by diffuse halos of intra-cluster light (ICL; *Zwicky*, 1933, 1951), which are observed to extend radially as far out as ≈1Mpc from the center of the BCG (*Zhang et al.*, 2018), and form as a result of BCG hierarchical growth (*Murante et al.*, 2007).

BCG's grow "inside-out" (*van Dokkum et al.*, 2010), following a two-phase formation scenario (*Oser et al.*, 2010) where at high redshifts ($z > 2$) a dense core forms via in-situ star formation, after which, the outer envelope grows hierarchically via major/minor mergers, which occur as a result of the dark matter halo's hierarchical assembly (*White and Rees*, 1978; *De Lucia and Blaizot*, 2007). The two-phase formation model is supported by both observations (*van Dokkum et al.*, 2010; *Huang et al.*, 2018) and dark matter only cosmological simulations which use empirical or semi-analytic models to quantify central galaxy stellar mass growth (e.g., *Croton et al.*, 2006; *De Lucia and Blaizot*, 2007; *Guo et al.*, 2011; *Tonini et al.*, 2012; *Shankar et al.*, 2015).

As a result of "inside-out" growth, all information about recent BCG stellar mass growth is contained in the BCG's outer envelope/ICL (*Oser et al.*, 2010; *van Dokkum et al.*, 2010). Moreover, recent observations suggest that the majority of the BCG's stellar mass is within 100kpc (*Huang et al.*, 2018), and that 100kpc may represent a transitional regime between the BCG's outer envelope and the ICL (*Zhang et al.*, 2018). Therefore, when characterizing BCG evolution associated with the parameters of the SMHM relation, it is vital to measure BCG photometry within large radial extents, as discussed in *Golden-Marx and Miller* (2019), referred to as GM&M19. More specifically, including stellar mass within large radii strengthens the correlation between BCG stellar mass and halo mass (*Moster et al.*, 2018; *Golden-Marx and Miller*, 2019).

One observational measurement inherently tied to BCG hierarchical growth is the magnitude gap (m_{gap}), the difference in r-band magnitude between the BCG and 4th (M14) brightest cluster member within half the radius enclosing 200x the critical density of the Universe (R_{200}) (*Dariush et al.*, 2010). We use M14 in this analysis because it correlates best with early formation (*Dariush et al.*, 2010). Using N-body simulations, *Solanes et al.* (2016) find that BCG stellar mass linearly increases with the number of progenitor galaxies. Since the BCG's central location leads to faster merger growth than that of non-central galaxies, as BCG's grow hierarchically, their stellar mass and magnitude increase, while those of the 4th brightest remain the same, increasing $\mathrm{m}_{\mathrm{gap}}$. Thus, hierarchical growth leads to a correlation between $\mathrm{m}_{\mathrm{gap}}$ and BCG stellar mass (*Harrison et al.*, 2012; *Golden-Marx and*

Miller, 2018). Therefore, it follows that $\mathrm{m_{gap}}$ is a latent parameter in the cluster SMHM relation, as shown by *Golden-Marx and Miller* (2018), which from here on is referred to as GM&M18.

GM&M18 incorporate $\mathrm{m_{gap}}$ into the cluster SMHM relation by adjusting Equation 5.1

$$\log_{10}(M_*) = \alpha + \beta\log_{10}(M_{halo}), \tag{5.1}$$

to Equation 5.2

$$\log_{10}(M_*) = \alpha + \beta\log_{10}(M_{halo}) + \gamma M14, \tag{5.2}$$

where α is the offset, β is the slope, and γ is the $\mathrm{m_{gap}}$ stretch parameter. In GM&M18, these parameters are measured using a hierarchical Bayesian MCMC analysis for the SDSS-C4 cluster sample (*Miller et al.*, 2005) with individually measured caustic halo masses (*Gifford et al.*, 2013). Using Equation 5.2 for the SMHM relation reduces σ_{int} to less than 0.1dex as well as the uncertainties on measured parameters for the SMHM relation (GM&M18).

The late time evolution of BCG's is dominated by hierarchical growth. Therefore, β may change with redshift since at earlier times fewer mergers will have occurred resulting in a lower BCG stellar mass. However, dark matter halos also assemble hierarchically, so the average halo mass decreases over time as well (*White and Rees*, 1978; *Springel et al.*, 2005; *De Lucia and Blaizot*, 2007), making the evolution of the SMHM relation unclear. The redshift evolution of the SMHM relation has been investigated using observations, empirical models, and simulations. Many prior observations (*Oliva-Altamirano et al.*, 2014; *Gozaliasl et al.*, 2016) were unable to constrain the SMHM relation's late time redshift evolution due to large uncertainties on β. However, GM&M19 place the first statistically significant observational constraints on the redshift evolution of the SMHM relation (discussed in more depth in Section 5.3) by incorporating m_{gap} and redshift evolution into the SMHM relation using Equation 5.3,

$$\log_{10}(M_*) = \alpha(1+z)^{n_1} + \beta\log_{10}(M_{halo})(1+z)^{n_2} + \gamma M14(1+z)^{n_3}, \tag{5.3}$$

where the n parameters are redshift evolution parameters. GM&M19 find that over the redshift range $0.03 < z < 0.30$, using SDSS-C4 (*Miller et al.*, 2005) and SDSS-redMaPPer (*Rykoff et al.*, 2014) clusters, the slope of the SMHM relation decreases by ≈0.20dex or 40%. Using empirical models with abundance matching techniques to infer halo masses, *Behroozi et al.* (2013a) and *Moster et al.* (2013) find that the slope decreases by 40-50% from z=0.0 to z=1.0. *Moster et al.* (2013) also detect moderate evolution out to z=0.5, similar to GM&M19. In contrast, *Pillepich et al.* (2018), using the Illustris TNG300 cosmological hydrodynamical simulation, measure little change in the slope between z=0.0 and z=1.0. In addition to the slope, the redshift evolution of σ_{int} has also been investigated using hydrodynamical simulations (*Matthee et al.*, 2017; *Pillepich et al.*, 2018), N-body simulations (*Gu et al.*, 2016), empirical models (*Behroozi et al.*, 2018; *Moster et al.*, 2018), and observations (GM&M19). However, these results are inconsistent, likely because of differences in how stellar masses (i.e., within what aperture) and halo masses as well as the associated uncertainties are estimated in each approach.

As previously described, including $\mathrm{m_{gap}}$ in the SMHM relation improves the precision of our measured parameters in the SMHM relation. Moreover, redshift evolution in β is only detected when m_{gap} is incorporated (GM&M19), further highlighting the importance of using Equation 5.2. Although no significant redshift evolution is detected in GM&M19, other parameters, such as γ may still evolve, which would inform us about BCG merger history and the fraction of stellar material ejected into the ICL via major/minor mergers. Since each parameter measures different characteristics of BCG formation, and may operate on different time scales, it is important to study how these parameters continue to evolve as well.

The outline for the remainder of this paper is as follows. In Section 5.3, we summarize the goals, methods, and results of GM&M18 and GM&M19. In Section 5.4, we discuss the observational and simulated data used to measure stellar masses, halo masses, and $\mathrm{m_{gap}}$ values for our SMHM relation. In Section 5.5, we describe the hierarchical Bayesian MCMC model used to evaluate the redshift evolution of the SMHM relation. In Section 5.6, we describe how we use the overlap between SDSS-redMaPPer and DES-redMaPPer to calibrate our higher-redshift measurements and the observational uncertainties associated with the DES data. In Section 5.7, we present our results. In Section 5.8 we discuss our findings and conclude.

Except for the case of simulated data, in which the cosmological parameters are previously defined (*Springel et al.*, 2005), for our analysis, we assume a flat ΛCDM universe, with Ω_M=0.30, Ω_Λ=0.70, H=100 h km/s/Mpc with h=0.7.

5.3 Summary of Golden-Marx & Miller 2018 and Golden-Marx & Miller 2019

The analysis presented in this paper builds on on GM&19, thus, we briefly summarize those results here. Since GM&M19 also relies on results from GM&M18, we first summarize those. Using the low redshift SDSS-C4 clusters (*Miller et al.*, 2005) with individual caustic halo masses (*Gifford et al.*, 2013) and stellar masses estimated using *von der Linden et al.* (2007) corrected Petrosian magnitudes, GM&M18 identify a stratification between stellar mass and m_{gap} such that at fixed halo mass, stellar mass and m_{gap} linearly correlate. Based on this trend, GM&M18 incorporate m_{gap} into the SMHM relation using Equation 5.2. GM&M18 also develop a hierarchical Bayesian framework, similar to the one described in Section 5.5, and find γ is definitively non-zero and σ_{int} decreases to less than 0.1dex. Moreover, incorporating m_{gap} explains the discrepancy between the amplitudes of previously published SMHM relations.

GM&M19 study the redshift evolution of the SMHM-m_{gap} relation (Equation 5.2) using the low-redshift SDSS-C4 sample from GM&M18 combined with the SDSS-redMaPPer sample (*Rykoff et al.*, 2014), which in total cover $0.03 < z < 0.30$. Since, the redMaPPer algorithm provides a membership criterion (P_{mem}) for each galaxy (*Rykoff et al.*, 2014), based on a comparison of the galactic populations for clusters identified in both the SDSS-redMaPPer and SDSS-C4 samples, our final sample of clusters require 4 member galaxies (including the BCG) with $P_{mem} > 0.984$ within $0.5R_{200}$. m_{gap} is then the difference in the r-band model magnitudes of the BCG and 4th brightest cluster member. To estimate stellar mass, we use g-, r-, and i-band magnitudes measured within 100kpc and SED fitting via EzGal (*Mancone and Gonzalez*, 2012), as done here. Halo masses for both samples are then estimated using a mass-richness relation. Using this higher redshift data, we find that the stratification observed in GM&M18 persists out to higher redshifts. This trend is also found in the *Guo et al.* (2011) semi-analytic prescription of the MILLENNIUM simulation at higher redshifts.

To quantitatively measure the redshift evolution of the SMHM relation, we use a hierarchical Bayesian MCMC model, nearly identical to the model presented in Section 5.5, which relies on Equation 5.7. We remind the reader that our Bayesian MCMC model is designed to measure the underlying or intrinsic SMHM-M14 relation parameters and their redshift evolution while accounting for the uncertainty in the stellar mass, halo mass, and m_{gap} estimates. As shown in GM&M18, using the *Henriques et al.* (2012) lightcone, our Bayesian infrastructure recovers the intrinsic SMHM relation parameters using projected data.

The primary result of GM&M19 is that for the first time using purely observational data, statistically significant late-time redshift evolution in β is measured. We find that n_2, the redshift evolution parameter associated with β (see Equation 5.3), is $3.5\sigma < 0.0$. This detection suggests that in the last 3.5 billion years, BCGs, when treated as a statistical sample, continue to grow hierarchically, likely via minor mergers. The second primary result of GM&M19 is that β increases as the radius within which the BCG's stellar mass is measured increases until asymptoting around 100kpc, signifying that the outer region of the BCG is more tightly correlated with the underlying dark matter halo than the central region, which follows from the two-phase formation scenario (*Oser et al.*, 2010). Additionally, we measure a steeper β when m_{gap} is incorporated.

5.4 Dark Energy Survey Data

The new observational data used in this analysis comes from redMaPPer (*Rykoff et al.*, 2014, 2016) v6.4.22 run on Year 3 data from the Dark Energy Survey (DES), which covers the redshift range $0.20 < z < 0.60$. Additionally, we use the same lower-redshift SDSS DR12 (*Alam et al.*, 2015) data from from the SDSS-redMaPPer v6.3 catalog (*Rykoff et al.*, 2014) and the SDSS-C4 (*Miller et al.*, 2005) cluster sample, which combine to cover the redshift range $0.03 < z < 0.30$. Since we study the redshift evolution of the SMHM relation, we include both SDSS and DES data to maximize the total redshift coverage. Therefore, it is necessary to measure m_{gap} values, BCG stellar masses, and halo masses in both SDSS-C4/redMaPPer and DES-redMaPPer data in a homogeneous manner. The uncertainties associated with each measurement are discussed in Section 5.6.

5.4.1 DES-redMaPPer m_{gap}

The redMaPPer algorithm uses galaxy color, spatial overdensity, and galaxy luminosity distribution to identify galaxy clusters. Simply put, redMaPPer is a red-sequence-based photometric cluster finding algorithm that is constructed using spectroscopically confirmed clusters. For each cluster, redMaPPer assigns every galaxy a membership probability, P_{mem}, which is dependent on the cluster's richness, density profile, and the background density (*Rykoff et al.*, 2014, 2016). The high-probability members are then used to estimate the cluster's photometric redshift, which is used in Equation 5.7. redMaPPer also provides a central galaxy probability for the five most likely BCG candidates and we identify the BCG as the most probable.

In GM&M19, we found that to match the red sequence membership for SDSS-C4 clusters, which rely on 6 SDSS colors (GM&M18), we require all member galaxies have $P_{mem} > 0.984$. Since we homogeneously measure m_{gap} values across our entire sample, we use that same criteria here. Additionally, for our final sample, we require all clusters have 4 or more members within 0.5 R_{200}, which we approximate using Equation 5.4 (*Rykoff et al.*, 2014; *McClintock et al.*, 2019):

$$R_{200} \approx 1.5 R_c(\lambda) \tag{5.4}$$

where λ is the redMaPPer richness, and R_c is the redMaPPer cutoff radius, given by Equation 5.5:

$$R_c(\lambda) = 1.0h^{-1}Mpc(\lambda/100)^{0.2}. \tag{5.5}$$

Thus, like in GM&M19, M14 is the difference in the r-band model magnitude of the BCG and 4th brightest cluster member with P_{mem} >0.984. Using a sample of 61 clusters in both our SDSS and DES-redMaPPer samples in the redshift range $0.20 < z < 0.30$, we get good agreement in the measured m$_{gap}$ values.

5.4.2 DES BCG photometry

In GM&M19, we found that the slope of the SMHM relation increases as the radius within which the BCG's stellar mass and photometry is measured increases, reaching an asymptote value near a radius of 100kpc. Since SDSS provides radial light profiles for every galaxy, we can measure 100kpc photometry. To homogeneously measure BCG stellar mass, we must measure BCG stellar masses within 100kpc for our DES BCGs. However, DES does not provide radial light profiles. Therefore, we follow the procedure described in *Zhang et al.* (2018), originally designed to study the ICL surrounding DES BCGs, to measure the BCG light profiles within 100kpc. Here, I briefly summarize the relevant methodology from *Zhang et al.* (2018).

Using the RA, Dec, and redshift of each BCG, in our subset of DES-redMaPPer clusters, we coadd and stack all DES photometry within 0.15° from the BCG. The coadded images, along with a list of all objects in the DES coadd catalog, which reaches a 10σ completeness limit at an i-band magnitude of 22.5 (*Zhang et al.*, 2018), allow us to mask all objects brighter than 30.0 magnitudes in the i-band, excluding the BCG, using a masking radius of 2.5R$_{kron}$. This masking magnitude limit was selected to minimize the difference between the photometry of BCGs observed as part of both SDSS and DES as well as the stellar mass estimate for the BCGs observed in both surveys. The masking procedure removes the majority of excess light associated with the neighboring galaxies, yielding a cleaner measurement of the radial light profile centered on the BCG, which includes the ICL as well. We then measure the BCG's radial light profile in annuli excluding the masked area.

Thus, we assume the BCG's light profile is spherically symmetric when we integrate over the annuli out to 100kpc. For each profile, the background is determined by taking the median value of the radial region beyond 500kpc from the BCG. This process is repeated for each of the DES griz-bands [1]. Additionally, we note that the SDSS griz and DES griz wave bands differ. Using the 61 BCGs in both DES and SDSS-redMaPPer we find that when the SDSS griz magnitudes are converted to DES griz magnitudes, the colors and magnitudes are within 1σ of one another, illustrating that we homogeneously measure BCG photometry across two completely different surveys over the redshift range $0.03 < z < 0.60$.

5.4.2.1 DES BCG Stellar Masses

To calculate BCG stellar masses, we follow the same procedure as in GM&M19, summarized here. We use SED fitting done in EzGal (*Mancone and Gonzalez*, 2012), an SED modeling software, to estimate stellar mass. For our SED, we assume a *Bruzual and Charlot* (2003) stellar population synthesis model, a *Salpeter* (1955) IMF, a formation redshift of $z = 4.9$, and a constant metallicity of 0.4 $z_{\odot}$. To determine the best fit SED, we use a Bayesian MCMC approach, done in emcee (*Foreman-Mackey et al.*, 2013), where we treat the absolute magnitude (the EzGal normalization parameter) as a free parameter, with a uniform prior, to determine the value that minimizes the chi-squared statistic between the EzGal modelled g, r, and i-band magnitudes measured at the observed redshift and the DES 100kpc g-, r-, and i-band magnitudes. In GM&M19, we found that $> 99\%$ of clusters have a minimized chi squared using a metallicity of 0.4 $z_{\odot}$, so here we keep metallicity fixed. Using this approach, we find excellent agreement between stellar masses estimated for clusters with both DES and SDSS photometry. Additionally, due to the trends found between photometric color and redshift, for clusters located at $z > 0.4$, we use DES r-, i-, and z-band photometry to estimate stellar mass. We note that this results in a slight change in the stellar mass measurements, but that the values calculated using gri photometry and riz photometry are within errors.

---

[1] Since GM&M19 only use SDSS gri band photometry to maintain homogeneity in our stellar mass measurement, for our calibration we use DES gri band photometry

5.4.3 DES Halo Masses

To determine halo masses for DES-redMaPPer clusters, we use a mass-richness relation, like in GM&M19. However, here we use the mass-richness relation from *McClintock et al.* (2019), which is calibrated for the DES Year 1 redMaPPer data, given by Equation 5.6,

$$M_{halo}/(h^{-1}M_{\odot}) = 10^{14.334}(\lambda/40)^{1.356}(\frac{1+z_{red}}{1+0.35})^{-0.30} \tag{5.6}$$

where z_{red} is the redMaPPer photometric redshift. We note that using the sample of clusters in both DES and SDSS-redMaPPer catalogs, we find excellent agreement for the richness measurements as well as the halo masses estimated with either the *Simet et al.* (2017) (used in GM&M19) or *McClintock et al.* (2019) mass-richness relations, which is unsurprising since these two mass-richness relations are in agreement once scaled to the same units. The only difference between the two is the small redshift evolution parameter in the *McClintock et al.* (2019) mass-richness relation.

5.4.4 DES Final Sample

We analyze how the SMHM relation evolves with redshift using two approaches. We first divide all of our data, including the SDSS-C4, SDSS-redMaPPer, and DES-redMaPPer data, into 4 bins and measure our Bayesian MCMC posteriors for each bin with redshift evolution parameters set to 0.0. Second, we incorporate redshift evolution using four additional parameters in Equation 5.7 and fit over all SDSS-C4, SDSS-redMaPPer, and DES-redMaPPer clusters. We note that we include all clusters, considered in GM&M19, not just those in the final sample (i.e., we include those galaxies that were previously removed as a result of our completeness analyses, since these analyses are redone here). In total, this multi-survey data set covers the redshift range $0.03 \leq z \leq 0.60$.

Following these criteria, there are 154 SDSS-C4 clusters, 984 SDSS-redMaPPer clusters, and 1577 DES-redMaPPer clusters with halo masses greater than $10^{14}M_{\odot}$, or a total sample of 2715 clusters. At this point, we have not applied any further halo mass limit; however, as in GM&M19, we expect this total sample of data to have differing halo mass lower limits as we move to higher redshift ranges. We also check for m_{gap} incompleteness since DES is a flux-limited survey.

Therefore, the DES-redMaPPer sample is divided into 4 redshift bins, each initially with ~ 679 clusters. For each bin, as in GM&M18 and GM&M19, we apply a m_{gap} completeness criteria based on the binning of the BCG and 4th brightest galaxy's absolute magnitudes against the BCG's apparent magnitude and $\mathrm{m}_{\mathrm{gap}}$ to determine the apparent magnitude limit of the sample (a redshift dependent limit) (*Colless*, 1989; *Garilli et al.*, 1999; *La Barbera et al.*, 2010; *Trevisan et al.*, 2017; *Golden-Marx and Miller*, 2018).

We account for halo mass incompleteness in each redshift bin in the same manner as in GM&M19. Since the halo mass distribution can be approximated as Gaussian, the peak indicates the mass that the sample becomes incomplete. However, we apply a lower halo mass cut located at the halo mass where the amplitude of the binned halo mass distribution decreases to 70% of the peak value to ensure high completeness out to higher redshifts. This halo mass criteria is conservative and results in a redMaPPer richness threshold of ≈ 22, well above the detection limit. However, when combined with the m_{gap} completeness analysis, these cuts shrink our available sample down to 2319 clusters, a reduction of $\sim 14.5\%$. A slightly more restrictive (higher) halo mass lower limit does not impact our final results.

5.4.5 Simulated Data

Just as in GM&M19, we also study the evolution of the SMHM - $\mathrm{m}_{\mathrm{gap}}$ relation using the *Guo et al.* (2011) semi-analytic model for the MILLENNIUM simulation. We use the *Guo et al.* (2011) simulation boxes analyzed at redshifts of 0.116, 0.208, 0.320, and 0.508, the redshifts which best match the median values of our binned sample and are snapshots number 58, 55, 52, and 48, respectively.

For each simulation box, we use the 3D information provided directly from the *Guo et al.* (2011) semi-analytic model for each cluster, including the halo masses, measured within $R_{200} \times \rho_{crit}$; the galaxy positions, x, y, z; R_{200}; the semi-analytic stellar masses; and the magnitudes. Cluster membership is determined using positional information (x, y, z) and a fit to the red sequence, such that cluster member candidates within 0.5 R_{200}, and within 2σ from the red sequence are identified as members. Thus, M14 is the difference between the 4th brightest member and BCG in the r-band. Since *Guo et al.* (2011) provides BCG stellar masses and we have access to the entire simulation box, we do not apply a completeness criteria to our simulated data. However, to make our samples comparable, we apply the halo mass distribution functions based on our binned SDSS, and DES clusters to the simulation snapshot at the corresponding redshift.

5.5 Bayesian MCMC model

We use a nearly identical hierarchical Bayesian MCMC model described in GM&M19 to determine the values of α, β, γ, σ_{int}, and the redshift evolution parameters given in Equation 5.7. The Bayesian approach works by convolving prior information for a given model with the likelihood of the observations given the model, to yield the probability of observing the data given the model, the posterior distribution up to a normalization constant called the Bayesian evidence.

To determine the posterior distributions for each parameter in the SMHM relation, our MCMC model generates values for the observed stellar mass, halo mass, and $\mathrm{m_{gap}}$ values at each step in our likelihood analysis, which are directly compared to our observed measurements.

5.5.1 Bayesian Model incorporating Redshift evolution

5.5.1.1 The Observed Quantities

As in GM&M19, we model the $\log_{10}$ BCG stellar masses (y), $\log_{10}$ halo masses (x), and M14 values (z) as being drawn from Gaussian distributions with mean values (locations) taken from our observed/measured results. The standard deviations are the uncertainties on each measurement, which are determined using the overlap sample (see Section 5.6) and include an estimate of the observational uncertainty (σ_{x_0}, σ_{y_0}, σ_{z_0}) as well as a stochastic component from a beta function, $\beta(0.5, 100)$ (GM&M18), which allows for realistic uncertainty on our observational errors. These error bars are treated statistically in the Bayesian model as free nuisance parameters σ_x, σ_y, and σ_z.

5.5.2 The Unobserved Quantities

As in GM&M19, our model incorporates redshift evolution through parameters related to α, β, γ, and σ_{int}. Since we study the cluster portion of the SMHM relation, the SMHM relation is modeled linearly as (See Equation 5.7):

$$y_i = \alpha(t)^{n_1} + (\beta(t)^{n_2})x_i + (\gamma(t)^{n_3})z_i, \tag{5.7}$$

where t is the ratio of the lookback time, calculated using the photometetric redshift determined via red sequence fitting from redMaPPer (*Rykoff et al.*, 2014, 2016), divided by the age of the universe. We also assume a Gaussian likelihood form, with σ_{int} that evolves with redshift: $\sigma_{int}(t)^{n_4}$. n_1, n_2, n_3, and n_4 measure the redshift evolution of α, β, γ, and σ_{int} respectively. For the redshift binned samples, these parameters are set to 0.0. Thus, just as in GM&M19, the zero redshift model from GM&M18 is nested within our new model, which allows us to interpret how much better a given model is (e.g., with redshift evolution vs. without) using only the posterior distribution. We note that we chose to model the redshift evolution differently than was done in GM&M19 because we cover a significantly wider range in redshift and we found that using Equation 5.3, instead of Equation 5.7, biased the results to be less strongly influenced by the late-time low redshift evolution. Additionally, we note that in Equation 5.7, the values of α, β, γ, and σ_{int}, represent the values at z=inf, unlike in Equation 5.3, where the posterior values represent the values at z=0.0.

This Bayesian model regresses the generated values against the observed stellar mass, halo mass, and $\mathrm{m_{gap}}$ values simultaneously and self-consistently. The parameters that model the underlying distributions and their uncertainties are nuisance parameters and thus are marginalized over when we present the posterior distributions. Each parameter in the Bayesian analysis, along with its prior is presented in Table 5.1. We discuss the strong priors on the observed uncertainties in Section 5.6.

Bayesian Analysis Parameters for the
Combined DES, SDSS-C4, and SDSS-redMaPPer Sample

Symbol	Description	Prior
α	The offset of the SMHM relation	$\mathcal{U}$(-20,20)
β	The high-mass power law slope	Linear Regression Prior
γ	The stretch parameter, which describes the stellar mass - M14 stratification	Linear Regression Prior
σ_{int}	The uncertainty in the intrinsic stellar mass at fixed halo mass	$\mathcal{U}(0.0, 0.5)$
y_i	The underlying distribution in stellar mass	Equation 5.7
x_i	The underlying halo mass distribution	$\mathcal{N}(14.29, 0.20^2)$
z_i	The underlying $\mathrm{m_{gap}}$ distribution	$\mathcal{N}(2.23, 0.65^2)$
n_1	The power law associated with the evolution of α	$\mathcal{U}(-10.0, 10.0)$
n_2	The power law associated with the evolution of β	$\mathcal{U}(-10.0, 10.0)$
n_3	The power law associated with the evolution of γ	$\mathcal{U}(-10.0, 10.0)$
n_4	The power law associated with the evolution of σ_{int}	$\mathcal{U}(-20.0, 20.0)$
$\sigma_{y_{0i}}$	The uncertainty between the observed stellar mass and intrinsic stellar mass distribution	0.08 or 0.05 dex
$\sigma_{x_{0i}}$	The uncertainty associated with the mass-richness relation	0.087 dex
$\sigma_{z_{0i}}$	The uncertainty between the underlying and observed m_{gap} distribution	0.15 or 0.48

Table 5.1: Bayesian Analysis Prameters for the Combined SDSS-C4, SDSS-redMaPPer, and DES-redMaPPer Nominal Sample using M14 and Incorporating Redshift Evolution. $\mathcal{U}(a, b)$ refers to a uniform distribution where a and b are the upper and lower limits. The linear regression prior is of the form $-1.5 \times log(1 + value^2)$. $\mathcal{N}(a, b)$ refers to a Normal distribution with mean and variance of a and b. Additionally, we note that for x_i and z_i, the means and widths given in this table are example values belonging to the lowest redshift bin.

We express the entire posterior as:

$$
p(\alpha, \beta, \gamma, \sigma_{int}, n_1, n_2, n_3, n_4, x_i, z_i, \sigma_{y_i}, \sigma_{x_i}, \sigma_{z_i}) \propto \underbrace{P(y_{0i}|\alpha, \beta, \gamma, \sigma_{y_i}, n_1, n_2, n_3, n_4, \sigma_{int}, x_i, z_i)\ P(x_{0i}|x_i, \sigma_{x_i})\ P(z_{0i}|z_i, \sigma_{z_i})}_{\text{likelihood}} \underbrace{p(x_i)\ p(z_i)\ p(\sigma_{x_i})\ p(\sigma_{y_i})\ p(\sigma_{z_i})\ p(\alpha)\ p(\beta)\ p(\gamma)\ p(\sigma_{int})\ p(n_1, n_2, n_3, n_4)}_{\text{priors}} \tag{5.8}
$$

where each i^{th} cluster is a component in the summed log likelihood.

This is a *hierarchical Bayes model* because the priors on the true halo masses (x_i) and M14 values (z_i) depend on models themselves (the observed halo mass and M14 distributions).

5.6 Calibration

For this paper, we are studying a much larger sample of data out to a significantly higher redshift ($z < 0.6$) than in GM&M19. This larger sample further reduces statistical noise in our measurements, while also allowing us to study the evolution in the SMHM relation over the last 6 billion years. This new data is from DES, not SDSS, which was solely used in GM&M19, and observed and reduced using different telescopes and pipelines. Therefore, to treat the data as a homogeneous sample that can be used to measure the parameters of the SMHM relation over this large redshift range, we must calibrate uncertainties associated with the DES data with respect to the uncertainty associated with the SDSS data. We do this using the sample of 61 clusters in both our SDSS-redMaPPer and DES-redMaPPer samples. Additionally to determine whether the uncertainty yielded by the comparison of clusters in both samples allows us to measure SMHM parameters that agree with one another, we use the DES clusters covering the redshift range $0.208 < z < 0.30$, which matches the highest redshift bin from GM&M19. Additionally, we apply the halo mass distribution function of those SDSS-redMaPPer clusters in the highest redshift bin to the DES data.

To verify that SDSS and DES-redMaPPer clusters are identified and measured homogeneously, we compare the redMaPPer richnesses and find excellent agreement between the two measurements: -0.6 ± 13.5. Using those richnesses, we then compare the halo mass estimates. In GM&M19, we use the *Simet et al.* (2017) mass-richness relation, while here we use the *McClintock et al.* (2019) mass-richness relation. As previously noted, when scaled to the same units, the two mass-richness relations are equivalent (except for the small redshift parameter in *McClintock et al.* (2019)) and we find that the difference in halo mass is 0.01 ± 0.11. Based on this comparison, and similarity of richnesses, we conclude that these values are equivalent and that the same uncertainty in the mass richness relation used in GM&$M19$, $\sigma_{x_0} = 0.087$ dex, can be used.

Perhaps the most interesting comparison is the stellar mass uncertainty. The deeper coverage from DES observations results in having more accurate (lower uncertainty) BCG photometry at higher redshifts (when compared to SDSS). This is particularly important since we measure stellar mass within 100kpc, a radial region which is strongly impacted by the ability to detect faint/diffuse light. Based on the comparison between the 61 clusters in both SDSS and DES, we find that the difference between our stellar mass measurements is: 0.02 ± 0.09. After accounting for the SDSS-redMaPPer measurement uncertainty, we estimate that $\sigma_{y_0} = 0.05$dex, for DES data, which is a slight reduction of the value used in GM&M19 for SDSS data (0.08dex). This follows since the DES data is deeper and hence more accurate than the SDSS data.

The deeper and higher redshift aspect of the DES data also impact our measurement of $\mathrm{m_{gap}}$. The DES observations lack spectroscopic coverage, so we expect some projection issues in our $\mathrm{m_{gap}}$ measurement. In GM&M19, we used $\sigma_{z_0} = 0.15$ dex, which was based on a comparison to the results from GM&M18 that were determined via a comparisons to 3D simulations. Given that we apply a restrictive P_{mem} criteria at high redshifts, we expect a larger σ_{z_0} for the DES-redMaPPer sample. The difference in M14 measurements for the 61 clusters in both samples is -0.13 ± 0.46. When this uncertainty is combined with the SDSS uncertainty (0.15), we estimate that $\sigma_{z_0} = 0.48$ a large increase from GM&M19.

It is important to highlight that using the 61 clusters in both our SDSS-redMaPPer and DES-redMaPPer samples, we find excellent agreement between the stellar masses, halo masses, and M14 values, such that each difference is well within 1σ from 0.0, despite the fact that the measurements come from different sources. Therefore, we believe that based on our measurement techniques, we have identified criteria which allow us to identify a homogeneous sample across this large range in redshift.

To verify that estimates for the uncertainty yield good agreement in the parameters of the SMHM relation, we calibrate the DES observational uncertainties, σ_{x_0}, σ_{y_0}, and σ_{z_0} using the previously described DES sub-sample which matches the SDSS-redMaPPer highest redshift bin. With this DES calibration sample, we treat σ_{x_0}, σ_{y_0}, and σ_{z_0} as nuisance parameters on a coarse grid centered on the estimates described above in the Bayesian analysis and solve for the mean values by requiring α, β, γ, and σ_{int} be within 1σ of the values found for the fourth bin of the SDSS-redMaPPer data.

The posterior distributions for the calibration samples are given in lines 1 and 2 of Table 5.3. We find excellent agreement between the SDSS-redMaPPer highest redshift bin and the DES calibration sample (within 1σ) for α, β, and γ, and σ_{int} when we use the same offset axes as in GM&M19 and set the stellar mass uncertainty to $\sigma_{y_0} \simeq 0.05$

dex, the magnitude-gap uncertainty to $\sigma_{z_0} \simeq 0.48$, and the inferred intrinsic scatter in the mass-richness relation to $\sigma(lnM_{200}|\lambda) = 0.20$, which corresponds to $\sigma_{x_0} = 0.087$ dex.

The above error calibration provides us with physically motivated estimates of the uncertainties on our observables. The values we obtain are reasonable and match our expectations. However, we remind the reader that we do not have good estimates on the errors associated with these observable measurement uncertainties. However, recall that Equation 5.8 allows for additional uncertainty in the observed errors. Therefore, although we set initial values described above (i.e., σ_{x_0}, σ_{y_0}, σ_{z_0}), the observational uncertainties used in our Bayesian analysis are actually nuisance parameters.

5.7 Results

In this section, we present the qualitative and quantitative results from our analysis of the combined SDSS-C4, SDSS-redMaPPer, and DES-redMaPPer Y3 data. Figure 5.1, which compares the 100kpc stellar masses for the SDSS and DES data, both estimated using EzGal (*Mancone and Gonzalez*, 2012) to the halo masses estimated using mass-richness relations (*Simet et al.*, 2017; *McClintock et al.*, 2019), color coded by M14, highlights the qualitative results of the study. In total Figure 2.1 includes 1016 SDSS clusters and 1306 DES clusters, and spans the redshift range $0.03 < z < 0.60$. Therefore, the stratification originally identified in GM&M18 continues to persist out to higher redshifts than explored in either GM&M18 or GM&M19. Furthermore, although not included, the stellar mass-M14 stratification can also be clearly seen in the binned data as well as in the *Guo et al.* (2011) prescription of the MILLENNIUM simulation as discussed in Section 5.7.1.

We evaluate the strength of the redshift evolution in the SMHM-M14 relation using our previously described MCMC model (Section 5.5), Bayesian formalism, and linear SMHM relation (Equation 5.7). The triangle plot, Figure 5.2, presents the 1D and 2D posterior distributions distributions for the eight SMHM relation parameters, α, β, γ, n_1, n_2, n_3, n_4, and σ_{int}. For this analysis, as well as the initial calibration analysis, we shifted the x and y axis to eliminate the covariance between α and β. For the calibration, we used the

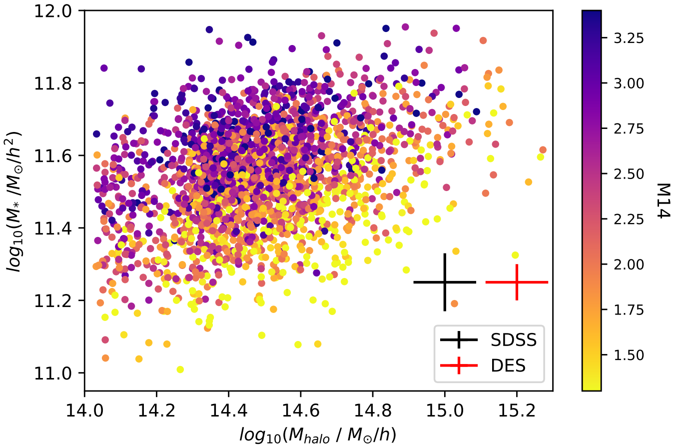

Figure 5.1: SHMH-M14 Relation for the SDSS-C4, SDSS-redMaPPer, and DES-redMaPPer Samples. The SMHM relation for the combined DES-redMaPPer, SDSS-redMaPPer, SDSS-C4 clusters colored via M14. As in GM&M18, and GM&M19 we see that a stellar mass - m_{gap} stratification exists at high redshifts. The black cross represents the error in halo mass, 0.087 dex, and stellar mass, 0.08 dex for the SDSS data and the red cross represents the error in halo mass, 0.087 dex, and stellar mass, 0.05 dex for the DES data.

Posterior Distribution Results with Redshift Evolution

Data	α(z=inf)	β(z=inf)	γ(z=inf)	σ_{int}(z=inf)	n_1	n_2	n_3	n_4
with M14	$-0.195^{+0.029}_{-0.035}$	$0.181^{+0.032}_{-0.027}$	$0.093^{+0.012}_{-0.011}$	$0.069^{+0.007}_{-0.006}$	$-0.144^{+0.097}_{-0.092}$	$-0.316^{+0.094}_{-0.091}$	-0.203 ± 0.072	$-0.142^{+0.056}_{-0.055}$

Table 5.2: Redshfit Evolution Bayesian MCMC Posterior Distributions for DES and SDSS data

same offsets as in GM&M19. However, here we subtracted the median values of the range covered by our stellar mass and halo mass distributions: ($x_{med} = 14.65$ and $y_{med} = 11.55$). The posterior results of this analysis are also given in Table 5.2 and discussed in the context of the GM&M19 results in Section 5.8.

In Figure 5.2, excluding the SMHM parameters and their associated evolution parameters, the same pairs of parameters as in GM&M19 are strongly covariant: α, and γ, α and n_3, γ and n_1, and n_1 and n_3. α and γ are covariant because shifting the axis causes the location of α to correspond where M14=0.0. Figure 5.2 illustrates that the primary results presented in GM&M18 and GM&M19 still hold true; γ is definitively non-zero, σ_{int} is less than ∼0.1 dex, and we again detect statistically significant redshift evolution in β, such

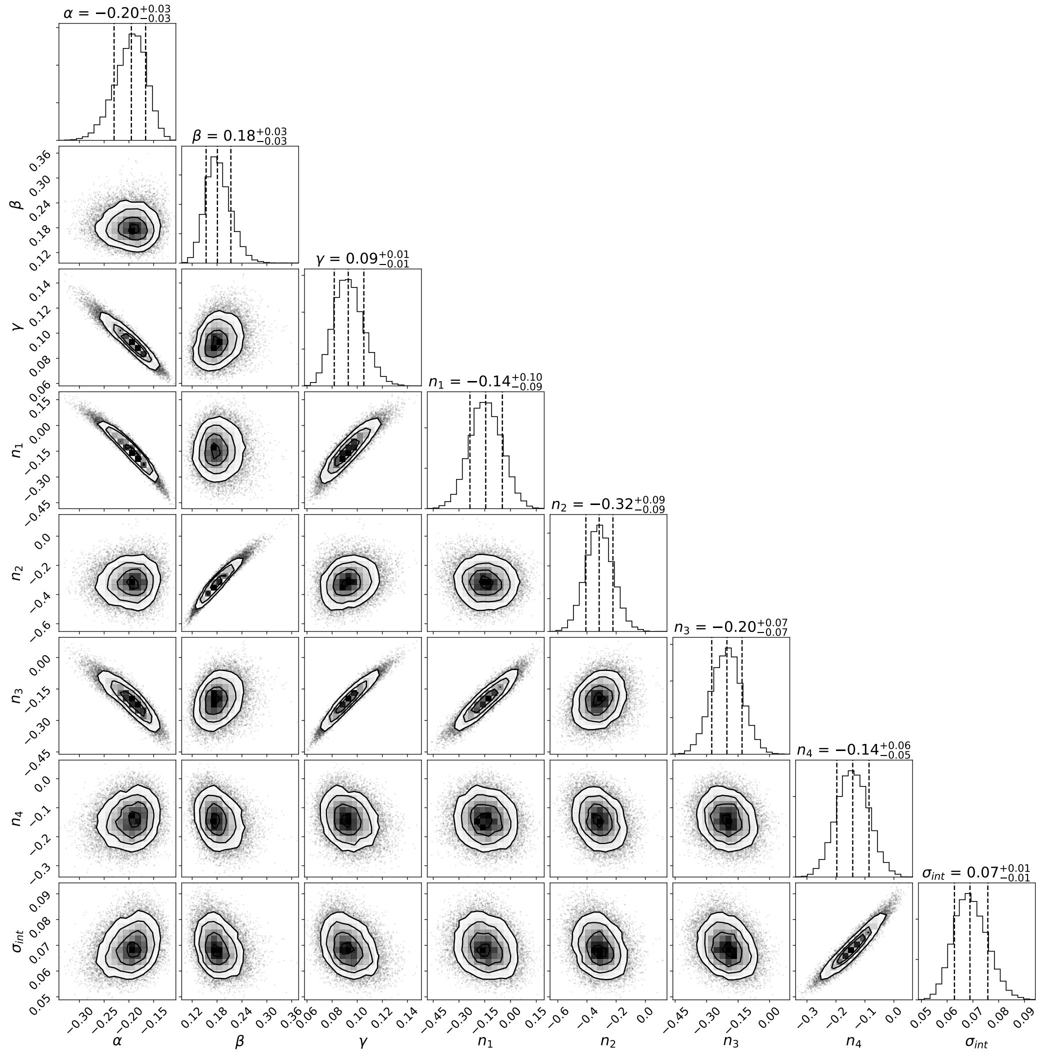

Figure 5.2: SMHM-M14 with Lookback Time Evolution Posterior Distributions. The posterior distribution for α, β, γ, n_1, n_2, n_3, n_4, and σ_{int}. As in GM&M18, we see that γ is significantly non-zero and σ_{int} is less than 0.1 dex. However, we note that as a result of the modified redshift evolution form given by Equation 5.7, the values are not directly comparable to the results from GM&M19. Instead, the posteriors measured here are extrapolations out to when the lookback time equals the age of the universe. To see the values at the redshifts measured in our study, see Figures 5.3, 5.4, 5.5, and 5.6. Additionally, the redshift parameter n_2 is no longer the only parameter that is significantly non-zero, all four parameters are farther than 1σ from 0.0 and n_3 is 2.5σ from 0.0. Therefore, some, albeit weak, redshift evolution in the parameters of the SMHM relation can be detected over $0.03 \leq z \leq 0.60$.

that n_2 is $>3\sigma$ from 0.0. Additionally, it is important to again emphasize that the posterior values shown in Figure 5.2 do not represent the same values as those in GM&M19 because of the change in form of how redshift evolution was modeled. In GM&M19, the posteriors represented the values at z=0.0. In contrast, here, the posteriors represent the asymptote values that the distributions reach when the lookback time is the age of the universe.

The key takeaways from Figure 4.4 are the significance of the redshift evolution parameters. We note that this significance is impacted by the inclusion of the DES data, which significantly reduces the error bars associated with each posterior distribution. Thus, unlike in GM&M19, n_1, n_2, n_3, and n_4 are all more than 1σ from 0.0. Like in GM&M19, n_2, is definitively non-zero ($>3\sigma$). However, incorporating the DES data, leads to more significant detection in each of the remaining parameters. In particular, n_3 is slightly less than 3σ from 0.0 and n_4 is $\approx 2.5\sigma$ from 0.0. Following the discussion in GM&M19, the redshift evolution of the slope and σ_{int} are perhaps the most significant because n_2 and n_4 are the only parameters that have no covariance associated with parameters other than the SMHM parameters they are associated with. Therefore, the results shown here are significant because we verify that the detection of statistically significant late time evolution in the slope, introduced in GM&M19, and also detect evolution in each of the additional parameters. However, we note that to improve our understanding of whether both α and γ are evolving or whether one parameter's evolution yields a non-zero n-parameter in the other, we must eliminate covariance between α and γ, without re-introducing covariance with β.

We obtain these results using a careful analysis to ensure that the lower redshift SDSS-C4 and SDSS-redMaPPer data and the higher redshift DES-redMaPPer data are homogeneous. We note that the homogeneity between the SDSS-C4 and SDSS-redMaPPer data is discussed in depth in GM&M19. Specifically, in this analysis, we have ensured that the SDSS and DES photometry, although observed using different instrumentation and reduced using different photometric pipelines yield BCG magnitudes and stellar masses that agree with one another (as discussed in Section 5.6), the SDSS and DES data use the same physical fixed-aperture photometry for all BCGs, the same cluster galaxy membership to define the magnitude gap (as set by P_{mem} from redMaPPer), the same algorithm and parameters to determine stellar masses, the same mass-richness technique to infer cluster masses, verified using the clusters in the SDSS and DES overlap sample, which are within errors, as discussed in Section 5.6, and the same algorithm to measure the completeness criteria used to define the underlying cluster samples in both $\mathrm{m_{gap}}$ and cluster halo mass. However, it is possible that there are systematic errors that we have missed in the SDSS sample when compared to the DES sample. However, because our goal is to extend the analysis of GM&M19 out to higher redshifts, we cannot remove the lower-redshift SDSS data without removing the ability to detect any observed late-time evolution. Therefore, it is only by treating the data in a homogeneous manner as done here, that we are able to determine how the SMHM relation evolves observationally out to higher redshifts.

5.7.1 Comparison to Binned Results

Here, we present how the SMHM relation parameters evolve by comparing the posterior results to those from the binned clusters. The results for each of the measured parameters, α, β, γ, and σ_{int}, for the binned data as well as for the *Guo et al.* (2011) prescription of the MILLENNIUM simulation are presented in Table 5.3. We note that for simplicity, we do not include the *Guo et al.* (2011) data in Figures 5.3, 5.4, 5.5, and 5.6. The *Guo et al.* (2011) measurements are taken on data samples described in Section 5.4.5. As a result of the limits of the *Guo et al.* (2011) simulation box size, using the halo mass distribution functions from our final sample of clusters significantly decreases the number of clusters, particularly in the higher redshift simulation boxes, yielding larger posterior uncertainties. To illustrate the trends we observe in Tables 5.2 and 5.3, in Figures 5.3, 5.4, 5.5, and 5.6, we display how the offset (α), slope (β), stretch factor (γ), and intrinsic scatter (σ_{int}) evolve as a function of lookback time divided by the age of the universe, as given by the posterior distributions shown in Figure 5.2.

Figure 5.4 illustrates that our Bayesian MCMC model which incorporates lookback time finds that β decreases with increasing lookback time for the combined SDSS and DES clusters, in agreement with the results from GM&M19. In contrast to the stronger evolution of β, Figures 5.3, 5.5, and 5.6 illustrate that using our Bayesian MCMC model, we observe

Posterior Distribution Results

Data	z_{min}	z_{max}	z_{med}	$log_{10}(M_{halo}/(M_{\odot}/h))_{min}$	$n_{clusters}$	α(z=z_{med})	β(z=z_{med})	γ(z=z_{med})	σ_{int}(z=z_{med})
GM&M19 bin4	0.208	0.300	0.247	14.39	210	-0.34 ± 0.03	0.32 ± 0.06	0.150 ± 0.013	0.082 ± 0.009
DES-Calibration	0.208	0.300	0.259	14.39	118	-0.28 ± 0.05	0.38 ± 0.07	0.139 ± 0.021	0.065 ± 0.014
All Data	0.030	0.173	0.127	14.03	619	-0.27 ± 0.02	0.42 ± 0.03	0.153 ± 0.008	0.086 ± 0.005
All Data	0.173	0.266	0.222	14.25	568	-0.27 ± 0.02	0.35 ± 0.03	0.145 ± 0.009	0.079 ± 0.005
All Data	0.266	0.410	0.336	14.29	589	-0.24 ± 0.02	0.31 ± 0.03	0.126 ± 0.009	0.085 ± 0.005
All Data	0.410	0.600	0.503	14.33	546	-0.25 ± 0.03	0.34 ± 0.04	0.127 ± 0.011	0.075 ± 0.006
Guo et al. (2011)	0.116	0.116	0.116	14.03	302	-0.28 ± 0.02	0.46 ± 0.03	0.220 ± 0.009	0.090 ± 0.004
Guo et al. (2011)	0.208	0.208	0.208	14.25	206	-0.30 ± 0.02	0.44 ± 0.04	0.218 ± 0.011	0.094 ± 0.005
Guo et al. (2011)	0.320	0.320	0.320	14.29	110	-0.34 ± 0.03	0.51 ± 0.04	0.263 ± 0.014	0.079 ± 0.005
Guo et al. (2011)	0.509	0.509	0.509	14.33	76	-0.34 ± 0.03	0.48 ± 0.08	0.248 ± 0.018	0.083 ± 0.007

Table 5.3: SDSS-C4, SDSS-redMaPPer, and DES-redMaPPer Binned SMHM Relation Posterior Results.

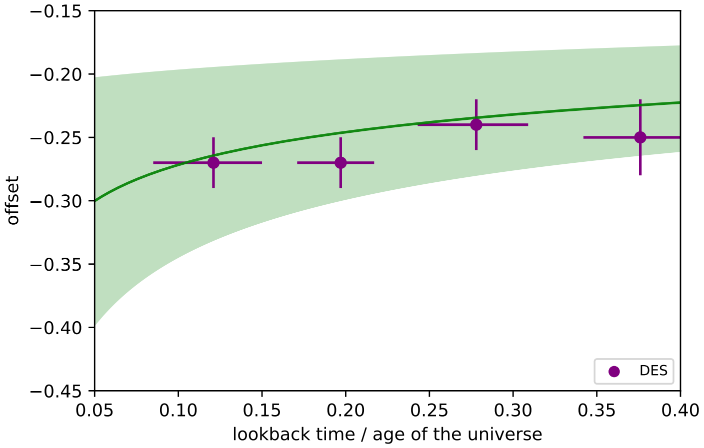

Figure 5.3: Evolution of α. The offsets and respective error bars are plotted as a function of lookback time divided by the age of the universe for the binned data comprised of SDSS and DES clusters. The green line represents how α evolves as given by the posterior results presented in Figure 5.2. The green shaded region illustrates the combined total error from uncertainty on n_1 and α. This comparison highlights that the offset of the SMHM relation weakly evolves over the redshift range $0.03 \leq z_{red} \leq 0.6$.

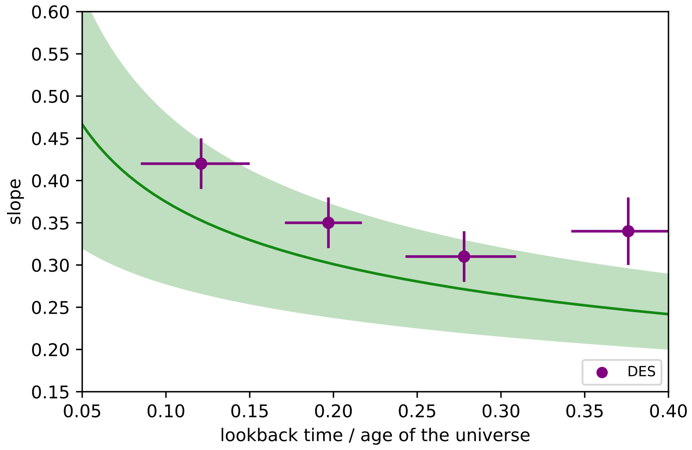

Figure 5.4: Evolution of β. The slopes and respective error bars are plotted as a function of lookback time divided by age of the universe for the binned samples of SDSS and DES clusters. The green line represents the evolution given by the posterior results presented in Figure 5.2. The green shaded region is the total error from the uncertainty on n_2 and β. This comparison highlights that the slope of the SMHM relation evolves over the redshift range $0.03 \leq z_{red} \leq 0.6$.

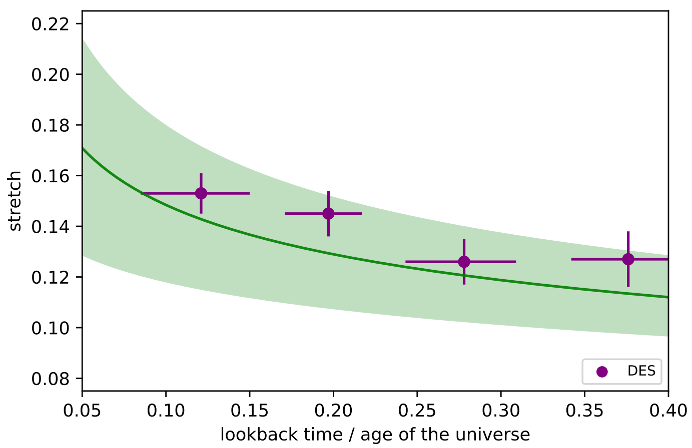

Figure 5.5: Evolution of γ. The stretch factors and respective error bars are plotted as a function lookback time divided by age of the universe for the final binned sample consisting of SDSS and DES clusters. The green line represents the evolution suggested via the posterior results presented in Figure 5.2. The green shaded region represents the combined uncertainty from n_3 and γ. This trend highlights that there is no weak evolution in γ in this redshift range.

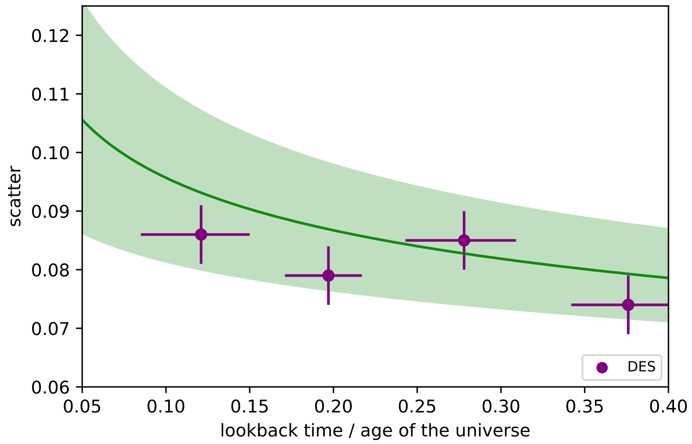

Figure 5.6: Evolution of σ_{int}. The intrinsic scatters and respective error bars are plotted as a function of lookback time divided by the age of the universe for the binned SDSS and DES clusters. The green line represents the redshift evolution suggested by the posterior results presented in Figure 5.2. The green shaded region represents the combined uncertainty of n_4 and σ_{int}. This trend highlights that there is weak redshift evolution in σ_{int}.

weaker evolution in the α, which is still largely in agreement with the results from *Zhang et al.* (2016), γ, and σ_{int}. We discuss the physical meaning of the observed evolution for these parameters in the context of hierarchical growth in Section 5.8.

5.7.2 Comparison to Golden-Marx & Miller 2019 results

The primary difference between the results presented here and those in GM&M19 stems from the different forms used to characterize the evolution (Equation 5.3 vs Equation 5.7), which in turn make a direct comparison between the measured values of α, β, γ, and σ_{int} difficult. However, we can still compare the significance of the evolution parameters as well as the uncertainties associated with each parameter. We note that including the DES clusters unsurprisingly reduces the uncertainties on each parameter, increasing the significance of each detection. Additionally, we note that the significance of n_2 is consistent between both works. However, for n_1, n_3, and n_4, we find that including the DES data increases the significance, partly due to the lowering of the uncertainties. The primary takeaway from comparing to the results of GM&M19 is that by incorporating many more clusters, we are able to detect even weak statistically significant evolution with very small measurement uncertainty and that the evolution of γ and σ_{int} have been detected observationally ($> 2\sigma$) for the first time.

5.8 Discussion

The evolution in the SMHM relation's slope and σ_{int} can provide insight into the hierarchical growth of BCGs. Using semi-analytic models, researchers have found that at late times BCG's grow by a factor of ≈1.5-2.0 (*De Lucia and Blaizot*, 2007; *Guo et al.*, 2011; *Shankar et al.*, 2015). In contrast observations have found that over this redshift range, much of the growth occurs in the BCG's outer envelope, including regions that have previously been classified as ICL (*van Dokkum et al.*, 2010; *Burke et al.*, 2015; *Huang et al.*, 2018), further highlighting the necessity of measuring the stellar mass out to a large radii.

In this work, we have extended the redshift evolution of the cluster scale SMHM presented in GM&M19 out to $z_{red} = 0.6$. Incorporating γ reduces σ_{int}, which along with the addition of the DES clusters, significantly reduces the uncertainty on β allowing us to detect redshift evolution. As in GM&M19, we interpret this result in the context of hierarchical growth. *Gu et al.* (2016) suggest that β steepens as a result of an increase in σ_{int}, which results from an increase in the diversity of the BCG's progenitor history. Moreover, the late time evolution of β that we observationally confirm suggests BCGs residing in more massive halos undergo more late time growth than BCGs in less massive halos, which may result from differences in the galactic populations of high and low mass clusters and the efficiency of mergers. In contrast to the results presented in GM&M18, here we detect more significant evolution in σ_{int}, such that the trend between σ_{int} and β agrees with the results presented by (*Gu et al.*, 2016), further supporting our claim that the observed late-time evolution in the SMHM relation results from recent BCG hierarchical growth.

Additionally, as shown in Table 5.3, we do not detect any noticeable redshift evolution in the *Guo et al.* (2011) prescription of the MILLENNIUM simulation. This differs slightly from GM&M19, where we found a slightly lower slope in the highest redshift bin, which we now note is likely due to both small sample size and the halo mass distribution function applied to that bin. The lack of evolution found in *Guo et al.* (2011) agrees with the absence of evolution found between z=0.0 and z=1.0 in the ILLUSTRIS TNG300 simulation (*Pillepich et al.*, 2018). Moreover, as noted in GM&M19, and confirmed for this higher redshift sample, redshift evolution is only identified when the 100kpc magnitudes are used. Since the semi-analytic model from *Guo et al.* (2011) is designed to reproduce the SDSS luminosity function which is constructed using Petrosian magnitudes, it is unsurprising that no redshift evolution is detected. Therefore, in order to determine whether simulations accurately account for redshift evolution, we must use simulations, such as ILLUSTRIS TNG300, which allow us to measure magnitudes within fixed physical apertures.

Unlike in GM&M19, our posterior distributions also support the notion that γ evolves over the redshift range $0.03 < z < 0.60$, as shown in Figure 5.5. This result can be interpreted as, with respct to the stellar mass, over time, $\mathrm{m}_{\mathrm{gap}}$ increases (at earlier times, $\mathrm{m}_{\mathrm{gap}}$ is lower, in agreement with hierarchical growth). This weak redshift evolution is intriguing because as discussed earlier $\mathrm{m}_{\mathrm{gap}}$ and stellar mass growth are correlated (*Solanes et al.*, 2016). Additionally, since our 100kpc stellar mass measurement includes the BCG's outer envelope, it likely includes the recent merger material which would be responsible for any evolution in $\mathrm{m}_{\mathrm{gap}}$ or stellar mass. The decreasing trend observed between γ and redshift would likely occur if BCGs had mergers with bright galaxies in the last 6 billion years and the resulting stellar mass was deposited primarily at radii beyond 100kpc. However, while major mergers are not expected to be common over this redshift range (*Burke et al.*, 2015), given that a fraction of the stellar material from a merger is ejected into the ICL, if minor mergers involving fainter galaxies (likely either the third or fourth brightest cluster member) were to occur, and deposit most of the stellar material at radii greater than 100kpc, this would possibly result in a larger increase in $\mathrm{m}_{\mathrm{gap}}$ than in stellar mass, which matches the trend shown in Figure 5.6.

In this work, we have focused on the late time evolution of the SMHM relation out to $z \sim 0.6$. As shown here, each of these parameters shows signs of some late-time evolution, and for the slope predominately over the redshift range $0.0 < z < 0.15$. We are left with two paths forward. To tighten the constraints on this late-time evolution, we must either incorporate more large statistically complete samples of low-redshift clusters $z < 0.1$ (there are fewer than 200 SDSS-C4 low-z clusters compared to 1500 DES high-z clusters), which are difficult to obtain. Or, we can forge ahead to higher redshifts to determine whether these parameters remain consistent out to $z = 1.0$, an approach which faces much of the same observational challenges as the data presented here and would require us to be able to place tight constraints on each of the observed measurements.

CHAPTER VI

Conclusions and Future Work

6.1 Conclusions

The primary focus of this dissertation is understanding and statistically constraining the galaxy-dark matter halo connection, the physical and statistical link between central galaxies and their dark matter halos (*Wechsler and Tinker*, 2018). As discussed in Chapter I, this connection stems from the hierarchical assembly of the cluster's dark matter halo, which in turn leads to the hierarchical assembly of the BCG (e.g., *White and Rees*, 1978; *Blumenthal et al.*, 1984; *De Lucia and Blaizot*, 2007). Over the past decade, this connection has proven to be particularly useful. Through a combination of observations, semi-analytic and empirical models, and simulations the galaxy-halo connection has been able to constrain cosmological parameters as well as parameters of models of galaxy formation and evolution (*Gu et al.*, 2016; *Tinker*, 2017; *Kravtsov et al.*, 2018). The galaxy-halo connection is a broad, wide-ranging subfield, relating many different measurements. One of the primary relations used to characterize the galaxy-halo connection is the SMHM relation, the main focus of this dissertation. Through the statistical relationship between BCG stellar mass and cluster dark matter halo mass, the galaxy-halo connection community continues to improve our understanding of how galaxies populate dark matter halos and as well as how the central galaxy and dark matter halo co-evolve over cosmic time. However, to improve our understanding of this correlation by placing tighter constraints on the measured parameters and uncertainties associated with the SMHM relation, we must identify latent parameters which can be incorporated into this relation, and have a statistically significant impact on the measured results, as done using observational and simulated data in *Golden-Marx and Miller* (2018) and *Golden-Marx and Miller* (2019).

6.1.1 Latent Parameters

From a statistical point of view, latent parameters are additional variables, which have previously been unaccounted for that correlate with one of the measurements used in a scaling relation. Latent parameters then improve or reduce the uncertainty associated with these scaling relations. From the perspective of the SMHM relation, the latent parameter would be a third parameter that correlates with either stellar mass or halo mass, and would minimize the uncertainty in the measured parameters as well as reduce σ_{int} below the consensus estimate of 0.15dex (*Tinker et al.*, 2017; *Zu and Mandelbaum*, 2015; *Pillepich et al.*, 2018; *Kravtsov et al.*, 2018). Based on how we have defined latent parameters, when determining whether the inclusion of a third parameter associated with a scaling relation is indeed a latent variable, it is important, as done in *Golden-Marx and Miller* (2018), *Golden-Marx and Miller* (2019), and Golden-Marx et al. (in prep.), to use nested models that allow for the variable associated with the latent parameter to equal zero. If this is done, then the validity of the latent parameter results entirely from the posterior distribution of the measured parameter associated with the latent variable.

Astronomy has a long and well-studied history with statistical scaling relations. Therefore, it is unsurprising that latent variables have previously been found to play an important role in improving those scaling laws. One important astronomical measurement, greatly impacted by latent variables, is the estimate of the distance to nearby galaxies. A simple method of estimating galactic distance is to compare the observed apparent magnitude of an object to its known luminosity. For elliptical galaxies, such as BCGs, the galaxy's luminosity can be estimated using the *Faber and Jackson* (1976) relation, given by Equation 6.1,

$$L_{elliptical} \propto \sigma^4 \tag{6.1}$$

where σ is the velocity dispersion of the elliptical galaxy. However, unlike with the *Tully and Fisher* (1977) relation, which is used to estimate distances to spiral galaxies, the *Faber and Jackson* (1976) relation has a larger uncertainty associated with it, resulting in a larger scatter associated with these distance estimates. This large uncertainty led astronomers to determine whether a latent parameter was associated with the luminosity of an elliptical galaxy. This avenue of inquiry resulted in the identification of the fundamental plane (*Djorgovski and Davis*, 1987), given by Equation 6.2,

$$R_e \propto \sigma^{1.2} I_e^{-0.8} \tag{6.2}$$

where R_e is the effective radius of the elliptical galaxy, and I_e is the observed surface brightness at R_e. In this example, R_e is the latent parameter in measuring distance. Using the fundamental plane relation along with the angular size measurement of a galaxy yields a much more tightly constrained distance measurement, which illustrates the impact of incorporating latent variables.

Based on the example of the fundamental plane, identifying latent parameters can greatly impact measurements made using scaling relations. However, it is equally as important to determine the physical motivation for what leads to the appearance of a latent parameter because understanding whether the selected measured latent variable is a proxy for another measurement will greatly improve our understanding of the physical processes that govern that scaling relation, in the case of the SMHM relation, the hierarchical assembly and evolution of the galaxy cluster.

6.1.1.1 The Magnitude Gap

Perhaps the most significant and impactful result of this dissertation is the introduction of the magnitude gap, the difference in brightness between the BCG and fourth brightest cluster member, as a latent parameter in the SMHM relation, in *Golden-Marx and Miller* (2018). We visually demonstrate that the magnitude gap may be a latent parameter in Figures 3.6, 3.7, 3.10, 3.11, 4.3, and 5.1, which show that at a fixed halo mass, a linear correlation between magnitude gap and stellar mass exists; as the BCG's stellar mass increases, so does the magnitude gap. As noted in Chapter I, the growth of the magnitude gap is related to the hierarchical assembly of the BCG, an idea which as discussed in Chapter III is supported by the identification of the same trend in the semi-analytic models of the MILLENIUM simulation (*Guo et al.*, 2011; *Henriques et al.*, 2012). Although the trend shown in the stellar mass, halo mass, and magnitude gap phase space suggests magnitude gap is a latent parameter in the SMHM relation, we relied on the posteriors of our Bayesian MCMC model to verify that this was the case and that incorporating magnitude gap would reduce the uncertainty (σ_{int}) associated with this relation. As illustrated by the posterior results shown in Figures 3.8, 3.9, 3.14, 3.15, and 4.4 from our hierarchical Bayesian MCMC model (see Sections 3.5, 4.5, 5.5), which nests the traditional SMHM relation (Equation 3.10) within our modified SMHM relation (Equation 3.8, Equation 4.7, or Equation 5.7), we find that γ the SMHM relation "stretch" parameter, which measures the strength of the correlation between stellar mass and magnitude gap,is significantly non-zero ($> 6\sigma$).

As discussed in *Golden-Marx and Miller* (2018), *Golden-Marx and Miller* (2019), and Golden-Marx et al. (in prep.), the inclusion of the magnitude gap as a third parameter in the SMHM relation significantly impacts the measured parameters associated with the SMHM relation. The most significant of these results, in agreement with the primary purpose of incorporating latent parameters, is that the inclusion of the magnitude gap in the SMHM relation significantly decreases σ_{int}. As discussed in Chapter I, the consensus value of σ_{int} is ≈0.15 dex (*Gu et al.*, 2016; *Tinker et al.*, 2017; *Zu and Mandelbaum*, 2015; *Kravtsov et al.*, 2018; *Pillepich et al.*, 2018), in agreement with the measurement from *Golden-Marx and Miller* (2018) when the magnitude gap is not included. However, incorporating magnitude gap into the SMHM relation reduces σ_{int} to ≈0.08 dex in the SDSS-C4 sample (*Golden-Marx and Miller*, 2018). Therefore, the inclusion of this latent parameter reduces σ_{int} as much as ≈50%. Moreover, this result still holds true when redshift evolution of the SMHM relation is accounted for, as shown in *Golden-Marx and Miller* (2019). The reduction of σ_{int} via the incorporation of the magnitude gap signifies that a previous portion of the unexplained σ_{int} results from comparing BCGs with differing magnitude gaps, which are at different stages within their hierarchical growth.

Additionally, another important result presented within this dissertation, as shown in *Golden-Marx and Miller* (2019), is that the measured slope of the SMHM relation is impacted by both by the incorporation of the magnitude gap and by the choice of radius within which the BCG's magnitude is measured. Chapter I and Chapter IV discuss how following the two-phase formation scenario (*Oser et al.*, 2010), the outer envelope of the BCG is more strongly correlated with the cluster than the core. Although this trend was discussed in the context of the EMERGE empirical model of galaxy formation (*Moster et al.*, 2018), this trend is identified for the first time observationally in this dissertation (Chapter IV *Golden-Marx and Miller*, 2019), and results in the slope of the SMHM relation increasing as the aperture radius used to measure stellar mass increases until reaching an asymptote near ≈100kpc (see Figure 4.2). Thus, the outer portion, which contains all information about recent merger growth is unsurprisingly more strongly correlated with the cluster's halo mass than the inner region, which forms prior to the cluster's final assembly, as shown in Figure 1.2. Figure 4.2 also highlights that we measure a significantly steeper increase in slope (and slope value) when the magnitude gap is incorporated into the SMHM relation, which is unsurprising given that like the outer regions, the magnitude gap results from the BCG and cluster's hierarchical assembly. Thus, accounting for the cluster's hierarchical assembly in the SMHM relation strengthens the correlation between the central galaxy and the cluster's dark matter halo.

6.1.2 Redshift Evolution

The second primary results from this dissertation, presented in *Golden-Marx and Miller* (2019) and Golden-Marx et al. (in prep.) stems from the measurement of the redshift evolution of the measured parameters associated with the SMHM relation. Given that both BCGs and their underlying dark matter halos grow hierarchically, prior to the work in this dissertation, it was unclear how the SMHM relation should evolve over time. Moreover, prior to this dissertation, observational works had been unable to place any constraints on the redshift evolution of the slope of the SMHM relation, in large part due to the large uncertainty associated with the slope measurement (*Oliva-Altamirano et al.*, 2014; *Gozaliasl et al.*, 2016). However, this dissertation had two advantages compared to other results and approaches. The first advantage is our use of a statistically large sample of galaxy clusters (≈ 1000 and ≈ 2500) covering large ranges in redshift ($0.03 < z < 0.3$ and $0.03 < z < 0.60$). The second advantage is that incorporating the magnitude gap as a third parameter in the SMHM relation reduces the uncertainty associated with the slope measurement (*Golden-Marx and Miller*, 2018). The combination of these factors greatly reduced the uncertainty associated with the slope and other parameters of the SMHM relation using our hierarchical Bayesian MCMC model, and allowed us to measure these parameters at a level of precision higher than many recent observational studies.

As a result of our unique approach, introduced in *Golden-Marx and Miller* (2019) and confirmed in Golden-Marx et al. (in prep.), we for the first time, observationally detect statistically significant late-time redshift evolution ($> 3.5\sigma$) in the slope of the SMHM relation, when redshift evolution is incorporated into the SMHM relation in the manner described by Equation 4.7. The most important thing to note about this result is that much of the evolution in the SMHM relation occurs relatively recently ($z < 0.15$), prior to which the slope was relatively constant at ($\beta \approx$0.35). The detection of the redshift evolution of the slope of the SMHM relation, which based on comparisons to simulations (*Gu et al.*, 2016), results from BCG hierarchical growth, highlights that at recent times, BCGs continue to grow hierarchically predominately via minor mergers. Moreover, it is important to note, that this strong evolution is only detected when the magnitude gap is incorporated (see Table 4.7.1). Therefore, in order to detect the continued hierarchical growth of BCGs, it is important to include a parameter that results from that same hierarchical growth. Additionally, in Golden-Marx et al. (in prep.), we highlight that by including the homogeneously measured DES data, we are able to detect redshift evolution in γ and σ_{int} for the first time as well, which allows us to speculate about which galaxies are involved in BCG hierarchical growth over the redshift range $0.03 < z < 0.60$ and whether hierarchical growth is responsible for σ_{int} in the SMHM relation.

6.1.3 Hierarchical Bayesian Infrastructure

Although not a directly publishable result of this dissertation, one of the most significant outputs that resulted from this dissertation is the creation of a hierarchical Bayesian MCMC infrastructure (Sections 3.5, 4.5, and 5.5), which is used throughout this dissertation to measure the parameters of the SMHM relation. Based on the testing of this model, described in *Golden-Marx and Miller* (2018), using the *Henriques et al.* (2012) prescription of the MILLENNIUM simulation, this model allows us to accurately measure the underlying (or intrinsic) parameters of the SMHM relation, while also accounting for the uncertainty in each measurement, (i.e., the stellar mass, halo mass, and magnitude gap values), which is significant because we will never have observed measurements without uncertainty. Additionally, this model uniquely accounts for the fact that the measurement uncertainties are themselves uncertain and adds a beta distribution function to the uncertainty of each parameter to account for this. While this model has been explicitly used to constrain the SMHM relation, it can be easily generalized to be applied to other astronomical scaling relations, correlations, or any simple linear relation. Additionally, as shown by comparing the models in *Golden-Marx and Miller* (2018) and *Golden-Marx and Miller* (2019), it can also be easily modified to incorporate additional measurement parameters, with future inclusions such as the cluster's formation redshift or halo concentration, into the SMHM relation. Therefore, the infrastructure designed in this dissertation will continue to serve as a fundamental part of the statistical portions of my research in the coming years.

6.2 Future Work

The statistical methods and tools that I've developed as part of this dissertation, along with the physical intuition I've gained from characterizing the impact of cluster assembly on the SMHM relation have provided me with an excellent jumping off point as I continue to strive to improve our understanding of the galaxy-halo connection. Since I will continue studying the galaxy-halo connection as a postdoctoral researcher at Shanghai Jiao Tong University, here, I describe a few possible avenues of inquiry related to the SMHM relation and the galaxy-halo connection that I plan to explore in the coming years.

6.2.1 Physical Motivation of the Magnitude Gap

Chapter III, introduced the magnitude gap as a latent parameter in the SMHM relation and via comparisons to semi-analytic models of the MILLENNIUM simulation (*Guo et al.*, 2011; *Henriques et al.*, 2012) found that the magnitude gap-stellar mass stratification results entirely from the hierarchical assembly of the cluster and BCG. Moreover, incorporating the magnitude gap impacts both the measurement of the slope and σ_{int} (*Golden-Marx and Miller*, 2018, 2019). Therefore, magnitude gap is indeed a latent parameter. Despite this identification, it is likely that the latent parameter is not exactly the magnitude gap and that we have instead identified an observational proxy for a more physically motivated latent parameter. Therefore, one of my primary objectives over the next few years is to determine exactly what physical parameter the magnitude gap-stellar mass stratification represents.

As discussed in Chapter I, using state-of-the art cosmological simulations *Matthee et al.* (2017), *Artale et al.* (2018), and *Zehavi et al.* (2018) find that a stellar mass-formation redshift stratification exists at fixed halo mass for lower mass halos ($log_{10}(M_{halo}/M_{\odot}) < 13.0$). Given the similarity of the stratification, illustrated in Figure 1.4, I believe that a correlation likely exists between the magnitude gap and a cluster's formation redshift, the redshift when half of the cluster's halo mass assembles. As further justification of this theory, *Zehavi et al.* (2018) note that earlier forming halos, housing more massive centrals, have fewer satellite galaxies because their earlier formation time allowed for the central (BCG) to merge with the satellites. In a hierarchical growth scenario, as discussed by *Solanes et al.* (2016), these mergers lead to an increase in the magnitude gap and serve as evidence that the magnitude gap may be an observational proxy for a cluster's formation redshift, a measurement which we are currently unable to estimate. As further support of this idea, *D'Onghia et al.* (2005) and *von Benda-Beckmann et al.* (2008) using N-body simulations identify a weak correlation between the formation redshift and the magnitude gap between the BCG and 2nd brightest cluster member. However, this earlier simulated result relied on a small sample of clusters and the identified correlation was never quantified and has since remained largely ignored.

To determine if magnitude gap and formation redshift correlate as well as the strength of such a correlation, I plan to use the Illustris TNG300 simulation (*Pillepich et al.*, 2018) or a similar state-of-the art cosmological simulation which is large enough to have a statistically significant number of galaxy clusters (100s). This analysis requires data that can be obtained easily from simulations: formation redshifts of the clusters will be measured via the halo merger trees; halo masses will be provided both directly from the simulation and via a richness measurement, allowing for observational comparisons, stellar masses will be measured by integrating the number of stellar particles within fixed physical radii; cluster membership will be determined using the red sequence and position within the simulation box; and BCG and 4th brightest cluster member galaxy magnitudes will be measured in the same manner as stellar mass, to measure M14, and provide an observational estimate of stellar mass. Using these measurements, I will first determine whether a simple correlation exists between formation redshift and magnitude gap, using a similar approach to my hierarchical Bayesian model. However, since, as shown in Figures 3.6, 3.7, 3.10, 3.11, 4.3, and 5.1, the stellar mass-magnitude gap stratification also is related to the slope of the SMHM relation such that BCGs with a given magnitude gap increase in stellar mass at higher halo masses, I will also create a multi-dimensional mapping between the stellar mass, halo mass, magnitude gap parameter space, and formation redshift using hierarchical Bayesian machine learning techniques (e.g., support vector machines), similar to the Bayesian MCMC infrastructure that I have built in this dissertation, to identify a likely complex non-linear relation. A similar analysis will then be done for different magnitude gaps to verify the result from *Dariush et al.* (2010) that M14 best correlates with an early formation time. The mappings strength will determine the level of correlation between BCG hierarchical growth and the halos hierarchical assembly as well as possibly determine a method to observationally estimate cluster formation redshifts.

Using this technique to estimate formation redshift would allow me to measure how the SMHM relation's slope and σ_{int} change with both observed and formation redshift. This change would only require a minor modification to the model presented in *Golden-Marx* *and Miller* (2019) and would allow me to verify that my previously described intuition is correct and that the reduction in scatter caused by incorporating the magnitude gap results from comparing only those BCGs at similar points in their evolution.

6.2.1.1 Assembly Bias

As just described, I plan to determine whether the magnitude gap can be used to trace a cluster's formation redshift. Currently, no observational proxy for formation redshift exists. One cosmological topic that would be greatly impacted by a formation redshift measurement is assembly bias, the dependence of halo clustering on a secondary property that is dependent on the halos formation redshift (*Lin et al.*, 2016), in clusters. Assembly bias strongly impacts cosmological constraint-reliant cluster statistics, such as the halo occupation distribution, which provides information about the number of galaxies within a halo of given mass, or the cluster richness, which is assumed to depend only on halo mass (*Wechsler et al.*, 2006). If richness depends on a cluster dark matter halos formation redshift, a bias may exist in richness-selected clusters (*Wu et al.*, 2008), such that early forming clusters may have a lower richness than late forming clusters because an early formation time would allow for more mergers to occur. If this bias were to exist, then it would likely have a significant impact on halo mass estimates done using the mass-richness relation (described in Section 1.4.1.4) because high-concentration, early-forming, high mass halos and low-concentration, late forming, low-mass halos will have the same richness (*Wechsler et al.*, 2006). As such the calibrations of the mass-richness relation may be incorrect. The impact on the mass-richness relation is key because this relation is commonly used to estimate cluster masses out to high redshifts, including for SDSS-redMaPPer (*Rykoff et al.*, 2012; *Simet et al.*, 2017) and DES-redMaPPer (*McClintock et al.*, 2019).

Although some recent studies have detected assembly bias signatures in clusters (*Miyatake et al.*, 2016), these detections were later revealed to result from projection effects (*Busch and White*, 2017; *Zu et al.*, 2017). Despite the lack of success in observationally detecting assembly bias signatures, assembly bias is found in numerical simulations such that low mass, high-concentration, early forming halos are more strongly clustered, and high mass, low concentration, late forming halos are more clustered; although, the trend is much weaker for high mass halos (*Wechsler et al.*, 2006). However, even in simulations, detecting assembly bias in clusters remains uncertain (*Mao et al.*, 2018). Therefore, identifying a new observational tracer for formation redshift provides an opportunity to measure assembly bias in both observations and simulations and determine its impact on our cosmological models.

Here, I outline how I plan to approach identifying assembly bias using the mapping described in Section 6.2.1 to estimate the formation redshift of clusters. Using SDSS and DES-redMaPPer catalogs (described in Sections 4.4, 5.4) I will use the mapping between stellar mass, halo mass, magnitude gap, and formation redshift to estimate the formation redshift of each cluster and identify a sample of self-similar (same halo mass and formation redshift clusters) in SDSS (*Rykoff et al.*, 2014) and DES-redMaPPer cluster catalogues over the redshift range $0.1 < z < 0.6$. Using this data, along with a measurement of the clustering of redMaPPer clusters, I can create a sample of BCGs with the same formation redshift across a range in observed redshift, which will allow me to study how assembly bias manifests in the observed universe by comparing the halo clustering measurements for our low, intermediate, and high magnitude gap samples. Comparing how clustering scales with the magnitude gap based formation redshift estimate will determine whether the redMaPPer richness measurements are biased. Additionally, since clustering measurements, formation redshifts, and magnitude gaps can all be measured in cosmological simulations, I can also do a similar analysis using simulations. Comparing the results of the simulations and observations would provide great insight into the impact of assembly bias and identify the parameters that need to be modified in our simulations and semi-analytic/empirical models to best match the observed universe.

6.2.2 Mass-Richness Relation Evolution

One key and possibly overlooked result from this dissertation is that *Golden-Marx and Miller* (2019) use the SMHM relation to constrain the scatter associated with the mass-richness relation. As discussed in Section 1.4.1.4, the mass-richness relation is a commonly used technique to measure halo masses for large photometric surveys out to high redshifts. Despite this common use, prior to the work introduced in *Golden-Marx and Miller* (2019), we were unable to place strong physically motivated constraints on the intrinsic scatter in the mass-richness relation.

Given that we are in an era of precision cosmology, it is unsurprising that the constraints on the systematic and statistical uncertainties associated with the mass-richness relation are quite small; *Simet et al.* (2017) estimate the total of both components is $\approx 7\%$. However, the intrinsic uncertainty associated with halo mass at fixed richness, $\sigma(M|\lambda)_{int}$, the width of the mass-richness relation, is suggested to be larger and not meaningfully constrained. As noted in *Golden-Marx and Miller* (2019), *Andreon* (2015) assume a large uncertainty in their caustic halo masses and report the scatter in the mass-richness relation to be as low as $\sigma(M|\lambda)_{int} < 0.05$ at a 90% confidence. In contrast, *Rozo et al.* (2015) find a significantly larger value of 0.17-0.21, depending on their assumption for the intrinsic scatter in cluster SZ masses and the associated co-variance with the observed richness measurement. Additionally, *Simet et al.* (2017) measure a value of 0.25 ± 0.03, but note that they are unable to constrain $\sigma(M|\lambda)_{int}$ using a top-hat prior covering the range 0.2 to 0.3 in their Bayesian MCMC model.

$\sigma(M|\lambda)_{int}$ is unconstrained because the uncertainty in the observed mass-richness relation, $\sigma(M|\lambda)_{obs}$, depends on the uncertainty in the mass estimate, $\sigma(M)_{data}$, as well as $\sigma(M|\lambda)_{int}$, which are described mathematically by Equation 6.3.

$$\sigma(M|\lambda)^2_{obs} = \sigma(M)^2_{data} + \sigma(M|\lambda)^2_{int} \tag{6.3}$$

To quantify these parameters, we require direct halo mass measurements independent of scaling relations, such as weak gravitational lensing mass estimates or dynamical masses estimated using the caustic technique (see Section 1.4.1.3). However, even with these measurements, additional parameter constraints are required to avoid degeneracies between the measurements of $\sigma(M)_{data}$ and $\sigma(M|\lambda)_{int}$.

In *Golden-Marx and Miller* (2019), we solve the degeneracy problem using the SMHM relation to simultaneously constrain both $\sigma(M)_{data}$ and $\sigma(M|\lambda)_{int}$ because *Golden-Marx and Miller* (2018) use caustic halo masses for the SDSS-C4 clusters and *Golden-Marx and Miller* (2019) use the mass-richness relation to estimate halo masses, including for a subset of SDSS-C4 clusters. Since these clusters have the same stellar masses and magnitude gaps, the posterior distributions from the SMHM relation must agree regardless of the technique used to measure halo mass. Since the slope of the SMHM relation depends on the associated halo mass uncertainty, and the halo mass uncertainty is correlated with $\sigma(M|\lambda)_{int}$, I can determine the values for $\sigma(M|\lambda)_{int}$ and $\sigma(M)_{data}$ that yield posteriors which agree with one another. Therefore, in *Golden-Marx and Miller* (2019), I introduce a joint mass-richness SMHM relation analysis, which places strong constraints on the uncertainties in the mass-richness relation and the caustic halo mass. To simplify the hierarchical Bayesian MCMC model, I removed σ_{int} as a free parameter and keep it fixed at 0.1 dex. Using this analysis, for the first time we place physically motivated error bars on the intrinsic uncertainty in the mass-richness relation: $\sigma(M|\lambda)_{int} = 0.20^{+0.03}_{-0.04}$

Although the result from *Golden-Marx and Miller* (2019) places a meaningful constraint on the $\sigma(M|\lambda)_{int}$, it was done only for a low redshift sample ($z_{med} = 0.086$), so it remains unknown how this measurement evolves with redshift. In fact in both *Golden-Marx and Miller* (2019) and Golden-Marx et al. (in prep.), we assume that this value does not evolve. Currently, the spectroscopic data does not exist to determine whether $\sigma(M|\lambda)_{int}$ evolves with redshift. However, in the coming years, I plan to extend this analysis to higher redshifts, using data from the Dark Energy Spectroscopic Instrument (DESI), which will provide a sizeable amount of spectroscopic data and yield a large sample of clusters with 10 or more member galaxies allowing for measurements of stacked caustic phase spaces that can be used to estimate the halo mass out to higher redshifts. In what follows, I outline how I plan to approach this project.

To determine how $\sigma(M|\lambda)_{int}$ evolves with redshift, I will build on my existing hierarchical Bayesian MCMC framework (*Golden-Marx and Miller*, 2019). Using DESI spectroscopic information, I will perform a similar analysis to what was previously described for the SDSS-C4 sample for the data covering the redshift range $z < 0.3$. To measure the required parameters needed for this analysis, I will use existing BCG and member galaxy photometry (within 0.5 R_{200}), to measure the magnitudes, stellar mass and magnitude gap (via the red sequence). DESI spectroscopic information will also be used, when available to reduce the measurement uncertainty on the magnitude gap by removing foreground outliers as well as provide precise spectroscopic redshift measurements for each cluster. I plan to calculate halo masses in two manners. First, using the radius-velocity phase spaces, I will measure the caustic halo masses in the manner described in *Gifford et al.* (2013) and Section 1.4.1.3. Since the number of galaxies used to measure the caustic radius-velocity phase space in DESI clusters will likely be low (10-15 galaxies) compared to the more heavily sampled low-z SDSS-C4 clusters, I will use the stacked caustics. Halo masses will also be estimated using a mass-richness relation given by a cluster-finding algorithm, such as redMaPPer (*Rykoff et al.*, 2014), run on the DESI data. Therefore, using galaxy clusters found within DESI, I will have stellar mass, magnitude gap, redshift, caustic halo mass, and mass-richness halo mass measurements for each cluster. Using a modified version of my hierarchical Bayesian MCMC model, I will incorporate the uncertainty in the caustic halo masses as a free parameter (with a uniform prior), the mass-richness relation uncertainty, which it is covariant with, as well as redshift evolution parameters for both halo mass uncertainties, increasing the number of free parameters for the model used in *Golden-Marx and Miller* (2019) and Golden-Marx et al. (in prep.) from 8 to 12. This analysis will allow me to confirm whether the uncertainty on the caustic halo masses or the mass-richness relation evolves as a function of redshift or correlates with any of the measured parameters in the SMHM relation associated with the galaxy-halo connection. This analysis would be particularly useful for our estimates of cosmological parameters, done via halo mass estimates and also improve our characterization of the SMHM relation's late-time redshift evolution presented in *Golden-Marx and Miller* (2019) and Golden-Marx et al. (in prep.).

BIBLIOGRAPHY

BIBLIOGRAPHY

Abell, G. O. (1958), The Distribution of Rich Clusters of Galaxies., *ApJS*, *3*, 211, doi:10.1086/190036.

Abell, G. O., H. G. Corwin, Jr., and R. P. Olowin (1989), A catalog of rich clusters of galaxies, *ApJS*, *70*, 1–138, doi:10.1086/191333.

Adelman-McCarthy, J. K., et al. (2006), The Fourth Data Release of the Sloan Digital Sky Survey, *ApJS*, *162*, 38–48, doi:10.1086/497917.

Aguerri, J. A. L., et al. (2011), Fossil groups origins. I. RX J105453.3+552102 a very massive and relaxed system at z ˜ 0.5, *A&A*, *527*, A143, doi:10.1051/0004-6361/201015364.

Aihara, H., et al. (2011), The Eighth Data Release of the Sloan Digital Sky Survey: First Data from SDSS-III, *ApJS*, *193*, 29, doi:10.1088/0067-0049/193/2/29.

Alam, S., et al. (2015), The Eleventh and Twelfth Data Releases of the Sloan Digital Sky Survey: Final Data from SDSS-III, *ApJS*, *219*, 12, doi:10.1088/0067-0049/219/1/12.

Andreon, S. (2015), Making the observational parsimonious richness a working mass proxy, *A&A*, *582*, A100, doi:10.1051/0004-6361/201526081.

Andreon, S., and M. A. Hurn (2010), The scaling relation between richness and mass of galaxy clusters: a Bayesian approach, *MNRAS*, *404*, 1922–1937, doi:10.1111/j.1365-2966.2010.16406.x.

Aragon-Salamanca, A., C. M. Baugh, and G. Kauffmann (1998), The K-band Hubble diagram for the brightest cluster galaxies: a test of hierarchical galaxy formation models, *MNRAS*, *297*, 427–434, doi:10.1046/j.1365-8711.1998.01495.x.

Artale, M. C., I. Zehavi, S. Contreras, and P. Norberg (2018), The impact of assembly bias on the halo occupation in hydrodynamical simulations, *MNRAS*, *480*, 3978–3992, doi:10.1093/mnras/sty2110.

Behroozi, P., R. Wechsler, A. Hearin, and C. Conroy (2018), UniverseMachine: The Correlation between Galaxy Growth and Dark Matter Halo Assembly from z=0-10, *ArXiv e-prints*.

Behroozi, P. S., C. Conroy, and R. H. Wechsler (2010), A Comprehensive Analysis of Uncertainties Affecting the Stellar Mass-Halo Mass Relation for 0 z 4, *ApJ*, *717*, 379–403, doi:10.1088/0004-637X/717/1/379.

Behroozi, P. S., R. H. Wechsler, and C. Conroy (2013a), The Average Star Formation Histories of Galaxies in Dark Matter Halos from z = 0-8, *ApJ*, *770*, 57, doi:10.1088/0004-637X/770/1/57.

Behroozi, P. S., R. H. Wechsler, and C. Conroy (2013b), On the Lack of Evolution in Galaxy Star Formation Efficiency, *ApJ*, *762*, L31, doi:10.1088/2041-8205/762/2/L31.

Bell, E. F., D. H. McIntosh, N. Katz, and M. D. Weinberg (2003), A First Estimate of the Baryonic Mass Function of Galaxies, *ApJ*, *585*, L117–L120, doi:10.1086/374389.

Bell, E. F., et al. (2006), Dry Mergers in GEMS: The Dynamical Evolution of Massive Early-Type Galaxies, *ApJ*, *640*, 241–251, doi:10.1086/499931.

Bellstedt, S., et al. (2016), The evolution in the stellar mass of brightest cluster galaxies over the past 10 billion years, *MNRAS*, *460*, 2862–2874, doi:10.1093/mnras/stw1184.

Bernardi, M., J. B. Hyde, R. K. Sheth, C. J. Miller, and R. C. Nichol (2007), The Luminosities, Sizes, and Velocity Dispersions of Brightest Cluster Galaxies: Implications for Formation History, *AJ*, *133*, 1741–1755, doi:10.1086/511783.

Bernardi, M., A. Meert, R. K. Sheth, V. Vikram, M. Huertas-Company, S. Mei, and F. Shankar (2013), The massive end of the luminosity and stellar mass functions: dependence on the fit to the light profile, *MNRAS*, *436*, 697–704, doi:10.1093/mnras/stt1607.

Bernstein, J. P., and S. P. Bhavsar (2001), Models for the magnitude-distribution of brightest cluster galaxies, *MNRAS*, *322*, 625–630, doi:10.1046/j.1365-8711.2001.04124.x.

Bhavsar, S. P., and J. D. Barrow (1985), First ranked galaxies in groups and clusters, *MNRAS*, *213*, 857–869, doi:10.1093/mnras/213.4.857.

Blanton, M. R., and S. Roweis (2007), K-Corrections and Filter Transformations in the Ultraviolet, Optical, and Near-Infrared, *AJ*, *133*, 734–754, doi:10.1086/510127.

Blanton, M. R., et al. (2001), The Luminosity Function of Galaxies in SDSS Commissioning Data, *AJ*, *121*, 2358–2380, doi:10.1086/320405.

Blumenthal, G. R., S. M. Faber, J. R. Primack, and M. J. Rees (1984), Formation of galaxies and large-scale structure with cold dark matter, *Nature*, *311*, 517–525, doi: 10.1038/311517a0.

Brough, S., K.-V. Tran, R. G. Sharp, A. von der Linden, and W. J. Couch (2011), Spatial kinematics of Brightest Cluster Galaxies and their close companions from Integral Field Unit spectroscopy, *MNRAS*, *414*, L80–L84, doi:10.1111/j.1745-3933.2011.01060.x.

Brown, M. J. I., A. Dey, B. T. Jannuzi, K. Brand, A. J. Benson, M. Brodwin, D. J. Croton, and P. R. Eisenhardt (2007), The Evolving Luminosity Function of Red Galaxies, *ApJ*, *654*, 858–877, doi:10.1086/509652.

Bruzual, G., and S. Charlot (2003), Stellar population synthesis at the resolution of 2003, *MNRAS*, *344*, 1000–1028, doi:10.1046/j.1365-8711.2003.06897.x.

Burke, C., M. Hilton, and C. Collins (2015), Coevolution of brightest cluster galaxies and intracluster light using CLASH, *MNRAS*, *449*, 2353–2367, doi:10.1093/mnras/stv450.

Busch, P., and S. D. M. White (2017), Assembly bias and splashback in galaxy clusters, *MNRAS*, *470*, 4767–4781, doi:10.1093/mnras/stx1584.

Cattaneo, A., et al. (2009), The role of black holes in galaxy formation and evolution, *Nature*, *460*, 213–219, doi:10.1038/nature08135.

Chabrier, G. (2003), Galactic Stellar and Substellar Initial Mass Function, *PASP*, *115*, 763–795, doi:10.1086/376392.

Coil, A. L., J. A. Newman, M. C. Cooper, M. Davis, S. M. Faber, D. C. Koo, and C. N. A. Willmer (2006), The DEEP2 Galaxy Redshift Survey: Clustering of Galaxies as a Function of Luminosity at z = 1, *ApJ*, *644*, 671–677, doi:10.1086/503601.

Colless, M. (1989), The dynamics of rich clusters. II - Luminosity functions, *MNRAS*, *237*, 799–826, doi:10.1093/mnras/237.3.799.

Collins, C. A., et al. (2009), Early assembly of the most massive galaxies, *Nature*, *458*, 603–606, doi:10.1038/nature07865.

Conroy, C., R. H. Wechsler, and A. V. Kravtsov (2007), The Hierarchical Build-Up of Massive Galaxies and the Intracluster Light since z = 1, *ApJ*, *668*, 826–838, doi: 10.1086/521425.

Contini, E., G. De Lucia, Á. Villalobos, and S. Borgani (2014), On the formation and physical properties of the intracluster light in hierarchical galaxy formation models, *MNRAS*, *437*, 3787–3802, doi:10.1093/mnras/stt2174.

Contini, E., S. K. Yi, and X. Kang (2018), The different growth pathways of Brightest Cluster Galaxies and the Intra-Cluster Light, *MNRAS*, doi:10.1093/mnras/sty1518.

Cooke, K. C., K. Fogarty, J. S. Kartaltepe, J. Moustakas, C. P. O'Dea, and M. Postman (2018), Stellar Mass and 3.4 μm M/L Ratio Evolution of Brightest Cluster Galaxies in COSMOS since z$\sim$ 1.0, *ApJ*, *857*, $122, doi: 10.3847/1538-4357/aab895$.

Croton, D. J., et al. (2006), The many lives of active galactic nuclei: cooling flows, black holes and the luminosities and colours of galaxies, *MNRAS*, *365*, 11–28, doi: 10.1111/j.1365-2966.2005.09675.x.

Dariush, A. A., S. Raychaudhury, T. J. Ponman, H. G. Khosroshahi, A. J. Benson, R. G. Bower, and F. Pearce (2010), The mass assembly of galaxy groups and the evolution of the magnitude gap, *MNRAS*, *405*, 1873–1887, doi:10.1111/j.1365-2966.2010.16569.x.

De Lucia, G., and J. Blaizot (2007), The hierarchical formation of the brightest cluster galaxies, *MNRAS*, *375*, 2–14, doi:10.1111/j.1365-2966.2006.11287.x.

De Lucia, G., G. Kauffmann, V. Springel, S. D. M. White, B. Lanzoni, F. Stoehr, G. Tormen, and N. Yoshida (2004), Substructures in cold dark matter haloes, *MNRAS*, *348*, 333–344, doi:10.1111/j.1365-2966.2004.07372.x.

de Vaucouleurs, G. (1948), Recherches sur les Nebuleuses Extragalactiques, *Annales d'Astrophysique*, *11*, 247.

Deason, A. J., C. Conroy, A. R. Wetzel, and J. L. Tinker (2013), Stellar Mass-gap as a Probe of Halo Assembly History and Concentration: Youth Hidden among Old Fossils, *ApJ*, *777*, 154, doi:10.1088/0004-637X/777/2/154.

Dekel, A., R. Sari, and D. Ceverino (2009), Formation of Massive Galaxies at High Redshift: Cold Streams, Clumpy Disks, and Compact Spheroids, *ApJ*, *703*, 785–801, doi: 10.1088/0004-637X/703/1/785.

Diaferio, A. (1999), Mass estimation in the outer regions of galaxy clusters, *MNRAS*, *309*, 610–622, doi:10.1046/j.1365-8711.1999.02864.x.

Diaferio, A., and M. J. Geller (1997), Infall Regions of Galaxy Clusters, *ApJ*, *481*, 633–643, doi:10.1086/304075.

Díaz-Giménez, E., H. Muriel, and C. Mendes de Oliveira (2008), Fossil groups in the Millennium Simulation. Evolution of the brightest galaxies, *A&A*, *490*, 965–973, doi: 10.1051/0004-6361:200809760.

Djorgovski, S., and M. Davis (1987), Fundamental properties of elliptical galaxies, *ApJ*, *313*, 59–68, doi:10.1086/164948.

D'Onghia, E., J. Sommer-Larsen, A. D. Romeo, A. Burkert, K. Pedersen, L. Portinari, and J. Rasmussen (2005), The Formation of Fossil Galaxy Groups in the Hierarchical Universe, *ApJ*, *630*, L109–L112, doi:10.1086/491651.

Dubinski, J. (1998), The Origin of the Brightest Cluster Galaxies, *ApJ*, *502*, 141–149, doi: 10.1086/305901.

Edge, A. C. (1991), On the relation between the X-ray properties of clusters of galaxies and their brightest cluster member, *MNRAS*, *250*, 103–110, doi:10.1093/mnras/250.1.103.

Eggen, O. J., D. Lynden-Bell, and A. R. Sandage (1962), Evidence from the motions of old stars that the Galaxy collapsed., *ApJ*, *136*, 748, doi:10.1086/147433.

Faber, S. M., and R. E. Jackson (1976), Velocity dispersions and mass-to-light ratios for elliptical galaxies, *ApJ*, *204*, 668–683, doi:10.1086/154215.

Faber, S. M., et al. (2007), Galaxy Luminosity Functions to z˜1 from DEEP2 and COMBO-17: Implications for Red Galaxy Formation, *ApJ*, *665*, 265–294, doi:10.1086/519294.

Fabian, A. C. (1994), Cooling Flows in Clusters of Galaxies, *ARA&A*, *32*, 277–318, doi: 10.1146/annurev.aa.32.090194.001425.

Fabian, A. C. (2012), Observational Evidence of Active Galactic Nuclei Feedback, *ARA&A*, *50*, 455–489, doi:10.1146/annurev-astro-081811-125521.

Foreman-Mackey, D., D. W. Hogg, D. Lang, and J. Goodman (2013), emcee: The MCMC Hammer, *PASP*, *125*, 306, doi:10.1086/670067.

Gao, L., A. Loeb, P. J. E. Peebles, S. D. M. White, and A. Jenkins (2004), Early Formation and Late Merging of the Giant Galaxies, *ApJ*, *614*, 17–25, doi:10.1086/423444.

Garilli, B., D. Maccagni, and S. Andreon (1999), Composite luminosity function of cluster galaxies, *A&A*, *342*, 408–416.

Ghigna, S., B. Moore, F. Governato, G. Lake, T. Quinn, and J. Stadel (2000), Density Profiles and Substructure of Dark Matter Halos: Converging Results at Ultra-High Numerical Resolution, *ApJ*, *544*, 616–628, doi:10.1086/317221.

Gifford, D., and C. J. Miller (2013), Velocity Anisotropy and Shape Bias in the Caustic Technique, *ApJ*, *768*, L32, doi:10.1088/2041-8205/768/2/L32.

Gifford, D., C. Miller, and N. Kern (2013), A Systematic Analysis of Caustic Methods for Galaxy Cluster Masses, *ApJ*, *773*, 116, doi:10.1088/0004-637X/773/2/116.

Gifford, D., N. Kern, and C. J. Miller (2017), Stacking Caustic Masses from Galaxy Clusters, *ApJ*, *834*, 204, doi:10.3847/1538-4357/834/2/204.

Golden-Marx, J. B., and C. J. Miller (2018), The Impact of Environment on the Stellar MassHalo Mass Relation, *ApJ*, *860*, 2, doi:10.3847/1538-4357/aac2bd.

Golden-Marx, J. B., and C. J. Miller (2019), The Impact of Environment on Late Time Evolution of the Stellar Mass - Halo Mass Relation, *arXiv e-prints*.

Gonzalez, A. H., A. I. Zabludoff, and D. Zaritsky (2005), Intracluster Light in Nearby Galaxy Clusters: Relationship to the Halos of Brightest Cluster Galaxies, *ApJ*, *618*, 195–213, doi:10.1086/425896.

Gonzalez, A. H., D. Zaritsky, and A. I. Zabludoff (2007), A Census of Baryons in Galaxy Clusters and Groups, *ApJ*, *666*, 147–155, doi:10.1086/519729.

Gozaliasl, G., A. Finoguenov, H. G. Khosroshahi, M. Mirkazemi, G. Erfanianfar, and M. Tanaka (2016), Brightest group galaxies: stellar mass and star formation rate (paper I), *MNRAS*, *458*, 2762–2775, doi:10.1093/mnras/stw448.

Graham, A. W., S. P. Driver, V. Petrosian, C. J. Conselice, M. A. Bershady, S. M. Crawford, and T. Goto (2005), Total Galaxy Magnitudes and Effective Radii from Petrosian Magnitudes and Radii, *AJ*, *130*, 1535–1544, doi:10.1086/444475.

Groenewald, D. N., R. E. Skelton, D. G. Gilbank, and S. I. Loubser (2017), The close pair fraction of BCGs since z = 0.5: major mergers dominate recent BCG stellar mass growth, *MNRAS*, *467*, 4101–4117, doi:10.1093/mnras/stx340.

Gu, M., C. Conroy, and P. Behroozi (2016), Hierarchical Galaxy Growth and Scatter in the Stellar Mass-Halo Mass Relation, *ApJ*, *833*, 2, doi:10.3847/0004-637X/833/1/2.

Gull, S. F. (1989), Developments in maximum entropy data analysis, in *Maximum Entropy and Bayesian Methods*, pp. 53–71, Springer Netherlands, doi:10.1007/978-94-015-7860-8_4.

Gunn, J. E., and J. R. Gott, III (1972), On the Infall of Matter Into Clusters of Galaxies and Some Effects on Their Evolution, *ApJ*, *176*, 1, doi:10.1086/151605.

Gunn, J. E., and J. B. Oke (1975), Spectrophotometry of faint cluster galaxies and the Hubble diagram - an approach to cosmology, *ApJ*, *195*, 255–268, doi:10.1086/153325.

Guo, Q., S. White, M. Boylan-Kolchin, G. De Lucia, G. Kauffmann, G. Lemson, C. Li, V. Springel, and S. Weinmann (2011), From dwarf spheroidals to cD galaxies: simulating the galaxy population in a ΛCDM cosmology, *MNRAS*, *413*, 101–131, doi:10.1111/j.1365-2966.2010.18114.x.

Hansen, S. M., E. S. Sheldon, R. H. Wechsler, and B. P. Koester (2009), The Galaxy Content of SDSS Clusters and Groups, *ApJ*, *699*, 1333–1353, doi:10.1088/0004-637X/699/2/1333.

Harrison, C. D., et al. (2012), The XMM Cluster Survey: The Stellar Mass Assembly of Fossil Galaxies, *ApJ*, *752*, 12, doi:10.1088/0004-637X/752/1/12.

Hausman, M. A., and J. P. Ostriker (1978), Galactic cannibalism. III - The morphological evolution of galaxies and clusters, *ApJ*, *224*, 320–336, doi:10.1086/156380.

He, Y. Q., X. Y. Xia, C. N. Hao, Y. P. Jing, S. Mao, and C. Li (2013), Photometric Properties and Luminosity Function of Nearby Massive Early-type Galaxies, *ApJ*, *773*, 37, doi:10.1088/0004-637X/773/1/37.

Hearin, A. P., and D. F. Watson (2013), The dark side of galaxy colour, *MNRAS*, *435*, 1313–1324, doi:10.1093/mnras/stt1374.

Henriques, B. M. B., S. D. M. White, G. Lemson, P. A. Thomas, Q. Guo, G.-D. Marleau, and R. A. Overzier (2012), Confronting theoretical models with the observed evolution of the galaxy population out to z= 4, *MNRAS*, *421*, 2904–2916, doi:10.1111/j.1365-2966.2012.20521.x.

Henriques, B. M. B., S. D. M. White, P. A. Thomas, R. Angulo, Q. Guo, G. Lemson, V. Springel, and R. Overzier (2015), Galaxy formation in the Planck cosmology - I. Matching the observed evolution of star formation rates, colours and stellar masses, *MNRAS*, *451*, 2663–2680, doi:10.1093/mnras/stv705.

Huang, S., A. Leauthaud, J. E. Greene, K. Bundy, Y.-T. Lin, M. Tanaka, S. Miyazaki, and Y. Komiyama (2018), Individual stellar haloes of massive galaxies measured to 100 kpc at 0.3 z 0.5 using Hyper Suprime-Cam, *MNRAS*, *475*, 3348–3368, doi: 10.1093/mnras/stx3200.

Inagaki, T., Y.-T. Lin, H.-J. Huang, B.-C. Hsieh, and N. Sugiyama (2015), Stellar mass assembly of brightest cluster galaxies at late times, *MNRAS*, *446*, 1107–1114, doi: 10.1093/mnras/stu2126.

Jeans, J. H. (1902), The Stability of a Spherical Nebula, *Philosophical Transactions of the Royal Society of London Series A*, *199*, 1–53, doi:10.1098/rsta.1902.0012.

Jones, C., and W. Forman (1984), The structure of clusters of galaxies observed with Einstein, *ApJ*, *276*, 38–55, doi:10.1086/161591.

Jones, L. R., T. J. Ponman, and D. A. Forbes (2000), Multiwavelength observations of an evolved galaxy group: an end-point of galaxy merging?, *MNRAS*, *312*, 139–150, doi: 10.1046/j.1365-8711.2000.03118.x.

Jones, L. R., T. J. Ponman, A. Horton, A. Babul, H. Ebeling, and D. J. Burke (2003), The nature and space density of fossil groups of galaxies, *MNRAS*, *343*, 627–638, doi: 10.1046/j.1365-8711.2003.06702.x.

Kaiser, N. (1984), On the spatial correlations of Abell clusters, *ApJ*, *284*, L9–L12, doi: 10.1086/184341.

Kereš, D., N. Katz, D. H. Weinberg, and R. Davé (2005), How do galaxies get their gas?, *MNRAS*, *363*, 2–28, doi:10.1111/j.1365-2966.2005.09451.x.

Khochfar, S., and J. Silk (2006), On the origin of stars in bulges and elliptical galaxies, *MNRAS*, *370*, 902–910, doi:10.1111/j.1365-2966.2006.10533.x.

Kravtsov, A. V., O. Y. Gnedin, and A. A. Klypin (2004), The Tumultuous Lives of Galactic Dwarfs and the Missing Satellites Problem, *ApJ*, *609*, 482–497, doi:10.1086/421322.

Kravtsov, A. V., A. A. Vikhlinin, and A. V. Meshcheryakov (2018), Stellar MassHalo Mass Relation and Star Formation Efficiency in High-Mass Halos, *Astronomy Letters*, *44*, 8–34, doi:10.1134/S1063773717120015.

Kron, R. G. (1980), Photometry of a complete sample of faint galaxies, *ApJS*, *43*, 305–325, doi:10.1086/190669.

Kundert, A., E. D'Onghia, and J. A. L. Aguerri (2017), Are Fossil Groups Early-forming Galaxy Systems?, *ApJ*, *845*, 45, doi:10.3847/1538-4357/aa7b88.

La Barbera, F., R. R. de Carvalho, I. G. de La Rosa, P. A. A. Lopes, J. L. Kohl-Moreira, and H. V. Capelato (2010), SPIDER - I. Sample and galaxy parameters in the grizYJHK wavebands, *MNRAS*, *408*, 1313–1334, doi:10.1111/j.1365-2966.2010.16850.x.

Lange, J. U., F. C. van den Bosch, A. Hearin, D. Campbell, A. R. Zentner, A. Villarreal, and Y.-Y. Mao (2018), Brightest galaxies as halo centre tracers in SDSS DR7, *MNRAS*, *473*, 2830–2851, doi:10.1093/mnras/stx2434.

Laporte, C. F. P., S. D. M. White, T. Naab, and L. Gao (2013), The growth in size and mass of cluster galaxies since z = 2, *MNRAS*, *435*, 901–909, doi:10.1093/mnras/stt912.

Larson, R. B. (1969), A model for the formation of a spherical galaxy, *MNRAS*, *145*, 405, doi:10.1093/mnras/145.4.405.

Larson, R. B. (1975), Models for the formation of elliptical galaxies, *MNRAS*, *173*, 671–699, doi:10.1093/mnras/173.3.671.

Lauer, T. R., M. Postman, M. A. Strauss, G. J. Graves, and N. E. Chisari (2014), Brightest Cluster Galaxies at the Present Epoch, *ApJ*, *797*, 82, doi:10.1088/0004-637X/797/2/82.

Lauer, T. R., et al. (2007), The Masses of Nuclear Black Holes in Luminous Elliptical Galaxies and Implications for the Space Density of the Most Massive Black Holes, *ApJ*, *662*, 808–834, doi:10.1086/518223.

Leauthaud, A., et al. (2012), New Constraints on the Evolution of the Stellar-to-dark Matter Connection: A Combined Analysis of Galaxy-Galaxy Lensing, Clustering, and Stellar Mass Functions from z = 0.2 to z =1, *ApJ*, *744*, 159, doi:10.1088/0004-637X/744/2/159.

Lidman, C., et al. (2012), Evidence for significant growth in the stellar mass of brightest cluster galaxies over the past 10 billion years, *MNRAS*, *427*, 550–568, doi:10.1111/j.1365-2966.2012.21984.x.

Lin, Y.-T., and J. J. Mohr (2004), K-band Properties of Galaxy Clusters and Groups: Brightest Cluster Galaxies and Intracluster Light, *ApJ*, *617*, 879–895, doi:10.1086/425412.

Lin, Y.-T., J. P. Ostriker, and C. J. Miller (2010), A New Test of the Statistical Nature of the Brightest Cluster Galaxies, *ApJ*, *715*, 1486–1496, doi:10.1088/0004-637X/715/2/1486.

Lin, Y.-T., M. Brodwin, A. H. Gonzalez, P. Bode, P. R. M. Eisenhardt, S. A. Stanford, and A. Vikhlinin (2013), The Stellar Mass Growth of Brightest Cluster Galaxies in the IRAC Shallow Cluster Survey, *ApJ*, *771*, 61, doi:10.1088/0004-637X/771/1/61.

Lin, Y.-T., R. Mandelbaum, Y.-H. Huang, H.-J. Huang, N. Dalal, B. Diemer, H.-Y. Jian, and A. Kravtsov (2016), On Detecting Halo Assembly Bias with Galaxy Populations, *ApJ*, *819*, 119, doi:10.3847/0004-637X/819/2/119.

Lin, Y.-T., et al. (2017), First Results on the Cluster Galaxy Population from the Subaru Hyper Suprime-Cam Survey. III. Brightest Cluster Galaxies, Stellar Mass Distribution, and Active Galaxies, *ApJ*, *851*, 139, doi:10.3847/1538-4357/aa9bf5.

Loh, Y.-S., and M. A. Strauss (2006), The bright end of the luminosity function of red sequence galaxies, *MNRAS*, *366*, 373–386, doi:10.1111/j.1365-2966.2005.09714.x.

Malumuth, E. M., and D. O. Richstone (1984), The evolution of clusters of galaxies. II - Tidal stripping versus mergers as a function of richness, *ApJ*, *276*, 413–422, doi:10.1086/161626.

Mancone, C. L., and A. H. Gonzalez (2012), EzGal: A Flexible Interface for Stellar Population Synthesis Models, *PASP*, *124*, 606–615, doi:10.1086/666502.

Mao, Y.-Y., A. R. Zentner, and R. H. Wechsler (2018), Beyond assembly bias: exploring secondary halo biases for cluster-size haloes, *MNRAS*, *474*, 5143–5157, doi:10.1093/mnras/stx3111.

Matthee, J., J. Schaye, R. A. Crain, M. Schaller, R. Bower, and T. Theuns (2017), The origin of scatter in the stellar mass-halo mass relation of central galaxies in the EAGLE simulation, *MNRAS*, *465*, 2381–2396, doi:10.1093/mnras/stw2884.

McClintock, T., et al. (2019), Dark Energy Survey Year 1 results: weak lensing mass calibration of redMaPPer galaxy clusters, *MNRAS*, *482*, 1352–1378, doi:10.1093/mnras/sty2711.

McNamara, B. R., and P. E. J. Nulsen (2007), Heating Hot Atmospheres with Active Galactic Nuclei, *ARA&A*, *45*, 117–175, doi:10.1146/annurev.astro.45.051806.110625.

Merritt, D. (1985), Relaxation and tidal stripping in rich clusters of galaxies. III - Growth of a massive central galaxy, *ApJ*, *289*, 18–32, doi:10.1086/162860.

Miller, C. J., et al. (2005), The C4 Clustering Algorithm: Clusters of Galaxies in the Sloan Digital Sky Survey, *AJ*, *130*, 968–1001, doi:10.1086/431357.

Milosavljević, M., C. J. Miller, S. R. Furlanetto, and A. Cooray (2006), Cluster Merger Variance and the Luminosity Gap Statistic, *ApJ*, *637*, L9–L12, doi:10.1086/500547.

Miyatake, H., S. More, M. Takada, D. N. Spergel, R. Mandelbaum, E. S. Rykoff, and E. Rozo (2016), Evidence of Halo Assembly Bias in Massive Clusters, *Physical Review Letters*, *116*(4), 041301, doi:10.1103/PhysRevLett.116.041301.

Moody, C. E., A. J. Romanowsky, T. J. Cox, G. S. Novak, and J. R. Primack (2014), Simulating multiple merger pathways to the central kinematics of early-type galaxies, *MNRAS*, *444*, 1475–1485, doi:10.1093/mnras/stu1444.

Moster, B. P., R. S. Somerville, C. Maulbetsch, F. C. van den Bosch, A. V. Macciò, T. Naab, and L. Oser (2010), Constraints on the Relationship between Stellar Mass and Halo Mass at Low and High Redshift, *ApJ*, *710*, 903–923, doi:10.1088/0004-637X/710/2/903.

Moster, B. P., T. Naab, and S. D. M. White (2013), Galactic star formation and accretion histories from matching galaxies to dark matter haloes, *MNRAS*, *428*, 3121–3138, doi:10.1093/mnras/sts261.

Moster, B. P., T. Naab, and S. D. M. White (2018), EMERGE - an empirical model for the formation of galaxies since z
10, *MNRAS*, *477*, 1822–1852, doi:10.1093/mnras/sty655.

Murante, G., M. Giovalli, O. Gerhard, M. Arnaboldi, S. Borgani, and K. Dolag (2007), The importance of mergers for the origin of intracluster stars in cosmological simulations of galaxy clusters, *MNRAS*, *377*, 2–16, doi:10.1111/j.1365-2966.2007.11568.x.

Naab, T., S. Khochfar, and A. Burkert (2006), Properties of Early-Type, Dry Galaxy Mergers and the Origin of Massive Elliptical Galaxies, *ApJ*, *636*, L81–L84, doi:10.1086/500205.

Naab, T., P. H. Johansson, and J. P. Ostriker (2009), Minor Mergers and the Size Evolution of Elliptical Galaxies, *ApJ*, *699*, L178–L182, doi:10.1088/0004-637X/699/2/L178.

Nelan, J. E., R. J. Smith, M. J. Hudson, G. A. Wegner, J. R. Lucey, S. A. W. Moore, S. J. Quinney, and N. B. Suntzeff (2005), NOAO Fundamental Plane Survey. II. Age and Metallicity along the Red Sequence from Line-Strength Data, *ApJ*, *632*, 137–156, doi:10.1086/431962.

Nipoti, C. (2017), The special growth history of central galaxies in groups and clusters, *MNRAS*, doi:10.1093/mnras/stx112.

Nipoti, C., T. Treu, and A. S. Bolton (2009), Dry Mergers and the Formation of Early-Type Galaxies: Constraints from Lensing and Dynamics, *ApJ*, *703*, 1531–1544, doi:10.1088/0004-637X/703/2/1531.

Nipoti, C., T. Treu, A. Leauthaud, K. Bundy, A. B. Newman, and M. W. Auger (2012), Size and velocity-dispersion evolution of early-type galaxies in a Λ cold dark matter universe, *MNRAS*, *422*, 1714–1731, doi:10.1111/j.1365-2966.2012.20749.x.

Norberg, P., et al. (2002), The 2dF Galaxy Redshift Survey: the dependence of galaxy clustering on luminosity and spectral type, *MNRAS*, *332*, 827–838, doi:10.1046/j.1365-8711.2002.05348.x.

Oemler, A., Jr. (1976), The structure of elliptical and cD galaxies., *ApJ*, *209*, 693–709, doi:10.1086/154769.

Oliva-Altamirano, P., et al. (2014), Galaxy And Mass Assembly (GAMA): testing galaxy formation models through the most massive galaxies in the Universe, *MNRAS*, *440*, 762–775, doi:10.1093/mnras/stu277.

Oser, L., J. P. Ostriker, T. Naab, P. H. Johansson, and A. Burkert (2010), The Two Phases of Galaxy Formation, *ApJ*, *725*, 2312–2323, doi:10.1088/0004-637X/725/2/2312.

Oser, L., T. Naab, J. P. Ostriker, and P. H. Johansson (2012), The Cosmological Size and Velocity Dispersion Evolution of Massive Early-type Galaxies, *ApJ*, *744*, 63, doi:10.1088/0004-637X/744/1/63.

Ostriker, J. P., and M. A. Hausman (1977), Cannibalism among the galaxies - Dynamically produced evolution of cluster luminosity functions, *ApJ*, *217*, L125–L129, doi:10.1086/182554.

Ostriker, J. P., and S. D. Tremaine (1975), Another evolutionary correction to the luminosity of giant galaxies, *ApJ*, *202*, L113–L117, doi:10.1086/181992.

Ostriker, J. P., E. Choi, A. Chow, and K. Guha (2019), MIND THE GAP: The Too Big To Fail Problem Resolved, *arXiv e-prints*.

Paranjape, A., and R. K. Sheth (2012), The luminosities of the brightest cluster galaxies and brightest satellites in SDSS groups, *MNRAS*, *423*, 1845–1855, doi:10.1111/j.1365-2966.2012.21008.x.

Partridge, R. B., and P. J. E. Peebles (1967), Are Young Galaxies Visible?, *ApJ*, *147*, 868, doi:10.1086/149079.

Peebles, P. J. E. (1965), The Black-Body Radiation Content of the Universe and the Formation of Galaxies., *ApJ*, *142*, 1317, doi:10.1086/148417.

Peebles, P. J. E. (1982), Large-scale background temperature and mass fluctuations due to scale-invariant primeval perturbations, *ApJ*, *263*, L1–L5, doi:10.1086/183911.

Petrosian, V. (1976), Surface brightness and evolution of galaxies, *ApJ*, *209*, L1–L5, doi:10.1086/182253.

Pillepich, A., et al. (2018), First results from the IllustrisTNG simulations: the stellar mass content of groups and clusters of galaxies, *MNRAS*, *475*, 648–675, doi:10.1093/mnras/stx3112.

Postman, M., and T. R. Lauer (1995), Brightest cluster galaxies as standard candles, *ApJ*, *440*, 28–47, doi:10.1086/175245.

Proctor, R. N., C. M. de Oliveira, R. Dupke, R. L. de Oliveira, E. S. Cypriano, E. D. Miller, and E. Rykoff (2011), On the mass-to-light ratios of fossil groups. Are they simply dark clusters?, *MNRAS*, *418*, 2054–2073, doi:10.1111/j.1365-2966.2011.19625.x.

Reddick, R. M., R. H. Wechsler, J. L. Tinker, and P. S. Behroozi (2013), The Connection between Galaxies and Dark Matter Structures in the Local Universe, *ApJ*, *771*, 30, doi: 10.1088/0004-637X/771/1/30.

Rhee, G. F. R. N., and H. J. Latour (1991), An X-ray optical study of 26 Abell clusters, *A&A*, *243*, 38–48.

Rozo, E., E. S. Rykoff, J. G. Bartlett, and J.-B. Melin (2015), redMaPPer - III. A detailed comparison of the Planck 2013 and SDSS DR8 redMaPPer cluster catalogues, *MNRAS*, *450*, 592–605, doi:10.1093/mnras/stv605.

Rozo, E., et al. (2009), Improvement of the Richness Estimates of maxBCG Clusters, *ApJ*, *703*, 601–613, doi:10.1088/0004-637X/703/1/601.

Ruszkowski, M., and V. Springel (2009), The Role of Dry Mergers for the Formation and Evolution of Brightest Cluster Galaxies, *ApJ*, *696*, 1094–1102, doi:10.1088/0004-637X/696/2/1094.

Rykoff, E. S., et al. (2012), Robust Optical Richness Estimation with Reduced Scatter, *ApJ*, *746*, 178, doi:10.1088/0004-637X/746/2/178.

Rykoff, E. S., et al. (2014), redMaPPer. I. Algorithm and SDSS DR8 Catalog, *ApJ*, *785*, 104, doi:10.1088/0004-637X/785/2/104.

Rykoff, E. S., et al. (2016), The RedMaPPer Galaxy Cluster Catalog From DES Science Verification Data, *ApJS*, *224*, 1, doi:10.3847/0067-0049/224/1/1.

Salpeter, E. E. (1955), The Luminosity Function and Stellar Evolution., *ApJ*, *121*, 161, doi:10.1086/145971.

Sandage, A. (1972a), The Redshift-Distance Relation. I. Angular Diameter of First Ranked Cluster Galaxies as a Function of Redshift: the Aperture Correction to Magnitudes, *ApJ*, *173*, 485, doi:10.1086/151440.

Sandage, A. (1972b), The redshift-distance relation. II. The Hubble diagram and its scatter for first-ranked cluster galaxies: A formal value for q_0., *ApJ*, *178*, 1–24, doi: 10.1086/151763.

Sandage, A., and E. Hardy (1973), The Redshift-Distance Relation. VII Absolute Magnitudes on the First Three Ranked Cluster Galaxies as Functions of Cluster Richness and Bautz-Morgan Cluster Type: the Effect of q_{o}, *ApJ*, *183*, 743–758, doi:10.1086/152263.

Schneider, D. P., J. E. Gunn, and J. G. Hoessel (1983), CCD photometry of Abell clusters. II - Surface photometry of 249 cluster galaxies, *ApJ*, *268*, 476–494, doi:10.1086/160973.

Schombert, J. M. (1986), The structure of brightest cluster members. I - Surface photometry, *ApJS*, *60*, 603–693, doi:10.1086/191100.

Searle, L., W. L. W. Sargent, and W. G. Bagnuolo (1973), The History of Star Formation and the Colors of Late-Type Galaxies, *ApJ*, *179*, 427–438, doi:10.1086/151882.

Sérsic, J. L. (1963), Influence of the atmospheric and instrumental dispersion on the brightness distribution in a galaxy, *Boletin de la Asociacion Argentina de Astronomia La Plata Argentina*, *6*, 41.

Shankar, F., et al. (2014), On the Intermediate-redshift Central Stellar Mass-Halo Mass Relation, and Implications for the Evolution of the Most Massive Galaxies Since z ˜ 1, *ApJ*, *797*, L27, doi:10.1088/2041-8205/797/2/L27.

Shankar, F., et al. (2015), Avoiding Progenitor Bias: The Structural and Mass Evolution of Brightest Group and Cluster Galaxies in Hierarchical Models since z ˜ 1, *ApJ*, *802*, 73, doi:10.1088/0004-637X/802/2/73.

Shen, S., X. Yang, H. Mo, F. van den Bosch, and S. More (2014), The Statistical Nature of the Brightest Group Galaxies, *ApJ*, *782*, 23, doi:10.1088/0004-637X/782/1/23.

Simet, M., T. McClintock, R. Mandelbaum, E. Rozo, E. Rykoff, E. Sheldon, and R. H. Wechsler (2017), Weak lensing measurement of the mass-richness relation of SDSS redMaPPer clusters, *MNRAS*, *466*, 3103–3118, doi:10.1093/mnras/stw3250.

Skibba, R. A., F. C. van den Bosch, X. Yang, S. More, H. Mo, and F. Fontanot (2011), Are brightest halo galaxies central galaxies?, *MNRAS*, *410*, 417–431, doi:10.1111/j.1365-2966.2010.17452.x.

Smoot, G. F., et al. (1992), Structure in the COBE differential microwave radiometer first-year maps, *ApJ*, *396*, L1–L5, doi:10.1086/186504.

Solanes, J. M., J. D. Perea, L. Darriba, C. García-Gómez, A. Bosma, and E. Athanassoula (2016), Forming first-ranked early-type galaxies through hierarchical dissipationless merging, *MNRAS*, *461*, 321–343, doi:10.1093/mnras/stw1278.

Somerville, R. S., R. C. Gilmore, J. R. Primack, and A. Domínguez (2012), Galaxy properties from the ultraviolet to the far-infrared: Λ cold dark matter models confront observations, *MNRAS*, *423*, 1992–2015, doi:10.1111/j.1365-2966.2012.20490.x.

Springel, V., et al. (2005), Simulations of the formation, evolution and clustering of galaxies and quasars, *Nature*, *435*, 629–636, doi:10.1038/nature03597.

Tasitsiomi, A., A. V. Kravtsov, R. H. Wechsler, and J. R. Primack (2004), Modeling Galaxy-Mass Correlations in Dissipationless Simulations, *ApJ*, *614*, 533–546, doi:10.1086/423784.

Tinker, J. L. (2017), Testing galaxy quenching theories with scatter in the stellar-to-halo mass relation, *MNRAS*, *467*, 3533–3541, doi:10.1093/mnras/stx287.

Tinker, J. L., et al. (2017), The Correlation between Halo Mass and Stellar Mass for the Most Massive Galaxies in the Universe, *ApJ*, *839*, 121, doi:10.3847/1538-4357/aa6845.

Tiret, O., P. Salucci, M. Bernardi, C. Maraston, and J. Pforr (2011), The inner structure of very massive elliptical galaxies: implications for the inside-out formation mechanism of z
2 galaxies, *MNRAS*, *411*, 1435–1444, doi:10.1111/j.1365-2966.2010.17768.x.

Tonini, C., M. Bernyk, D. Croton, C. Maraston, and D. Thomas (2012), The Evolution of Brightest Cluster Galaxies in a Hierarchical Universe, *ApJ*, *759*, 43, doi:10.1088/0004-637X/759/1/43.

Tremaine, S. D., and D. O. Richstone (1977), A test of a statistical model for the luminosities of bright cluster galaxies, *ApJ*, *212*, 311–316, doi:10.1086/155049.

Trevisan, M., G. A. Mamon, and H. G. Khosroshahi (2017), Do the stellar populations of the brightest two group galaxies depend on the magnitude gap?, *MNRAS*, *464*, 4593–4610, doi:10.1093/mnras/stw2588.

Tully, R. B., and J. R. Fisher (1977), A new method of determining distances to galaxies, *A&A*, *54*, 661–673.

Uson, J. M., S. P. Boughn, and J. R. Kuhn (1991), Diffuse light in dense clusters of galaxies. I - R-band observations of Abell 2029, *ApJ*, *369*, 46–53, doi:10.1086/169737.

Vale, A., and J. P. Ostriker (2004), Linking halo mass to galaxy luminosity, *MNRAS*, *353*, 189–200, doi:10.1111/j.1365-2966.2004.08059.x.

Vale, A., and J. P. Ostriker (2008), A non-parametric model for linking galaxy luminosity with halo/subhalo mass: are brightest cluster galaxies special?, *MNRAS*, *383*, 355–368, doi:10.1111/j.1365-2966.2007.12544.x.

van der Wel, A., E. F. Bell, F. C. van den Bosch, A. Gallazzi, and H.-W. Rix (2009), On the Size and Comoving Mass Density Evolution of Early-Type Galaxies, *ApJ*, *698*, 1232–1243, doi:10.1088/0004-637X/698/2/1232.

van Dokkum, P. G. (2005), The Recent and Continuing Assembly of Field Elliptical Galaxies by Red Mergers, *AJ*, *130*, 2647–2665, doi:10.1086/497593.

van Dokkum, P. G., et al. (2010), The Growth of Massive Galaxies Since z = 2, *ApJ*, *709*, 1018–1041, doi:10.1088/0004-637X/709/2/1018.

VanderPlas, J. (2014), Frequentism and Bayesianism: A Python-driven Primer, *arXiv e-prints*.

von Benda-Beckmann, A. M., E. D'Onghia, S. Gottlöber, M. Hoeft, A. Khalatyan, A. Klypin, and V. Müller (2008), The fossil phase in the life of a galaxy group, *MNRAS*, *386*, 2345–2352, doi:10.1111/j.1365-2966.2008.13221.x.

von der Linden, A., P. N. Best, G. Kauffmann, and S. D. M. White (2007), How special are brightest group and cluster galaxies?, *MNRAS*, *379*, 867–893, doi:10.1111/j.1365-2966.2007.11940.x.

Wake, D. A., et al. (2011), Galaxy Clustering in the NEWFIRM Medium Band Survey: The Relationship Between Stellar Mass and Dark Matter Halo Mass at 1 z 2, *ApJ*, *728*, 46, doi:10.1088/0004-637X/728/1/46.

Wechsler, R. H., and J. L. Tinker (2018), The Connection Between Galaxies and Their Dark Matter Halos, *ARA&A*, *56*, 435–487, doi:10.1146/annurev-astro-081817-051756.

Wechsler, R. H., A. R. Zentner, J. S. Bullock, A. V. Kravtsov, and B. Allgood (2006), The Dependence of Halo Clustering on Halo Formation History, Concentration, and Occupation, *ApJ*, *652*, 71–84, doi:10.1086/507120.

Welch, G. A., and G. N. Sastry (1971), Photographic Detection of “intergalactic” Matter in the Coma Cluster, *ApJ*, *169*, L3, doi:10.1086/180801.

White, S. D. M., and C. S. Frenk (1991), Galaxy formation through hierarchical clustering, *ApJ*, *379*, 52–79, doi:10.1086/170483.

White, S. D. M., and M. J. Rees (1978), Core condensation in heavy halos - A two-stage theory for galaxy formation and clustering, *MNRAS*, *183*, 341–358, doi:10.1093/mnras/183.3.341.

Wu, H.-Y., E. Rozo, and R. H. Wechsler (2008), The Effects of Halo Assembly Bias on Self-Calibration in Galaxy Cluster Surveys, *ApJ*, *688*, 729–741, doi:10.1086/591929.

Yang, X., H. J. Mo, and F. C. van den Bosch (2009), Galaxy Groups in the SDSS DR4. III. The Luminosity and Stellar Mass Functions, *ApJ*, *695*, 900–916, doi:10.1088/0004-637X/695/2/900.

Zarattini, S., et al. (2014), Fossil group origins. IV. Characterization of the sample and observational properties of fossil systems, *A&A*, *565*, A116, doi:10.1051/0004-6361/201323351.

Zarattini, S., et al. (2015), Fossil group origins. V. The dependence of the luminosity function on the magnitude gap, *A&A*, *581*, A16, doi:10.1051/0004-6361/201425506.

Zehavi, I., S. Contreras, N. Padilla, N. J. Smith, C. M. Baugh, and P. Norberg (2018), The Impact of Assembly Bias on the Galaxy Content of Dark Matter Halos, *ApJ*, *853*, 84, doi:10.3847/1538-4357/aaa54a.

Zehavi, I., et al. (2005), The Luminosity and Color Dependence of the Galaxy Correlation Function, *ApJ*, *630*, 1–27, doi:10.1086/431891.

Zehavi, I., et al. (2011), Galaxy Clustering in the Completed SDSS Redshift Survey: The Dependence on Color and Luminosity, *ApJ*, *736*, 59, doi:10.1088/0004-637X/736/1/59.

Zentner, A. R., A. P. Hearin, and F. C. van den Bosch (2014), Galaxy assembly bias: a significant source of systematic error in the galaxy-halo relationship, *MNRAS*, *443*, 3044–3067, doi:10.1093/mnras/stu1383.

Zhang, Y., et al. (2016), Galaxies in X-Ray Selected Clusters and Groups in Dark Energy Survey Data. I. Stellar Mass Growth of Bright Central Galaxies since z˜1.2, *ApJ*, *816*, 98, doi:10.3847/0004-637X/816/2/98.

Zhang, Y., et al. (2018), Dark Energy Survey Year 1 results: Detection of Intra-cluster Light at Redshift $\sim$ 0.25, *arXiv e-prints*.

Zheng, Z., A. L. Coil, and I. Zehavi (2007), Galaxy Evolution from Halo Occupation Distribution Modeling of DEEP2 and SDSS Galaxy Clustering, *ApJ*, *667*, 760–779, doi:10.1086/521074.

Zibetti, S., S. D. M. White, D. P. Schneider, and J. Brinkmann (2005), Intergalactic stars in z˜ 0.25 galaxy clusters: systematic properties from stacking of Sloan Digital Sky Survey imaging data, *MNRAS*, *358*, 949–967, doi:10.1111/j.1365-2966.2005.08817.x.

Zu, Y., and R. Mandelbaum (2015), Mapping stellar content to dark matter haloes using galaxy clustering and galaxy-galaxy lensing in the SDSS DR7, *MNRAS*, *454*, 1161–1191, doi:10.1093/mnras/stv2062.

Zu, Y., R. Mandelbaum, M. Simet, E. Rozo, and E. S. Rykoff (2017), On the level of cluster assembly bias in SDSS, *MNRAS*, *470*, 551–560, doi:10.1093/mnras/stx1264.

Zwicky, F. (1933), Die Rotverschiebung von extragalaktischen Nebeln, *Helvetica Physica Acta*, *6*, 110–127.

Zwicky, F. (1937), On the Masses of Nebulae and of Clusters of Nebulae, *ApJ*, *86*, 217, doi:10.1086/143864.

Zwicky, F. (1951), The Coma Cluster of Galaxies, *PASP*, *63*, 61, doi:10.1086/126318.

Zwicky, F. (1952), Luminous Intergalactic Matter, *PASP*, *64*, 242, doi:10.1086/126484.